Origins and geochemical characterization of the Iron-Oxide-Copper-Gold deposits in the Great Bear Magmatic Zone, NWT, Canada

by

Pedro Acosta

A thesis submitted in partial fulfillment of the requirements for the degree of

Doctor of Philosophy

Department of Earth and Atmospheric Sciences

University of Alberta

Abstract

The Great Bear magmatic zone (GBMZ) in the Northwest Territories, Canada, contains the NICO (Au-Co-Bi±Cu-W) and Sue Dianne (Cu-Ag-Au-±U-Co) deposits, and the DAMP and FAB prospects, all of which represent iron-oxide dominated polymetallic systems with comparable alteration and mineralization styles similar to iron-oxide copper gold (IOCG) deposits in Chile and Australia. Also in the study area, is the vein hosted Nori/RA (Mo-U±Cu-REE), which has less affinity to the IOCG class of deposits.

In this work, trace and major element analyses, along with stable (C, H, S, O and Cu), radiogenic isotopes (Re-Os), and fluid inclusion studies were used to constrain the origin of the IOCG systems, and the Nori/RA showing, and to suggest the potential of magnetite as a mineral indicator in till sampling exploration surveys.

Regionally, the Cr/Co ratio is higher in barren and pre-ore magnetite compared to that of magnetite co-precipitated with ore minerals and/or present in ore-rich veins and breccias. At DAMP and Sue Dianne the Co/Ni ratio is extremely high and clearly different from those of other GBMZ magnetite samples.

Collectively, the analytical data supports a magmatic-hydrothermal origin for all these systems that are temporally associated with the emplacement of the Great Bear volcanic arc between 1875 and 1865 Ma. However, some sulfur, copper and arsenic could have been recycled from carbonate-rich

metasedimentary and rocks and incorporated in the ore-bearing fluids as is suggested for the NICO deposit. Some copper might have also been leached from felsic volcanic rocks and metasedimentary rocks and incorporated into the GBMZ mineralized systems. In NICO deposit, Ca-Na-Bi(Au?)-bearing, and saline (~20 wt.% NaCl equiv + $CaCl_2$ equiv) to hyper-saline aqueous fluids (>42 wt. % NaCl equiv.) formed at 4 to 8 km depth. The Au mineralization in this system occurred via: (i) remobilization of refractory gold and Bi(?) from Fe-S-As-S mineral phases during re-crystallization of the latter, and (ii) scavenging of Au by Bi melts from co-existing hydrothermal fluids.

Despite the stable isotopes signature, and the geochronological constraints, mass balance calculations shows that felsic volcanic and metasedimentary rocks hosting these deposits are feasible sources of metals (e.g., Au, Co and Cu) for the GBMZ IOCG systems. However, for this to be true, it would require high permeabilities and efficient fluids capable of leaching, concentrating and re-precipitating metals at a single site, and a suitable hydraulic regime.

Preface

The research conducted for this thesis is a joined scientific collaboration under the Geomapping for Energy and Minerals program (GEM; Great Bear magmatic zone/Iron-Oxide-Copper-Gold deposits project) led by Dr. Louise Corriveau from the Geological Survey of Canada. The institutions involved in this project and in particular with this piece of work correspond with: the University of Alberta, Geological Survey of Canada (GSC), University of Windsor, Northwest Territories Geoscience Office (NWTGO) and Fortune Minerals Limited. Significant funding was also provided by the Natural Sciences and Engineering Research Council of Canada (NSERC) as grants given to Dr. Sarah A. Gleeson and Dr. Iain M. Samson and by the Canada Research Affiliate program (RAP) in the form of a 4 year grant given to Pedro Acosta Góngora.

This thesis comprises four scientific papers corresponding with chapters 2, 3, 4 and 5. Chapter 1 is already in press as: Acosta-Góngora, P., Gleeson, S.A., Samson, I.M., Ootes, L., and Corriveau, L., Trace elements in magnetite and its relationship to Cu-Bi-Co-Au-Ag-U-W mineralization in the Great Bear magmatic zone, NWT, Canada: Economic Geology. I was responsible for the data collection and analysis as well as the manuscript composition. S.A. Gleeson and I.M. Samson were the supervisory authors and were involved with the concept, formation and editing of the manuscript. The latter co-author also facilitated the analytical instruments for the trace element analysis. L. Ootes and L. Corriveau helped on the data collection and also contributed with the editing of the manuscript.

Chapter 2 has recently been accepted with major revisions as: Acosta-Góngora, P., Gleeson, S.A., Samson, I.M., Corriveau, L., Ootes, L., Mechanisms of gold refining at the Au-Co-Bi±Cu-W iron oxide dominated NICO deposit, NWT: Economic Geology. I was responsible for the data collection and analysis as well as the manuscript composition. S.A. Gleeson, and I.M. Samson were the supervisory authors and were involved with the concept, formation and editing of the manuscript. The latter co-author also facilitated the analytical instruments for

the trace element analysis. L. Ootes and L. Corriveau helped with the data collection and also contributed to the editing of the manuscript.

Chapters 3 and 4 are still to be submitted as: i) Acosta-Góngora, P., Gleeson, S.A., Samson, I.M., Corriveau, L., Ootes, L., The formation of the Iron-Oxide-Cobalt-Gold-Bismuth NICO deposit, Northwest Territories, Canada: evidence from isotope geochemistry and fluid inclusions, and ii) Acosta-Góngora, P., Gleeson, S.A., Samson, I.M., Jackson, S., Corriveau, L., Ootes, L., Constraints on the origin of polymetallic (Cu-Au-Co-Bi-U±Ag) iron-oxide-dominated systems in the Great Bear magmatic zone, Northwest Territories, Canada. For both papers, I was responsible for the data collection and analysis as well as the manuscript composition. S.A. Gleeson, and I.M. Samson were the supervisory authors and were involved with the concept, formation and editing of the manuscript. The latter co-author also facilitated the analytical instruments for the trace element analysis. B.E. Taylor performed the in-situ sulfur isotopes analyses, at the Geological Survey of Canada.The Cu isotopes analysis were performed in S. Jackson laboratory in the GSC. Ootes and L. Corriveau helped with the data collection and also contributed with the editing of the manuscript.

In the text, chapter 2 is cited as Acosta-Góngora et al. (in press). Similarly, chapters 3 and 4 are regarded as Acosta-Góngora et al. (in revision) and Acosta-Góngora et al. (in prep.), respectively.

Acknowledgements

Many people and organizations were involved in this project. Firstly, I would like to express my gratitude to my supervisor, Dr. Sarah Gleeson for trusting and letting me take on this project. Her continuous guidance, patience and encouragement throughout my stay in Canada brought out the best of me, as a person and scientist. I also want to extend my sincere appreciation to Dr. Iain Samson, who co-supervised this project. He provided access to laboratory facilities, as well as multiple and very valuable scientific insights along with extensive revisions of diverse manuscripts. Overall, I feel very privileged to have had such a couple of stupendous supervisors and friends. I owe special gratitude to Luke Ootes and Val Jackson. Both are great geologists from whom I learned (well… still a way to go) how to do real fieldwork. Moreover, they became very close friends and indirectly, are the ones responsible for my current marital status. In particular, I thank Luke for his unconditional friendship and innumerable scientific discussions that ultimately shed light on specific parts of the project.

I also want to extend my thanks to Dr. Louise Corriveau who, along with Sarah, also placed her trust in me and let me be part of the GEM project. Apart from the financial aid, Louise also gave me important insights on the role of alteration minerals in IOCG deposits. Her thorough reviews and critical comments helped make the scientific arguments contained in this study stronger. I owe special gratitude to Fortune Minerals and in particular to Robin Goad who let us work on the NICO and Sue Dianne properties during the summers of 2010 and 2011. Collectively, I thank the University of Alberta Earth and Atmospheric Sciences department for providing financial means and laboratory facilities. I am also grateful for other project collaborators like Dr. Robert Creaser, Dr. Bruce Taylor and Dr. Simon Jackson, for letting me use their facilities at the University of Alberta and the Geological Survey of Canada (Ottawa), respectively. I would also like to acknowledge Dr. Jeremy Richards for facilitating the Fluid Inclusions laboratory at the University of Alberta, and for multiple discussions along the way. In addition, an acknowledgement goes to Dr. Karlis Muehlenbachs for

facilitating his laboratory at University of Alberta and carrying out some of the oxygen isotopes analyses. Furthermore, I would like to thank Dr. Tom Chacko, Dr. Claire Curry, and Dan Marshall, for their valuable comments and critics on specific parts of the manuscript.

On a personal note, I would like to thank my family for their unconditional support and love, in particular to my parents and sister Pedro Acosta Nino and Patricia Gongora Vieto, and Daniela Acosta Gongora, and grandparents, Miriam Vieto Asch and Jaime Acosta Nino. As well, my gratitude to my Canadian family, Marguerite Sullivan and Tony Lee, for not only helping Maddy and myself in many respects, but also for being the best example of true and dedicated love that I had ever seen. A special mention goes to my uncle Jaime Acosta Nino, with whom I have had the most interesting conversations about life (in many countries) and who planted the seed of travelling and exploring new countries and cultures, on me.

To my old time friends Pablo Ruiz, Carlos Vargas, Jose Benavides and Carlos Benavides, a big thank you for always being there, despite the distance. To my many friends in Edmonton, but especially to Jos Hantelman and Nelson Bernal, thank you very much guys for those beer breaks. Life in Canada was a bit warmer with you around.

Last, but not least, I would like to thank my beautiful wife Madeline Lee. It has been a tough road, and multiple personal and professional sacrifices were made to keep our bond as strong as it is now. Thank you Maddy, for being my best friend and very patient with me. I cannot wait to start our new life together and for both of us to fullfil our personal and professional goals in life.

'Caminante son tus huellas el camino y nada más; caminante no hay camino, se hace camino al andar…Al andar se hace camino, y al volver la vista atrás se ha de ver la senda que nunca se ha de volver a pisar. Caminante no hay camino, si no estelas en la mar…'

Antonio Machado

Table of Contents

Appendix

List of Figures

List of Tables

List of Symbols and Abbreviations

~	Approximately
‰	parts per thousand or per mille
BIF	Banded iron formation
Cm	Centimeter
Cps	Counts per second
$\delta^{13}C$	Carbon isotope composition relative to the international V-PDB standard
$\delta^{65}Cu$	Copper isotope composition relative to the Bouganville standard
ºC	Celsius degrees
HT Ca-Fe	High Temperature calcium-iron alteration type
HT-K-Fe	High temperature potassic-iron alteration type
LT-K-Fe	Low temperature potassic iron alteration type
Ca-Fe-K	Calcium-iron-potassium alteration type
δD	Hydrogen isotope composition relative to the international V-SMOW standar
e.g.	For example
Ga	Giga annum, Billions of years ago
GBMZ	Great Bear magmatic zone
i.e.	That is
INAA	Instrumental neutron activation analysis
ICP-OES	Inductively coupled plasma atomic emission spectrometry
IOCG	Iron-Oxide-Copper-Gold deposits
Km	Kilometers
Kbar	Kilobar
LT K-Fe	Low temperature potassic-iron alteration assemblage
HT-K-Fe	High temperature potassic-iron alteration

	assemblage
LA-ICP-MS	Laser ablation inductively coupled plasma mass spectrometry
LV	Liquid-Vapor bearing fluid inclusions
LVS	Liquid-Vapor-Solid bearing fluid inclusions
Ma	Mega annum, Millions of years ago
Max	Maximun value
Min	Minimum value
M	Meter
Mm	Millimeter
N	Number of analyses
N	Number of samples
NIST	National Institute of Standard
fO_2	Oxygen fugacity
$\delta^{18}O$	Oxygen isotope composition relative to the international V-SMOW standard
Ppb	Parts per billion
Ppm	Parts per million
SEM	Scanning electron microscope
TLG	Treasure Lake Group
Σ	Sigma or One standard deviation of the mean
$\delta^{34}S$	Sulfur isotope composition relative to the international V-CDT standard
Th	Homogenization temperature
Tm_i	Final ice melting temperature
Tm_{hh}	Final hydrohalite melting temperature
Tm_h	Final halite melting temperature
Tm_{ant}	Final antarcticite melting temperature
Te	First melting temperature
$T_{l\text{-}v}$	Liquid-vapor homogenization temperature

µm	Microns
V-CDT	Vienna-Canyon Diablo Troilite
VHMS	Volcanic hosted massive sulfides deposit
V-PDB	Vienna-Pee-Dee-belemnite standard
V-SMOW	Vienna-Standard Mean Ocean Water
XRD	X-ray diffractometry
XRF	X-ray fluorescence
wt.%	Weight percent
wt.% NaCl equiv	Salinity of a fluid given in weight percent and in terms of the halite concentration
wt.% $CaCl_2$equiv	Salinity of a fluid given in weight percent and in terms of the calcium chloride concentration
vol.%	Volume percent
atm. %	Atomic percent

Mineral abbreviations

Magnetite types (as given in Chapter 2)

Dmag	DAMP prospect magnetite
Fmag1	FAB prospect magnetite 1
Fmag2	FAB prospect magnetite 2
NImag1	NICO deposit magnetite 1
Nimag2	NICO deposit magnetite 2
Nimag3	NICO deposit magnetite 3
Nomag1	Nori/RA prospect magnetite 1
Nomag2	Nori/RA prospect magnetite 2
NomaQks	Nori/RA prospect magnetite in quartz feldspar veins
Sdmag	Sue Dianne deposit magnetite
Temag	Terra magnetite-apatite body magnetite
T1mag	Lower siltstone unit magnetite, Treasure Lake Group

T2mag	Carbonate unit magnetite, Treasure Lake Group

Generic abbreviations for minerals

Act	Actinolite
Amp	Amphibole
Ap	Apatite
Apy	Arsenopyrite
apy-s	Arsenopyrite with a seived texure
Au	Gold
Bi	Bismuth
Bm	Bismuthinite
Bn	Bornite
Bt	Biotite
Calc	Calcite
Car	Carrollite
Ccp	Chalcopyrite
Chl	Chlorite
Cob	Cobaltitie
cob-s	Cobaltite with a sieved texture
Cv	Covellite
Cpx	Clinopyroxene
Emp	Emplectite
Ep	Epidote
Fhbn	Ferrohornblende
Fluorite	Fl
Grt	Garnet
Hem	Hematite
Lol	Loellingite
Mag	Magnetite
Mrc	Marcasite

Mol	Molybdenite
Ms	Muscovite
K-fsp	K-feldspar
Po	Pyrrhotite
Py	Pyrite
Qz	Quartz
Ser	Sericite
Tur	Tourmaline
Urn	Uraninite
Wit	Wittichenite

1 Introduction

The discovery of the giant iron oxide-rich Cu-Au-U-Ag-REE Olympic Dam (Gawler Craton, Australia) deposit in 1975, and subsequent discoveries of other polymetallic iron oxide-rich systems in the Cloncurry district in Australia (e.g., Starra, Osborne and Ernest Henry;), along with other Andean deposits (e.g., La Candelaria), led to the Iron-Oxide-Copper-Gold (IOCG) deposit classification (as per Hitzman et al., 1992; Porter, 2000). Since then, these deposits have been a worldwide exploration target for mining companies due their large tonnages and high grades. The IOCG grouping have many disparate features in terms of metal budgets, mineralization style, alteration, the age and nature of the host rocks and the mineralizing fluids. Globally, the origin of these oxidizing hydrothermal fluids is poorly understood, and various models have been proposed for the genesis of these solutions (e.g., Williams, 1994; Barton and Johnson, 1996; Pollard, 2000; Williams et al., 2005; Richards and Mumin, 2013).

Historically, Canada has not been considered as an important target for exploration for IOCG systems. However more recently, some junior mining companies and workers from the Geological Survey of Canada (GSC) have suggested that the Great Bear magmatic zone (GBMZ), in the Northwest Territories is a fertile metallogenic province for these type of deposits (e.g., Corriveau, 2007; Corriveau et al., 2010). The rock types and the Proterozoic age of these in this area are similar to the ones encountered in Olympic Dam, and in the smaller Tennant Creek district ironstone Cu-Au-Bi±Ag hosted deposits in Australia. Two polymetallic iron oxide dominated systems, the NICO (Au-Co-Bi±Cu-W) and Sue Dianne (Cu-U-Ag±Co-Bi) deposits, have been identified in the GBMZ; they are hosted by Proterozoic shallow marine metasedimentary and felsic volcanic rocks, respectively. Other smaller prospects such as DAMP (Cu-U±Co) and FAB (Cu-U) are also contained within felsic volcanic rocks. The vein hosted Mo-U±Cu Nori/RA prospect is hosted by the same metasedimentary rock unit as the NICO deposit.

Exploration for IOCG deposits in Canada has some unique challenges as glaciers have modified the bedrock surface and deposited great amounts of glacial sediments over extensive areas. Hence, alternative exploration methods such as remote sensing (e.g., gravity and magnetic surveys) and till sampling have been used to search for new exploration trargets. Magnetite is commonly found in the IOCG deposits of the GMBZ and is usually mechanically and chemically preserved in till sediments (e.g., Razjigaeva and Naumova, 1992; McMartin et al., 2011). Recent studies on the geochemistry of magnetite have demonstrated that the fractionation of Al, Si, Ca, Mg, V, Ni, Co, Cr and Ti into these iron oxides can be sometimes useful to establish differences between ore deposit types (e.g., Dupuis and Beaudoin, 2011) and with respect to its origin (e.g., metamorphic vs hydrothermal; Nadoll et al., 2012). The fractionation of trace elements into magnetite is a function of multiple factors (e.g., host rock fluid interaction, solubility of metals, oxygen, fugacity, and co-precipitated minerals; Tian et al., 2012; Toplis and Corgne, 2002; Dare et al., 2012). These factors are, in most cases, characteristic of individual hydrothermal systems, and hence, not the same in all magnetite-bearing deposits (even of the same type). Moreover, the lack of detailed petrographic descriptions and the absence of 'background' controls in those studies are also important constraints to further understand the applicability of magnetite as potential indicator mineral.

The present study provides in its second chapter a detailed petrographic and trace element study of magnetite from the different deposits, prospects and barren locations within the GBMZ. This chapter aims to explain the possible factors influencing the fractionation of trace elements into magnetite, but most importantly, to demonstrate the potential of magnetite as an indicator mineral in mineral exploration surveys (till sampling) within the study area.

Polymetallic and sedimentary hosted As–S–Au–Bi ±Co–Cu–Te–rich iron oxide–dominated systems (e.g., the NICO deposit, Tennant Creek district, Idaho Cobalt belt; Kuusamo Schist Belt; Guelb deposit) form an atypical subgroup of the IOCG deposits, which have been rarely studied. In these systems, Au can occur spatially associated with sulfarsenides (especially arsenopyrite) and Bi±Te

and it has been suggested that are associated with various degrees and stages of metamorphic-hydrothermal metasomatism. The link between pyrite and arsenopyrite and Au has been well documented in other deposit types such as orogenic (e.g., Zachariáš et al., 2004), skarn (e.g., Cepedal et. al., 2008) and volcanic hosted massive sulfide (VHMS) deposits (e.g., Törmanën and Koski, 2005). In some of these systems, remobilization of structurally bound gold from sulfarsenides (arsenopyrite and loellingite) took place after retrograde metasomatism or mineral re-crystallization (e.g., Mumin et al. 1994; Tomkins and Mavrogenes, 2001; Wagner et al. 2007). Recent studies (e.g., Tooth et al., 2008; 2011) have demonstrated that the Au-Bi±Te associations in multiple deposits can be explained by the significant Au-scavenging properties of native Bi(±Te) melts (271.3°C, melting point; Okamoto and Massalski, 1986) when they co-exist with hydrothermal fluids (also known as the "liquid bismuth collector model"; Douglas, 2000). The scarcity of these anomalous IOCG systems and the limited research done on them, means here are many issues to be resolved, e.g., what is the nature of the association between Au and sulfarsenides-arsenides, and with Bi and Te? Are the host alteration and mineralization assemblages paragenetically associated? Do the host rocks control to some extent the metal precipitation?

In this study, we wanted to address these questions and test if Au remobilization and the Au-scavenging by Bi may be responsible for the Au refining at the NICO deposit and if so, this would increase our understanding significantly of the formation of this group of IOCG deposits. In Chaper 3, we present the results of detailed petrographic studies, along with electron microprobe (EMPA), scanning electron microscope (SEM) element concentration maps and in-situ laser ablation inductively coupled mass spectrometer (LA-ICP-MS) analyses to test these hypotheses.

One of the most debated aspects of the IOCG systems is the origin of the fluids. On the basis of $\delta^{18}O$, $\delta^{34}S$, $\delta^{13}C$ and $\delta^{37}Cl$ values it has been suggested that the mineralizing fluids in various IOCG deposits originated as magmatic-hydrothermal, evaporitic, formation, metamorphic and sea-water derived fluids or

as mixtures of some of those end-members (e.g. Oreskes and Einaudi, 1992; Williams, 1994; Pollard, 2000; 2006; Chiaradia et al., 2006; Benavides et al., 2007; de Haller and Fontboté, 2009; Gleeson & Smith, 2009). Further fluid inclusion studies (e.g., Perring et al. 2000; Bastrakov, et al. 2007; Mark et al. 2005) have shown that in general IOCG brines are commonly hypersaline, and have high $CaCl_2$ contents. The latter serves as evidence in support of a non-magmatic origin (e.g., evaporitic sequences) for the salinity in some of these IOCG systems. Although, the isotopic evidence may constrain possible sources of O, S, and C in these systems, they do not constrain the origin of the metals. The IOCG systems are well known for developing extensive alteration zones (> 7km) that can leach metals content from the host rocks (e.g., Na-Ca alteration type), and some of these elements can be re-precipitated in subsequent ore-bearing alteration stages (e.g., K-Fe alteration type; Oliver et al. 2006; Montreuil et al., 2013). This generates important questions such as, are metals and/or other ore-mineral forming elements (e.g., S) originally de-coupled from up-welling magmas (e.g., Cu-porphyries, epithermal deposits)? Or conversely, can these magmatic-hydrothermal fluids can effectively scavenge significant amounts of Cu, Au, Bi and Co from the wallrocks and re-precipitate them in more structurally and geochemically favorable zones?

In chapters three and four we ascertain the origin of the NICO deposit (chapter 4) and provide important constraints on the genesis of the Sue Dianne deposit and other smaller prospects in the GBMZ (chapter 5) on the basis of their S, Cu, C, O and H isotopic signatures and fluid inclusion studies. In the particular case of the NICO deposit, additional geochronological studies (Re-Os dating) were carried out on the main mineralization. Collectively, these results classify the GBMZ IOCG deposits into the IOCG family end-members described above. Finally, using simple mass balance calculations we estimated the metal budget contained in the least altered rocks equivalent to those hosting the NICO and Sue Dianne deposits. This calculation allows to discuss if it is feasible for the host metasedimentary (NICO) and the felsic volcanic (Sue Dianne) rocks to be

potential sources of metals (or not) that might have contributed to the formation of these IOCG deposits.

1.1 References

Barton, M.D., and Johnson, D.A., 1996, Evaporitic-source model for igneous-related Fe oxide-(REE-Cu-Au-U) mineralization: Geology 24:259-262.

Benavides J., Kyser, T.K., Clark, A.H., Oates, C.J., Zamora, R., Tarnovschi, R., Castillo, B., 2007, The Manto Verde Iron-oxide-Copper-Gold district, III Región, Chile: the role of regionally derived, nonmagmatic fluids in chalcopyrite mineralization: Economic Geology v., 102, p. 415-440.

Cepedal, A., Fuertes-Fuente, M., and Martin-Izard, A., 2006, Gold bearing As-rich pyrite and arsenopyrite from the El Valle gold deposit, Asturias, northwestern Spain: Canadian Mineralogist, v. 46, p. 233-247.

Chiaradia M., Banks, D.A., Cliff, R., Marschik, R., and de Haller, A., 2006 Origin of fluids in iron oxide-copper-gold deposits: constraints from delta Cl-37, Sr-87/Sr-86(i) and Cl/Br: Mineralium Deposita v. 41, p.565-573.

Cook, N.J. and Chryssoulis, S.L., 1990, Concentrations of ‘‘invisible’’gold in the common sulfides: Canadian Mineralogist, v. 28, p. 1–16.

Corriveau, L., Mumin, A.H., and Setterfield, T., 2010, IOCG environments in Canada: Characteristics, geological vectors to ore and challenges, *in* Porter, T.M., ed., Hydrothermal iron oxide copper-gold & related deposits. A global perspective, Adelaide, PGC Publishing v.4, p. 311-343.

Corriveau, L., 2007, Iron oxide-copper-gold deposits: A Canadian perspective, *in* Goodfellow, W.D., ed., Mineral deposits of Canada: A synthesis of major deposit-types, district metallogeny, the evolution of geological provinces and exploration methods: Geological Association of Canada, Special Publication 5, p. 307-328.

Dare, S.A.S., Barnes, S.J., and Beaudoin, G., 2012, Variation on trace element content of magnetite crystallized from fractionating sulfide liquid, Sudbury, Canada: Evidence for provenance discrimination: Geochimica et Cosmochimica Acta v. 88, p. 27-50.

De Haller, A., and Fontboté, L., 2009, The Raúl-Condestable iron oxide copper-gold deposit, central coast of Peru: ore related hydrothermal alteration, sulfur isotopes, and thermodynamic constrainst: Economic Geology v. 104, p. 365-384.

Douglas, N., Mavrogenes, J., Hack, A. and England, R., 2000, The liquid bismuth collector model: an alternative gold deposition mechanism, *in* C. G., Silbeck and T. C. T., Hubble eds., Understanding planet Earth; searching for a sustainable future; on the starting blocks of the third millennium, 15th Australian Geological Convention, eds: Geological Society of Australia, Sydney, 135 p.

Dupuis, C., and Beaudoin, G., 2011, Discriminant diagrams for iron oxide trace element fingerprinting of mineral deposit types: Mineralium Deposita, v. 46, p. 319-335.

Fisher, L.A. and Kendrick, M.A., 2008, Metamorphic fluid origins in the Osborne Fe oxide-Cu-Au deposit, Australia: evidence from noble gases and halogens: Mineralium Deposita v. 43, p. 483-497.

Gleeson, S.A. and Smith, M.P., 2009, The sources and evolution of mineralising fluids in iron oxide-copper-gold systems, Norrbotten, Sweden: Constraints from stable Cl isotopes of fluid inclusion leachates: Geochimica Cosmochimica Acta, v. 73, p. 5658-5672.

Hitzman, M., Oreskes, N., and Einaudi, N., 1992, Geological characteristics and tectonic setting of Proterozoic iron oxide (Cu-U-Au-REE) deposits: Precambrian Research v. 58 p. 241-287.

Montreuil, J.F., Corriveau, L., and Grunsky, E., 2013, A compositional data analysis of IOCG systems, Great Bear magmatic zone, Canada: To each alteration types its own geochemical signature: Geochemistry: Exploration, Environment, Analysis, doi: 10.1144/geochem2011-101.

Nadoll, P., Mauk, J.L., Hayes, T.S., Koening, A.E., and Box, S.E., 2012 Geochemistry of magnetite from hydrothermal ore deposits and host rocks in the Proterozoic Belt Supergroup: Economic Geology v. 107, p. 1275-1292.

Okamoto, H., and Massalski, T.B., 1986, Au-Bi (gold-bismuth), *in* TB., Massalski, J. L. Murray, L. H. Bennet and H., Baker, eds., Binary Alloy Phase Diagrams: Ac-Au to Fe-Rh: American Society for Metals, v. 1, p. 238-240.

Oliver, N.H., Rubennach, B., Baker, T., Blenkinsop, T.G., Cleverly, J.S., Marshall, L.J., and Pridd, P.J., 2006, Granite-related overpressure and volatile release in the mid crust: Fluidized breccias from the Cloncurry district, Australia: Geofluids, v. 6, p. 346-358.

Oreskes, N. and Einaudi, M.T., 1992, Origin of Hydrothermal Fluids at Olympic Dam: Preliminary Results from Fluids Inclusions and Stable Isotopes: Economic Geology, v.87, p. 64-90.

Pollard, P.J., 2006, An intrusion-related origin for Cu-Au mineralization in iron oxide-copper-gold (IOCG) provinces: Mineralium Deposita v. 41, p. 179-187.

Porter, T.M., 2000, Hydrothermal iron oxide copper-gold and related deposits: A global perspective: PGC Publishing, Adelaide vol. 1, 349 p.

McMartin, I., Corriveau, L., and Beaudoin, G. 2011, An orientation study of heavy mineral signature of the NICO Co-Au-Bi deposit, Great Bear magmatic zone, NW Territories, Canada: Geochemistry: Exploration, Environment, Analysis, v. 11, p. 293-307.

Mumin, A.H., Fleet, M.E., and Chryssoulis, S.L., 1994, Gold mineralization in As-rich mesothermal gold ores of the Bogosu-Prestea mining district of the Ashanti Gold Belt, Ghana: remobilization of "invisible" gold: Economic Geology, v. 29, p. 445-460.

Richards, J.P., and Mumin, H., 2013, Magmatic-hydrothermal processes within an evolving earth: Iron oxide-copper-gold and porphyry Cu±Mo±Au deposits: Geology, v. 41, p. 767-770.

Razjigaeva, N.G., and Naumova, V., (1992) Trace element composition of detrital magnetite from coastal sediments of northwestern Japan Sea for provenance study: Journal of Sedimentary Petrology, v. 62, p. 802-809.

Tian, Y., Etschmann, B., Liu, W., Borg, S., Mei, Y., Testemale, D., O'Neill, B., Rae, N., Sherman, D.M., Ngothai, Y., Johannessen, B., Glover, C. and

Brugger, J., 2012, Speciation of nickel (II) chloride complexes in hydrothermal fluids: In situ XAS study: Chemical Geology, v. 334, p. 345-363.

Tomkins, A.G., and Mavrogenes, J.A., 2001, Redistribution of Gold within arsenopyrite and loellingite during pro- and retrograde metamorphism: application to timing of mineralization: Economic Geology, v. 96, p. 525-534.

Tooth, B., Ciobanu, C.L., O'Neill, B., Green, L., and Brugger, J., 2011, Melt formation and gold scavenging from hydrothermal fluids: an experimental study: Geochimica Cosmochimica Acta v. 75, p. 5423-5443.

Tooth, B., Brugger, J., Ciobanu, C., and Liu, W., 2008, Modeling of gold scavenging by bismuth melts coexisting with hydrothermal fluids: Geology 36, p. 815-818.

Toplis, M.J., and Corgne, A., 2002, An experimental study of element partitioning between magnetite, clinopyroxene and iron-bearing silicate liquids with particular emphasis on vanadium: Contributions to Mineralogy and Petrology v. 144, p. 22-37.

Törmanën, T.O., and Koski, R.A., 2005, Gold enrichment and the Bi-Au association in pyrrhotite-rich massive sulfide deposits, Escanaba Trough, Gorda Ridge: Economic Geology, v. 100, p. 1135-1150.

Wagner, T., Klemd, R., Wenzel, T., and Mattson, B., 2007, Gold upgrading in metamorphosed massive sulfide ore deposits: direct evidence from-laser-ablation-inductively coupled plasma-mass spectrometry analysis of invisible gold: Geology, v. 35, p. 775-778.

Williams, P.J., Barton, M.D., Johnson, D.A., Fontboté, L., de Haller, A., Mark, G., Oliver, N.H.S. and Marschik, R., 2005, Iron oxide copper-gold deposits: Geology, Space-time distribution, and possible modes of origin: Economic Geology, 100th anniversary volume, p. 371-405.

Williams, P.J., 1994, Iron mobility during synmetamorphic alteration in the Selwyn Range area, NW Queensland; implications for the origin of ironstone-hosted Au-Cu deposits: Mineralium Deposita, v. 29, p. 250-260.

Zachariáš, J., Frýda, J., Paterová, B., and Mihaljevic, M., 2004, Arsenopyrite and As-bearing pyrite from Roudný deposit, Bohemian: Mineralogical Magazine, v. 68, p. 31-46.

2 Trace element geochemistry of magnetite and its relationship to Cu-Bi-Co-Au-Ag-U-W mineralization in the Great Bear magmatic zone, NWT, Canada

2.1 Introduction

The Great Bear magmatic zone (GBMZ) in the Northwest Territories, Canada, is host to the NICO (Au-Co-Bi±Cu-W) and Sue Dianne (Cu-Ag-Au-±U-Co) deposits and other smaller iron-oxide dominated polymetallic systems that have comparable alteration and mineralization styles to iron-oxide copper gold (IOCG) deposits in Chile and Australia, e.g., Olympic Dam, La Candelaria, and Raúl-Condestable (Goad et al., 2000; Corriveau, 2007; Corriveau et al., 2010b). Magnetite is a common phase in many of the mineral deposits, alteration zones, and host rocks of the GBMZ. Previous studies, including those of Sidor (2000), Corriveau et al. (2007; 2010a,b), Mumin et al. (2007, 2010) and Montreuil et al. (2013), have documented multiple stages of magnetite precipitation, and a systematic evolution in the types of magnetite-bearing alteration. The results presented here are framed, therefore, within an existing multi-stage alteration model for the region.

Dupuis and Beaudoin (2011) and Nadoll et al. (2012) showed that magnetite composition differs between major deposit types (e.g., IOCG vs porphyry deposits) and with respect to origin (e.g., magmatic versus hydrothermal). Because magnetite is ubiquitous in several types of deposits including IOCGs, its trace element compositions can potentially provide important insights about ore depositional processes associated with the chemical and temperature gradients prevailing during the genesis of iron oxide, alkali-altered hydrothermal systems and host rocks, as defined by Porter (2010).

In early studies of magnetite chemistry, metal ratios were used to constrain the origin of this mineral in different environments (Kisvaransanyi and Proctor,

1967; Freitsch, 1970; Parak, 1975; Loberg and Horndahl, 1983; Bajwah et al., 1987; Nyström and Henriquez, 1994; Gregory, 2006). More recently, Rusk et al. (2010) used Mn/V and Mn/Ti ratios in magnetite from the Cloncurry district in Queensland, which includes the Ernest Henry deposit, to differentiate between mineralized and barren iron-oxide breccias. Magnetite chemistry is, however, complex, and trace-element fractionation is affected by a number of variables including fluid chemistry and temperature (Ilton and Eugster, 1989), stoichiometry, co-precipitation of other mineral phases (Dare et al., 2012), and redox conditions (Toplis and Corgne, 2002). Unfortunately, a lack of experimental data on the partitioning of trace elements between magnetite and hydrothermal fluids restricts our ability to rigorously interpret the controlling factors that lead to the trace-element signatures of this iron oxide. Crystallization of magnetite in iron-oxide dominated systems can take place at temperatures of 400˚C (e.g., Oreskes and Einaudi, 1992; Oliver et al., 2006) and may occur during solid-state recrystallization (Corriveau et al., 2010b). Hence, partitioning of elements among minerals can also be a controlling factor during the metasomatic crystallization of magnetite during regional metamorphism (e.g., Yang and Rivers, 2000). Irrespective of the origin of magnetite (e.g., magmatic vs metamorphic), empirical discrimination of magnetite trace-element signatures in terms of alteration and mineralization types would allow for its optimization as an mineral vector for exploration in the GBMZ and analogous metallogenic provinces, and could provide an important tool in the exploration for new polymetallic iron-oxide-dominated deposits.

In northern Canada, glaciers have partially eroded and exposed bedrock and covered large areas with glacial sediments. Till distribution and composition have become important tools in mineral exploration, together with geophysical methods such as induced polarization, and gravity and magnetic surveys (Hallof and Pelton, 1980; Dentith et al., 1994). Indicator mineral studies have been successful in the exploration for diamonds (garnets; e.g., Fipke et al., 1995) as well as for Mississippi Valley-Type deposits (fluorite; e.g., MacClenaghan, 2005), and for other deposit types as reviewed by Gent et al. (2011). The common

mechanical and chemical preservation of magnetite is demonstrated by its occurrence in till and river sediments (e.g., Razjigaeva and Naumova, 1992; McMartin et al., 2011). Within the GBMZ, its usefulness as an indicator mineral in exploration surveys is highlighted by the distinct Ti+V content of magnetite in glacial till upflow and above the NICO deposit (McMartin et al., 2011). Dupuis and Beaudoin (2011) recently designed a series of ore deposit discriminant diagrams based on average trace element contents in magnetite and hematite from numerous deposits. However, before magnetite can be used successfully to prospect for IOCG deposits in the GBMZ, it is necessary to determine the composition of this iron oxide phase in both mineralized and barren environments and its spatial and paragenetic relationships to the ore minerals.

This paper presents the results of a petrographic and geochemical study of magnetite spatially associated with ore minerals at the NICO (Au-Co-Bi±Cu) and Sue-Dianne (Cu±U) deposits, as well as with the DAMP (Cu-U), FAB (Cu-U) and Nori/Ra (Mo-Cu-U) prospects in the central and southern GBMZ, and in a magnetite-apatite body located 300 m southeast of the past-producing Terra mine (vein-hosted Ag-Ni-Bi-U; north-central GBMZ). In addition, petrographic and trace element studies were carried out on magnetite in host rocks that are not spatially associated with mineralization, to assess whether these differ geochemically from sulfide-stage magnetite. The whole-rock chemistry of the unmineralized host rocks is also compared here to magnetite chemistry in order to test the role of the former in controlling the latter. Based on these petrographic and geochemical analyses, and on supporting fieldwork and alteration mapping (Jackson, 2008; Corriveau et al., 2010a, b; Jackson and Ootes, 2012; Montreuil et al., 2013; this study), we discuss the possible factors that may have controlled the chemical signature of the magnetite and its utility as an indicator mineral.

2.2 Regional Geology

For the purposes of this paper, the Wopmay orogen is divided into three major zones, from east to west: the Archean Slave craton and Paleoproterozoic Coronation margin, and Hottah terrane (Fig. 2.1). The Hottah terrane is basement

to the GBMZ (Hildebrand et al., 1987, 2010a) and is separated from the Slave craton and Coronation margin by the Wopmay fault zone (medial zone of Hildebrand et al., 1991, 2010a). Near Hottah Lake (Fig. 2.1), the Hottah terrane consists of <1970 Ma to >1875 Ma metasedimentary and metavolcanic rocks that are intruded by ca. 1930 to 1910 Ma plutons. This sequence is unconformably overlain by the ca. 1906 to 1895 Ma Bell Island Bay Group (e.g., Bowring, 1984; Reichenbach, 1991; Newton, 2011; Ootes et al., 2012). From bottom to top, the Bell Island Group comprises the Beaverlodge Lake sandstone, subaerial Zebulon Formation, Conjuror Bay Formation, and Bloom basalts and associated Fishtrap gabbro dikes (Fig. 2.2).

The youngest component of the Hottah terrane is the Treasure Lake Group (TLG). These metasedimentary rocks were deposited after 1885 Ma, but before 1875 Ma, as determined by detrital zircon U-Pb ages (Gandhi and van Breemen, 2005; Bennett and Rivers, 2006), and were folded and metamorphosed and subsequently intruded and unconformably overlain by igneous rocks of the GBMZ arc ca. 1873 Ma (e.g., Goad et al., 2000; Gandhi and van Breemen, 2005; Bennett and Rivers, 2006; Ootes et al., 2010). The oldest exposed bedrock in the study area is the TLG, which hosts the NICO deposit and the Nori/RA prospect, and may be correlative with sedimentary rocks hosting the past-producing Terra mine. Calc-alkaline volcano-plutonic rocks of the GBMZ having primarily felsic to intermediate compositions intrude and were deposited on the TLG in the southern portion of the study area and host, among others, the Sue Dianne deposit and the FAB and DAMP prospects.

2.2.1 Treasure Lake Group

Based on observations of a type section southeast of the NICO property, the TLG is a shallowing-upward sequence consisting of four main units, which from oldest to youngest are: the Lower siltstone; Carbonate; Quartz-arenite; and Upper siltstone (Figs. 2.2, 2.3A; Gandhi and van Breemen, 2005). Lithological descriptions made by these authors are summarized as follows. The Lower siltstone (T1) is an approximately 1-km-thick quartzofeldspathic unit, bedded on a centimeter scale, which contains weakly to strongly magnetic, argillaceous beds.

Overlying the lower siltstone, the Carbonate unit (T2) is approximately 100 m thick and is dominated by marble, but also includes calcareous argillite and calc-silicate beds, and thin (0.2-1 cm thick), magnetite-rich layers and elongate lenses. Our field observations suggest that thrust faults are present within this unit, although the amount of stratigraphic duplication currently is not constrained. This unit pinches out rapidly to the northwest at Lou Lake, where a bedded, amphibole-magnetite-altered siltstone-argillite subunit occurs at the same stratigraphic level. The top of the calc-silicate unit is intercalated with quartz arenite, which is overlain by a 300-500-m thick quartzite. The Quartz-arenite (T3) grades into a zone of thinly to thickly bedded siltstone (T4) that is reported to be more than 300 m thick (Gandhi and van Breemen, 2005). A reconnaissance traverse across the type section failed to confirm such large proportions of Upper siltstone (T4), but found abundant granitic sills and some quartzite beds. Cordierite formed in the more aluminous beds, particularly those proximal to granite bodies. Field mapping of alteration zones and subsequent megascopic studies by Corriveau et al. (2010a, b, 2011) have shown localized to intense, pervasive and penetrative, replacement-type post-metamorphic alteration throughout the TLG and is associated with local to multikilometer-long hydrothermal and fault-related breccias (Corriveau et al., 2010a, b; Montreuil et al., accepted). Towards the type section, the TLG rocks are less altered. Locally, they contain post-metamorphic altered zones comprising amphibole, magnetite, biotite, K-feldspar, garnet, tourmaline, and minor scapolite (Corriveau et al. 2007; this study).

2.2.2 Great Bear magmatic zone

The GBMZ crops out over a strike length of 450 x 100 km and can be traced to the south for 500 km and to the west beneath a thin Paleozoic cover (e.g., Coles et al., 1976; Hoffman, 1987). Volcanic rocks of the GBMZ are assigned to the MacTavish Supergroup and have an aggregate thickness of more than 10 km in the north and 5 km in the south (Hoffman, 1980, 1984). The volcano-sedimentary sequences have been divided into four groups from west to east across the zone, and from oldest to youngest (Fig. 2.2): the age equivalent

LaBine and Dumas groups are overlain in the north by the Sloan Group (Hoffman and McGlynn, 1977; Hildebrand et al., 1987) and in the South by the Faber Group (Gandhi, 1994; Gandhi et al., 2001). In the present study, only the LaBine and Faber groups are of interest. The LaBine Group consists primarily of andesite, dacite, and rhyodacite with minor basalt (Hildebrand, 1981; Hildebrand et al., 1987, 2010b; Gandhi and Prasad, 1995); they that were intruded by numerous intermediate-composition plutons between 1870 and 1850 Ma (e.g., Bowring, 1984; Gandhi et al., 2001; Bennett and Rivers, 2006; Hildebrand et al., 2010b; Bennett et al., 2012; Jackson and Ootes, 2012). The Terra and Camsell River formations of the LaBine Group are host to the past-producing Terra mine (Ag-Ni-Co-Bi-U) and a series of magnetite-apatite bodies (Badham and Morton, 1976; Hildebrand, 1986; Hildebrand et al., 2010b). The Faber Group mostly comprises rhyolite and ignimbrite (Gandhi et al., 2001) that are, together with the underlying TLG, intruded by a series of 1873 to 1856 Ma calc-alkaline felsic plutons (Gandhi, 1989; Gandhi et al., 2001; Camier, 2002). These volcanic rocks and plutons host the Sue Dianne and FAB prospects.

2.3 Local Geology and Magnetite Occurrences

2.3.1 Nori/RA prospect

The ca. 1874 Ma Nori/RA (Cu-Mo-U ± W, REE) prospect is located in the south-central GBMZ on the northwest side of DeVries Lake (Figs. 2.1, 2.3B; Ootes et al. 2010). It is hosted by undifferentiated deformed and metamorphosed siltstone of the TLG (Gandhi, 1994; Bennett and Rivers, 2006; Ootes et al., 2010). The mineralization is in hydrothermal veins, which are up to one meter thick, and includes molybdenite and uraninite that precipitated contemporaneously with major amounts of biotite, tourmaline, and K-feldspar, and minor magnetite (Fig. 2.4A; Gandhi and Prasad, 1993; Gandhi, 1994; Ootes et al., 2010). The veins are folded, and have 1-mm- to 2-cm-thick biotite selvages (Ootes et al., 2010). The presence of tension gashes of quartz and K-feldspar, with lesser amounts of chalcopyrite, pyrite, magnetite, and molybdenite, may indicate an early to syn-deformational origin of the veins (Ootes et al., 2010). Primary fluid inclusions in

tourmaline suggest that the parental ore fluid was CO_2-rich, with homogenization temperatures of >260ºC, possibly as high as 400 ºC (Ootes et al., 2010).

2.3.2 The NICO deposit

The NICO deposit, in the southern GBMZ, is located just south of Lou Lake (unofficial name; Figs. 2.1, 2.5A). Reserves are 33 Mt grading 1.02 g/t Au, 0.112% Co, 0.14% Bi, and 0.04 % Cu (Puritch et al., 2012) and are hosted mainly within amphibole-biotite-magnetite ± K-feldspar-altered and subordinate albitized rocks of the Treasure Lake Group; some late-stage mineralized veins are within strongly potassic-altered felsic volcanic rocks of the Faber Group (Gandhi and Lentz, 1990; Gandhi, 1994; Sidor, 2000; Goad et al., 2000; this study). The TLG at NICO has been divided by Sidor (2000) into the Lower, Middle, and Upper units that are correlative, respectively, with the Lower siltstone (T1), Carbonate (T2), and Upper quartz-arenite (T3) units of Gandhi and van Breemen (2005). The Middle unit, which hosts most of the mineralization, has a pervasive alteration assemblage composed of magnetite, biotite, amphibole (actinolite and tremolite), and K-feldspar. Goad et al. (2000) argued that the precursor of the amphibole-magnetite rich rocks is a subarkosic wacke. Therefore, we assume that most of the precursor rocks of the Middle unit are correlative with the metasiltstone described by Gandhi and van Breemen (2005) because the Carbonate unit pinches out towards Lou Lake. Principal ore minerals are cobaltian arsenopyrite, cobaltian loellingite, cobaltite, native bismuth, bismuthinite, and native gold, with minor amounts of chalcopyrite and scheelite (Goad et al. 2000). The suite of ore minerals occurs in veins 2 mm to 10 cm wide (Fig. 2.4B), amphibole-rich breccias, aggregates, and disseminated within stratabound ore lenses along the bedding and/or local foliation planes.

2.3.3 Terra magnetite-apatite stocks

The Terra mine is near Camsell River, just south of Great Bear Lake in the northern GBMZ (Figs. 2.1, 2.5B). Historically, Ag-Ni, Co-arsenides, Bi, and U were mined at Terra from a series of polymetallic veins (Badham, 1975). In addition to the Ag-Ni-Co deposit, Badham and Morton (1976) identified two localities with massive magnetite-apatite-actinolite mineralization in veinlets and

skarn (~1873 Ma; Davies et al., 2011) to the southeast (Fig. 2.4C). This study only incorporates data from the largest (200 x 75 m) magnetite-apatite-actinolite body, immediately southeast of the former mine site (Fig. 2.5B). Host rocks to both the deposit and the magnetite-apatite body consist of an intensely hydrothermally altered, volcano-sedimentary caldera sequence (Shegelski, 1973; Badham, 1973; Badham and Morton, 1976; Hildebrand, 1986).

2.3.4 DAMP prospect

The Damp prospect is situated east of Longtom Lake (Figs. 2.1, 2.6A) and comprises polymetallic (Cu-U-Co-V ± Zn-Pb) mineralization hosted by rhyodacitic ignimbrites of undefined GBMZ affinity, either the LaBine or Faber groups or equivalents (Gandhi and Prasad, 1995; Acosta et al., 2011). Mineralization occurs in a breccia zone where the host rocks are thoroughly albitized. The matrix of the host breccia (Fig. 2.7A) consists of abundant iron oxides such as hematite (var. specularite) and magnetite, together with K-feldspar, quartz, disseminated pyrite, chalcopyrite, covellite, carrollite ($CuCo_2S_4$), bornite, and pitchblende (Gandhi and Prasad, 1995; Acosta et al., 2011; this study).

2.3.5 Sue-Dianne deposit

The Cu-Au-Ag Sue Dianne deposit has resources of 8.4 Mt @ 0.8 % Cu, 0.07 g/t Au, and 3.2 g/t Ag (Hennessey and Puritch, 2008) and is situated along the north arm of Dianne Lake, at the intersection of the Mar and Dianne faults, and is hosted by a Faber Group rhyodacite ignimbrite (Gandhi, 1989; Gandhi et al., 2001; Figs. 2.1 and 2.6B). This deposit has been interpreted as occurring in a volcanic diatreme with an age of ~1868 Ma (Camier, 2002; Ootes et al., 2010). The mineralization is principally hosted by an iron oxide-rich breccia zone (Fig. 2.7B) approximately 600 m long, 500 m wide, and 350 m deep (Goad et al., 2000). Within the breccia, the lithoclastic portion is strongly potassically (K-feldspar) altered. In the matrix, chalcopyrite, pyrite, bornite, covellite, and lesser amounts of emplectite ($CuBiS_2$), wittichenite (Cu_3BiS_3), and carrollite, are disseminated, occur in microveins, and partially replace and/or overgrow iron oxides and iron-rich silicates (Gandhi, 1989; Goad et al., 2000; Camier, 2002; this work). Iron oxides and sulfides are also spatially associated with abundant

fluorite, epidote, apatite, and minor quartz. Local Au enrichment (concentrations not reported) is confined to the eastern part of the breccia complex (Camier, 2002). Uranium occurs marginally to Cu enrichment and is constrained to fractures, breccias, micro-veins (0.5 cm to <1mm thick) as pitchblende or its weathering products (Goad et al., 2000; Camier, 2002).

2.3.6 FAB prospect

The FAB (Cu-U) prospect is situated along the eastern flank of Fab Lake, east of Faber Lake (Figs. 21, 2.8). The Cu-U mineralization is hosted by felsic volcanic rocks (rhyodacite, dacite) and hypabyssal porphyries (granite; Gandhi, 1988, 1994; Azar, 2007). The mineralization is within a potassic-iron alteration assemblage that consists of U-Cu-bearing K-feldspar-magnetite/hematite-biotite veins, alteration fronts, and minor breccias (Fig. 2.7C; Montreuil et al., in prep; Potter et al., 2013). Veins are widely distributed in a north-trending zone 7 km long and 2 km wide. The breccia matrix and veins mainly contain pyrite, chalcopyrite, and iron oxides such as magnetite, and to a lesser extent, hematite. Within the mineralization, pitchblende and fluorite commonly occur in veinlets and fracture fillings, accompanied by only small amounts of apatite and actinolite (Gandhi, 1994).

2.4 Analytical Techniques

Twenty-one magnetite-bearing samples from the GBMZ were analyzed for major and trace elements. This group of samples includes two from the Lower metasiltstone (T1), one from the Carbonate unit (T2), six and two samples from the Nori/Ra prospect and NICO deposit, respectively, and one, two, five, and two from the Terra, DAMP, Sue Dianne, and FAB prospects respectively (Table 2.3).

A major- and trace-element geochemical study of GBMZ magnetite was carried out using a CAMECA-SX-100 electron microprobe (EMPA) at the University of Alberta, analyzing for Fe, Al, Mg, Si, V, Ti, Mn, Cr, and Ni. Co concentrations were not determined because the CoKα line interferes significantly with the FeKβ line. Further analysis of the CoKα line to obtained concentrations of Co were not carried out. Two sets of data were acquired by wavelength-

dispersive spectrometry. For the first set, the electron gun was operated at an accelerating voltage of 15 kV and beam current of 20 nA, with background and peak counting times of 10s and 10-20s, respectively. For the second set, instrument conditions and parameters are analogous to those described in Dupuis and Beaudoin (2010), using an accelerating voltage of 15 kV, current of 100 nA, and background and peak counting times of 10s and 20-30s, respectively. The detection limits for the EMPA study is given by the lowest concentration of the element present that is statistically above the background continuum level by three sigma.

Polished thin sections with a thickness of 100 μm were prepared for trace-element analysis by laser ablation-inductively coupled plasma-mass spectrometry (LA-ICP-MS). The data were acquired using a Thermo X Series II inductively coupled quadrupole mass spectrometer linked with a Quantronix Integra C 785 nm, diode-pumped, YLF (yttrium-lithium fluoride) ultra-fast (130 femtosecond) laser, at the Great Lakes Institute for Environmental research (GLIER), University of Windsor. Analyses employed an energy of approximately 0.03 mJ, producing a spot size of ~10 μm. For individual analyses, a gas background signal was collected for 60 s before the beginning of ablation. The LA-ICP-MS data were processed using the Aabel 3.0® graphics/statistics software package and in-house Excel® spreadsheets. Quantitative results for ^{48}Ti, ^{51}V, ^{52}Cr, ^{55}Mn, ^{59}Co, ^{60}Ni, ^{63}Cu, ^{75}As, ^{89}Y, ^{108}Pd, ^{111}Cd, ^{121}Sb, ^{191}Pt, ^{208}Pb, ^{209}Bi, ^{232}Th, ^{238}U, ^{139}La, ^{149}Sm, ^{171}Yb, and ^{197}Au were obtained through calibration of relative sensitivities using the NIST-610 standard. Electron microprobe data for Fe were used as the internal standard concentration. Detection limits in magnetite were generally 5.0-0.1 ppm for most elements.

Over 200 traverses were done on magnetite grains with an average length of 100 μm. The Aabel software allows the user to pick the portion of the spectrum used for quantification. Each spectrum was examined for any evidence of mineral inclusions. The portion used for quantification was selected where a spectrum was nearly flat (i.e. ~ constant counts as a function of ablation time). Counts for each element as function of time were compared to those for ^{57}Fe. Elements for which

the signal co-varied with ^{57}Fe were taken to be homogeneously distributed through the magnetite structure and, therefore, were used to assess magnetite composition. A minimum of 10s of spectra was used for most individual analyses. However, for fine-grained (<25μm) magnetite that contains abundant silicate inclusions, only 5 to 9s of spectra were processed. The NIST-610 standard was analyzed twice before and after every 20 magnetite analyses, thus allowing correction for instrumental drift.

LA-ICP-MS data obtained here are divided into the (October) OC, (April) AP, and (March) MR series. The element suite analyzed differed among the three series (see appendix D). Interference between ^{57}Fe and ^{58}Ni in the AP series did not allow for the calculation of Ni contents, hence concentrations for Ni are only available for the OC and MR series, where ^{60}Ni was used to quantify Ni.

Trace element data for the TLG rocks were obtained from the type section and two samples from the FAB porphyries that are interpreted as least altered, which are host rocks at the FAB prospect. Whole-rock trace element concentrations were determined by Activation Laboratories, Canada, using ICP-MS and ICP-OES methods. The ICP-MS instrument was a Perkin Elmer Sciex ELAN 6000, 6100, or 9000. A sodium peroxide fused blank was run in triplicate for every 22 samples, duplicates were run every 10 samples, and the instrument was recalibrated every 44 samples. The ICP-OES instrument used was either a Varian 735ES or a Thermo 6500. Every 10^{th} sample was prepared and analyzed in duplicate and a blank was run every 30 samples. Analytical precision of the instruments is ± 100% at detection limit, ± 20% at ±10x detection limit, and 5% at 100x detection limit.

Gandhi (1989) provided geochemical data for least-altered dacitic to rhyodacitic rocks of the Mazenod assemblage from the Dianne Lake area that are considered equivalent to Sue Dianne precursor volcanic rocks. In addition, unpublished data (L. Ootes) are reported for the Swan and Bode lakes dacitic porphyries and rhyolites, which are considered correlative with the rhyodacitic protolith hosting the DAMP prospect.

2.5 Results

2.5.1 Magnetite paragenesis

A petrographic study was carried out on 70 polished thin sections from the NICO and Sue-Dianne deposits, the Terra magnetite-apatite body, and the DAMP, FAB, and Nori/Ra prospects, and from units T1 and T2 of the Treasure Lake Group.

Treasure Lake Group: The Lower siltstone magnetite (T1mag) generally forms euhedral, unzoned, disseminated grains in biotite-rich quartzofeldspathic beds, and decreases in abundance up-section. The metasiltstone comprises biotite, microcline, magnetite, quartz and minor muscovite. Magnetite (up to 12 vol. %) is fine grained (5 to 30 μm) and evenly disseminated throughout the rock. Straight contacts exist between magnetite and silicate grains (Fig. 2.9A). In the Carbonate unit, magnetite (T2mag) only occurs as unzoned crystals in centimeter- to decimeter-thick amphibole-rich beds. The T2mag forms euhedral disseminated grains with euhedral amphibole (30 to 300 μm), with both phases exhibiting straight contacts and no crosscutting relationships (Fig. 2.9B).

Nori/RA prospect: The Nori/RA prospect contains two generations of magnetite within the mineralized zones. The earlier magnetite (Nomag1) is an important component (up to 15 vol. %, 20μm) of the metasiltstone, which comprises an assemblage of biotite, K-feldspar, magnetite ± muscovite. The Nomag1 magnetite is fine grained and generally consists of inclusion-free, euhedral crystals (Fig. 2.10A) that occur evenly disseminated in the wall rock. The younger generation of magnetite (Nomag2) is an accessory mineral (<1 vol. %; 50 to 200μm) within the tourmaline-biotite veins, and displays straight contacts with pyrite, molybdenite, and uraninite (Figs. 2.9 C; 2.10B, C). This magnetite is also found in the K-feldspar- and quartz-rich tension gash veins (NoQKmag; 40 to 80μm). The veins comprise monomineralic aggregates of magnetite and magnetite-pyrite that generally are randomly distributed along the vein contacts with the veins and the host rocks, and within the veins, respectively.

NICO deposit: The NICO samples have three identifiable generations of magnetite. The earliest generation (NImag1) selectively replaced the host rocks along bedding planes as amphibole-biotite-magnetite ± K-feldspar lenses that completely overprint primary sedimentary structures, and also form centimeter-thick veins. Magnetite NImag1 is typically fine-grained (20μm to 50μm), sub- to euhedral, and overgrows and pervasively replaces the host rock silicates (Figs. 2.9D, 2.10D). As a result, this magnetite contains small, randomly distributed silicate inclusions (Fig. 2.10D). In other cases, inclusions are localized within concentric growth zones (Fig. 2.9D). The next phase of magnetite (NImag2) is generally euhedral, and coarser (0.5 to 2mm) than NImag1. Zoning is absent, although very small silicate inclusions (<2 μm) are randomly disseminated in some grains (Figs. 2.9E, 2.10E). NImag2 is found in veins, lenses, and along the bedding spatially associated with ore minerals such as arsenopyrite, scheelite, loellingite, and cobaltite, and with minor gangue minerals including pyrite, green amphibole, green-brown biotite, and quartz. Contacts between magnetite and ore and gangue minerals are straight to slightly wavy (Fig 2.9E, 2.10E). The last stage of magnetite (NImag3; 20 to 40 μm) lacks obvious zoning or visible silicate inclusions (Figs. 2.10F, 2.11A), and is predominantly found in millimeter- to micron-thick veins cutting sulfarsenide minerals (Figs. 2.10F, 2.11A). Magnetite NImag3 occurs with pyrite, native Bi, bismuthinite, and minor quartz and amphibole mostly in the micrometer-thick veins. A later mineral assemblage is found within microveins cutting and replacing the Co-As-Fe-rich sulfides and replacing native Bi and bismuthinite; it consists of chalcopyrite, hematite, quartz, and hastingsite, chlorite, and minor emplectite, whittichenite, and carbonates.

Terra magnetite-apatite body: Magnetite (Temag) is coarse grained, moderately to intensively fractured, forming euhedral and inclusion-free crystals (Fig. 2.11B). Zoning has not been recognized (Fig. 2.11B). Magnetite and apatite have variable grain sizes with angular shapes, ranging from 10 x 20 μm to 1.0 x 0.8 cm (Figs. 2.11B, 2.12A); grains have straight contacts and are cut by a late generation of actinolite-apatite-quartz veins.

DAMP prospect: Magnetite in this prospect is coarse-grained and moderately to highly fractured (Dmag), and crystallized as part of the matrix to an extensive brecciated zone. This magnetite comprises unzoned euhedral crystals (Fig. 2.11C) that typically exhibits straight contacts with pyrite, K-feldspar, and minor quartz, calcite, albite, specular hematite, and epidote. Pyrite is coarse grained and highly fractured, and displays well developed sharp contacts with magnetite (Fig. 2.12B). Magnetite is partially to totally pseudomorphed by hematite. Chalcopyrite inclusions (<10μm) are commonly present within the larger magnetite grains. Chalcopyrite, with accessory carrollite bornite, and emplectite typically cut pyrite, and to a lesser extent, magnetite (Figs. 2.11C, 2.12B). Locally, the fractures served as alteration pathways along which chalcopyrite replaced pyrite. In places where specular hematite is predominant with respect to magnetite, chalcopyrite and bornite are replaced by covellite and chalcocite.

Sue-Dianne deposit: Magnetite at Sue-Dianne is more abundant at deeper levels of the breccia complex (this study; Camier, 2002; Mumin et al., 2010). Here, the bulk of magnetite (SDmag) forms masses of euhedral, medium-grained (40 to 150 μm) crystals (Figs. 2.11D; 2.12C, D). However, less important (<2 vol. %) fine-grained magnetite (<10 μm) has also been recognized in shallower parts of the system in late epidote-rich veins. Significant amounts of epidote, fluorite, K-feldspar, and minor quartz, specular hematite, and sparse carrollite and pyrite exhibit straight contacts with SDmag (Figs. 2.12C, D). Some magnetite grains have small inclusions (<3 μm) of chalcopyrite and more commonly, silicate minerals (Figs. 2.11D, 2.12D). As is the case at DAMP and to a lesser extent in FAB, hematite has partially to totally pseudomorphed magnetite, and in Sue Dianne it typically occurs in the shallower parts of the system together with sericite (this study; Camier, 2002; Mumin et al., 2010). The bulk of the Cu-(±Bi-Co) mineralization is represented by chalcopyrite and subordinate bornite, emplectite, wittichenite, and carrollite, and post-dated magnetite deposition as suggested by the presence of abundant infill textures (Figs. 2.11D, 2.12C). Characteristically, bornite replaces chalcopyrite and chalcocite, whereas covellite

replaces chalcopyrite and bornite. Both covellite and bornite are spatially associated with other gangue minerals such as chlorite and fine-grained fluorite, epidote, quartz, specular hematite, and apatite. Late quartz-epidote veins and stockworks cut the earlier stages.

FAB prospect: Magnetite within the mineralization sampled at FAB occurs in two generations having different grain sizes (5-20 μm and 20-80 μm). The finer grained generation (Fmag1) is euhedral to subhedral and disseminated through the aphanitic matrix of the rhyodacitic host rock. It preferentially forms at the edges of the predominant K-feldspar, and less-abundant quartz phenocrysts. Inclusions in Fmag1 of host-rock matrix minerals such as quartz and feldspar are common (Fig. 2.12E). Locally, Fmag1 is spatially associated with recrystallized K-feldspar that differs from the host-rock phenocrysts. The younger, coarser magnetite phase (Fmag2) comprises unzoned (Figs. 2.11E, 2.12F), inclusion-free euhedral to subhedral grains, distributed along fractures. This magnetite forms mineral aggregates together with coarse-grained pyrite, as well as with epidote, quartz, K-feldspar, and accessory fluorite. Chalcopyrite inclusions (3-10 μm) typically occur within Fmag2. Hematite has partially to totally pseudomorphed the magnetite grains. The main phase of Cu mineralization is represented by chalcopyrite (Fig. 2.11E), accompanied by minor amounts of bornite and chlorite that mostly occur interstitially to Fmag2 and pyrite within micro-veins, the breccia matrix, or as replacements of pyrite.

A summary of magnetite paragenetic sequences, and host rock and mineralization characteristics (style and sulfide-mineral associations) is given in Figure. 2.13 and Table 2.1.

2.5.2 Trace element geochemistry of the GBMZ host rocks

Twenty one samples from units of the TLG type section (T1, T2, T3) were used for trace element studies. These rocks, except for TL-014A (Ca-Fe alteration), are representative of the least-altered portion of TLG unaffected by the Nori/RA, NICO, and Sue Dianne alteration envelopes. Therefore, they are not typical IOCG alteration assemblages. The complete data sets of the TLG rocks and FAB prospect host rocks are given in Table 2.2. Data for Sue Dianne and

DAMP host rocks were obtained from Gandhi (1989) and L. Ootes (unpublished data), respectively.

Unit T1 of the TLG has the highest whole rock Ti and V contents (4050 ppm and 109 ppm, respectively), compared to those of metasedimentary units and felsic volcanics of the GBMZ. Conversely, rhyodacites hosting the Sue-Dianne deposit have the lowest V (38 ppm), Ni (9 ppm), and Cr (24 ppm) concentrations (Gandhi, 1989). Overall, host-rock concentrations of Co vary from 3 to 13 ppm. Contents of other metals of economic interest, such as Cu and Bi, are generally between 2 ppm and 15 ppm (Cu) and <2 ppm (Bi).

2.5.3 Trace elements in GBMZ magnetite

Major element analyses by EMPA reveal that Fe contents vary between 70 and 73 wt. % (Table 2.3), which is consistent with magnetite stoichiometry. No other spinel group end members (e.g., ilmenite) were recognized. Trace elements such as Si, Al, Ti, Mn, and commonly V (except in T2mag, NICO, and Sue Dianne) were consistently detected by EMPA in most of the deposits generally under Set 2 conditions. Conversely, Mg, Ni and Cr were only sporadically detected, and thus, most EMPA analyses for those elements yield concentrations below detection limits (see Table 3). However, V, Cr, Co, Ni, Mn, and Ti, and in lesser amounts Cu, Sb, and Pb, were routinely detected by LA-ICP-MS. Other elements such as Th, U, Bi, Sm, La, Y, Yb, As, and Au were also detected locally. The LA-ICP-MS traverses reveal no evidence of compositional zoning. In magnetite NImag1, which has silicate inclusion-rich zones, no significant differences exist in the trace element contents (LA-ICP-MS suite) between inclusion-rich and inclusion-poor zones. The samples suite and number of analyses performed in each magnetite phase, as well as the average concentration of elements in the various magnetite types, together with other statistical data, are presented in Table 2.3 and Table 2.4.

Treasure Lake Group: The T2mag has lower V, Ni, Cr, and Co concentrations than T1mag (Figs. 2.14A; 2.15B-D), with average concentrations of 202 ppm, 31 ppm, 178 ppm, and 10 ppm, respectively. Average concentrations

of V, Ni, Cr, and Co in T1mag are 655 ppm, 151 ppm, 661 ppm, and 67 ppm, respectively (Figs. 2.15B-D).

Nori/RA: Magnetite from the Nori/Ra prospect has the highest concentrations of Cr (Nomag1, 1411 ppm; Fig. 2.15B). Concentrations of V are significantly higher in Nomag1 (1053 ppm) compared to Nomag2 (522 ppm), but lower than NoQksmag (1514 ppm; Fig. 2.14B). In contrast, Ni contents are higher in Nomag2 (596 ppm). Nickel concentrations in the NoQksmag samples were not acquired due to isotopic interferences. The Cr contents are also distinctly different: those in Nomag1 (1411 ppm) are up to two orders of magnitude higher than in Nomag2 (15 ppm) and NoQkmag (169 ppm; Fig. 2.14B). Conversely, Nomag1 has a narrow range of Co concentrations, with an average of 73 ppm. Except for two outliers close to 1000 ppm, most of the Co data is centered at 100 ppm (Fig. 2.15B). Magnetite from the K-feldspar-quartz segregations (NoQkmag) shows a bimodal distribution of Cr and V (Figs. 2.15 B, C). The population with lower Cr and V has similar values to those of Nomag2; the population with higher concentrations have values comparable to those of Nomag1.

NICO: Relative to magnetite from the other GBMZ sites, NICO magnetite contains, on average, the highest concentration of Si, Al, and Mg. These higher values could reflect mineral inclusions assimilated from the host rocks and/or phases that exsolved during mineral growth. Textural relations suggest that inclusions randomly distributed in NImag1 grains (Fig. 2.10D) are consistent with relict silicate minerals having been replaced by magnetite; a broad correlation between Si and Mg in NImag1 (Fig. 2.15A) supports this hypothesis. However, mineral inclusions can differ significantly in composition (e.g., quartz vs amphibole), and thus, this correlation might not be present in all cases. The presence of Si-Al-Mg-rich inclusions within concentric and/or parallel growth zones (only recognized in NImag1) (Fig. 2.9D) is more consistent with an origin by exsolution. Generally, both inclusion types occur in the same grain, which makes it impossible to analyze them via EMPA separately or even to conclusively evaluate their origin (inclusions vs exsolution). This applies not only to NICO magnetite, but to the other sampled locations in the GBMZ (e.g., Sue Dianne and FAB; Fig. 2.15A). It is nevertheless difficult to assess whether the high Si, Al, and Mg values correspond to the true partitioning of those elements into

magnetite, or if they are the result of micrometer-scale (<2μm) mineral inclusions. As a result, the data for these elements are not discussed further.

The Co, V, and Ni concentrations in NICO magnetite are the lowest of the entire suite. The Cr and V concentrations vary up to two orders of magnitude in the different magnetite phases (NImag1 to NImag3; Figs. 2.14C, 2.15B-D). A gradual decrease in Cr contents exists from NImag1 to NImag3 (30 ppm to 1 ppm; Figs. 2.14C, 2.15B). The V contents are similar in NImag1 (118 ppm) and NImag2 (169 ppm), but significantly lower in NImag3 (37 ppm) (Figs. 2.14C, 2.15C). Cobalt and Ni concentrations vary little and, for the most part, are each <10 ppm in all magnetite generations (Figs. 2.14C, 2.15B, D).

Terra: Terra magnetite has, on average, low Cr contents of 15 ppm (Figs. 2.14C, 2.15B), although most contain <1 ppm (Fig. 2.14C). The Temag is relatively enriched in Al (997 ppm), with values similar to those of NICO (NImag2). Vanadium concentrations (1201 ppm) are relatively high, and only slightly higher than those of Nomag1.

Sue-Dianne and DAMP: Magnetites from these deposits are enriched in Co (465 ppm and 415 ppm, respectively) compared to the other GBMZ magnetites (Figs. 2.14D, 2.15B). However, the V concentration in Sue-Dianne magnetite (140 ppm) is consistently lower than that from DAMP (719 ppm) (Fig. 2.14D). In contrast, Sue Dianne has higher Ni (62 ppm) compared to DAMP (13 ppm).

FAB: Contents of V and Cr in Fmag1 and Fmag2 are highly variable. The average Cr concentration of Fmag1 (388 ppm) is higher than that of Fmag2 (40 ppm), but concentrations in different grains vary from 36 to 1300 ppm in Fmag1 and from 0.7 to 187 ppm in Fmag2 (Fig. 2.14E). Cobalt concentrations in Fmag2 also vary over a wide range (14 to 342 ppm), with an average of 111 ppm. Fmag1 and Fmag2 have similar average Ni contents of 1270 and 1028 ppm, respectively, which correspond to the highest values among the GBMZ suite.

In summary, the range of transition metal concentrations in magnetite from the GBMZ varies over three to five orders of magnitude. In all cases,

different generations of magnetite from the same occurrence show differences in transition metal concentrations.

2.6 Discussion

2.6.1 Petrography

Magnetite textures, paragenesis, and geochemistry are documented here for a variety of alteration/mineralization stages across the GBMZ including mineralized and barren localities. Barren magnetite from the TLG group, specifically T1mag and Nomag1, is evenly disseminated within wall rock. Moreover, the presence of straight intergrain contacts, and lack of replacement textures and crosscutting relationships with other major minerals (biotite and K-feldspar) in the host metasiltstones, at the scale of observation, suggest that T1mag and Nomag1 are metamorphic in origin. In the case of T2mag, the magnetite and amphibole have selectively replaced carbonate-rich beds and share mineralogical similarities with the pre-sulfide, magnetite-amphibole alteration assemblage at the NICO deposit (NImag1), providing evidence for its (T2mag) metasomatic origin.

Magnetite is co-precipitated with cobaltite, loellingite, and Co-bearing arsenopyrite (NImag2) and bismuthinite-native bismuth (NImag3) at NICO, and with uraninite and molybdenite at Nori/RA (Nomag2). The paragenetically early magnetite in the altered metasedimentary rocks at NICO (NImag1) and Nori (Nomag1) are clear examples of pre-sulfide magnetite, because each is cut by later magnetite- (Nomag2-NomagQks and NImag2-NImag3) and sulfide-bearing veins. Conversely, magnetite in the Terra magnetite-apatite body does not appear to have crystallized with any sulfide minerals. In addition, the presence of highly fractured grains and a wide range of grain sizes is consistent with syn- to post-depositional brecciation. Magnetite in breccias and veins at DAMP (Dmag), Sue-Dianne (SDmag), and FAB (Fmag2) crystallized together with minor amounts of carrollite (in SDmag) and with traces of chalcopyrite that form inclusions in early-crystallized magnetite. The crosscutting relationships and replacement textures, however, indicate that most chalcopyrite and carrollite (in DAMP) precipitated

after magnetite. Chalcopyrite from Sue-Dianne and DAMP (SDmag and Dmag) is commonly replaced by chalcocite, bornite, and covellite. The latter minerals most likely co-precipitated, together with some hematite and other gangue minerals such as quartz, fluorite, chlorite, and epidote.

The temporal association of Fmag1 and Fmag2 is not well established as there are no evident crosscutting relationships due to the disseminated and fine-grained nature of Fmag1. However, we assume that Fmag2 is later, as it occurs in sulfide veins cutting the Fmag1-rich host rocks.

2.6.2 Metamorphic magnetite

In order to evaluate the chemical differences among magnetite phases of the GBMZ, it is important to first distinguish between hydrothermal (syn- and pre-sulfide) magnetite and metamorphic or recrystallized, high-temperature metasomatic magnetite. In the study area, magnetite formed under greenschist- to amphibolite-facies conditions during regional-scale metamorphism, but also during contact metamorphism and related metasomatic events. Hence, magnetite may have originated by the metamorphic conversion of precursor Fe-rich silicates and oxides (e.g., hematite, biotite, chlorite, clays), cements, and/or microgranules (as defined by Rassmussen et al., 2013), or by the recrystallization of pre-existing magnetite. Within the rocks studied, T1mag and Nomag1 are in textural equilibrium with K-feldspar, biotite, and quartz (± muscovite), and in Nori/Ra they formed prior to coarse-grained, hydrothermal biotite selvages along the sulfide-rich veins (Ootes et al., 2010), which postdate Nomag1. Therefore, we consider T1mag and Nomag1 to be the best candidates for magnetite derived from regionally metamorphosed, least-altered siltstones. As such, we use data for them as a benchmark for barren magnetite relative to those for sulfide-related hydrothermal magnetite.

2.6.3 Comparision of GBMZ magnetite with magnetite from other deposits

Dupuis and Beaudoin (2011) published a series of diagrams that use magnetite and hematite to classify different ore deposits based on average contents of selected trace elements analyzed by EMPA. Data from our EMPA and LA-ICP-MS analyses are plotted on their Ti + V vs. Ni/(Cr+Mn) diagram (Fig.

2.16E) in order to compare the geochemistry of GBMZ magnetite with that of other mineral deposits. The majority of the GBMZ data plots in the skarn field or outside of the diagram limits, except analyses for Nomag2, Fmag1, and Fmag2, all of which plot close to the Opemiska and Kiruna fields. The Opemiska (Canada) deposit consists of Cu-Au veins hosted by chlorite schist. Pyrite, chalcopyrite, and pyrrhotite are the most abundant sulfides in the main stage of mineralization, accompanied by significant amounts of scheelite and molybdenite (Guha, 1984). The main stage is overprinted by a molybdenite-pitchblende stage (Guha, 1991), similar to that co-precipitated with Nomag2 in the Nori/Ra prospect. However, it is unclear in Dupuis and Beaudoin (2011) if the magnetite analyzed was from the main Cu-Au vein or from the later Mo-U stage.

Regionally, the south-central part of the GBMZ contains magnetite that is characterized by low Ni concentrations of <200 ppm (except for Fmag2, Nomag2, and most of Fmag1), which are close to the detection limit (185 ppm) reported by Dupuis and Beaudoin (2011). These low Ni contents suggest that such low values (and perhaps those of other elements) were not taken into account during the construction of the Ti+V vs. Ni/(Cr+Mn) diagram. Consequently, a significant proportion of GBMZ magnetite has low Ni/(Cr+Mn), resulting in the observed "skarn-like" signature.

Work done by Muller et al. (2006), Nystrom and Enriquez (1994), and Loberg and Horndahl (1983) has shown that magnetite from Kiruna-type deposits contains up to 2500 ppm V and up to 2400 ppm Mn, and that the V contents of Kiruna magnetite-apatite ores are higher when compared to those of magnetite having a sedimentary origin (e.g., banded iron formation, V <100 ppm). The Terra magnetite has V and Mn concentrations consistent with the aforementioned studies, although average Mn of Terra magnetite (628 ppm) is generally lower than that for Kiruna magnetite (~1980 ppm) if compared to the data of Muller et al. (2006). When V and Mn concentrations in Terra magnetite are compared to those of other GBMZ magnetites from DAMP (Mn), Nori/RA (Nomag1 and NQksmag, V), FAB (Fmag1, V), and the TLG (T2mag, Mn), the differences are negligible. Thus, it is not possible to differentiate among the Kiruna and IOCG-

related, and barren and metamorphic magnetite from the GBMZ, solely on the basis of V and Mn contents.

Results of our work imply that the geochemical signature of magnetite from iron-oxide and alkali-rich mineralizing systems can be highly variable, most likely due to regional and/or local variations in temperature, redox conditions, and trace element budgets in fluids and host rocks. As a result, the classification of Dupuis and Beaudoin (2011) and other classifications (e.g., Nystrom and Enriquez, 1994, for magnetite-apatite ores) should be used with caution when comparing the geochemistry of magnetite from different mineralizing systems or metallogenic provinces.

2.6.4 Relationship of magnetite to IOCG alteration

In this section we relate the magnetite described in the present study to specific IOCG alteration types using sulfide and gangue mineral assemblages described in the alteration model of Corriveau et al. (2010a, b). Moreover, we assess the magnetite geochemical signatures to determine whether there is any correlation with geochemical footprints of the IOCG systems and related alteration zones in the GBMZ, as documented recently by Montreuil et al. (2013).

The IOCG alteration model describes the characteristics of five main stages (Corriveau et al. 2010a, b); magnetite is an important component in three of these. Predominant alteration assemblages, from high to low temperature and from oldest to youngest, are: (1) sodic to sodic-calcic, characterized by the presence of albite and albitites, (2) high-temperature, calcic-iron (HT Ca-Fe) that produced diverse assemblages of magnetite + amphibole ± apatite, and in places led to iron oxide-apatite mineralization; (3) high-temperature, potassic-iron (HT K-Fe) (K-feldspar, biotite, magnetite variants) with associated sulfide disseminations within alteration gangue minerals or as veins or breccia infillings; (4) K-feldspar felsite breccias at the magnetite to hematite transition, or skarn assemblages with K-feldspar, clinopyroxene, and garnet spatially associated with sulfides; and (5) low-temperature, potassic-iron (LT K-Fe) in which K-feldspar, sericite, hematite (± magnetite), carbonate, chlorite, and sulfides are closely associated. In the GBMZ, development of these alteration stages varies from

kilometer to centimeter scales. Commonly, in hand specimens or meter-wide outcrops, several alteration stages can be identified as a series of overprints expressed as veins or alteration fronts (e.g., albitite cut by K-feldspar-magnetite veins).

At the NICO deposit and in the TLG, NImag1, NImag2, NImag3, and T2mag co-precipitated with variable amounts of amphibole and, therefore, this assemblage is comparable to that produced by the high-temperature Ca-Fe alteration. Magnetite from DAMP and Sue-Dianne can be considered part of the high-temperature (HT) K-Fe alteration zone transitional to the low-temperature (LT) K-Fe zone, as these are spatially associated with sulfides, hematite, and minor K-feldspar. The Fmag1 and Fmag2 are predominantly associated with pyrite and K-feldspar, and are therefore grouped with the HT K-Fe alteration. At Sue Dianne and DAMP, specular hematite co-precipitated with magnetite, where the former is predominant. Pseudomorphs of magnetite (martitization) by hematite are more common in these systems. At Sue Dianne, it is well documented that martitization and the occurrence of sericite are more conspicuous at shallower levels and presumably in lower temperature regimes (Camier, 2002; Mumin et al., 2010; this study). These relationships therefore suggest an overprinting of the initially predominant HT K-Fe by the LT K-Fe alteration.

Because Nomag2 in the U-Mo±Cu veins at the Nori/RA prospect is scarce (<1% vol. %), there is no clear association with an IOCG alteration phase. In this study, we consider the mineralogy of Terra magnetite from the magnetite-apatite bodies to be consistent with formation of the high-temperature Ca-Fe alteration associated with the iron oxide-apatite variant of Corriveau (2010a,b). Therefore, in the following discussion this magnetite will be framed within the spectrum of IOCG-type alteration. However, as discussed above, we acknowledge that the geochemistry of Terra magnetite also shares similar features with those of magnetite-apatite Kiruna-type deposits.

Montreuil et al. (2013) document element depletions (e.g., Fe, Co, Ni, Mg, Mn, V) of the early Na-Ca alteration relative to the subsequent HT Ca-Fe, HT K-Fe, and LT K-Fe alteration zones, and suggest that these alteration phases (Ca-Fe

and K-Fe) constitute important geochemical sinks. Montreuil et al. (2013) state that in the GBMZ, irrespective of the initial host rock composition, each alteration type ultimately reaches a systematic and diagnostic geochemical signature. However, significant internal variation of a particular alteration composition can be a function of the mineral assemblage present (magnetite-amphibole vs magnetite only or magnetite-sulfides), hence appreciable variation within a single alteration type can be expected.

The occurrence of magnetite in the Na-Ca alteration is uncommon and is not observed in our samples. Therefore, in this work we only discuss the differences in magnetite composition within the HT Ca-Fe (NICO, TLG) and K-Fe alteration stages (DAMP, Sue Dianne, FAB). Our data show an enrichment of Co and locally, of V in magnetite of the HT-K-Fe (FAB, Fmag2) and HT-K-Fe alteration transitional to the LT K-Fe alteration stage (magnetite- to hematite-dominated alteration phase, DAMP and Sue-Dianne), relative to the HT Ca-Fe alteration magnetite (NICO and altered TLG); the exception is Terra magnetite (magnetite-apatite variant), which has V and some Co contents that overlap those of the HT-K-Fe alteration (Fig. 2.15B, C). Hence, variations of V, Ni, and Co concentrations in magnetite from the amphibole-magnetite and magnetite-apatite Ca-Fe alterations may constitute a useful tool to distinguish these alteration stages.

HT-K-Fe-altered rocks at the FAB prospect display local enrichments in V, Co, and Ni (relative to early sodic alteration) associated with Cu-rich mineralization (Montreuil et al., in prep). Our data from Fmag1 and Fmag2 also show relatively high contents (with respect to other GBMZ magnetite) of V, Ni, and less of Co (Fmag2; Figs. 2.15B-D), and therefore the magnetite geochemistry for FAB might be correlative with that of the HT-Fe-K alteration. Comparatively lower values of magnetite in the HT Ca-Fe alteration (magnetite-amphibole variant) relative to other GBMZ magnetite (locally up to two orders of magnitude) is inconsistent with the enrichment of those elements in this alteration type (Montreuil et al., 2013). This contrast suggests that magnetite geochemistry is not solely representative of its host alteration composition. Instead, other possible

factors such as fluid-rock equilibration, Fe-rich fluid chemistry, co-precipitating mineral phases, and fO_2 might have affected the partitioning of trace elements in magnetite. These possibilities are discussed in the following sections involving the distribution of selected metal ratios.

2.6.5 Influence of host rocks on magnetite chemistry

The Cr/Co, V/Co, and V/Ni ratios of magnetite from the Ca-Fe alteration stage (amphibole-magnetite variant) are shown in Figures 2.16B, D. These data plot broadly in the same field as the ratios for metamorphic (T1mag1 and Nomag1), barren, and pre-ore HT K-Fe (Fmag1) alteration magnetite, part of the NoQKmag, as well as for the bulk composition of the TLG and rhyodacitic host rocks. This pattern is consistent with inheritance of these magnetite-based element ratios from the host rocks, specifically as a result of (i) metamorphism of precursor Fe-rich minerals in the metasedimentary rocks, and (ii) post-metamorphic metasomatic replacement of silicates in the metasedimentary rocks and rhyodacites, and/or in precursor iron oxides.

Ordóñez-Calderón et al. (2008) and Brugger et al. (2000) have shown the restricted mobility of transition elements such as V, Co, Ni, and Cr during greenschist- to amphibolite-facies conditions, which are equivalent to those that affected the TLG. Work done by Ordóñez-Calderón et al. (2008) on amphibolized mafic and ultramafic rocks from the Ivisaartoq greenstone belt (West Greenland) show that Co, Cr, Ni, and V were immobile during pre-metamorphic seafloor hydrothermal alteration, as well as during later regional metamorphic events. Their data demonstrate the preservation of Cr/Co and V/Ni ratios in ultramafic and mafic amphibolitic units compared to their metasomatized calc-silicate rich equivalents (e.g., unmetasomatized ultramafic units, Cr/Co = 24, vs. metasomatized ultramafic units Cr/Co = 17). Similar results were obtained by Brugger et al. (2000) for magnetite in the Val Ferrera (Swiss Alps) metamorphosed Fe-Mn deposits, which formed syngenetically as chemical sediments around marine springs and have significant contents of Ba, Sb, As, V, Be, and W. A restricted redistribution of those elements occurred during blueschist- to greenschist- facies regional metamorphism; syn-deformation

minerals such as hematite represent important sinks of trace elements released by the re-crystallization or breakdown of primary phases as a result of prograde metamorphism (Brugger et al., 2000). Consequently, a similar inheritance of transition elements could explain the preservation of the Cr/Co, V/Co, and V/Ni signatures in metamorphic magnetite from the GBMZ. Moreover, the subsequent metasomatic replacement of precursor silicates, carbonates, and metamorphic magnetite (T1mag) by post-metamorphic hydrothermal magnetite (Fmag1, T2mag, NImag1) at low fluid/rock ratios may have produced a similar inheritance. In addition, the similarity of some of the NImag2 data to those for the metasedimentary rocks and NImag1 (Figs. 4.15E, 4.16D) could be a consequence of partial dissolution of NImag1 by NImag2-rich fluids and the precipitation of NImag2, resulting in a mixed geochemical signature. For NoQksmag, most magnetite grains having high Cr/Co ratios crystallized along the contact between the host rocks and the segregations. Thus, we interpret this generation of magnetite to be a coarser grained re-crystallization of Nomag1.

2.6.6 Oxygen fugacity and temperature

At NICO, V/Co and Cr/Co ratios in magnetite decrease from the earliest to the latest generation due to the lower concentrations of Cr and V in NImag1 compared to NImag3 (Figs. 2.15E, 2.16A). This pattern could reflect changes in temperature and/or redox conditions. Owing to a lack of studies on the fractionation of trace elements between magnetite and hydrothermal solutions, it is difficult to assess the behavior of V, Cr, Ni, and Co in magnetite at different temperature and redox conditions in hydrothermal and metamorphic systems. However, experimental work and geochemical modeling carried out on silicate melts (e.g., Toplis and Corgne, 2002) and aqueous solutions (e.g., Takeno, 2005) provide some insights into the behavior of V in NICO magnetite. The oxidation state of V in natural environments varies from +II to +V, but the +II state is only found in extremely reduced systems (e.g., Takeno, 2005), whereas the common fugacity range permits the occurrence of V^{3+}, V^{4+}, and V^{5+}. Among these species, V^{+3} has the highest compatibility with the spinel structure of magnetite (e.g., Balan et al., 2006; Righter et al. 2006). In silicate melt experiments, the

fractionation of V into magnetite, D(V), is a function of fO_2 and temperature (unlike Co and Ni; Toplis and Corgne, 2002; Righter et al., 2006). The magnetite/liquid partition coefficient for V or D(V) decreases with increasing fO_2, as V^{3+} is less stable under these conditions. Phase diagrams of V aqueous species (Takeno, 2005) also show a predominance of V^{3+} in reducing environments, and that even a small increase in fO_2 could convert it to V^{4+}, which is less compatible with the magnetite structure. In the Ernest Henry deposit in Queensland, Carew (2004) recognized a depletion in the V content of magnetite as the system evolved from early sodic to later potassic alteration, and to magnetite associated with Cu-Au mineralization; this pattern was interpreted to reflect an increase in fO_2 of the fluids with time. Thus, the trend of gradual V depletion observed in NICO magnetite, from NImag2 to NImag3, which is similar to that at Ernest Henry, could record an increase in fO_2 of the system. However, it is also possible that the gradual depletion of Cr and V might reflect a depletion with time of those elements in the hydrothermal fluids.

Future studies to determine if V partitioning in hydrothermal magnetite is analogous to that in magmatic melts should focus on the concentrations of this element in magnetite from a single system having a complete, or nearly complete, spectrum of IOCG alteration assemblages. In the present study, we are limited in comparing V contents from the HT Ca-Fe and HT to LT K-Fe alteration assemblages from different systems of the GBMZ. It might be assumed that higher concentrations of V occur in magnetite from the HT Ca-Fe alteration assemblage (higher temperature and comparatively more reducing conditions) and, in contrast, lower V contents in magnetite that co-precipitated with hematite of HT to LT-K-Fe alteration assemblage (lower temperature and relatively more oxidized). However, our data show that magnetite from Sue Dianne and DAMP (HT to LT-K-Fe alteration) lacks a significant depletion of V relative to the HT Ca-Fe alteration assemblage (amphibole-magnetite variant). Conversely, DAMP magnetite is up three orders of magnitude more V-rich, comparable to V contents in magnetite from the Terra magnetite apatite body (Ca-Fe alteration type, apatite-magnetite variant). Hence, other factors discussed below, such as geochemistry of

the fluids and co-precipitating mineral phases, might be responsible for the contents of V and other trace elements (e.g., Co and Ni) in the HT- to LT-K-Fe alteration magnetite.

2.6.7 Fluid geochemistry: evidence from Co/Ni ratios

As explained above, the Cr/Co, V/Co, and V/Ni ratios of magnetite from Ca-Fe (amphibole-magnetite variant) and pre-ore HT-K-Fe alteration assemblages are analogous to those of their host rocks. This similarity suggests that equilibration between the Fe-bearing fluids and country rocks might be recorded in magnetite chemistry. However, significant deviations from the host rock ratios are observed in later magnetite generations from NICO (NImag2 and NImag3), Nori/RA (Nomag2-NoQksmag), and Sue Dianne and DAMP. The NoQksmag data having low Cr/Co ratios correspond to those of magnetite that co-precipitated with pyrite, similar to Nomag2, thus implying that both magnetites crystallized from similar parental hydrothermal fluids. In the case of NICO, these differences might be triggered by changes in redox conditions. Therefore, and in the absence of suitable evidence suggesting otherwise, this pattern implies that distinct metal ratios could reflect the chemistry of the magnetite-depositing fluids. However, the co-precipitation of sulfides and magnetite is an important factor that limits our ability to characterize the geochemistry of the Fe-bearing fluids based only on trace elements contents in magnetite (see section below), although recent studies on the solubility of Co and Ni provide insights into the relative abundance of these metals in hydrothermal fluids (e.g., Migdosov et al., 2011; Liu et al., 2011; Tian et al., 2012). In this section, we discuss the partitioning of Co and Ni in magnetite from Sue Dianne and DAMP as a function of fluid geochemistry using the Co/Ni ratio as a proxy.

The magnetite Co/Ni ratios define two populations (Fig. 2.16C). One, represented by magnetite from Nori/Ra, NICO, FAB, Terra, and TLG, has low Co/Ni ratios; generally less than two, with a few outliers slightly below four. The second population, represented by Sue-Dianne and DAMP, has distinctly higher Co/Ni ratios of 7 to 94. These high ratios cannot be attributed to equilibration of fluids with felsic host rocks because the latter have Co/Ni ratios of less than two,

although the lithogeochemical signature of the country rocks may have been modified by pre-ore hydrothermal alteration, as suggested by Montreuil et al. (2013). These high ratios could reflect: (i) magnetite derived by different geological processes (e.g., magmatic, hydrothermal, metamorphic); (ii) equilibration of the magnetite-forming fluids with other rock units along the flow path, such as Bloom basalts and Fishtrap gabbros stratigraphically underlying the TLG; or (iii) preferential solubility of Co over Ni in the hydrothermal fluids at the stage of alteration reached. These hypotheses are discussed below in detail.

The Co/Ni ratio has been used by Freitsch (1970) to characterize magnetite derived from different geological processes. For the most part, he found this ratio to be <1 except for mafic magmatic rocks (1-3), stratified ores (~1), and few skarn iron ores (~4). The data of Parak (1975) and Cann (1976) indicate that accessory igneous magnetite from felsic, intermediate, mafic and ultramafic rocks, has low Co/Ni (<1). This is in agreement with recent work done by Dare et al. (2012) on igneous magnetite co-precipitated with massive sulfides from deposits in the Sudbury district, which have Co/Ni of 0.01 to 0.03. Cobalt/nickel values in magnetite from a variety of hydrothermal ore deposits are also generally low (<2); Big Cadia (0.6 to 3.0; Bajwah, 1987), Ernest Henry (0.018-1.80), Lightning Creek (0.29-2.36), Starra (0.51-0.81), and Osborne (0.53-1.16) (Carew, 2004), and Lucky Friday mine (0.1-0.3; Nadoll et al., 2012). Gregory (2006) and Nadoll et al. (2012) reported data for metamorphic magnetite with a Co/Ni of 0.4-0.7 and 0.1-0.7, respectively. Therefore, regardless of its origin, magnetite Co/Ni values are usually <4 and hence, magnetite formed through a variety of geological processes cannot be equated with the high ratios in the magnetite from DAMP and Sue-Dianne, which, to our knowledge, are the highest reported to date.

If the average Co/Ni ratio for oceanic crust (N-MORB) is used as a proxy for the Bloom basalts and other mafic units in the LaBine Group, these units would be expected to have ratios between ca. 0.2 and 0.7 (Thompson et al., 1980; Niu et al., 1999; Lehnert et al., 2000). In addition, data from other types of mafic igneous rocks, such as serpentinite (0.03-0.70) and gabbro (0.15-0.55), have even lower Co/Ni ratios in which Ni contents are up to two orders of magnitude higher

than Co contents (Deschamps et al., 2012; Augustin et al., 2012). The Basaltic trachyandesite has ratios that are mostly >1, but rarely greater than 4.6 (Deng et al., 2012) because these rocks have lower Ni contents (<5 ppm). The TLG has Co/Ni ratios of 0.2 to 0.7, which are very close to those of average upper continental crust (0.31), shale (0.38), and marine sediments (0.13-2.15), as compiled by Li (2000). Similar results were obtained for Cretaceous oceanic red beds (0.11-0.41; Bak, 2007; Neuhuber and Wagreich, 2009, 2011). Consequently, the Co/Ni ratio in DAMP and Sue-Dianne magnetites is unlikely to be solely a result of re-equilibration with rocks along the flow path of the hydrothermal fluids. However, some of the Co could have been leached from mafic units underlying the TLG and GBMZ, such as the Fishtrap gabbros and Bloom basalts, or from other mafic components in the Hottah terrane underlying the LaBine and Faber groups.

Estimates of the solubility of Co and Ni in chlorine-rich aqueous solutions at temperatures between 26 and 400 ºC suggest that these metals form complexes mostly with Cl (e.g., $CoCl^{+}$, $CoCl_2^{0}$, $CoCl_3^{-}$, $CoCl_4^{-2}$) and to a lesser extent, in the case of Co, with HS^{-} ($\leq$ 200 ºC; Migdisov et al., 2011; Tian et al., 2011; Liu et al., 2012). The formation of $Ni(Co)Cl_2$-tetrahedral complexes with water molecules increases the solubility of these metals in aqueous solutions (Liu et al., 2011; Tian et al., 2012). Experimental studies indicate that full stability of the Co-tetrahedral complexes in aqueous solutions is reached at lower temperatures (250 ºC) than those of Ni (i.e., 369ºC; Liu et al., 2011). Tian et al. (2012) obtained similar results by comparing the dissolution of pentlandite and Co-pentlandite in saline aqueous solutions, where the solubility of the latter is 100x greater than that of pentlandite. This behavior of Co and Ni may explain why Ni-rich hydrothermal deposits are scarce compared to hydrothermal Co-rich deposits (Tian et al., 2012). Such a preferential enrichment of Co over Ni in hydrothermal solutions might also explain the high Co/Ni ratio in magnetite from DAMP and Sue-Dianne, and suggest that this ratio represents the Co/Ni ratio of the Fe-rich parental hydrothermal fluids from which the magnetite and carrollite precipitated. Moreover, this ratio may be diagnostic for transitional HT to LT K-Fe alteration

assemblages having significant amounts of Co and scarce to absent sulfides that co-precipitated with magnetite. Consequently, in these case examples (DAMP and Sue-Dianne), the Co/Ni ratio constitutes an important signature of magnetite associated with Cu-U (± Co) iron oxide breccia systems in the GBMZ, and possibly in other IOCG systems worldwide.

2.6.8 Co-precipitating sulfarsenides and sulfides

It is important to note that magnetite deposited from a Co-rich fluid can still have low Co contents if it co-precipitated with Co-rich sulfarsenides (e.g., NImag2). Cobalt and Ni are siderophile elements, and as such, Fe sulfides and sulfarsenides are capable of competing more effectively for them than oxides. In several deposits from the Sudbury district, Ni, Co, Zn, Mo, Sn, and Pb are present in magnetite just above detection limits (LA-ICP-MS and EMPA) where it co-precipitated with sulfides (Dare et al., 2012). Moreover, Ni, Mo, and Co are compatible in Fe-rich monosulfide solution (MSS) and thus co-crystallizing Fe-oxide is depleted in these elements (Dare et al., 2012). Conversely, magnetite that crystallized later with Cu-rich intermediate solid solution (ISS) is relatively enriched in Ni, Mo, and Co because Fe-rich MSS is absent from this younger assemblage (Dare et al., 2012). Similarly, compared to NICO, DAMP and Sue Dianne represent sulfur-deficient systems in which magnetite co-precipitated only with trace amounts of sulfides, because most of the chalcopyrite and carrollite are paragenetically later. The DAMP and Sue Dianne systems thus favored the partitioning of Co into magnetite. Moreover, the preferential partitioning of Ni and Co could also explain the correlation (or lack thereof) between the geochemistry of magnetite and that of coeval altered host rocks. In cases where the magnetite and associated alteration have analogous compositions (in terms of the studied elements), magnetite chemistry controls the overall alteration signature. The FAB prospect is an example wherein high concentrations of V occur in the K-Fe alteration assemblage (Montreuil et al., in prep.), which hosts V-rich magnetite (>1000 ppm, this study). In contrast, where elements are more compatible with co-precipitating minerals (e.g., sulfides, other spinels), then the geochemical signatures of magnetite and its host alteration assemblage will differ.

2.6.9 Summary of geochemical implications

The arguments presented above suggest that metal ratios determined in magnetite most likely reflect diverse and complex geochemical processes, which are responsible for the partitioning of trace elements into the magnetite. Such processes in the GBMZ could be associated with: (i) equilibration between fluids and host rocks; (ii) regional metamorphism and post-metamorphic metasomatism as suggested by similar Cr/Co, V/Ni, and V/Co ratios between TLG host rocks and most magnetite (T1mag, T2mag, NImag1± NImag2); (iii) preferential solubility of elements in Fe-rich hydrothermal fluids (e.g., Co>Ni), thus explaining the high Co/Ni ratios in DAMP and Sue Dianne; (iv) changes in fO_2, which is implied by the gradual depletion of V from NImag1 and NImag2 to NImag3, although this depletion can also be caused by a depletion of V in the fluid with time; and (v) co-precipitation of sulfides and/or sulfarsenides (NICO, DAMP, and Sue Dianne), a process that might have competed more effectively for Co and Ni, thus resulting in the low concentrations of these elements in magnetite derived from Co(± Ni)-rich fluids. Conversely, in sulfur-deficient systems and in the absence of co-precipitating sulfides, Co and Ni partitioning into magnetite will be favored (e.g., DAMP and Sue Dianne).

2.7 Exploration applications

McMartin et al. (2012) carried out a preliminary study in the Lou Lake area and at the NICO deposit reporting K, Ca, Al, Si, Ti, and Mg with a 20 ppm detection limit (EMPA), 50 ppm for Mn, Cr, and V, 200 ppm for Cu and Ni, and 400 ppm for Zn. They noted that the Ti+V (%) content of hematite and magnetite in samples of till and hydrothermally-altered bedrock and that of the polymetallic mineralization at NICO is lower than the contents from the bedrock and the till near the Fe-oxide TAN prospect (10 km NE of NICO). Thus, McMartin et al. (2012) suggested that the geochemistry of iron oxides could potentially be used as an indicator mineral for exploration.

Our data show that a significant overlap in Ti+V contents of magnetite exists between ore-related samples from NICO and the other polymetallic systems

and from barren (metamorphic) magnetite. In contrast, Cr/Co, V/Co, Co/Ni, and V/Ni ratios appear to be more diagnostic. The ratio of Cr/Co is distinctly higher in pre-ore (NImag1 and Fmag1) and barren (metamorphic and T2mag) magnetite from the TLG, compared to those (Cr/Co <1) in magnetite coeval with ore minerals and/or hosted by iron-oxide (± sulfide)-dominated breccias and veins (Cr/Co <1) (Fig. 2.16D). However, some NImag2 magnetite has elevated Cr/Co ratios similar to those of non-ore-related magnetite, which suggests there are transitional compositions between the barren and ore-associated signatures, and that these diagrams should be used with caution when interpreting the geochemistry of magnetite. Magnetite in the Terra magnetite-apatite body also has very low Cr/Co ratios, and although this magnetite lacks a direct link to ore minerals, it is spatially associated with the quartz vein-hosted polymetallic ores at the Terra-Norex deposits. The V/Ni ratio of magnetite is less useful on a regional scale, but in the DeVries Lake area, this ratio distinguishes between metamorphic (Nomag1) and vein-hosted (Nomag2) magnetite (Fig. 11B). The Co/Ni ratio (7-94; Fig. 11C) successfully differentiates Sue-Dianne and DAMP magnetite from magnetite elsewhere in the GBMZ. In summary, this study has demonstrated that, despite a lack of knowledge of specific physicochemical controls on trace element compositions, magnetite has distinctive geochemical signatures that make this iron oxide a potentially useful indicator mineral in exploration surveys.

2.8 References

Acosta-Góngora, P., Gleeson S.A., Ootes, L., Jackson, V.A., Lee, M.D., and Samson, I., 2011, Preliminary observations on the IOCG mineralization at the DAMP, Fab, and Nori showings and Terra-Norex mines, Great Bear Magmatic Zone: NWT Open File 2011-01, 11p.

Augustin, N., Paulick, H., Lackschewitz, K.S., Eisenhauer, A., Garbe-Schönberg, D., Kuhn, T., Botz, R., and Schmidt, M., 2012, Alteration at the ultramafic-hosted Logatchev hydrothermal field: Constraints from trace element and Sr-O isotope data: Geochemistry, Geophysics, Geosystems, v. 13, doi:10.1029/2011GC003903.

Azar, B., 2007, The lithogeochemistry of volcanic and subvolcanic rocks of the FAB Lake area, Great Bear magmatic zone, Northwest Territories, Canada: Unpublished B.Sc. thesis, Toronto, University of Toronto, 96 p.

Badham, J.P.N., 1973, Calc-alkaline volcanism and plutonism from the Great Bear batholith, N.W.T: Canadian Journal of Earth Sciences, v. 10, p. 1319-1328.

Badham, J.P.N., 1975, Mineralogy, paragenesis and origin of the Ag-Ni-Co arsenide mineralization, Camsell River, N.W.T. Canada: Mineralium Deposita, v. 10, p. 153-175.

Badham, J.P.N., and Morton, R.D., 1976, Magnetite-apatite intrusions and calc-alkaline magmatism, Camsell River, N.W.T: Canadian Journal of Earth Sciences, v. 13, p. 348-354.

Bajwah, Z.U., Seccombe, P.K., and Offler, R., 1987, The trace element distribution, Co/Ni ratios and genesis of the Big Cadia iron-copper deposit, New South Wales, Australia: Mineralium Deposita, v. 22, p. 292-300.

Bak, K., 2007, Deep-water facies succession around the Cenomanian–Turonian boundary in the outer Carpathian basin: Sedimentary, biotic and chemical records in the Silesian nappe, Poland: Palaeogeography, Palaeooclimatology, Palaeoecology, v. 248, p. 255-290.

Balan, E., De Villers, J.P.R., Eeckhout, S.G., Glatzel, P., Toplis, M.J., Fristsch, E., Allard, T., Galoisy, L., and Calas, G., 2006, The oxidation state of vanadium in titanomagnetite from layered basic intrusions: American Mineralogist, v. 91, p. 953-956.

Bennett, V., and Rivers, T., 2006, U-Pb ages of zircon primary crystallization and inheritance for magmatic rocks of the southern Wopmay orogen, Northwest Territories: NWT Open File 2006-006, 65 p.

Bennett, V., Rivers, T., and Jackson, V.A., 2012, A compilation of U-Pb zircon primary crystallization and depositional ages from the Paleoproterozoic southern Wopmay orogen, Northwest Territories: NWT Open File Report 2012-003, 157 p.

Bowring, S.A., 1984, U-Pb zircon geochronology of Early Proterozoic Wopmay orogen, N.W.T. Canada: An example of rapid crustal evolution: Unpublished Ph.D. thesis, Lawrence, Kansas, University of Kansas, 148 p.

Brügger, J., 2000, Origin and distribution of some trace elements in metamorphosed Fe-Mn deposits, Val Ferrera, eastern Swiss Alps: Canadian Mineralogist, v. 38, p. 1075-1101.

Camier, W.J., 2002, Geology of the Sue-Dianne Proterozoic Cu-Ag-Fe oxide breccia complex, Mazenod Lake district, Northwest Territories: Unpublished M.Sc. thesis, London, University of Western Ontario, 210 p.

Cann, R.M., 1976, Genesis of magnetite-apatite lodes: Unpublished B.Sc. thesis, Vancouver, University of British Columbia, 193 p.

Carew, M.J., 2004, Controls on Cu-Au mineralization and Fe oxide metasomatism in the Eastern Fold Belt, N.W. Queensland, Australia: Unpublished Ph.D. thesis, Townsville, James Cook University, 293 p.

Coles, R.L., Haines, G.V., and Hannaford, W., 1976, Large-scale magnetic anomalies over western Canada and the Arctic: A discussion: Canadian Journal of Earth Sciences, v. 13, p. 790-802.

Corriveau, L., 2007, Iron oxide-copper-gold deposits: A Canadian perspective, in Goodfellow, W.D., ed., Mineral deposits of Canada: A synthesis of major deposit-types, district metallogeny, the evolution of geological provinces and exploration methods: Geological Association of Canada, Special Publication 5, p. 307-328.

Corriveau, L., Ootes, L., Mumin, H., Jackson, V., Bennett, V., Cremer, J.F., Revard, B, McMartin, I., and Beaudoin, G., 2007, Alteration vectoring to IOCG(U) deposits in frontier volcanic-plutonic terrains, Canada: International Conference on Mineral Exploration, 5th, Canada, 9-12 September 2007, Proceedings, p. 1171-1177.

Corriveau, L., Mumin, A.H., and Setterfield, T., 2010a, IOCG environments in Canada: Characteristics, geological vectors to ore and challenges, in Porter, T.M., ed., Hydrothermal iron oxide copper-gold & related deposits: A global perspective,: Adelaide, PGC Publishing, v. 4, p. 311-343.

Corriveau L., Williams, P.J., and Mumin A.H, 2010b, Alteration vectors to IOCG mineralization from uncharted terranes to deposits, in Corriveau, L., and Mumin, A.H., eds., Exploring for iron oxide copper-gold deposits: Canada and global analogues: Geological Association of Canada Short Course 20, p. 89–110.

Dare, S.A.S, Barnes, S.J., and Beaudoin, G., 2012, Variation on trace element content of magnetite crystallized from fractionating sulfide liquid, Sudbury, Canada: Evidence for provenance discrimination: Geochimica et Cosmochimica Acta, v. 88, p. 27-50.

Davis, W., Corriveau, L., van Breemen, O., Bleeker W., Montreuil, J.F., Potter, E., and Pelletier, E., 2011, Timing of IOCG mineralizing and alteration events within the Great Bear magmatic zone: Yellowknife Geoscience Forum , 39th , Canada, 15-17 November 2011, Abstracts, p. 97.

Deng, J., Yang, X., Sun, W., Huang, Y., Chi, Y., Yu, L., and Zhang, Q., 2012, Petrology, geochemistry, and tectonic significance of Mesozoic shoshonitic volcanic rocks, Luzong volcanic basin, eastern China: International Geology Review, v. 54, p. 714-736.

Dentith, M.C., Frankcombe, K.F., and Trench, A., 1994, Geophysical signatures of Western Australian mineral deposits: An overview: Exploration Geophysics, v. 25, p. 103-160.

Deschamps, F., Godard, M., Guillot, S., Chauvel, C., Andreani, M., Hattori, K., Wunder, B., and France, L., 2012, Behavior of fluid-mobile elements in serpentinites from abyssal to subduction environments: Examples from Cuba and Dominican Republic: Chemical Geology, v. 313, p. 93-117.

Dupuis, C., and Beaudoin, G., 2011, Discriminant diagrams for iron oxide trace element fingerprinting of mineral deposit types: Mineralium Deposita, v. 46, p. 319-335.

Fipke, C.E., Gurney, J.J., and Moore, R.O., 1995, Diamond exploration techniques emphasizing indicator mineral geochemistry and Canadian examples: Geological Survey of Canada Bulletin 423, 86 p.

Frietsch, R., 1970, Trace elements in magnetite and hematite mainly from northern Sweden: Sveriges Geologiska Underskøning, v. 64, 136 p.

Gandhi, S.S., 1988, Volcano-plutonic setting of U-Cu bearing magnetite veins of FAB claims, southern Great Bear magmatic zone, Northwest Territories: Geological Survey of Canada Paper 88-1C, p. 177-187.

Gandhi, S.S, 1989, Rhyodacite ignimbrites and breccias of the Sue-Dianne and Mar Cu-Fe-U deposits, southern Great Bear magmatic zone, Northwest Territories: Geological Survey of Canada Paper 89-1C, p. 263-273.

Gandhi, S.S., 1994, Geological setting and genetic aspects of mineral occurrences in the southern Great Bear magmatic zone, Northwest Territories, in Sinclair, W.D., and Richardson, D.G., eds., Studies of rare-metal deposits in the Northwest Territories: Geological Survey of Canada Bulletin 475, p. 63-96.

Gandhi, S.S., and Lentz, D.R., 1990, Bi-Co-Cu-As and U occurrences in the metasediments of the Snare Group and felsic volcanics of the southern Great Bear magmatic zone, Lou Lake, Northwest Territories: Geological Survey of Canada Paper 90-1C, p. 239-253.

Gandhi, S., and Prasad, N., 1993, Regional metallogenic significance of the Cu, Mo, and U occurrences at the DeVries Lake, southern Great Bear magmatic zone, Northwest Territories: Geological Survey of Canada Paper 93-1C, p. 29-39.

Gandhi, S., and Prasad, N., 1995, Geological setting of Bode copper and Damp polymetallic prospects, central Great Bear magmatic zone, Northwest Territories: Northwest Territories Geoscience Office, Open File 1995-C, p. 201-212.

Gandhi, S.S., and van Breemen, O., 2005, SHRIMP U–Pb geochronology of detrital zircons from the Treasure Lake Group – new evidence for Paleoproterozoic collisional tectonics in the southern Hottah terrane, northwestern Canadian Shield: Canadian Journal of Earth Sciences, v. 42, p. 833-845.

Gandhi, S.S., Mortensen, J.K., Prasad, N., and van Breemen, O., 2001, Magmatic evolution of the southern Great Bear continental arc, northwestern Canadian

Shield: Geochronological constraints: Canadian Journal of Earth Sciences, v. 38, p. 767–785.

Gent, M., Menendez, M., Toraño, J., and Torno, S., 2011, A review of indicator minerals and samples processing methods for geochemical exploration: Journal of Geochemical Exploration, v. 110, p. 47-60.

Goad, R.E., Mumin, A.H., Duke, N.A., Neale, K.L., Mulligan, D.L., and Camier, W.J., 2000, The NICO and Sue-Dianne Proterozoic, iron oxide-hosted, polymetallic deposits, Northwest Territories: Application of the Olympic Dam model in exploration: Exploration and Mining Geology, v. 9, p. 123–140.

Gregory, M.J., 2006, Copper mobility in the Eastern Creek volcanics, Mount Isa, Australia: Evidence from laser ablation ICP-MS of iron-titanium oxides: Mineralium Deposita, v. 41, p. 691-711.

Guha, J., 1984, Hydrothermal systems and correlation of mineral deposits in the Chibougamau mining district—An overview, in Guha, J., and Chown, E.H., eds., Chibougamau stratigraphy and mineralization: Canadian Institute of Mining and Metallurgy, Special volume 34, p. 517-534.

Guha, J., 1991, Metallogeny of the eastern extremity of the Abitibi belt, in Guha, J., Chown, E.H., and Daigneault, R., eds., Litho-tectonic framework and associated mineralization of the eastern extremity of the Abitibi greenstone belt, Quebec (Fieldtrip 3): Geological Survey of Canada, Open File 2158, p. 33-37.

Hallof, P.G., and Pelton, W.H., 1980, Spectral IP survey Elura deposit (line 50 800N) Cobar, NSW: Bulletin of the Australian Society of Exploration Geophysics, v. 11, p. 54-58.

Hennessey, T., and Putrich, E., 2008, New resource estimate for Sue-Dianne copper-silver deposit: Press Release, 22nd February 2008: http://www.fortuneminerals.com/News/Press-Releases.

Hildebrand, R.S., 1981, Early Proterozoic Labine Group of Wopmay orogen: Remnant of a continental volcanic arc developed during oblique convergence, in Campbell, F.H.A., ed., Proterozoic basins of Canada: Geological Survey of Canada Paper 81–10, p. 133–156.

Hildebrand, R.S., 1982, Geological map of the Rainy Lake-Eagle Falls area, District of Mackenzie: Geological Survey of Canada Map 1589A, scale 1:50 000.

Hildebrand, R.S., 1986, Kiruna-type deposits: Their origin and relationship to intermediate subvolcanic plutons in the Great Bear magmatic zone, northwest Canada: Economic Geology, v. 81, p. 640-659.

Hildebrand, R.S., Hoffman, P.F., and Bowring, S.A., 1987, Tectono-magmatic evolution of the 1.9-Ga Great Bear magmatic zone, Wopmay orogen, northwestern Canada: Journal of Volcanology and Geothermal Research, v. 32, p. 99–118.

Hildebrand, R.S., Paul, D., Pietikainen, P., Hoffman, P.F., Bowring, S.A., and Housh, T., 1991, New geological developments in the internal zone of Wopmay orogen, District of Mackenzie: Geological Survey of Canada Paper 91–1C, p. 157–164.

Hildebrand, R.S., Hoffman, P.F., and Bowring, S.A., 2010a, The Calderian orogeny in Wopmay orogeny (1.9 Ga) northwestern Canadian Shield: Geological Society of America Bulletin, v. 122, p. 794-814.

Hildebrand, R.S., Hoffman, P.F., Housh, T., and Bowring, S.A., 2010b, The nature of volcano-plutonic relations and shapes of epizonal plutons of continental arcs as revealed in the Great Bear magmatic zone, northwestern Canada: Geosphere, v. 6, p. 812-839.

Hoffman, P.F., 1980, Wopmay orogen: A Wilson cycle of Early Proterozoic age in the northwest of the Canadian Shield, in Strangway, D.W., ed., The continental crust and its mineral deposits: Geological Association of Canada, Special Paper 20, p. 523–549.

Hoffman, P.F., 1984, Geology of the northern internides of Wopmay orogen, District of Mackenzie, Northwest Territories: Geological Survey of Canada Map 1576A, scale 1:250,000.

Hoffman, P.F., 1987, Proterozoic foredeeps, foredeep magmatism and Superior-type iron-formations in the Canadian Shield, in Kroner, A., ed., Proterozoic

lithospheric evolution: Washington, D.C., American Geophysical Union, Geodynamic Monograph 17, p. 85–98.

Hoffman, P.F., and McGlynn, J.C., 1977, Great Bear batholith: A volcano-plutonic depression, in Baragar, W.R.A , Colemean, L.C. and Hall, J.M., eds., Volcanic regimes in Canada: Geological Association of Canada, Special Paper 16, p. 170-192.

Ilton, E., and Eugster, H.P., 1989, Base metal exchange between magnetite and chloride-rich hydrothermal fluid: Geochimica et Cosmochimica Acta, v. 53, p. 291-301.

Jackson, V.A., 2008, Preliminary geologic map of part of the southern Wopmay orogen (parts of NTS 86B and 86C; 2007updates); descriptive notes to accompany 1:100,000 scale map: NWT Open File 2008-007, http://www.nwtgeoscience.ca.

Jackson, V.A., and Ootes, L., 2012, Preliminary geologic map of the south-central Wopmay orogen, results from 2008 to 2011: NWT Open File 2012-04, http//www.nwtgeoscience.ca.

Kisvarsanyi, G., and Proctor, P.D., 1967, Trace elements content of magnetites and hematites, southeast Missouri iron metallogenic province, U.S.A.: Economic Geology, v. 62, p. 449-471.

Lehnert, K., Su, Y., Langmuir, C.H., Sarbas B., and Nohl, U., 2000, A global geochemical database structure for rock: Geochemistry, Geophysics, Geosystems, v. 1, doi:10.1029/1999GC000026.

Li, Y.H., 2000, A compendium of geochemistry from solar nebula to the human brain: Princeton, Princeton University Press, 475 p.

Liu, W., Stacey, J.B., Testmale, D., Etschmann, B., Hazemann, J.L., and Bugger, J., 2011, Speciation and thermodynamic properties for cobalt chloride complexes in hydrothermal fluids at 35-440 oC and 600 bar: An in-situ XAS study: Geochimica et Cosmochimica Acta, v. 75, p. 1227-1248.

Loberg B.E., and Horndahl, A.K., 1980, Ferried geochemistry of Swedish Precambrian iron ores: Mineralium Deposita, v. 18, p. 487–504.

McClenaghan, M.B., 2005, Indicator mineral methods in mineral exploration: Geochemistry: Exploration, Environment, Analysis, v. 5, p. 233–245.

McMartin, I., Corriveau, L., and Beaudoin, G., 2011, An orientation study of heavy mineral signature of the NICO Co-Au-Bi deposit, Great Bear magmatic zone, NW Territories, Canada: Geochemistry: Exploration, Environment, Analysis, v. 11, p. 293-307.

Migdisov, A.A., Zezin, D., and Williams-Jones, A.E., 2011, An experimental study of cobalt (II) complexation in H2S-bearing hydrothermal solutions: Geochimica et Cosmochimica Acta, v. 75, p. 4065-4079.

Montreuil, J.F., Corriveau, L., and Grunsky, E., 2013, A compositional data analysis of IOCG systems, Great Bear magmatic zone, Canada: To each alteration types its own geochemical signature: Geochemistry: Exploration, Environment, Analysis, doi: 10.1144/geochem2011-101.

Montreuil, J.F., Corriveau, L., and Potter, E. (accepted), Albitite-hosted uranium development within IOCG systems: The southern breccia, Great Beat magmatic zone, Northwest Territories, Canada: Mineralium Deposita.

Müller, B., Axelsson, M.D., and Öhlander, B., 2006, Trace elements in magnetite from Kiruna, northern Sweden, as determined by LA-ICP-MS: GFF, v. 125, p. 1-5.

Mumin, A.H., Corriveau L., Somarin, A.K., and Ootes, L., 2007, Iron oxide copper-gold-type polymetallic mineralization in the Contact Lake belt, Great Bear magmatic zone, Northwest Territories, Canada: Exploration and Mining Geology, v. 16, p. 187-208.

Mumin, A.H., Somarin, A.K., Jones, B., Corriveau, L., Ootes, L., and Camier, J., 2010, The IOCG-porphyry-epithermal continuum of deposits types in the Great Bear magmatic zone, Northwest Territories, Canada, in Corriveau, L. and Mumin, H., eds., Exploring for iron oxide copper-gold deposits: Canada and global analogues: Geological Association of Canada, Short Course 20, p. 59-79.

Nadoll, P., Mauk, J.L., Hayes, T.S., Koening, A.E., and Box, S.E., 2012, Geochemistry of magnetite from hydrothermal ore deposits and host rocks in the Proterozoic Belt Supergroup: Economic Geology, v. 107, p. 1275-1292.

Neuhuber, S., and Wagreich, M., 2009, Geochemical characterization of Santonian cyclic oceanic red beds in the Alpine Tethys (Rehkogelgraben section, Austria), in Hu, X.M.,Wang, C.S., Scott, R.W., Wagreich, M., and Jansa, L., eds., Cretaceous oceanic red beds: Stratigraphy, composition, origins, paleoceanographic, and paleoclimatic significance: Society for Sedimentary Geology, Special Publication 91, p. 199–207.

Neuhuber, S., and Wagreich, M., 2011, Geochemistry of oceanic red beds—A synthesis: Sedimentary Geology, v. 235, p. 72-78.

Newton, L., 2011, Metamorphism and provenance of the Holly Lake metamorphic complex, Hottah terrane, NWT: A petrographic and SHRIMP U-Pb detrital zircon study: Unpublished, B.Sc. thesis, Halifax, Dalhousie University, 51 p.

Niu, Y., Collerson, K., Batiza R., Wendt, I., and Regelous, M., 1999, Origin of enriched-type mid-ocean ridge basalt at ridges far from mantle plumes, the East Pacific Rise at 11º20 ′ N: Journal of Geophysics Research, v. 104, p. 7067-7087.

Nyström, J.O., and Henriquez, F., 1994, Magmatic features of iron ores of the Kiruna type in Chile and Sweden: Ore textures and magnetite geochemistry: Economic Geology, v. 89, p. 820-839.

Oliver, N.H., Rubennach, B., Baker, T., Blenkinsop, T.G., Cleverly, J.S., Marshall, L.J., and Pridd, P.J., 2006, Granite-related overpressure and volatile release in the mid crust: Fluidized breccias from the Clonclurry district, Australia: Geofluids, v. 6, p. 346-358.

Ootes, L., Davis, W., Jackson, V.A., Acosta-Gongora, P., and Shakotko, P., 2012, The Hottah–Great Bear stratigraphic continuum: Implications for IOCG mineralization and plate interactions in the western Canadian Shield: Yellowknife Geoscience Forum, 40th, Canada, 13-15 November 2012, Abstracts, p. 35.

Ootes, L., Goff, S., Jackson, V., Gleeson, S.A., Creaser, R.A., Samson, I.M., Evenson, N., Corriveau, L., and Mumin, H., 2010, Timing and thermochemical constraint on multi-element mineralization at the Nori/RA Cu-Mo-U prospect, Great Bear magmatic zone, Northwest Territories, Canada: Mineralium Deposita, v. 45, p. 549-566.

Ordónez-Calderón, J.C., Polat, A., Fryer, B.J. Gagnon, J.E. Raith, J.G., and Appel, P.W.U., 2008, Evidence for HFSE and REE mobility during calc-silicate metasomatism, Mesoarchean (~3075 Ma) Ivisaartoq greenstone belt, southern West Greenland: Precambrian Research, v. 161, p. 317-340.

Oreskes, N., and Einaudi, M.T., 1992, Origin of hydrothermal fluids at Olympic Dam: Preliminary results from fluid inclusions and stable isotopes: Economic Geology, v. 87, p. 64-90.

Parak, T., 1975, The origin of the Kiruna iron ores: Sveriges Geologiska Underskøning, v. 69, 206 p.

Porter, T.M., 2010, Current understanding of iron oxide associated-alkali altered mineralized systems;
Part 1 An overview; Part 2 A review, in Porter, T.M., ed., Hydrothermal iron oxide copper-gold & related deposits: A global perspective: Adelaide, PGC Publishing, v. 3, p. 5-106.

Potter, E.G., Montreuil, J.-F., Corriveau, L., and DeToni, A., 2013, Geology and hydrothermal alteration of the Fab Lake region, Northwest Territories: Geological Survey of Canada, Open File 7339.

Puritch, E., Ewert, W., Armstrong, T., Brown, F., Orava, D., Pearson, J.L., Hayes, T., Duggan, T., Holmes, G., Uceda, D., Sumners, W., Mackie, D., Rougier, M., Bocking, K., Mezei, A., and Horne, B., 2012, Technical report and updated mineral reserve estimate and front-end engineering and design (FEED) study on the NICO gold-cobalt-bismuth-copper deposit, Mazenod Lake area, Northwest Territories, Canada: NI 43-101 Technical Report No. 247 prepared for Fortune Minerals Ltd., 307 p.

Razjigaeva N.G., and Naumova V., 1992, Trace element composition of detrital magnetite from coastal sediments of northwestern Japan Sea for provenance study: Journal of Sedimentary Petrology, v. 62, p. 802-809.

Reichenbach, I.G., 1991, The Bell Island Bay Group, remnant of an Early Proterozoic ensialic marginal basin in Wopmay orogen, District of Mackenzie: Geological Survey of Canada Paper 88–28, 43 p.

Righter, K., Leeman, W.P., and Hervig, R.L., 2006, Partitioning of Ni, Co, and V between spinel-structured oxides and silicate melts: Importance of spinel composition: Chemical Geology, v. 227, p. 1-25.

Robb, L., 2005, Introduction to ore forming processes: Victoria, Blackwell Publishing, 368 p.

Rusk, B.G., Oliver, N., Cleverley, J., Blenkinsop, T., Zhang, D., Williams, P., and Haberman, P., 2010, Physical and chemical characteristics of the Ernest Henry iron oxide copper gold deposit, Cloncurry, QLD, Australia; Implications for IOCG genesis, in Porter, T.M., ed., Hydrothermal iron oxide copper-gold & related deposits: A global perspective: Adelaide, PGC Publishing, v. 3, p. 187-204.

Shegelski, I.R.J., 1973, Geology and mineralogy of the Terra Silver mine, Camsell River, N.W.T.: Unpublished M.Sc. thesis, Toronto, The University of Toronto, 169 p.

Sidor, M., 2000, The origin of the black rock alteration overprinting iron-rich sediments and its genetic relationship to disseminated polymetallic sulfide ores, Lou Lake, Northwest Territories, Canada: Unpublished M.Sc. thesis, London, University Western Ontario, 190 p.

Spandler, C., Hermann, J., and Arculus, R., 2003, Redistribution of elements during prograde metamorphism from lawsonite blueschist to eclogite facies: Implications for deep subduction-zone processes: Contributions to Mineralogy and Petrology, v. 146, p. 205-222.

Takeno, N., 2005, Atlas of Eh-pH diagrams: Intercomparison of thermodynamic data bases: Geological Survey of Japan Open File 419, 285 p.

Tang, H.F., and Liu, C.Q., 2002, Trace element geochemistry during metamorphic dehydration: A case study from the Xingzi Group of Lushan, southeast China: Geochemical Journal, v. 36, p. 545-561.

Thompson, G., Bryan W.B., and Melson, W.G., 1980, Geological and geophysical investigation of the mid-Cayman rise spreading center: Geochemical variations and petrogenesis of basalt glasses: Journal of Geology, v. 88, p. 41-55.

Tian, Y., Etschmann, B., Liu, W., Borg, S., Mei, Y, Testemale, D., O'Neill, B., Rae, N., Sherman, D.M., Ngothai, Y., Johannessen, B., Glover, C. and Brugger, J., 2012, Speciation of nickel (II) chloride complexes in hydrothermal fluids: In situ XAS study: Chemical Geology, v. 334, p. 345-363.

Toplis, M.J., and Corgne, A., 2002, An experimental study of element partitioning between magnetite, clinopyroxene and iron-bearing silicate liquids with particular emphasis on vanadium: Contributions to Mineralogy and Petrology, v. 144, p. 22-37.

Yang, P., and Rivers, T., 2000, Trace element partitioning between coexisting biotite and muscovite from metamorphic rocks, western Labrador: Structural, compositional and thermal controls: Geochimica et Cosmochimica Acta, v. 64, p. 1451–1472.

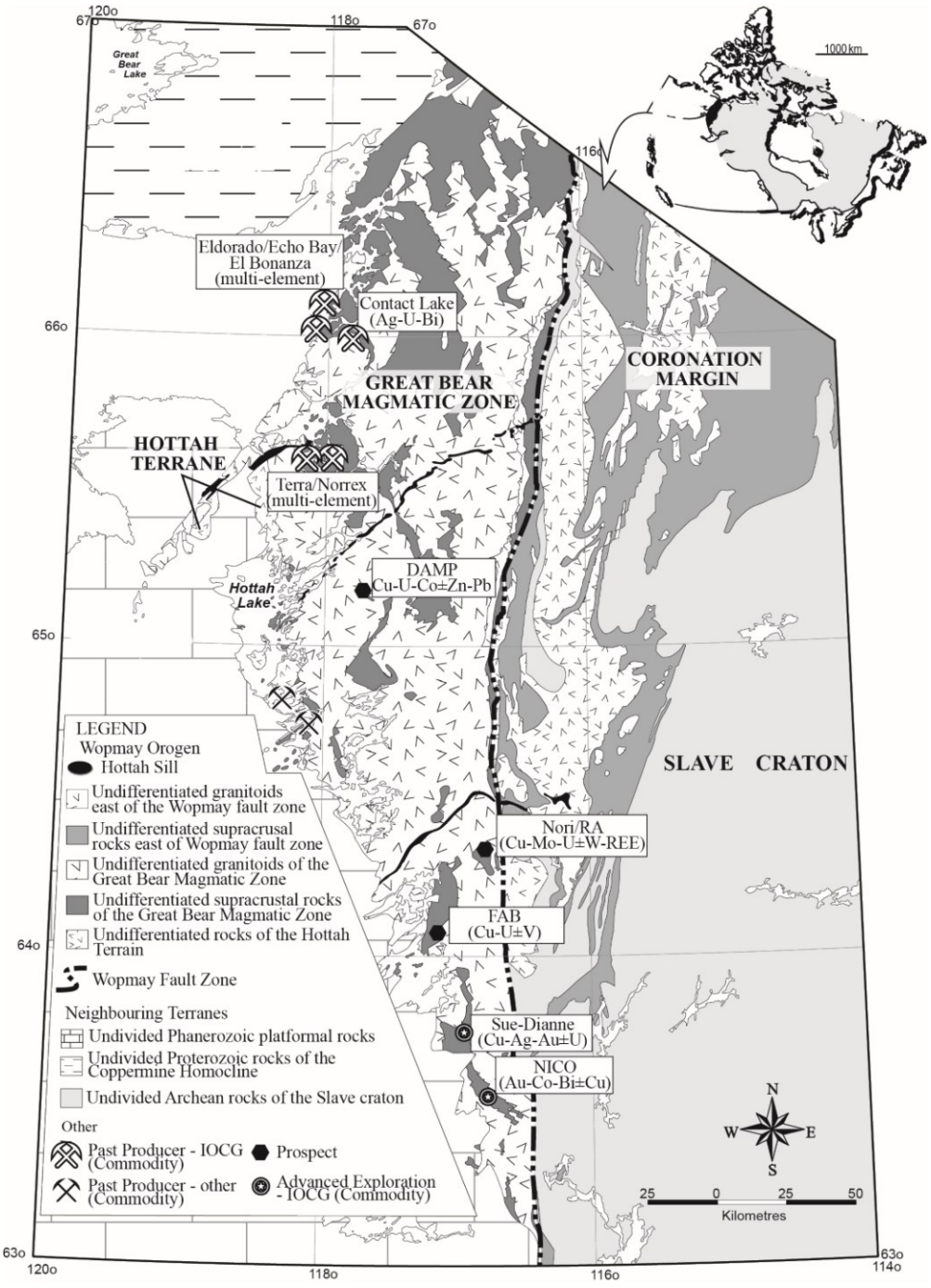

Figure 2.1. Regional geology of the study area.
Regional geology of the Great Bear Magmatic Zone and locations of selected prospects, past-producer mines and advanced exploration projects. Modified after Ootes et al. (2010).

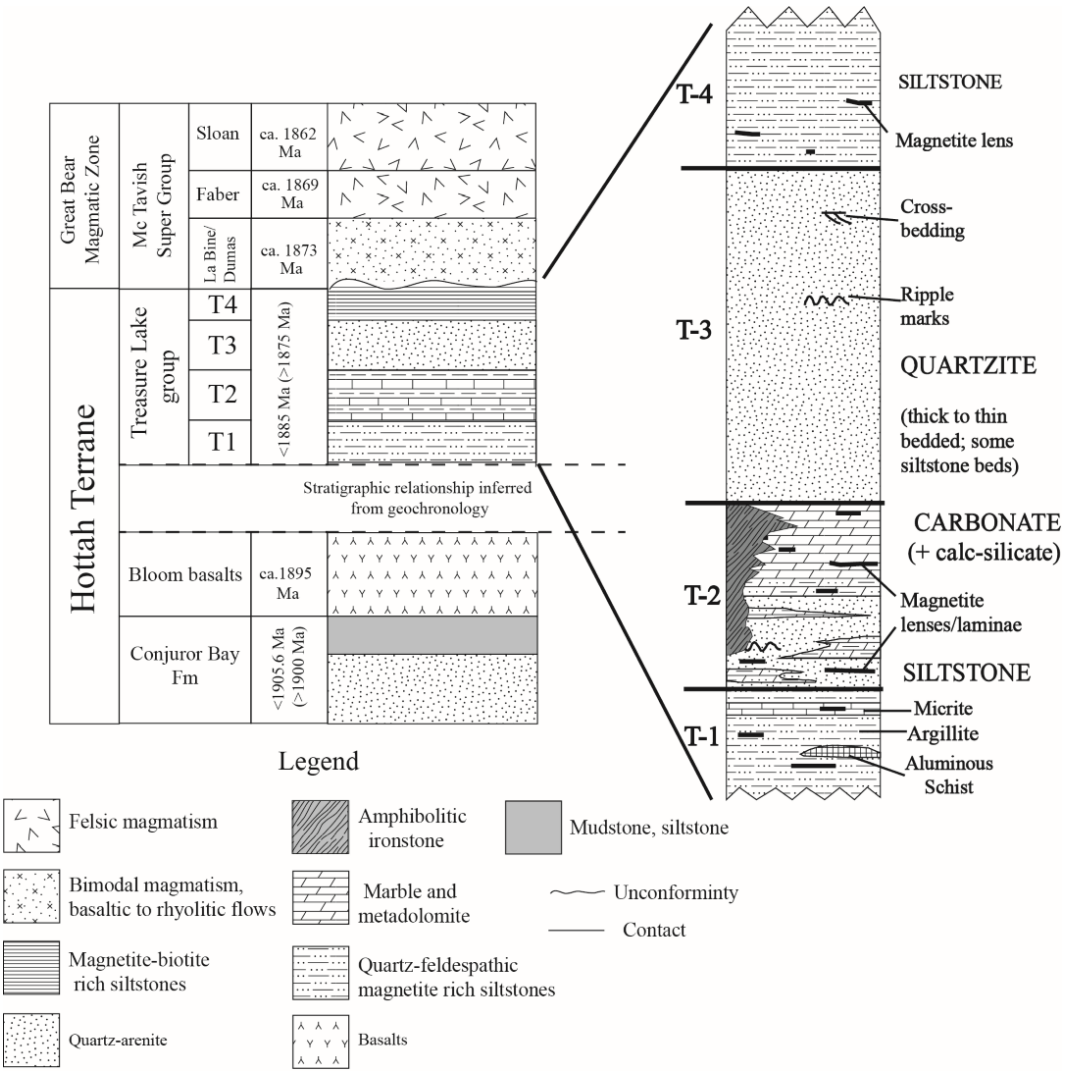

Figure 2.2. Chronostratigraphic column.
Chronostratigraphic column of the GBMZ and the upper Hottah Terrane after Hildebrand et al. (1987, 2010b), Reichenbach (1991), and Gandhi et al. (2001).

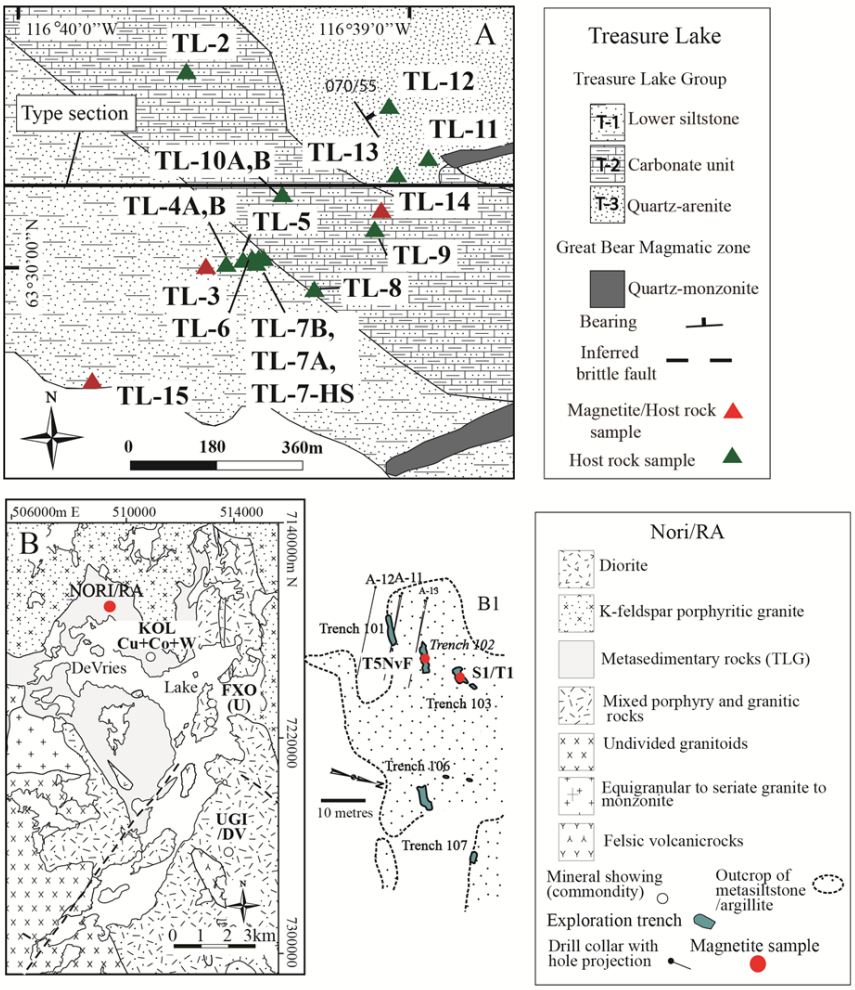

Figure 2.3. Geology of the TLG and the Nori/RA propsect
(A) Geology of the Treasure Lake Group by the type section (modified from Gandhi and van Breemen, 2005). (B) Geology of the DeVries Lake area and location of the Nori/RA prospect and other mineralized zones. Geology is modified from Gandhi and Prasad (1993) and Jackson (2008). Outcrop map modified from Ootes et al. (2010) of the Nori/RA prospect depicting location of trenches and drill collar and the magnetite sample location.

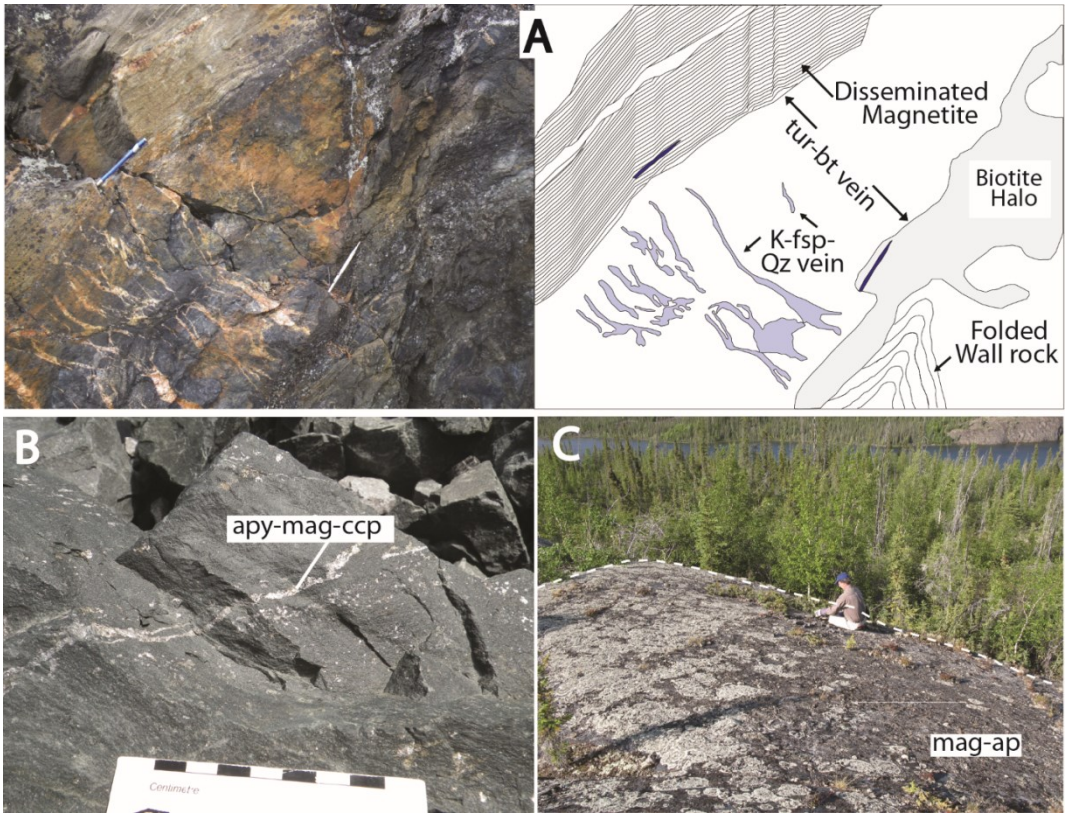

Figure 2.4. Magnetite occurrences in Nori/RA, NICO and Terra systems
(A) Nori/RA prospect. Tourmaline (tur)-biotite (bt) veins main host for molybdenite (mol), uraninite (urn), pyrite and minor magnetite. The veins are crosscutting magnetite rich metasiltstones. Potassic feldspar (k-fsp)-quartz (qz) veins (tension gashes) perpendicular to the vein (illustrative sketch of the veins at the right side). (B) NICO deposit. Arsenopyrite (apy)-chalcopyrite-magnetite-bismuthinite (bm) in veins and disseminated in the amphibole-magnetite TLG rocks. (C) Terra magnetite-apatite body. Magnetite and apatite occur as a massive dome-like shape stock.

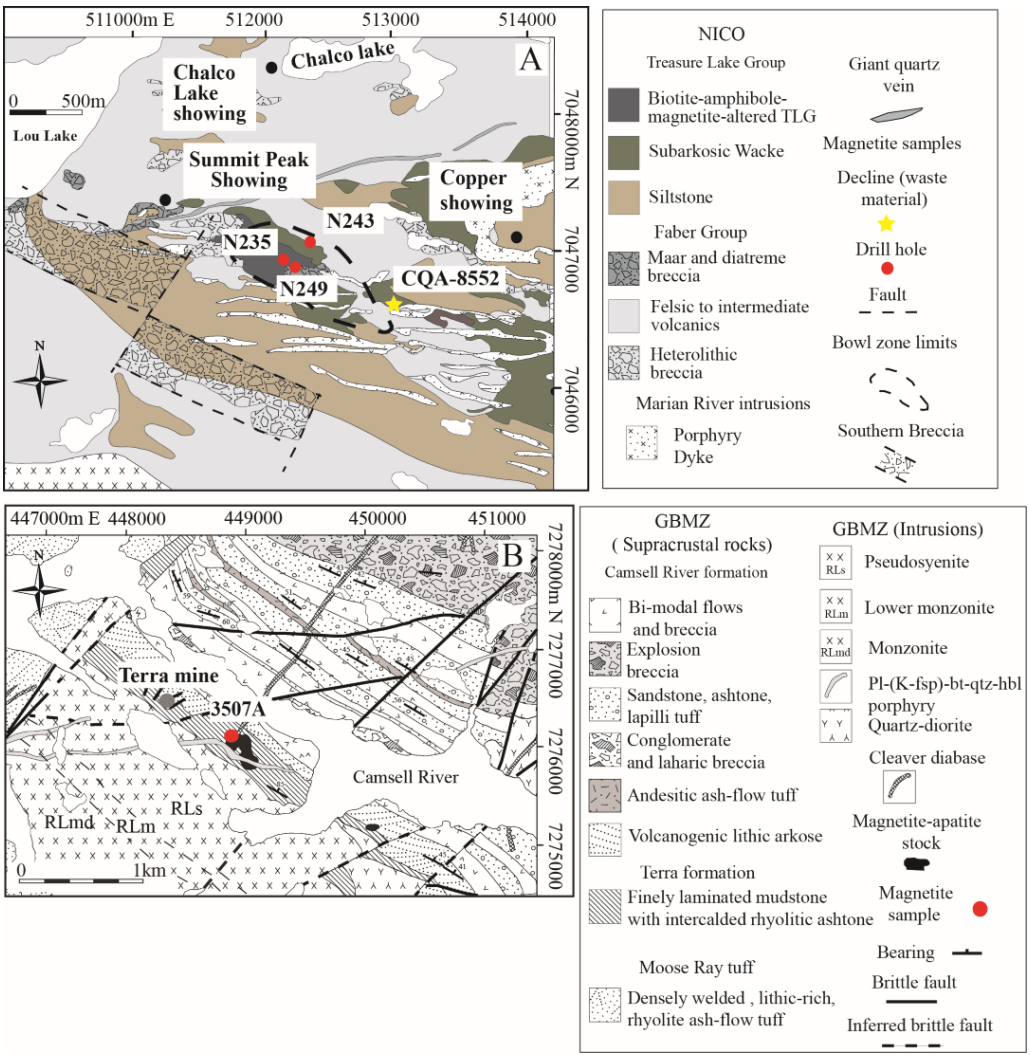

Figure 2.5. Geology of the NICO deposit and Terra mine area
(A) Geology of the central NICO claims and the Bowl Zone deposit modified from Goad et al. (2000). In the Figure are also shown the drill holes sampled for magnetite, and a sample (CQA-8552) taken from the decline waste material. (B) Geology of the Camsell River area (Hildebrand, 1982).

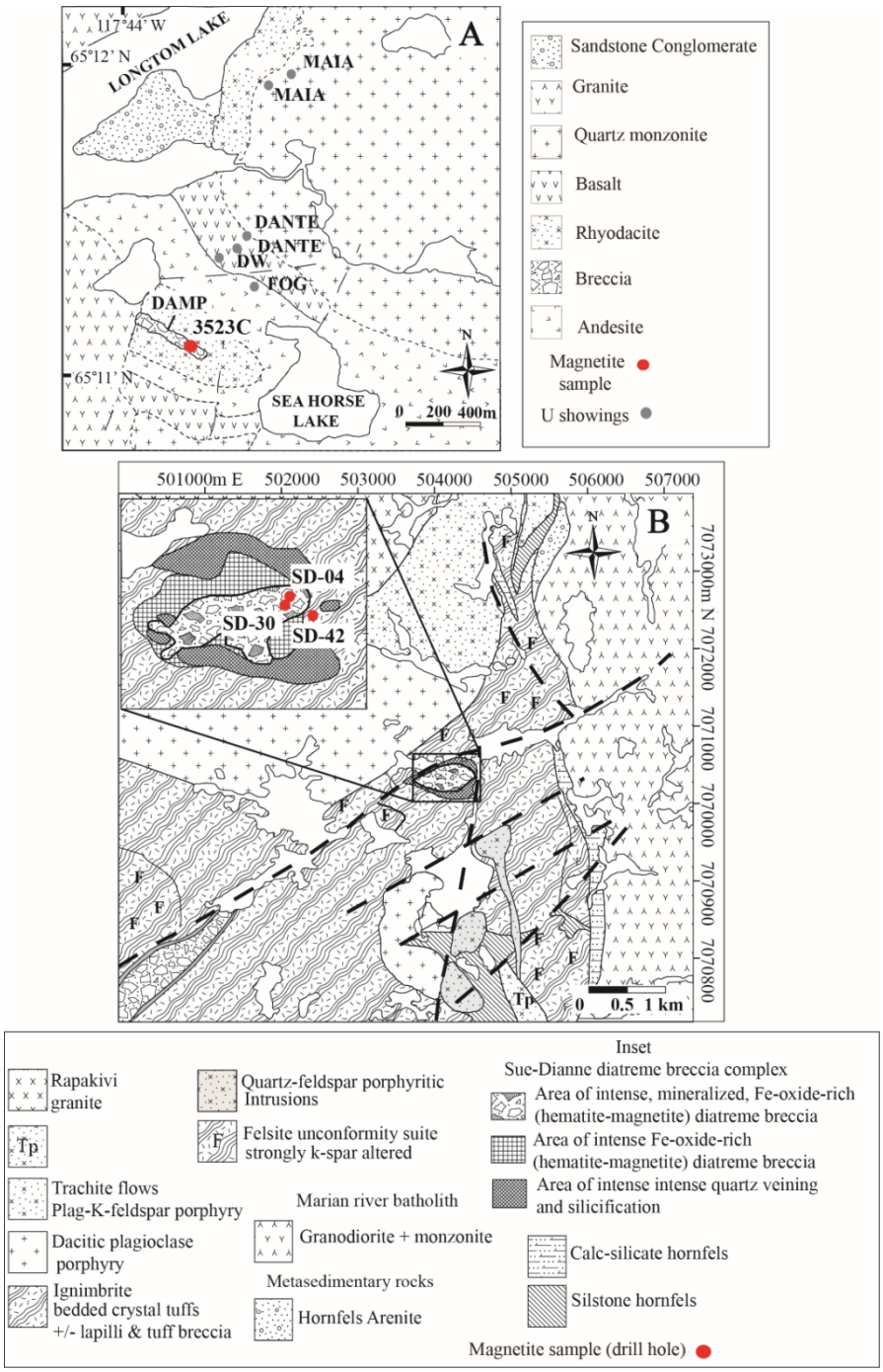

Figure 2.6. Geology of the DAMP and Sue Dianne systems
(A) Geology of the northeast section of the Longtom Lake area and location of DAMP and other uranium prospects. (B) Modified from Gandhi and Prasad (1995). Geology of the Sue-Dianne complex after Goad et al. (2001).

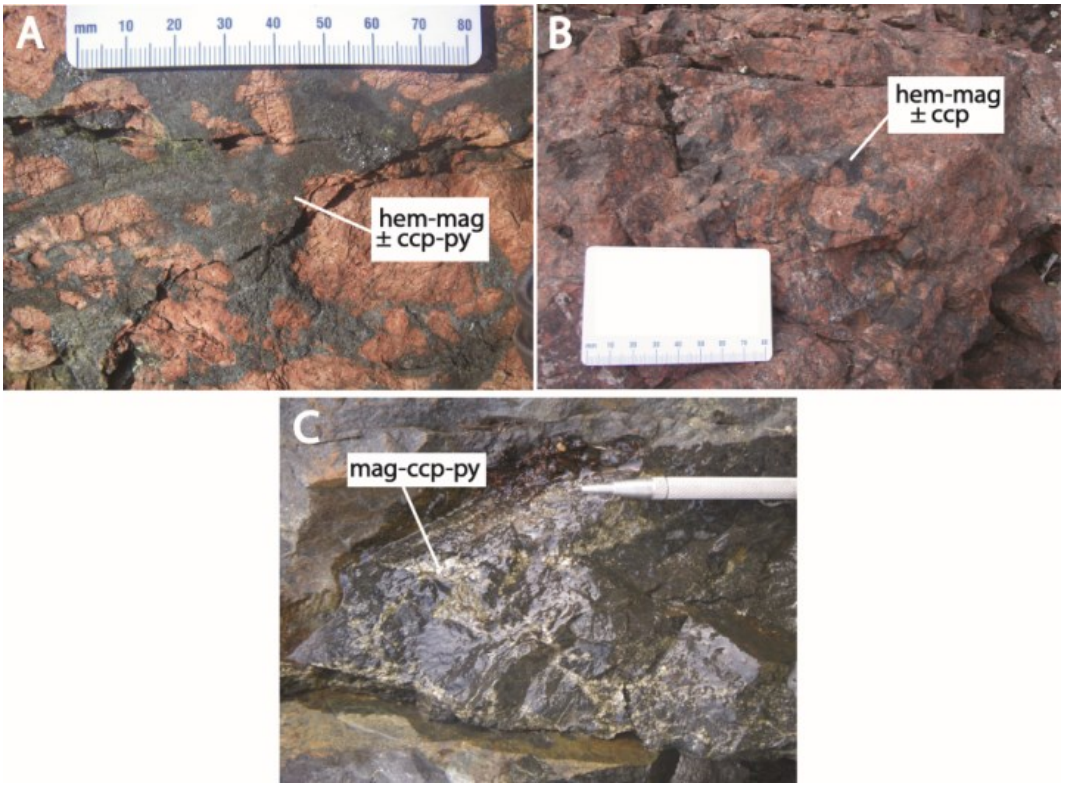

Figure 2.7. Magnetite in felsic volcanic rocks of the GBMZ
(A) Damp prospect. Copper and uranium occurring in hematite (hem)-magnetite (mag)-rich rhyolitic breccias, with disseminated sulfides like pyrite (py) and chalcopyrite (ccp). (B) Sue-Dianne breccia complex. Disseminated copper-rich sulfides are found with magnetite and hematite as part of the breccia matrix. (C) FAB prospect. Magnetite-pyrite-chalcopyrite recognized as main components of the veins and breccia matrix.

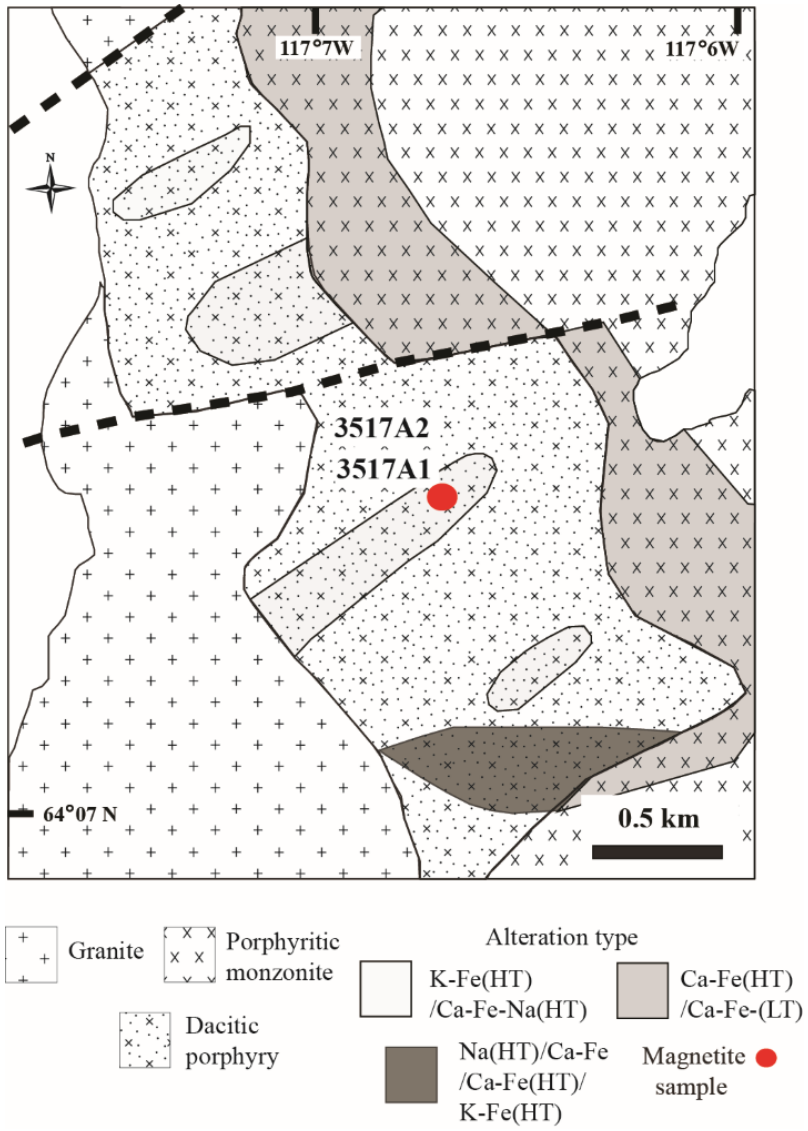

Figure 2.8. Geology of the FAB propect
Geology and alteration map of the FAB prospect in the eastern section of the Faber Lake (modified from Potter et al., 2013). The alteration assemblages are divided into high (HT) and low (LT) temperature.

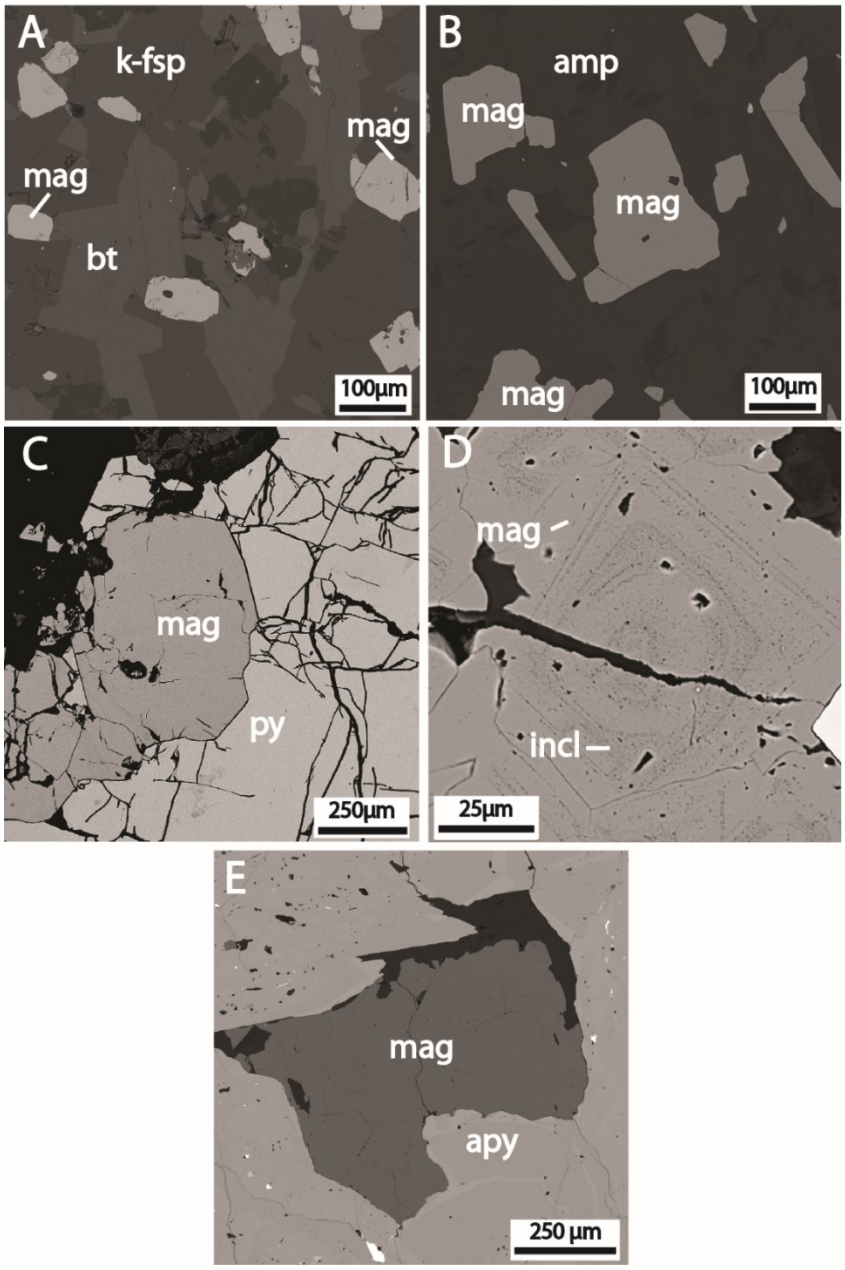

Figure 2.9. BSE images from the TLG, Nori/RA and NICO systems
A-B, TLG magnetite (mag). (A) Fine-grained magnetite (T1mag) disseminated in biotite (bt)-K-feldspar (k-fsp) metasiltstones of the TLG Lower unit (T1). (B) disseminated magnetite (T2mag) in an HT Ca-Fe altered lamination of the Carbonate unit (T2). (C) Nori/RA prospect. Unzoned coarse-grained magnetite (Nomag2) co-precipitated with pyrite (py). D-F, NICO deposit. (D) Concentric zoning of silicate inclusion (incl)-rich and -poor pre-ore magnetite (NImag1). (E) Unzoned magnetite (NImag2) co-precipitated with arsenopyrite (apy).

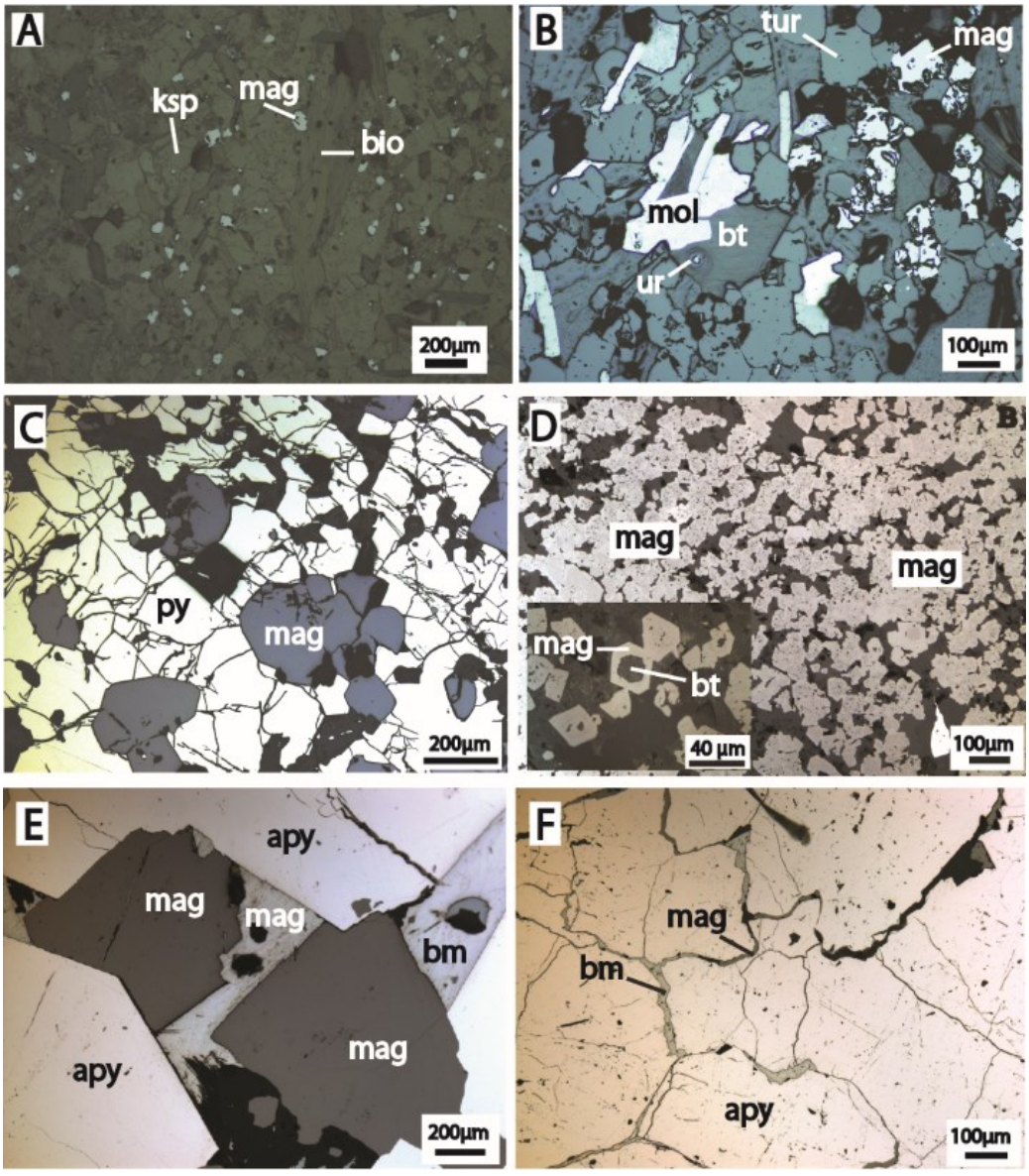

Figure 2.10. P Petrography from Nori/RA prospect and NICO systems
(A) Biotite-K-feldspar-quartz-magnetite (Nomag1) metasiltstone. Nomag1 occurs as fine grains randomly disseminated in the metasiltstone. (B) Magnetite (Nomag2) co-precipitated with tourmaline (tur)-biotite (bt)-uraninite (urn)-molybdenite (mol) (±pyrite, py; chalcopyrite, ccp) in veins. (C) Nomag2 co-precipitated with pyrite (py) in ore veins. D-G, NICO deposit. (D) Fine-grained pre-ore magnetite (NImag1) disseminated along the bedding. NImag1 has multiple silicate inclusions as it overgrows and replaces silicates. (E) Coarse grained NImag2 magnetite co-precipitated with arsenopyrite, Late bismuthinite (bm) is intergranular to both. (F) Magnetite (NImag3) and bismuthinite (bm) inter-granular and filling fractures in arsenopyrite.

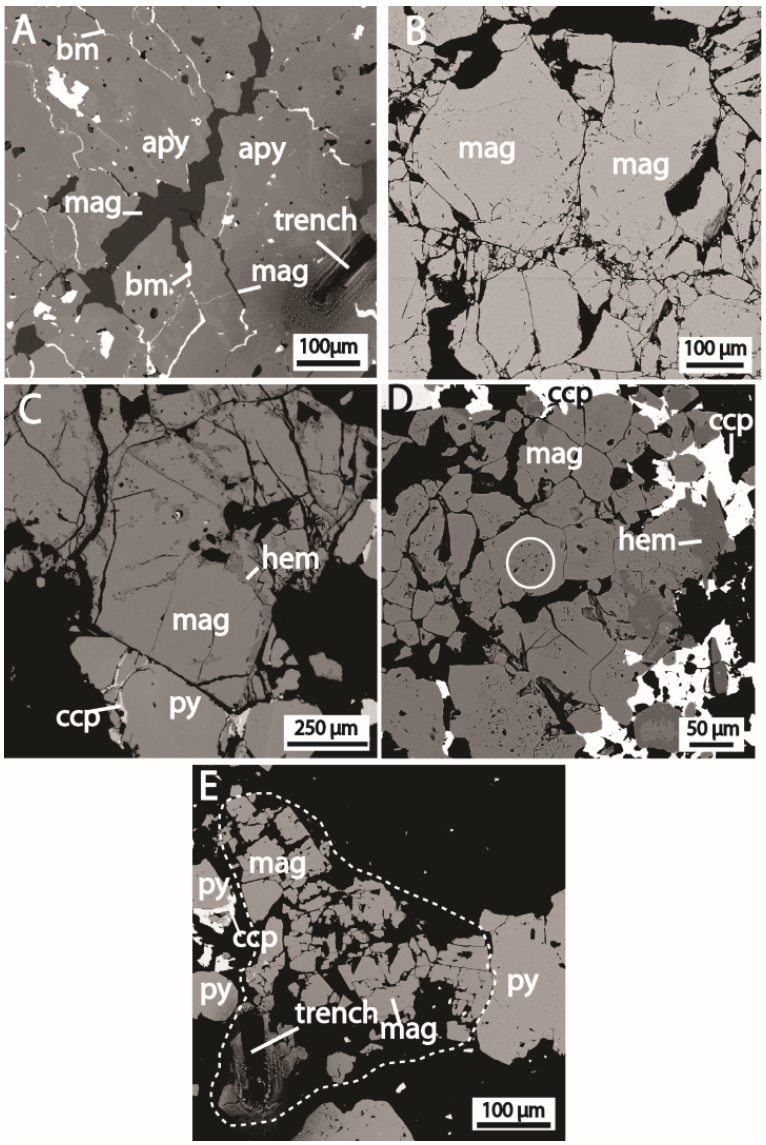

Figure. 2.11. BSE images from the TLG, Nori/RA and NICO magnetite (A) Magnetite (NImag3)-bismuthinite veins crosscutting arsenopyrite. (B) Terra magnetite-apatite body. Coarse-grained euhedral fractured magnetite with no apparent zoning. (C) DAMP prospect. Unzoned euhedral grains of magnetite coeval with pyrite. Hematite incipiently replaces magnetite along fracture planes, whilst chalcopyrite veins crosscut the pyrite grains. (D) Sue-Dianne deposit. Euhedral grains of magnetite. These grains have silicate inclusion-rich zones shown in the white circle. Hematite strongly pseudomorphs magnetite grains; chalcopyrite is inter-granular to magnetite. (E) FAB prospect. The dashed zone encloses euhedral to subhedral unzoned grains of magnetite co-precipitated with pyrite (Fmag2). Chalcopyrite crosscuts and replaces pyrite crystals

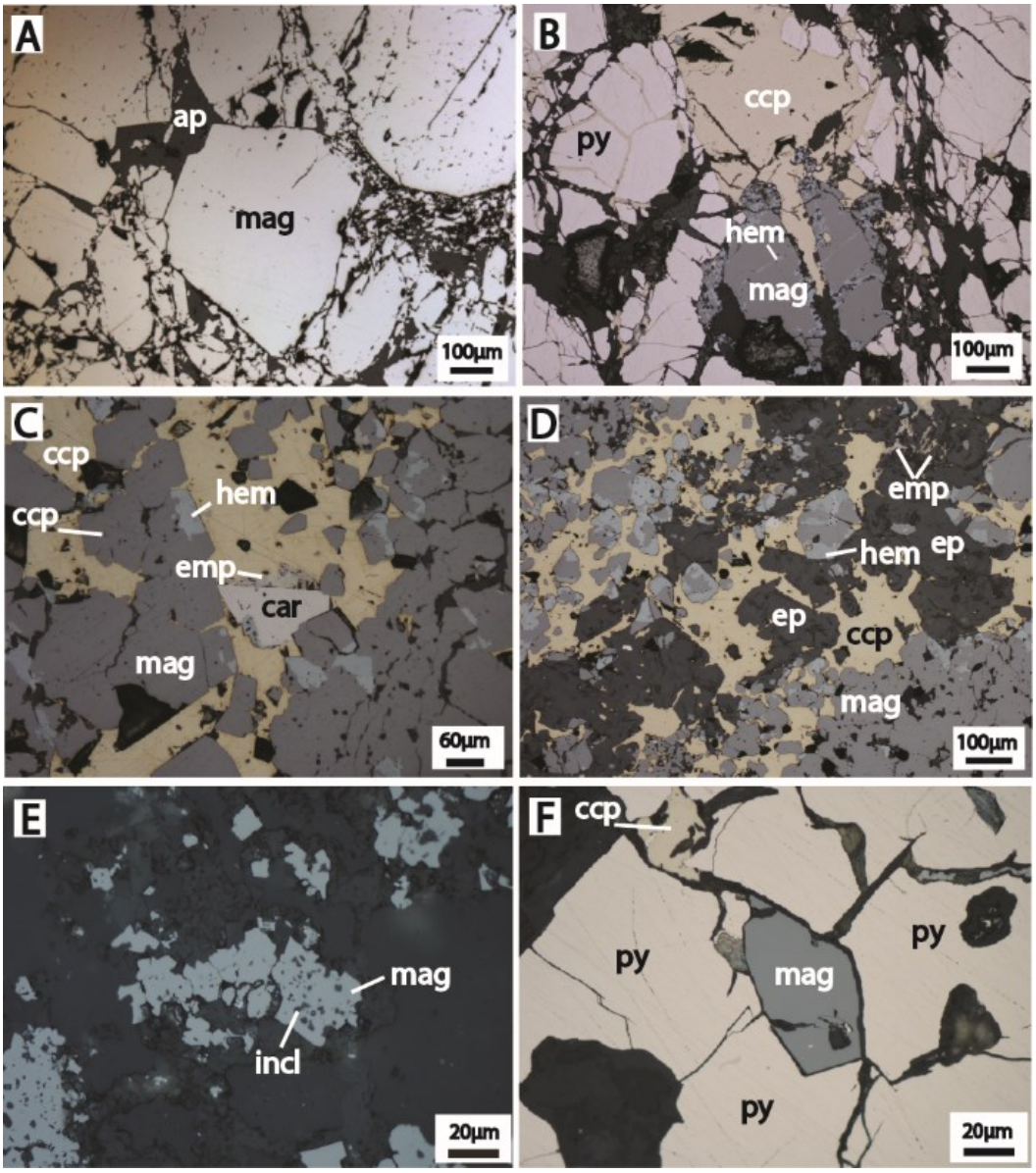

Figure 2.12. Petrography from Terra, DAMP and FAB and Sue Dianne
(A) Coarse-grained magnetite from the Terra magnetite-apatite (ap) body (Temag) co-precipitated with apatite. (B) DAMP prospect. Chalcopyrite crosscutting coarse grains of pyrite and magnetite. C-D, Sue-Dianne deposit. (C) Magnetite and carrollite (car) co-precipitated; late chalcopyrite intergranular to both. Hematite is pseudomorphing magnetite. (D) Epidote and magnetite co-precipitated with late chalcopyrite and emplectite (emp) intergranular to them. In the top right corner hematite pseudomorphs magnetite. E-F, FAB prospect. (E) Fine-grained magnetite (Fmag1) with silicate inclusions (incl). (F) Magnetite (Fmag2) occurring in a vein co-precipitated with pyrite.

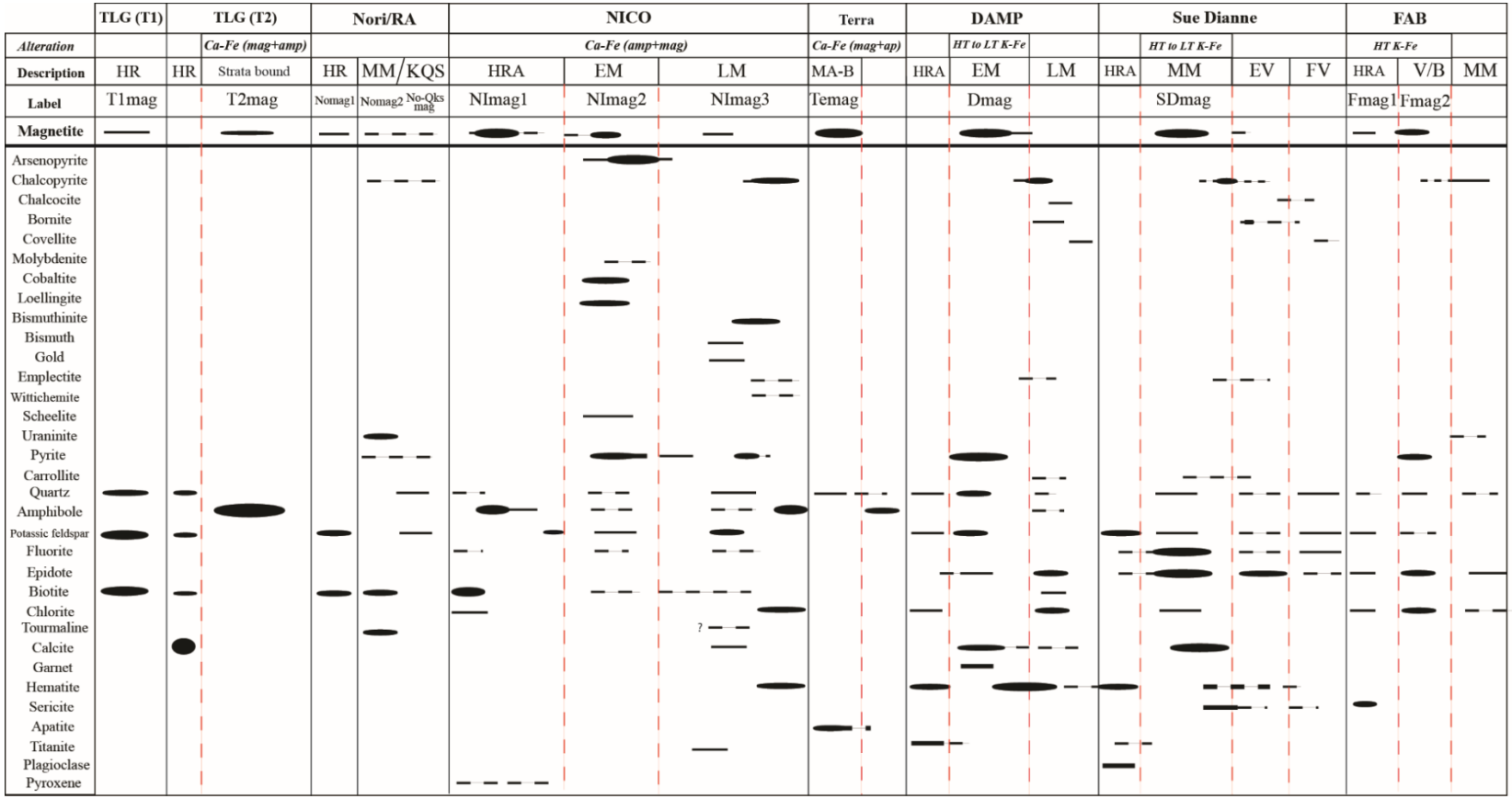

Figure. 2.13. Paragenetic sequences.
HR, host rock; HRA, host rock alteration; EM, early mineralization; LM, late mineralization, ;EV, epidote veins; FV, fluorite veins; V/B, veins-breccia.

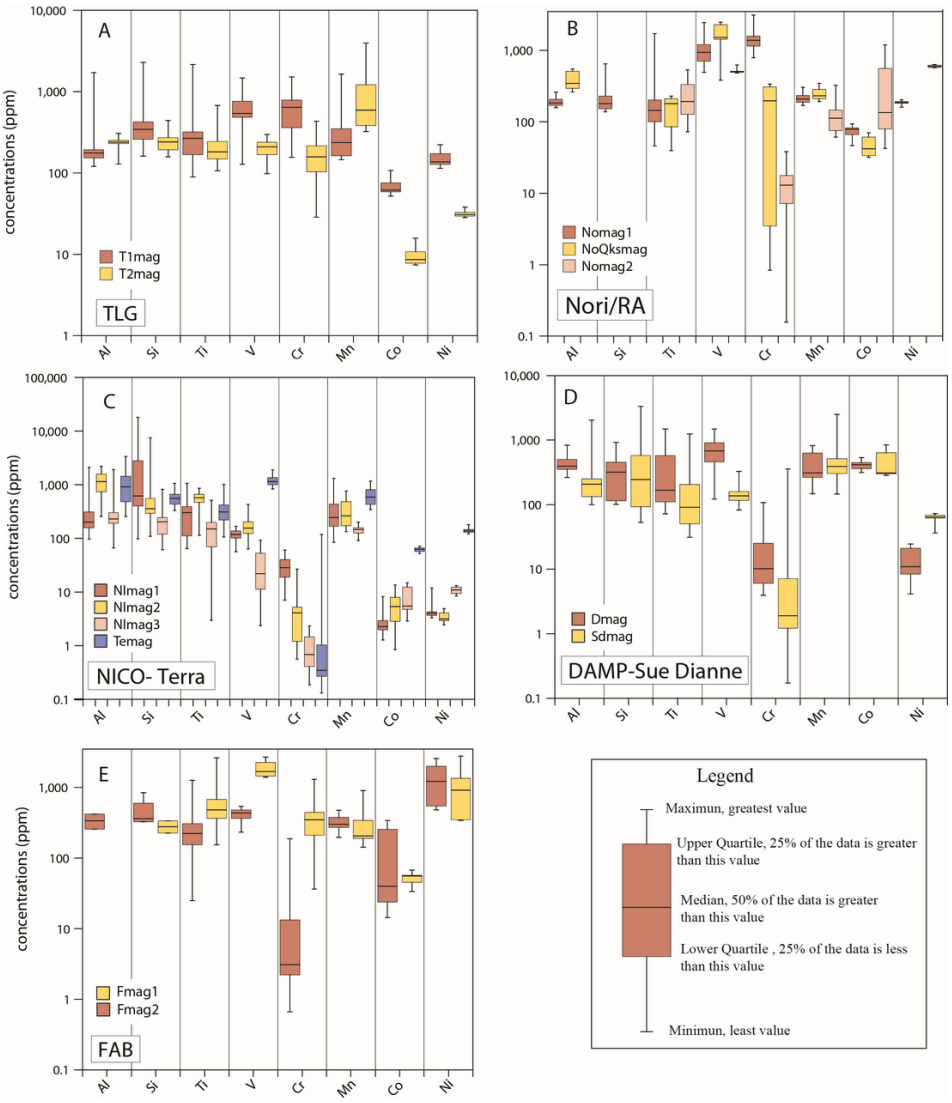

Figure. 2.14. Data distribution, box-whisker plots
(A) TLG, (B) Nori/RA, (C) NICO deposit and Terra magnetite body and (D) Sue Dianne-DAMP and (E) FAB. The box-whisker plots show the variability in element concentrations.

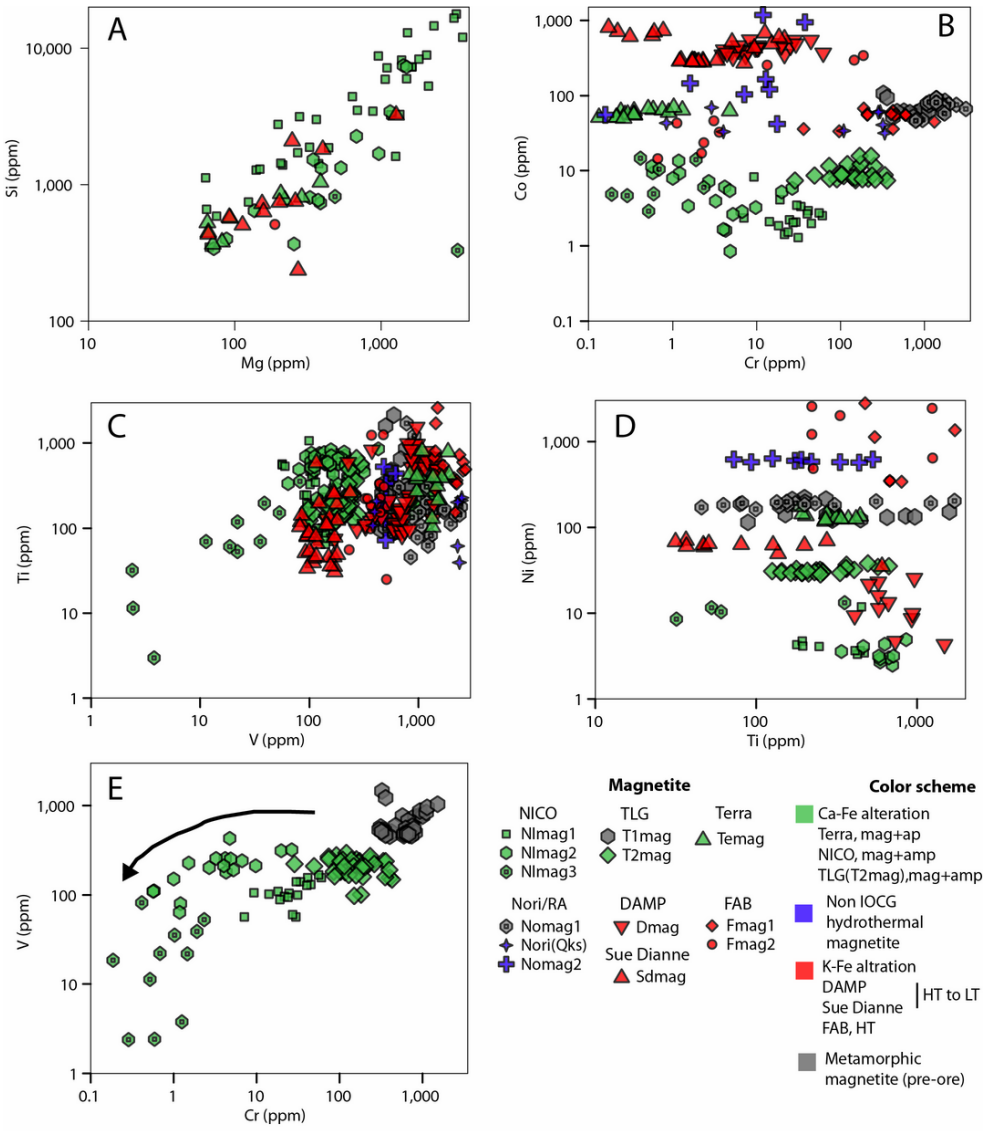

Figure. 2.15. Geochemistry of the GBMZ magnetite
Plots include LA-ICP-MS and EMPA data. (A) There is some positive correlation between Si and Mg correlation consistent with the occurrence of amphibole and/or biotite inclusions. (B) NICO magnetite and the T2mag have the lowest Co contents (HT-Ca-Fe alteration, magnetite-amphibole variant). Metamorphic magnetite exhibits similar Co and Cr values. (C) NICO deposit (NImag3) has in average the lowest V concentrations. Conversely, the Temag V amounts are an order of magnitude greater. The HT- to LT-K-Fe alteration phases have an overall higher V contents than those of the HT-Ca-Fe (magnetite-amphibole variant). (D) The Ni contents are generally below 200 ppm, except for Terra and FAB. (E) Roughly decreasing trend of V and Cr from NImag1 to NImag3.

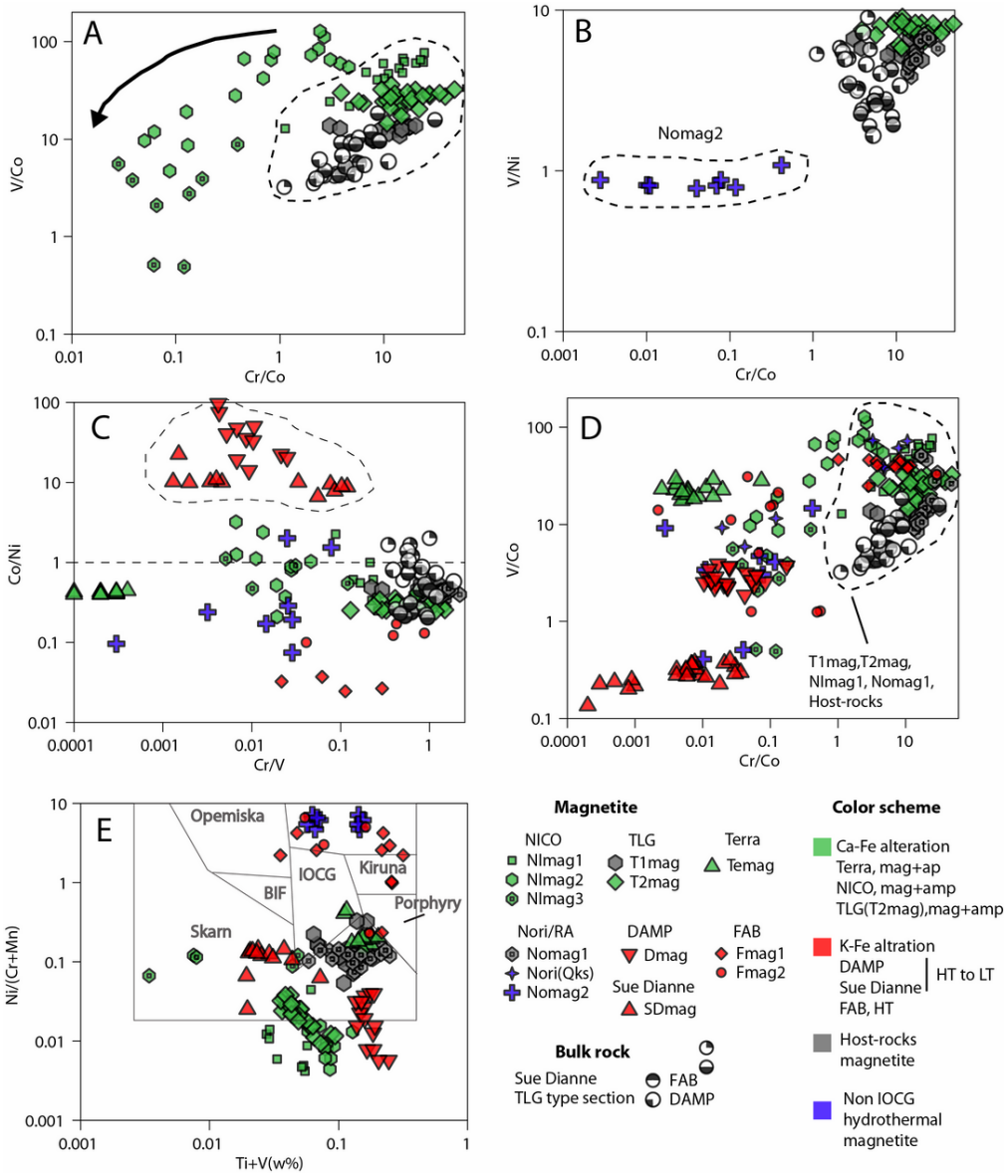

Figure. 2.16. Geochemistry of the GBMZ, exploration applications
Plots include LA-ICP-MS and EMPA data. (A) The Cr/Co of the TLG rocks and NImag1 magnetite is distinctively different from most of NImag2 and NImag3. NICO magnetite transitionally decreases its Cr/Co from NImag1 to NImag3. (B) The V/Ni and Cr/Co positively distinguish between the TLG magnetite and the magnetite placed in veins (Nomag2) at Nori/Ra prospect. (C) Anomalously high Co/Ni of Sue-Dianne and DAMP compared to the rest of the magnetite suite and host rocks of the GBMZ and the TLG. (D) Higher Cr/Co is more characteristic of barren magnetite and pre-ore stages from NICO and FAB. (E) The LA-ICP-MS data plotted on Dupuis and Beaudoin (2011) diagram shows the low affinity of the GBMZ with IOCG field.

Table 2.1. Summary of magnetite occurrences. Relationship of magnetite with host rocks, alteration and ore-association in the study area

Location	Mineralization style	Ore minerals	Host rocks	Magnetite phase	Magnetite occurnrence	*Alteration	Concomitant mineral phases
Treasurne Lake Group	-	-	Bt-mc>ms-qz metasiltstone	T1mag	Disseminated	Metamorphic	Bt, mc, qz
			Dominant marble, with local quartzo-feldspathic beds	T2mag	Disseminated	HT Ca-Fe	Amp
Nori/Ra	Veins	Mol, urn, ±ccp	Bt-mc>qz metasiltstone	Nomag1	Disseminated	Metamorphic	Bt-mc>qz>ms
				Nomag2	Veins	-	Py, mol, urn
				NoQksmag	Segregations	-	Qz-k-fsp±py, mol
NICO	Veins, disseminated, patches and minor breccias	Apy,cob, lol, bm, native Bi, ccp, sch, Au-Bi and Au-Te alloys	Amphibolitic ironstones	NImag1	Disseminated, veins	HT Ca-Fe (mag-amp)	±Amp
				NImag2	Veins (<disseminated)	HT Ca-Fe (mag-amp)	Lol, cob, apy, ± amp-bt
				NImag 3	micro-veins	HT Ca-Fe (mag-amp)	Native Bi, ±bm
Terra	Magnetite stocks	-	Volcaniclastics	Temag	Stocks	Ca-Fe (mag-ap)	Ap>qz
DAMP	Breccia	Ccp, ± car-emp-bn, cv-cc	Rhyodacite, dacites	Dmag	Breccia	HT-K-Fe (transitional to LT-K-Fe)	Py, ±hem-k-fsp (±ccp?)
Sue Dianne	Breccia	Ccp ±car	Rhyodacite, dacites	SDmag	Breccia	HT-K-Fe (transitional to LT-K-Fe)	Fl, ep, k-fsp, hem (±car)
FAB	Disseminated	Ccp	Rhyodacite	Fmag1	Disseminated	HT-K-Fe	K-fsp, qz
	Veins, breccia			Famg2	Veins(<breccia)	HT-K-Fe	Py±k-fsp-qz (±ccp?)

Ore minerals recognized in this study

*Alteration assemblage associated with magnetite relative to Corriveau (2007b) model

Abbreviations: apatite = ap, amphibole = amp, arsenopyrite = apy, biotite= bt, bmmuthinite = bm , carrolite = car, chalcocite = cct, chalcopyrite = ccp, cobaltite = cob, covellite = cv, emplectite = emp, epidote = ep, fluorite = fl, hematite = hem, loellingite = lol, microcline = mc, molybdenite = mol, muscovite = ms, potassic feldspar = k-fsp, pyrite = py, quartz = qz, urnaninite = urn, schelite= sch

Table 2.2. Whole rock trace element data (ppm) from the TLG

Location	Sample	Alteration	Ti	V	Cr	Mn	Co	Ni	As	Bi	Lithology
TLG	TL-015-camp	Incipient amp	3800	102	80	376	18.1	40	20	< 2	Lower siltstone unit (T1)
TLG	TL-003	Incipient amp	4100	109	100	242	18.7	40	< 10	< 2	Lower siltstone unit (T1)
TLG	TL-1004	Incipient amp	4200	105	80	283	10.4	40	< 10	< 2	Lower siltstone unit (T1)
TLG	TL-1004B	Incipient K-Fe (k-fsp)	4100	112	70	299	9.4	40	< 10	< 2	Lower siltstone unit (T1)
TLG	TL-005	Advanced K (k-fsp), ep-grt	3800	109	100	909	11.2	50	10	< 2	Lower siltstone unit (T1)
TLG	TL-006A	Pervasive K (k-fsp), ep-grt	4300	116	110	314	12.1	60	< 10	< 2	Lower siltstone at the T1-T2 contact
TLG	TL-007B	Moderate ep, K (k-fsp), ±tur	1900	72	30	539	7.8	30	< 10	< 2	Carbonate unit at the T1-T2 contact
TLG	TL-007-HS	Moderate ep, K (k-fsp), ±tur	2000	76	40	649	8.4	40	< 10	< 2	Carbonate unit at the T1-T2 contact
TLG	TL-007A-carb-cont	Moderate ep, K (k-fsp), ±tur	2100	91	50	744	8.7	30	< 10	< 2	Carbonate unit (T2)
TLG	TL-002A	Moderate ep, K (k-fsp), ±tur	1900	53	< 30	1060	8.4	20	20	< 2	Carbonate unit (T2)
TLG	TL-008A	Moderate ep, K (k-fsp), ±tur	2600	68	60	4680	16.1	30	< 10	< 2	Carbonate unit (T2)
TLG	TL-009A	Advanced ep-Grt, incipient (amp)	2600	82	50	1040	9.3	30	< 10	< 2	Carbonate unit (T2)
TLG	TL-010A	Advanced K (k-fsp), incipient (amp-mag)	1900	62	< 30	5590	13.9	20	< 10	< 2	Carbonate unit (T2)
TLG	TL-010B	Advanced K (k-fsp), incipient (amp-mag)	2100	85	40	11200	4.6	20	10	< 2	Carbonate unit (T2)
TLG	TL-014A	Pervasive Ca-Fe (amp-mag)	2900	70	40	6910	14.7	20	< 10	< 2	Carbonate unit (T2)
TLG	TL-013	Moderate (bt-k-fsp-cpx)	1600	58	< 30	2030	4.4	20	20	< 2	Carbonate unit (T2)
TLG	TL-011QA	Incipient K(k-fsp)	1300	46	90	1690	2.9	< 10	20	< 2	Quartz arenite unit (T3)
TLG	TL-012QA	Incipient K(k-fsp)	900	44	< 30	1010	3.2	< 10	20	< 2	Quartz arenite unit (T3)

FAB	06NS2154	Moderate chl, amph, ep,calc	1700	47	< 30	459	4.7	10	< 10	< 2	Porphyry
FAB	06BA3103	Minor ser and chlorite	4400	128	130	837	22.5	50	< 10	< 2	Porphyry
FAB	06ST5091B	Moderate qz-ep-calc veins	3200	62	< 30	504	6.7	20	20	< 2	Porphyry

Abbreviations. Amphibole = amp, biotite = bt, calcite = calc, clinopyroxene = cpx; chlorite = chl, epidote = ep, garnet =grt, magnetite= mag, potassic feldspar = k-fsp, tourmaline = tur and sericite = ser.
Incipient: alteration overprinted <5% of the precursor hostrock
Moderate: alteration overprinted >5% to 15% of the precursor rock
Advanced: alteration has overprinted >15% to 30% of the precursor host rock
Pervasive: alteration has overprinted >30%
All concentrations given in ppm

Table 2.3. Samples analyzed and number of analyses per sample

Location	Sample	Magnetite	*Number of Analyisis
TLG	TL-15 camp	T1mag	31
	TL-003	T1mag	4
	TL-14A	T2mag	47
Nori/RA	T5NvF	Nomag1	29
	S1/T1	Nomag1	12
	T5NvF	Nomag2	9
	S1/T1	NomagQks	14
NICO	N-210-243	NImag1	57
	N-80-235	NImag1	1
	CQA-8552	NImag1	17
	N-25-235	NImag1	24
	N-16-235	NImag1	10
	N-52-249	NImag2	72
	N-80-235	NImag3	38
	N-16-235	NImag3	6
Terra	3507A	Temag	51
DAMP	3523C	Dmag	67
	3523B	Dmag	10
Sue Dianne	SD-153-42	SDmag	70
	SD-139-04	SDmag	13
	SD-137-30	SDmag	9
	SD-140-42	SDmag	22
FAB	3517A1	Fmag1	9
	3517A	Fmag1	5
	3517A2	Fmag1	5
	3517A1	Fmag2	7
	3517A	Fmag2	8
	3517A2	Fmag2	3

*Total number of analyses performed via EMPA and LA-ICP-MS in a single sample. See table 2.4 for more detailed information about each element.

Table 2.4. Average trace elements concentrations (ppm) in the GBMZ. Iron concentration is given in wt. %.

Location	Magnetite		Fe	Mg[1]	Al[1]	Si[1]	Ti[2]	V[2]	Cr[2]	Mn[2]	Co[3]	Ni[2]
		D.L(LA-ICP-MS) ppm	-	-	-	-	0.21	0.56	0.8	5.43	0.03	0.03
		D.L (EMPA, Set 1) ppm	492	193	222	220	241	223	277	284	-	311
		D.L (EMPA, Set 2) ppm	189	57	63	49	73	95	86	133	-	137
Treasure Lake Group	T1mag	***Average***	***71.1***	***<56***	***271***	***469***	***401***	***655***	***661***	***308***	***67***	***151***
	N=2	*Median*	-	-	*166*	*344*	*267*	*552*	*642*	*229*	*61*	*136*
	nt=35	Min	-	-	120	160	89	127	156	146	52	114
		Max	-	-	1699	2287	2143	1466	1509	1628	107	222
		n	-	-	21	21	32	35	35	22	14	16
	T2mag	***Average***	***71.3***	***<56***	***236***	***243***	***222***	***202***	***178***	***936***	***10***	***31***
	N=1	*Median*	-	-	*238*	*242*	*180*	*209*	*159*	*465*	*9*	*31*
	nt=47	Min	-	-	129	158	106	98	29	321	7	28
		Max	-	-	308	441	670	297	430	3933	16	38
		n	-	-	25	25	47	47	38	47	22	22
Nori/Ra	Nomag1	***Average***	***71.1***	***<57***	***189***	***213***	***258***	***1053***	***1411***	***211***	***73***	***185***
	N=2	*Median*	-	-	*183*	*178*	*144*	*935*	*1373*	*207*	*78*	*186*
	nt=41	Min	-	-	157	137	46	488	786	169	46	160
		Max	-	-	257	649	1711	2440	3109	303	93	202
		n	-	-	14	18	27	41	36	22	21	17
	Nomag 2	***Average***	***71.1***	***<57***	***<186***	***<198***	***242***	***522***	***15***	***127***	***347***	***596***
	N=1	*Median*	-	-	-	-	*191*	*500*	*13*	*112*	*134*	*593*
	nt=9	Min	-	-	-	-	73	480	0	61	42	567
		Max	-	-	-	-	532	624	38	325	1190	634
		n	-	-	-	-	9	9	9	9	8	9
	NoQksmag	***Average***	***71.1***	***<186***	***382***	***<245***	***152***	***1569***	***169***	***248***	***47***	***<315***
	N=1	*Median*	-	-	*345*	-	*179*	*1514*	*196*	*231*	*42*	-
	nt=14	Min	-	-	262	-	39	382	1	192	32	-
		Max	-	-	542	-	229	2482	336	342	70	-
		n	-	-	6	-	8	14	8	8	8	-
NICO	NImag1	***Average***	***71.1***	***1021***	***361***	***2331***	***304***	***118***	***30***	***357***	***3***	***5***
	N=5	*Median*	-	*784*	*200*	*618*	*305*	*119*	*28*	*246*	*2*	*4*
	nt=109	Min	-	63	97	99	65	57	7	85	1	3
		Max	-	3606	2090	17853	1065	167	60	1304	8	12
		n		37	71	91	69	45	18	47	18	9
	NImag2	***Average***	***71.1***	***575***	***1123***	***803***	***553***	***169***	***6***	***322***	***6***	***3***
	N=1	*Median*	-	*387*	*1136*	*354*	*573*	*155*	*4*	*261*	*5*	*3*
	nt=72	Min	-	72	256	109	114	64	1	134	1	2
		Max	-	1497	2180	7499	856	430	27	756	13	5

		n		15	54	54	72	53	18	38	18	10
	NImag3	***Average***	***71.1***	***1911***	***293***	***212***	***166***	***37***	***1***	***145***	***8***	***11***
	N=2	*Median*	-	*1911*	*229*	*205*	*150*	*22*	*1*	*147*	*5*	*11*
	nt=44	Min	-	485	66	62	3	2	0.2	91	3	9
		Max	-	3337	1922	817	513	93	2	201	15	13
		n		2	28	25	24	13	11	13	8	4
		Average	***71.3***	***164***	***1050***	***571***	***351***	***1201***	***15***	***628***	***62***	***139***
	Temag	*Median*	-	*93*	*906*	*556*	*310*	*1151*	*0.4*	*585*	*63*	*137*
Terra	N=1	Min	-	65	254	330	106	830	0	347	52	121
	nt=51	Max	-	386	3327	1060	1015	1893	119	1153	72	180
		n	-	9	29	31	48	51	21	40	20	14
		Average	***71.3***	***<57***	***437***	***348***	***350***	***719***	***22***	***413***	***415***	***13***
	Damg	*Median*	-	-	*394*	*320*	*168*	*677*	*10*	*309*	*414*	*11*
DAMP	N=2	Min	-	-	264	101	72	122	4	148	314	4
	nt=77	Max	-	-	831	914	1488	1485	107	817	532	25
		n	-	-	50	8	60	77	25	67	23	11
	SDmag	***Average***	***70.7***	***294***	***252***	***435***	***182***	***140***	***18***	***461***	***465***	***62***
	N=4	*Median*	-	*202*	*208*	*243*	*91*	*137*	*2*	*388*	*308*	*64*
Sue Dianne	nt=114	Min	-	66	100	53	31	82	0.2	146	283	36
		Max	-	1270	2042	3303	1236	327	356	2479	843	72
		n	-	11	54	49	39	59	26	83	25	12
		Average	***72.8***	***<188***	***<263***	***279***	***673***	***1900***	***388***	***276***	***52***	***1028***
	Fmag1	*Median*	-	-	-	*277*	*482*	*1681*	*348*	*205*	*55*	*908*
	N=3	Min	-	-	-	224	153	1388	36	143	34	339
	nt=19	Max	-	-	-	337	2618	2680	596	899	68	2785
FAB		*n*	-	-	-	3	18	19	17	14	13	7
	Fmag2	***Average***	***72.8***	***<188***	***335***	***470***	***347***	***417***	***40***	***317***	***111***	***1270***
	N=3	*Median*	-	-	*335*	*358*	*222*	*433*	*3*	*298*	*40*	*1207*
	nt=18	Min	-	-	254	324	25	232	1	195	14	482
		Max	-	-	416	837	1251	540	187	472	342	2563
		n	-	-	2	7	13	18	9	10	10	11

[1] EMPA data, [2] EMPA and LA-ICP-MS data, [3]LA-ICP-MS data
D.L., detection limits
N, total number of samples
nt, total number of analysis (EMPA and LA-ICP-MS, when both techniques were performed)
n, number of analysis above detection limits used for statistical analysis. In the case of Co, *n*, is representative of the total analysis performed via LA-ICP-MS. For Fe, Si, Al and Mg, their concentrations were obtained only via EMPA.

3 Mechanisms of gold refining at the Au-Co-Bi± Cu-W iron-oxide dominated NICO deposit, NWT, Canada

3.1 Introduction

The occurrence of gold in As-bearing phases such as pyrite and arsenopyrite has been widely recognized in gold deposits (e.g., Wells and Mullens, 1973; Cabri et al., 1989) such as orogenic (e.g., Zachariáš et al., 2004; Large et al., 2007; Oberthür and Weiser, 2008; Thomas et al., 2011), volcanic hosted massive sulfides (e.g., Törmanën and Koski, 2005) and skarn deposits (e.g., Cepedal et al., 2008). In metamorphic settings, As-bearing melts can incorporate and remobilize significant amounts of gold and other metals of economic importance (e.g., Tomkins and Mavrogenes 2001, 2002; Tomkins et al., 2004). In hydrothermal sulfides (e.g., pyrite) and sulfarsenides (e.g., arsenopyrite), multiple studies have suggested that the presence of arsenic alone enhances the gold concentrations in these minerals (e.g., Cook and Chryssoulis, 1990; Fleet and Mumin 1997; Reich et al., 2005). However, Cook et al. (2009) and Ciobanu et al. (2012) have argued that As-free pyrite from the Dongping, Huangtualiang and Hougou deposits in China have significant gold amounts (up to 1 wt.%) as a result of multiple post-depositional Au-refining processes.

The coupling of Au with Bi and Te in some of these S-As-rich systems has also been documented (Sakellaris, 2004; Törmanën and Koski, 2005; Oberthür and Weiser, 2008; Slack, 2012) due to the remarkable Au-scavenging properties of Bi (Douglas et al., 2000) and Te in a wide variety of hydrothermal systems (e.g., Ciobanu et al., 2005; Cockerton and Tomkins, 2012). The discovery of unusual As-S-Au-Bi ±Co-Au-Cu-Te-rich iron oxide-dominated systems, part of the Iron-Oxide Copper Gold deposit (IOCG) family (e.g., the NICO deposit, Tennant Creek district, Idaho Cobalt belt, Kuusamo Schist Belt; Guelb deposit)

suggests that Bi and Te could have had major a role in the gold enrichment in these deposits.

Gold can occur in association with arsenopyrite or As-rich pyrite in two ways: as "invisible" gold, which refers to gold in solid solution or as <0.1μm inclusions, concomitantly precipitated from the parental hydrothermal fluid (e.g., Wu and Delbove, 1989; Genkin et al., 1998; Maddox et al., 1998; Simon et al., 1999; Ashley et al., 2000); and "visible" (micrometer to decimeter) native gold inclusions (e.g., Mumin et al., 1994; Tomkins and Mavrogenes, 2001; Sung et al., 2009). The latter are commonly related to post-depositional processes such as re-crystallization and dissolution-reprecipitation reactions (e.g. Mumin et al., 1994; Tomkins and Mavrogenes, 2001; Cook et al., 2009; Sung et al., 2009).

Bismuth and Te are frequently associated with visible Au, within microveins or interstitial to the aforementioned sulfides and sulfarsenides (e.g., Goad et al., 2000; Cook and Ciobanu, 2004; Törmanën and Koski, 2005; Oberthür and Weiser, 2008), which has been used to demonstrate the ability of these elements to scavenge gold from hydrothermal fluids (Douglas et al., 2000; Wagner, 2007; Ciobanu et al., 2005; Tooth et al., 2008; Tooth et al., 2011, 2013). In the specific case of Bi, this behavior has been described by the liquid bismuth collector model (Douglas et al., 2000). Bismuth has a low melting point (271.4ºC; Okamoto and Massalski, 1986) and the model suggests that Bi may form an immiscible melt with the hydrothermal fluids under low sulfur fugacity conditions and temperatures greater than ~271ºC. Once partitioned from the hydrothermal fluid, liquid Bi can then scavenge up to 20 wt. % Au from coexisting hydrothermal fluids (Douglas et al., 2000).

Thermodynamic modeling carried out by Tooth et al. (2008) has also demonstrated that the Au concentrations in Bi melts are several orders of magnitude higher than those in the co-existing hydrothermal fluids. Furthermore, experimental work by Tooth et al. (2011) indicates that the Au enrichment of Bi-melts precipitated from hydrothermal fluids can take place in natural systems as a consequence of fluid-rock and fluid-fluid reactions. Therefore, the direct fractionation of Bi-Au melts from a hydrothermal fluid, or precipitation of a Bi-

melt followed by partitioning of Au from the ambient fluid, provides alternative mechanisms for the enrichment of low abundance ore components, such as Au, without requiring fluid saturation with respect to an Au mineral (Tooth et al., 2011).

Economic Au-Co-Bi±Cu-REE iron oxide-dominated systems are not common, but examples include the Au-Cu-Bi Tennant Creek district (Skirrow and Walshe, 2002), the Co-Cu-Au-Bi-Y-REE Idaho Cobalt belt (Slack, 2012), the Kuusamo Schist belt (Cu-Co-Au-Cu-Bi) (Vanhanen, 2001), and the Guelb deposit (Cu-Au-Co±Ni-Bi-Te-Ag) (Kolb et al. 2006). These are atypical IOCG-like deposits that formed contemporary to regional metamorphism, or were subsequently metamorphosed.

The Great Bear magmatic zone (GBMZ), NWT, Canada, hosts the NICO (Au-Bi-Co±Cu-W) and Sue Dianne (Cu-U-Ag-Au±Bi) deposits, along with other smaller iron-oxide dominated polymetallic systems (Fig. 3.1). Many of these deposits and showings have alteration and mineralization styles analogous to IOCG deposits in Chile and Australia (Corriveau, 2007; Corriveau et al., 2007; Mumin et al., 2007; Corriveau et al., 2010; Acosta-Góngora et al., in press). The NICO deposit contains Au-Co-Bi (±Cu-W) mineralization, hosted in the amphibole-magnetite-biotite altered metasedimentary rocks of the Treasure Lake Group. At NICO, the principal ore minerals are Co-rich arsenopyrite and loellingite, cobaltie, native Bi, bismuthinite, chalcopyrite and Cu-Bi sulphides, which are associated with native Au and Au-tellurides (Goad et al 2000; Sidor, 2000). This mineralogy is similar to that of the aforementioned atypical iron-oxide dominated Au-Co-Bi-Cu deposits from other districts. The NICO deposit post-dates regional metamorphism, and comprises multiple phases of intense hydrothermal stratabound to discordant alteration and localized breccia development.

In this work, we use petrographic observations, *in situ* trace and major element (EMPA and LA-ICP-MS) analyses on the main ore minerals at NICO, to argue that the origin of the Au-Bi mineralization associated with Fe, Co, and/or Ni sulfides, sulfarsenides and arsenides is associated with post-depositional

remobilization processes and the occurrence of Bi-melts (the liquid bismuth collector model). In doing so, we provide new insights on the importance of Bi and Te in the formation of this sub-category of IOCG deposits.

3.2 The NICO deposit

The NICO Au-Co-Bi±Cu-W deposit is within the southern GBMZ (Figs. 3.1, 3.2A) and has reserves of 33 Mt grading 1.02 g/t Au, 0.112% Co, 0.14% Bi, and 0.04 % Cu in the Bowl Zone (Puritch et al., 2012) (Fig. 3.2A). NICO is hosted by the Treasure Lake Group (TLG), a sequence of 1885-1875 Ma metasedimentary rocks that are the youngest component of the Hottah terrane (Goad et al., 2000; Gandhi and van Breemen, 2005; Bennett and Rivers, 2006; 2012). The TLG has been metamorphosed to greenschist-amphibolite facies. Regional metamorphism was associated with the development of a steeply-dipping fabric across the southern GBMZ and predates the emplacement of felsic volcanic rocks and porphyritic intrusions of the Great Bear arc at 1.87 Ga (e.g., Hildebrand, 1987; Hildebrand et al., 2010). Consequently, regional metamorphism predates hydrothermal alteration and mineralization across the Treasure Lake Group.

The TLG is intruded and unconformably overlain by K-feldspar altered Faber Group volcanic rocks of the GBMZ, with minor mineralized veins and breccias occuring at the unconformity (Gandhi and Lentz, 1990; Gandhi, 1994; Sidor, 2000; Goad et al., 2000) (Fig. 3.2A). At NICO, Sidor (2000) divided the TLG into the Lower, Middle and Upper units.

The Middle unit, termed as amphibolitic ironstones by Sidor (2000), hosts most of the mineralization within the Bowl Zone (Fig. 3.2B) and consists of magnetite, biotite, actinolite, ferrohornblende with or without orthoclase, microcline and hedenbergite. The Upper unit is a quartz-arenite that contains stratabound biotite-amphibole alteration and it is interlayered with metasiltstones (Corriveau et al., 2010). The upper quartz-arenite is unconformably overlain by the Faber Group rhyolites and associated volcanic rocks that are strongly potassically (orthoclase-biotite±microcline) altered. In places, these volcanic

rocks also host zones of magnetite±orthoclase-microcline alteration. Porphyritic dykes intrude the altered TLG rocks, mainly in the southeastern part of the deposit. Uranium-Pb zircon geochronology of two subvolcanic porphyries, one of which was overprinted by the NICO mineralization and the other crosscuts the ore lenses, constrains the timing of mineralization to a short period ca. 1869-1871 Ma (Davis et al., 2011).

The mineralization is mostly hosted by metasedimentary rocks that have been subjected to a ferrohornblende-actinolite-biotite-magnetite±orthoclase-microcline alteration type (Figs. 3.3A-D; 3.4A, B), but some also occurs in albitized metasedimentary rocks. The ore minerals are constrained to several closely stacked sulfide-bearing ore lenses that are stratabound at the scale of the deposit (Fig. 3.2B), but that show both stratabound (e.g., Figs. 3.3A, D) and discordant relationships (e.g., Figs. 3.3A-C) to the sedimentary layering at the macroscopic scale. The ore consists of cobaltian arsenopyrite, cobaltian loellingite, cobaltite, native Bi, bismuthinite, and native Au; the latter occurs as inclusions (<1 to >100μm) in arsenopyrite, disseminated in the various types of amphibole-magnetite alteration (Goad et al., 2000; Sidor, 2000), and is commonly associated with native Bi and tellurides. Copper, tungsten and molybdenum occur in minor amounts as chalcopyrite, scheelite and molybdenite (Goad et al., 2000).

The ore minerals in the lenses occur in veins (2-10 cm wide; Figs. 3.3A, C; 3.4B), breccias, alteration fronts (Fig. 3.4A), massive mineral aggregates (Fig. 3.3B) and disseminated within stratabound alteration zones along bedding and/or local foliation planes (Figs. 3.3A, D) (Goad et al., 2000; Corriveau et al., 2010). Recent work on altered rocks from this deposit (Corriveau et al., 2010; Corriveau et al., 2011; Montreuil et al., 2013) has characterized in detail several alteration types consistent with the IOCG classification. Moreover, these workers suggest that the NICO system extends south of the Bowl Zone, where a 3 x 0.5 km U (±Cu-Mo) albitite breccia zone was found and named as the Southern Breccia (Fig. 3.2B). The main ore minerals here are chalcopyrite, molybdenite and uraninite. The Southern breccia has not been affected by regional metamorphism, however, locally developed brittle-ductile deformation of albitite clasts and

magnetite alteration suggests a restricted post-orogenic deformational event, that took place contemporaneously with the emplacement of the GBMZ. Further evidence for brittle-ductile deformation regimes in the study area is given by the localized ductile deformation of arsenopyrite-rich veins in the Bowl Zone (Fig. 3.4B).

3.3 Analytical techniques

Major element analyses of NICO sulfides, sulfarsenides and arsenides were carried out on a CAMECA-SX-100 and a JEOL 8900 EMPA at the University of Alberta. The electron beam had an acceleration voltage of 15kV and current of 20 nA with counting times between of 10-40s on both instruments. The elements analyzed include Co, Fe, Ni, As, S, Te, Cu, Bi, Sn, Sb and Pb. A summary of the operating conditions and standards used for each element is given in Table 3.1.

Trace element LA-ICP-MS analyses were carried out on six sulfarsenide-arsenide-rich samples from drill-core material from the Bowl Zone (Fig. 3.2A, B). The data was acquired at the Great Lakes Institute for Environmental research (GLIER), University of Windsor, using a Thermo X Series II inductively coupled quadrupole mass spectrometer coupled with a Quantronix Integra C 785 nm, diode-pumped, YLF (yttrium-lithium fluoride) ultra-fast (130 femtosecond) laser. An approximately 10 μm spot size was used and an energy of approximately 0.03 mJ. A gas background signal was collected for 60 s before the beginning of ablation for each analysis. The processing of the LA-ICP-MS data was carried out using the Aabel 3.0® graphics/statistics software package and in-house Excel® spreadsheets. Background readings for individual analyses were collected for 10 s before the ablation started. The ablation times varied from 5 to 40 s (see detailed description below).

Quantification of the following isotopes was obtained through calibration of relative sensitivities using the NIST 610 standard: ^{48}Ti, ^{51}V, ^{52}Cr, ^{55}Mn, ^{59}Co, ^{60}Ni, ^{63}Cu, ^{75}As, ^{89}Y, ^{108}Pd, ^{109}Ag, ^{111}Cd, ^{119}Sn, ^{121}Sb, ^{130}Te ^{191}Pt, ^{208}Pb, ^{209}Bi, and ^{197}Au. Electron microprobe data for Fe were used as the internal standard

concentration. Detection limits were generally <10 ppm for most elements. However, due to the extreme variability of Fe concentrations in the arsenopyrite from NICO and to ensure the quality of the data, the sections were re-polished after the ablations and the Fe concentrations obtained (via EMPA) for each individual sample close to the analyzed traverses.

Analysis of sulfides using NIST 610 were compared with values obtained using the Po725 sulfide standard (Sylvester et al., 2005), which is certified for the PGE and Au. Concentrations for Pd, Pt and Au, for which NIST 610 is certified, were within 5 to 25% of the values calculated using Po725. Similarly, concentrations of Pd, Pt and Au calculated for Po725 using NIST 610 as the standard were within 30% of the true value. The imprecision associated with using NIST 610 to analyze sulfides is therefore estimated to be <30%. This error is significantly less than the variations in trace element concentrations discussed below (Au, Bi and Te), which range over several orders of magnitude.

In NICO samples, the laser ablation analyses were carried out by traversing across the surface of sulfide, sulfarsenides and arsenide grains. Over 100 traverses were carried out, most of them on arsenopyrite and with an average length of 200 μm. In most cases, a single traverse contains multiple Fe-Co-As-S phases that were ablated. Portions of the spectra with a minimum of 10s were used for most individual phase analyses. However, for fine grains (<25μm) and/or remnant phases (e.g., loellingite, ~40 μm) contained within arsenopyrite II only 5 to 9s of spectra were processed.

The Aabel program permits the user to pick the portion of the spectra used for quantification. Each spectrum was examined for any evidence of mineral inclusions and such segments were eliminated in the quantification process. The portion of a spectrum used for quantification was selected where a spectrum exhibited approximately constant counts as a function of ablation (traverse) time. However, some analyses of Au-rich arsenopyrite, cobalite and loellingite do contain Au-Te-Bi inclusions and these could not be removed from the final

quantification process for these samples. These data are clearly indicated in the text and figures.

3.4 Results

3.4.1 Host rocks alteration and mineralization

This section describes the multiple alteration/mieralization stages recognized at the NICO deposit, which are summarized in Figure 3.5**.**

Barren Fe-Ca-K alteration: the alteration is pervasive, and for the most part, stratabound (e.g., Fig. 2A) with minor amounts in veins and/or patches in the TLG and as alteration fronts or as massive replacement in the felsic units (Figs. 3G, H). It consists of fine grained Fe and Fe-Ca-rich amphibole (ferrohornblende, actinolite), magnetite, biotite, and orthoclase.

This Fe-Ca-K alteration has distinct mineral assemblages depending on the protolith types. In the feldspar porphyries and felsic volcanic rocks, that intrude and cap the TLG, the alteration consists of Fe-Ca-K-rich silicates. This alteration consists of fine grained (20-40μm) bitotite I (±magnetite I) alteration fronts typically overprinting the porphyritic texture (Fig. 3.4G).

In the metasedimentary rocks, the alteration comprises pervasive replacements along millimiter to centimeter thick bedding by fine (25-50 μm) to medium grained (50-80 μm) green-brown bitotie I, ferrohornblende I, actinolite I, magnetite I, hedenbergite I, orthoclase I and quartz I (Figs. 3.6A, B). In most cases, the precursor minerals have been totally overprinted, and only remnants of quartz and orthoclase are observed (Fig. 3.6A). The ferrohornblende I, actinolite I, biotite I and magnetite I are the dominant phases, with minor hedenbergite I, plagioclase I and quartz I. Concentric zoning observed in ferrohornblende I (Fig. 3.6B) and magnetite I grains (Acosta-Góngora et al., in press) provides evidence for a cyclical build-up of this alteration. A pre-ore, barren quartz ± ferrohornblende-orthoclase-calcite vein set (Set 1; 2-3 cm thick) crosscuts these rocks.

The Co-rich Fe-Ca-K alteration stage: in the feldspar porphyries this stage is represented by pervasive and massive replacement of the matrix and

phenocrysts of the former intrusions by K-feldspars (orthoclase II, microcline II) (Fig. 3.4D). Normally, the sulfarsenides and arsenides occur disseminated or as irregular veins (~1 cm thick; Fig. 3.4D).

In the TLG this stage is emplaced as millimeter- centimeter-thick veins, minor breccias and alteration fronts cutting the amphibolitic ironstones, disseminated along the bedding or irregularly disseminated (e.g., Figs. 3.3A-D). This stage consists of moderately to highly fractured arsenopyrite, cobaltite, loellingite, pyrite (py-I), magnetite II, ferrohornblende II, actinolite II and green-brown biotite II, with minor scheelite and molybdenite, orthoclase II, quartz and fluorite (Figs. 3.6C, D). This phase is commonly coarser grained (50 to >100 μm) than the barren Fe-Ca-K alteration stage (Figs. 3.4A; 3.6C, D). Replacement of magnetite I and silicate minerals (ferrohornblende I, actinolite I, biotite I) from the barren Fe-Ca-K alteration by the sulfarsenides, arsenides, ferroactinolite II, magnetite II and actinolite II resulted in the preservation of multiple inclusions (5 to 20μm) of the former minerals in the sulfarsenide, arsenides and amphibole grains (e.g., Figs. 3.6D; 3.7A). Locally the sulfarsenides and arsenides have also pyrrhotite inclusions and cores suggesting an earlier replacement of this sulfide by the later phases (Fig. 3.7C, 3.8A).

The ferrohornblende II, actinolite II and biotite II have euhedral grains (Figs. 3.6C, D). Actinolite typically has a radiating habit (Fig. 3.6C). Cobaltite, loellingite, and arsenopyrite I crystals are euhedral to anhedral (e.g., Figs. 3.7A-D). Usually the cores of these grains are floating in arsenopyrite II crystals (Figs. 3.7A, 3.8A, B). Occasionally, well-defined rims of arsenopyrite III overgrow arsenopyrite II (Fig. 3.8B). A characteristic brownish-pinkish sieve-textured arsenopyrite (apy-s) occurs within or coating arsenopyrite grains (Figs. 3.7F, 3.8D).

The sieve-textured comprises an intergrowth of (5-20μm) euhedaral arsenopyrite grains, magnetite and/or silicates. Depending on the degree of replacement by the host grain, the shapes of the patches vary. Lower degrees of replacement have resulted in angular to subrounded zones of well-preserved arsenopyrite intergrown or spatially associated with silicates. A higher intensity of

replacement resulted in rounded shapes of a brown-pink arsenopyrite almost devoid of the angular arsenopyrite crystals and of silicates (Figs. 3.7F, 3.8D). In both cases, Bi and to a lesser degree, chalcopyrite and emplectite and wittichinite crosscut and preferentially replace, these zones (e.g., Fig. 3.8D). In places, the sieve-textured arsenopyrite replaces arsenopyrite II (Fig. 3.8C)

The pyrite-marcasite-magnetite alteration stage: This alteration assemblage is localized within the Co-rich Fe-Ca-K alteration. Intergrowths of marcasite, pyrite, hastingsite (Fig. 3.7E) and magnetite are commonly observed to be intergranular to arsenopyrite and have partially replaced this sulfarsenide. The intergrowth assemblages are: pyrite-magnetite, marcasite-hastingsite, marcasite-pyrite ± magnetite and masses of fine-grained (5 to 20μm) euhedral (square-shaped) marcasite, intergrown with hastingsite grains. The first assemblage is distinctive because it comprises masses of square-shaped intergrowths of magnetite and pyrite or monomineralic aggregates of marcasite (Fig. 3.7F). The second and third marcasite styles consist of lamellar intergrowths of marcasite and hastingsite and/or marcasite-pyrite and magnetite (Fig. 3.7E). Massive pyrite (py-m) also coats the sulfarsenides and arsenides (Fig. 3.9A).

The Bi-Au-Cu-rich Fe-K alteration: The Bi-Au-Cu stage occurs as inclusions in sulfarsenides (e.g., Figs. 3.7B, D), interstitially to earlier assemblages, as micro-veins (e.g., Figs. 3.7C, E; 3.8E; 3.9C, D) crosscutting the previous stages (in the porphyries and TLG) and as disseminations on the Fe-Ca-K altered TLG host rocks (Fig. 3.9E). The micro-veins acted as conduits to areas of replacement, where, most commonly chalcopyrite, or less commonly bismuthinite, has replaced arsenopyrite, pyrite and marcasite (± molybdenite) (Fig. 3.7E).

This stage is dominated by native Bi, bismuthinite, chalcopyrite, native Au (<5 to 15μm inclusions) and minor emplectite ($CuBiS_2$) and wittichenite (Cu_3BiS_3). Hastingsite, hematite, quartz, and variable amounts of, magnetite, fluorite, quartz, and orthoclase and microcline, occur with the ore minerals. Bismuthinite and minor chalcopyrite replace the sieve- textured arsenopyrite. These phases and native Bi also occur as isolated bleb-like to angular inclusions

with irregular shapes (e.g., Fig. 3.7B, D; 3.8A) and variable sizes (<5μm to 30μm). These inclusions are commonly adjacent to micro-veins of the same composition or as linear trails and clusters, mostly in arsenopyrite and to a lesser extent in cobaltite and loellingite (Fig. 3.8D, E). In places micro-shear textures were observed, and these were will filled with native Bi and bismuthinite (Fig. 3.9D). These zones of bismuth, bismuthinite and chalcopyrite inclusions are not exclusively observed in the arsenides and sulfarsenides, but also occur as inclusions in, and fill interstices between, magnetite grains. Locally, linear and arcuate trails (<3 μm thick and 400-1000 μm length) of globular-shaped native Bi are well preserved in scheelite and the pre-ore quartz veins (set 1) (Fig. 3.9C).

Native Au occurs as micro-veins usually associated with native Bi and bismuthinite that crosscut, or are disseminated in, arsenopyrite crystals (Figs. 3.8F). Gold also occurs disseminated in the host rocks as 5 to 20 μm grains (Fig. 3.9B), and is spatially associated with bismuthinite and native bismuth grains. Three main Bi, Au and Au-Bi inclusion styles have been identified. The first one corresponds with isolated inclusions in arsenopyrite grains (Fig. 3.7B). The second style comprises clusters of inclusions in arsenopyrite (Fig. 3.7D). The last inclusion assemblage consists of disseminations in the barren and Co-rich Ca-Fe-K altered rocks, where Au is usually contained within bismuthinite (Fig. 3.8F, 3.9B).

The Cu-Bi-Au stage is represented by two dominant mineral assemblages. The first assemblage consists of native Bi-bismuthinite-native Au- magnetite III (±quartz) assemblage in which bismuthinite locally replaces native Bi (Fig. 3.9D). The second mineral association comprises chalcopyrite-hastingsite-clinochlore-hematite±bismuthinite-emplectite-wittichenite-calcite assemblage (Figs. 3.7E, 3.9E, F), in which bismuthinite is locally replaced by emplectite and chalcopyrite.

Vapor- and halite- saturated fluid inclusions containing native Bi have been recognized in the Bi-rich trails (Fig. 3.9C). An Au-like inclusion has also been observed in one of the trails, but due to its minute size and position in the thin section it could not be analyzed by electron microprobe.

Post-mineralization barrren veins: Locally, the Fe-As-S phases are crosscut by another set (set 2) of quartz ± amphibole-microcline-orthoclase veins (0.5 to 1 cm thick). Moreover in the upper parts of the system another set (set 3) of coarse-grained (0.5 to 5 cm) quartz-calcite-ankerite (± chalcopyrite-titanite- K-orthoclase) veins occur. The latter is crosscut by later clinochlore veins. Titanite from one such vein has been dated (U-Pb) at ca. 1.85 Ga by Davis et al. (2011).

3.4.2 Major element analysis

Major element contents of arsenides, sulfarsenides and sulfides: Electron microprobe analyses determined the presence of Co-bearing arsenopyrite, cobaltite and Co-rich loellingite. A summary of the compositions of these minerals is given in Table 3.2. In arsenopyrite I, II and III, the Co, Fe, S and As concentrations range from 0.1 to 14 mol.%, 19 to 34 mol.%, 26 to 34 mol.% and 32 to 40 mol.%, respectively. Loellingite has very consistent values for As (64 mol %) and S (2-4 mol.%); conversely, Fe and Co concentrations range from 15 to 25 wt.% and from 8 to 18 mol.%, respectively.

The variation of Co and Fe reflects the solid solution between loellingite ($FeAs_2$) and safflorite ($CoAs_2$). The As (34-36 mol.%) and S (30-34 mol.%) contents of cobaltite are very consistent and those of Co (26-33 mol.%) and Fe (1-4 wt.%) have less variation than that seen in the arsenopyrite and loellingite. However, cobaltite can have up to 4 mol.% Ni, indicating solid solution along the cobaltite (CoAsS)-gersdorffite (NiAsS) series.

The sieve-textured sulfarsenides fall into three main compositional groups based on their Co (and Fe) contents. The first is Co-rich and lies closest to the cobaltite end-member, with 27-30 mol.% Co, 4-6 mol.% Fe, 32-33 mol.% S and 33-34 mol.% As. The second type is closer in composition to alloclasite ((Co,Fe)AsS), with 22-23 mol.% Co, 10-12 mol.% Fe, 30-33 mol.% S and 33-36 mol.% As. The third compositional group has a chemistry similar to that of Co-rich arsenopyrite, with 6-14% mol.% Co, 20-29 mol.% Fe, 28-33 mol.% S and 33-37 mol.% As, and here is termed apy-*s*. In the absence of X-ray diffraction analysis, it is difficult to conclusively distinguish between cobaltite and alloclasite, and thus, we will refer to both as cobaltite with a sieve-texture (co-*s*).

The Fe (33-34 mol.%) and S (65-66 mol.%) contents in pyrite (py-1 and py-m) are very consistent, with only a ~1 mol. % variation for each element. The back-scattered electron images reveal texturally complex zoning of arsenopyrite (Fig. 3.8C), although, some grains do have a well-defined outer-rim zone (Fig. 3.8B). In contrast, cores and euhedral grains of cobaltite and Co-rich loellingite hosted by arsenopyrite are homogeneous (Figs. 3.8A, B). High contents of Co in arsenopyrite II (up to 14 mol.%) are spatially associated with the presence of Co-rich loellingite and cobaltite cores. This phase of arsenopyrite displays some of the highest contents of Co measured in this study (Fig. 3.8B). Conversely, recrystallization rims that formed around arsenopyrite II (arsenopyrite III) have less Co (e.g., 3 mol. %; Fig. 3.8B). Arsenopyrite grains without loellingite and/or cobaltite cores have, on average, lower Co contents of 0.1 to 4 mol.% (Fig. 3.10C), except apy-*s* which has up to 14 mol.% Co.

3.4.3 LA-ICP-MS analysis

Where possible, inclusion-free regions of grains were selected for analysis, and indeed some of the spectra reflect an absence of inclusions, as the counts vary little as a function of traverse time. In many cases, however, the spectra clearly indicate that inclusions of other minerals or native phases were encountered (most notably phases containing Au, Bi, Cu and Te; e.g., Figs. 3.11A-C), both in grains that were known to contain inclusions and in apparently inclusion-free grains. The latter, however, contain flat portions of spectra, or ‘baselines’, with counts that are several orders of magnitude above background for some elements, although, for Te, Au, Ag, Cd and Pt, most of the spectra have a ‘baseline’ close to the background (very low concentrations; Figs. 3.11A-C). In all cases, we interpret this baseline to represent lattice-bound trace elements. Steady changes in the spectra baseline are interpreted as zoning of the aforementioned structurally bound elements.

Analyses were carried out on 94 arsenopyrite, 10 pyrite, 3 loellingite and 3 cobaltite grains. Representative trace element data for arsenopyrite, pyrite (py-m), cobaltite and loellingite are presented in Table 3.3. Selenium, Pb, Sb, Ni and Cu were routinely detected. Conversely, Ag, Cu, Te and Au were occasionally

detected. Other elements, such as V, Cr, Pd, Cd, Pt and Sn, were also detected, but were close to their detection limits (mainly <1 ppm). Few analyses showed evidence of zoning in single arsenopyrite grains. This zoning was mostly observed in Sb, Ni and Pb, and to a minor extent Se and Ag. Locally, Au, Te and Cu visible inclusion-rich regions (not structurally bound) were recognized in arsenopyrite II (Fig. 3.11A, B). Conversely, invisible inclusions (<0.1 μm) or clustered inclusions were detected in cobaltite, loellingite and arsenopyrite I (Figs. 3.11A, C). Although, we did not find significant evidence for consistent zoning of trace elements in the analyzed mineral phases, this is probably due to the *in-situ* scope of the study. We acknowledge that further scanning of individual grains via LA-ICP-MS and construction of trace element concentration maps, may show a more defined element zoning.

This study demonstrates that Au in arsenopyrite is either structurally bound or occurs as inclusion arsenopyrite. Structurally bound Au and Te contents in the sulfarsenides are generally <0.1 ppm, but can range up to 6 ppm. When one or more Au inclusions were included in the integration region, Au concentrations vary between 0.7 and 81 ppm, respectively. Where, Au present its counts broadly correlate with those of Bi, even when Au has low concentrations (Figs. 3.11A-C), but Bi-rich inclusions are not necessarily always associated with Au-rich inclusions. In some analyses, spectral correlations of Au with Te were also observed (Figs. 3.11A-C).

The few analyses of loellingite and cobaltite show that Au and Te concentration in these minerals varies from 3 to 92 and 2 to 39 ppm, respectively, which is up to 4 orders of magnitude higher than in most arsenopyrite grains (Figs. 3.12A, B). In addition, single traverses through Au-bearing and Au-deficient arsenopyrite I and II and loellingite-arsenopyrite II grain assemblages reveal higher amounts of both Bi and Au at the interface between those mineral phases (Figs. 3.11A, B). Overall, the highest Au contents in arsenopyrite-rich samples are spatially associated with the Au-bearing arsenopyrite I, cobaltite, Co-rich loellingite, and arsenopyrite II that replaced the earlier minerals. However, the presence of these sulfarsenide Au-bearing phases (e.g. arsenopyrite I) is

erratic within the samples analyzed and also the deposit itself. The Au contents in pyrite (py-m) range from 0 to 1.3 ppm, where it is mainly structurally bound. Despite the spectral correlation of Au and Bi (±Te) in Au-rich minerals, the binary plots of element concentration presented in Fig. 3.12A and 3.12B display no correlation between Au and Bi and Te.

3.5 Discussion

3.5.1 Textural evidence: relative timing of mineralizing events

The petrographic analysis presented here, indicate that there are three broad paragenetic stages of ore formation overprinting the barren Fe-Ca-K alteration at NICO deposit. The first episode (Co-rich Fe-Ca-K alteration) corresponds with the precipitation of Au-bearing (nanometer-sized Au particles and/or structurally bond Au) Co-rich sulfarsenides and arsenides (arsenopyrite I, loellingite and cobaltite) and the co-precipitation of ferrohornblende II, actinolite, II, magnetite II, biotite II and pyrite (Fig. 3.5, 3.13A). The subsequent ore stage corresponds with the deposition of Bi and visible Au along magnetite (±bismuthinite-quartz). It is very likely that the replacement of the early sulfarsenides by arsenopyrite II-III also took place during this stage (see discussion below; Figs. 3.5; 3.13A). The latest mineralization phase is the Cu±Bi-rich Fe-K alteration, which comprises the deposition of chalcopyrite-bismuthinite-hastingsite-chlorite-hematite-emplectite-wittichenite assemblages (Figs. 3.5; 3.13B).

The sieve-textured arsenopyrite (apy-s; probably also applicable to co-s) was described by Mumin et al. (1994) and interpreted to be the result of the replacement of pyrrhotite by marcasite and pyrite, and overprinted by arsenopyrite. In agreement with the Mumin et al. (1994) observations, textures of apy-s and co-s in this study resemble those exhibited by marcasite (Fig. 3.7F). Recent work done by Qian et al. (2010, 2011) supports the latter, and further demonstrates that the formation of marcasite and pyrite can result from the replacement of magnetite and/or pyrrhotite at low $pH_{21°C}$ (<4) values, however, pyrite can also form at alkaline conditions ($pH_{21°C}$ = 12-13). Overall, the

replacement rate of magnetite by Fe disulfide is higher at low $pH_{120°C}$ (1-4) conditions and with an increasing temperature (120-190°C) (Qian et al., 2010). Apart from the temperature and pH constraints, the formation of marcasite at the expense of pyrrhotite can also be favored by occurrence of S(-II) poor hydrothermal fluids (saturation index << 1000), while pyrite crystallization is dominant in solutions with a high saturation index (>1000) (Qian et al., 2011).

3.5.2 The Fe-Co-Ni distribution in the sulfarsenides and arsenides

The sulfarsenides and arsenides from NICO deposit largely overlap the compositional fields defined in literature and from other vein hosted deposits (Fig 14A). The large variations in Fe, Co and Ni concentrations, but in this case, predominantly Fe and Co are commonly associated with temperature changes (e.g., Klemm, 1965; Hem and Mackoviky, 2004). However, other factors such as salinity changes (e.g., Migdisov et al., 2011) and proportional inheritance of, e.g., Co (in arsenopyrite II and III) from the precursor arsenide or sulfarsenide grains could also play a significant role in the concentration of Fe-Co-Ni into the sulfarsenides and arsenides. In this section we will address these hypotheses.

Klemm (1965) developed a series of geothermometers for arsenides and sulfarsenides based on the substitutions of Fe-Ni-Co in these mineral phases. However, this gethermometer has important limitations (e.g., pressure effect) and thus, the results presented here should be interpreted with caution. The data from loellingite (both Co-rich) suggest that this mineral might have been formed at temperatures >400°C (Fig. 3.13A). Cobaltite and arsenopyrite I have two data populations (Fig. 3.14A), one overlapping the temperature range given by loellingite phases (>400 to 650°C) and second one suggesting a lower temperature of formation (<300°C and 300-500°C, respectively).

The experimental data from Hem and Makovicky (2004) suggest that at high temperatures (650°C) co-existence between loellingite and arsenopyrite, and alloclasite and diarsenide solid solution (dss) is favored by the incorporation of Co (at the expense of Fe) into arsenopyrite and of Fe (at the expense of Co) into the alloclasite structure (Fig 3.14B). Most of our data for arsenopyrite I and cobaltite (co-eval with loellingite) overlap these fields. The ‘lower temperature’

cobaltite and arsenopyrite I data also plots well within their respective stability fields indicating that a temperature gradient is not necessary to explain the compositional differences between the cobaltite populations. At lower temperatures (500°C) these stability fields retreat significantly (Fig. 3.14B**),** and most of our arsenopyrite I-cobaltite data falls out the fields. The lack of zoning observed in arsenopyrite I, cobaltite and loellingite grains and cores, suggest that these were deposited in equilibrium with the source fluid, and thus, the geothermometry data could be pointing to either a temperature increase consistent with a prograde metasomatic event that peaked at temperatures >400°C, or the occurrence of two different generations of arsenopyrite I and/or cobaltite formed at different temperatures. Overall, the geothermometry analysis and the comparison of our data with Hem and Mackoviky (2004) stability fields, suggests that loellingite, cobaltite and arsenopyrite co-existed at temperatures >400°C.

Contrariwise, the complex zoning exhibited by arsenopyrite II and the sieve-textured cobaltite and arsenopyrite suggests strong disequilibrium with the parental solutions, which makes the geothermometric interpretations less reliable. However, the more scattered temperature data from these phases (Fig. 3.14A) might be consistent with a gradual temperature decrease of the fluid precipitating these minerals associated with a retrograde metasomatic event.

Solubility estimates for Co, Fe and Ni in chlorine-rich aqueous solutions at temperatures between 25 and 700ºC (0.4-2 kbar), suggest that these metals are complexed mostly by Cl (e.g., $CoCl_4^{-2}$; $FeCl_4^{-2}$; $NiCl_2(H_2O)_2$; Testemale et al., 2009; Migdisov et al., 2011; Tian et al., 2011; Liu et al., 2012). Hydrated Cl-octahedral complexes are found to be more stable at higher temperatures (> ~200ºC) and salinity values (e.g., >2 m), which results in an overall increase of the solubility of Co, Fe and Ni in hydrothermal solutions (e.g., Susak and Crerar, 1985; Testemale et al., 2009; Tian et al., 2011; Liu et al., 2012). Therefore, fluctuations in the fluids salinity, e.g., fluid mixing between a Cl-rich magmatic fluid and meteoric waters, could also affect the amount of Fe-Co-Ni partitioned from the hydrothermal fluid into the sulfarsenides and arsenides.

Another empirical factor that might affect the accommodation of Fe and Co into the arsenopyrite structure is the local inheritance of those elements by a newly formed phase (e.g., arsenopyrite II replacing cobaltite). The arsenopyrite richest in Co at NICO commonly contains cores and/or inclusions of cobaltite and Co-rich loellingite. As a result, Co was incorporated into the newly formed arsenopyrite structure (II or III) at the expense of Fe as it replaced the early Co-rich Fe-As-S phase. The EMPA suggest that the arsenopyrite II and III have Co contents that are roughly proportional to their precursor sulfarsenide. For example, arsenopyrite that has replaced cobaltite and Co-rich loellingite will have greater amounts of Co (e.g., Co=15 wt.%), with respect to arsenopyrite formed after precursor sulfarsenides with less amounts of Co (e.g., Co= 5 wt. %), that will have significantly lower Co concentrations (Fig. 3.10C).

3.5.3 Gold remobilization

The complex association between Au and arsenides, sulfides and sulfarsenides suggests that significant Au might have been initially introduced during the Co-rich stage in As-S-bearing minerals, either in solid solution or as nanoparticles (<0.1 μm). In this section we argue that some Au was then reconstituted during conversion of Au-bearing loellingite, cobaltite and arsenopyrite I into native Au inclusions in arsenopyrite II.

The experimental work of Tomkins and Mavrogenes (2001) shows that the conversion of arsenopyrite and pyrrhotite to loellingite during peak metamorphism can result in the incorporation of Au into loellingite by diffusion. If loellingite is subsequently replaced by retrograde arsenopyrite, the refractory Au is liberated from the loellingite crystal structure, but the liberated Au cannot partition into the resulting arsenopyrite (Tomkins and Mavrogenes, 2001). Thus, Au occurs as inclusions in the arsenopyrite, and at the interface with loellingite (Tomkins and Mavrogenes, 2001). This conclusion is supported by the work of Mumin and Fleet (1994), Wagner et al. (2007), and Sung et al. (2009), who have demonstrated the importance of post-depositional re-crystallization during metamorphism of Au-bearing arsenopyrite and pyrite as an efficient Au-refining mechanism. In these studies, Au is released from the host mineral

(arsenopyrite/pyrite) after re-crystallization and re-deposited as Au-inclusions and remobilized into fractures crosscutting arsenopyrite and pyrite. In fact, Wagner et al. (2007) showed that in metamorphosed volcanic-hosted massive sulfides (VHMS), arsenopyrite and pyrite with the greatest degree of re-crystallization have very low concentrations of Au (0 to 3 ppm), and instead Au is found in veins and in other lower strain sites.

The NICO deposit post-dates regional metamorphism in the area of study, but pervasive hydrothermal alteration of the host-rocks was triggered by the emplacement of the GBMZ at ca. 1875 (Hildebrand et al. 1987; Goad et al. 2000, Corriveau et al., 2010; Hildebrand et al., 2010). This alteration can be considered, broadly speaking, as a contact metamorphic effect, and, where fluid-rock ratios were low, and represents equivalent prograde and retrograde metasomatic regimes to those described by Tomkins and Mavrogenes (2001) for regional metamorphism.

Our data show that structurally bound Au concentrations of the arsenopyrite from NICO are low (0-6 ppm) and that values in arsenopyrite not directly associated with Au-rich cobaltite and Co-loellingite have the lowest values (0.01 to 0.1 ppm). The highest lattice-bound Au values are observed in arsenopyrite with abundant Au inclusions, but those are still below 10 ppm. These relatively Au-enriched grains have Au-rich arsenopyrite I and loellingite cores (Figs. 3.11A, B), and coat and partially replace cobaltite grains. Moreover, LA-ICP-MS transects through Au-rich loellingite and Au-inclusion rich arsenopyrite II (Fig. 3.11A) have higher Au-Bi concentrations in loellingite and at the interface between both minerals in arsenopyrite II, which is in agreement with the observations of Tomkins and Mavrogenes (2001). However, visible inclusions at this interface, or the clear formation of composite loellingite-pyrrhotite-arsenopyrite grains, as defined by Tomkins and Mavrogenes (2001), were not recognized in this study. Single or clusters of Au(Bi) inclusions are also present in cobaltite and loellingite, but they were not optically recognized, suggesting that their grain sizes are $<0.1\mu m$.

Thus, the textural evidence, ablation profiles, and gold concentrations (in Au-rich samples) are consistent with an up-grading of gold in arsenopyrite derived from Au-bearing arsenopyrite I, loellingite and cobaltite. This up-grading, was triggered by the remobilization of structurally bound Au during the replacement of the latter mineral phases by arsenopyrite II (Fig. 3.13A). Although less common, the close association of Au and Bi in the inclusions, might suggest that similarly to Au, nanometer sized particles of Bi were initially contained within early sulfarsenides and arsenides and then remobilized with Au (Fig. 3.13A, see discussion below).

3.5.4 Gold scavenging by Bi

The close association of Au with Bi, either in fractures within Co-rich phases or disseminated and in fractures in the Fe-Ca-amphibole-biotite-magnetite rich host rocks, suggests that scavenging of Au by liquid Bi may have occurred during the lower temperature recrystallization of the early Co-bearing sulfarsenides (arsenopyrite I, cobaltite and loellingite) in the presence of hydrothermal fluids (Fig. 11B).

Both invisible and visible Au inclusions are associated with Bi(±Te). However, due to the nature of the native gold grains (as inclusions in native Bi and bismuthinite, or in the vicinity of those phases), the lack of identifiable stable Au-Bi phases (e.g. maldonite or jonassonite), and the fact that not all Bi-rich samples are enriched in Au, but all Au-bearing samples are associated with Bi, the correlation between the two elements is difficult to observe (Fig. 10B).

Well-preserved trails of globular native Bi in scheelite and the pre-ore vein set 1 from NICO are similar to those described by Tomkins and Mavrogenes (2002), Ciobanu et al. (2006), and Cook et al. (2009), which are interpreted as healed fractures containing droplets of what was molten Bi at the time of entrapment, and which coexisted with hydrothermal fluids during the evolution of NICO system. This is supported by the presence of globular native Bi in saline fluid inclusions within the trails. The Bi droplets may have scavenged Au from the lower temperature Bi-Au-Cu fluids and subsequently solidified in micro-veins in arsenopyrite II, and as disseminations in the host rocks (cf. Douglas et al.,

2000; Tooth et al., 2008, 2011; Fig 3.13B). Some of this Au in solution, might have been released and dissolved during the formation of arsenopyrite II and subsequently scavenged by the Bi melts (e.g., Cockerton and Tomkins, 2012) (Fig. 3.13B).

The Au-refining event was temporarlly associated with brittle-ductile deformation, as suggested by the micro-shearing textures and microveins in arsenopyrite grains filled with Au, Bi, and bismuthinite (Fig. 3.9D) and by the local ductile deformation of arsenopyrite veins (Fig. 3.4B). Since the Bi-rich zones at the scale of this study and at the deposit scale are not necessarily associated with Au, the Au mineralization seems to be localized within the ore-lenses as opposed to the more homogeneously distributed Fe-Co-As-S ore. The Au-mineralization commonly occurs as Bi-Au inclusions within arsenopyrite grains, this might indicate that invisible (nanometer-sized particles) Au and Bi were released from its host sulfarsenide and/or arsenide grain during alteration to arsenopyrite II, and that Au was synchronously *in situ* scavenged ('locked in') by adjacent metallic Bi droplets in a molten state (Fig. 3.13A). As a result of this process larger micrometer-scale Bi-Au inclusions will be formed in arsenopyrite II (Fig. 3.13A).

Cook et al. (2009) described a somewhat analogous process in pyrite, in which coupled dissolution reprecipitation reactions released Au-LMCE (low melting point chalcophile elements) droplets that pooled out of the fluid at the reaction fronts and filled the voids continually formed during the reaction. Unfortunately, such well-developed porous textures in association with Au-Bi-rich inclusion zones, analogous to those that result from coupled dissolution-reprecipitation reactions, have not been observed at NICO deposit. However, the sieve-textured textures cobaltite and arsenopyrite in spatial association with interstitial native Bi and bismuthinite might be a local representation of this process. Oberthür and Weiser (2008) also suggested that remobilization of gold and its subsequent association with Bi at the Viceroy mine was a result of the conversion of arsenides and sulfarsenides. The specific mechanisms of how this process takes place are not argued. There, native Au and Bi, bismuthinite and

sulfarsenides are associated with interconversions between pyrrhotite, loellingite and arsenopyrite, as observed in NICO. Oberthür and Weiser (2008) also suggested that secondary hydrothermal reactions are probably a key factor controlling Au distribution in this deposit, perhaps leading to subsequent enrichment.

Törmänen and Koski (2005) and Tooth et al. (2011) have pointed out the importance of appropriate reducing conditions to maintain the stability of the Bi melts. The latter results in the reduction of Bi^{3+} ($Bi(OH)_3$) to Bi^0 by interacting with reduced phases such as pyrrhotite and graphite (Tooth et al., 2011). In addition, the precipitation of Fe^{3+} bearing phases (e.g., magnetite and epidote) can also cause a reduction of coexisting Bi^{3+} to its native state (Cockerton and Tomkins, 2012).

The interconversion between pyrrhotite, loellingite and arsenopyrite (and in this case also of cobaltite) recognized in retrograde metamorphic and hydrothermal systems takes place at temperatures close to the Bi melting point (Neumayr et al., 1993; Tomkins and Mavrogenes, 2001) and the dissolution of As minerals is likely to occur under highly reducing conditions (Pokrovski et al., 2002). Skirrow and Walshe (2002) have also shown that interaction of Cu-Au-Bi bearing fluids with magnetite-hematite-rich ironstones will decouple Au and Bi via desulfidation-oxidation reactions by destabilizing reduced sulfur bearing complexes ($Bi_2S_2(OH)_2$ or $HBi_2S_4^-$). However, to date there has not been any experimental proof of the importance of sulfide species to increase the solubility of Bi in hydrothermal solutions. Despite the later, the retrogression from arsenopyrite I, cobaltite and loellingite to arsenopyrite II and III (reducing environment), the co-precipitation of native Bi with magnetite and the interaction of Co-Au-Bi-Cu±W bearing fluids with Fe-Ca-amphibole-biotite-magnetite altered rocks are consistent with the formation of stable Bi-melt phases, which ultimately led to local Au concentration at NICO. Although Te-rich mineral phases were not identified in this study, Sidor (2000) and Goad et al. (2000) have pointed out an important link between tellurides and Au at NICO.

Our ablation profiles show good correlation between Au and Te. Ciobanu et al. (2005) have argued that the Au-scavenging properties of Te and Bi-Te melts are analogous to those of Bi in different ore deposits styles, from epithermal to orogenic environments. Therefore, Te might also be a source of Au refining following similar mechanisms to those discussed above for Bi.

The common occurrence of bismuthinite-Au assemblages is not analogous to the Au-Bi association, that is, where bismuthinite represents a melt scavenging Au, because of its high melting point (775ºC, Lin et al., 1996). The bismuthinite-Au assemblage may, however, be the result of the replacement of native Bi by bismuthinite in response to a retrograde process (Tooth et al., 2011), local increase of the sulfur fugacity conditions (e.g. Cockerton and Tomkins, 2012), or result from the decomposition of maldonite due to sulfidation reactions which converted this mineral into bismuthinite and native Au (Ciobanu et al., 2010). Maldonite, however, was not identified in this study. The petrographic evidence presented above is consistent with the first and second hypotheses, as typically bismuthinite replaces native Bi.

3.5.5 Estimation of P-T conditions: constraints from geothermometry and mineralogy

The direct estimation of the pressure and temperature conditions for the formation of the sulfarsenides and arsenides at NICO deposit is very difficult to carry out, due to the lack of co-precipitated gangue minerals (e.g., quartz and carbonates) suitable for stable isotope geothermometric studies and also capable of hosting primary fluid inclusions. The only link to the mineralizing fluids is the occurrence of the native Bi-bearing fluid inclusions found in the set 1 veins (P. Acosta-Góngora, unpublished data). The following discussion will argue the possible P-T conditions at NICO deposit on the basis of sulfarsenide geothermometry, occurrence of native Bi and emplectite, and deformation constraints.

The ore mineralogy at the NICO deposit is somewhat similar to that of polymetallic (Ag-Co-Ni-Bi-Cu±U-Au-Zn-Pb) vein-hosted systems worldwide (e.g., Canada, Terra, Cobalt; Germany, Bieber and Wenzel; Zimbawe, Viceroy;

Morocco, Bou Azzer). These vein-hosted systems have abundant carbonates and quartz as dominant gangue phases, and it has been suggested they formed under epithermal conditions, where temperatures of mineralization mostly range from 100 to 350°C and pressures from 0.2 to 2.5 kbar (Changkakoti et al. 1986; Marshall et al. 1993; Oberthür et al., 1994; Wagner and Lorentz, 2002; En-Naciri et al., 1997). Contrary to these deposits, the lack of quartz and carbonates and the pervasive pre- and syn-ore Fe-Ca-amphibole-biotite-magnetite alteration assemblages at NICO deposit suggest a more reducing system compared to that of epithermal deposits, but also, a metasomatic origin. The formation of magnetite-rich (±Fe-rich mica-amphibole-alkali feldspar) IOCG alteration assemblages, similar to those of the barren and Co-rich Fe-Ca-K alterations in NICO, is typically constrained between 300-600°C, but for the most part >400°C (Skirrow and Walshe, 2002; Bastrakov et al., 2007; Somarin and Mumin, 2013; Rusk et al., 2010), which overlaps the crystallization temperatures suggested by the early Co-rich loellingite, Ni-Fe-rich cobaltite and arsenopyrite I (300-650°C; prograde Co-rich Fe-Ca-K alteration). Thus, it is reasonable to consider a temperature of ~400 °C as a minimum upper end of the estimated temperature of the mineralizing system.

The lower end is given by the occurrence of molten Bi droplets, bismuthinite and emplectite in the retrograde mineralization stages. Native bismuth is replaced by bismuthinite, and then by emplectite in the later stages of retrograde mineralization. For this series of replacements to occur, the native Bi most have been in a solid state first, which indicates a temperature of below 271 °C. A further constraint is given by the precipitation of emplectite, as this mineral is stable until to 320°C, where experimental work (Cu-Fe-Bi-S system) has shown it gets replaced by its high temperature equivalent phase, cuprobismuthite. Therefore, the maximum temperature for the final stage of the retrograde mineralization is ~270°C, but probably emplectite and chalcopyrite crystallization took place at much lower temperatures (Fig 3.13B).

The pressure conditions are consistent with those of a brittle-ductile regime. Micro-shears filled up with native Bi and bismuthinite (Fig. 3.9D) and the

local ductile deformation recognized in drill core samples (Fig. 3.4B) suggest such conditions of formation. Moreover, the youngest porphyry dated in the NICO area (ca.1871 Ma; Davis et al., 2011), crosscuts the mineralization and is undeformed, which rules out the possibility of significant post-mineralization regional deformation. In other IOCG deposits (e.g., Tennant Creek district; Ernest Henry; Lightning Creek) also formed under brittle-ductile deformation conditions similar to those of NICO the associated pressure regime is mostly constrained between 1.5 and 2.5 kbar (Skirrow, 1993; Perring et al., 2000; Rusk et al., 2010). Hence, we think that this pressure range could also represent the formation conditions at NICO deposit.

3.5.6 NICO mineralization

This work suggests that Au and Bi were initially deposited as nanoparticles and Au as structurally bound elements in early Co-rich arsenides and sulfarsenides at >400 ºC during prograde metasomatism (Fig 3.13A). A gradual decrease in temperature and/or change in fluid salinity, along with synchronous brittle-ductile deformation triggered recrystallization (retrograde metasomatism; <400 to ~270°C) to arsenopyrite II and III and the formation of the marcasite-bearing assemblage at the expense of pyrrhotite, and magnetite. These processes locally re-distributed Co into the newly formed arsenopyrite, and, more importantly, promoted the remobilization of Au and Bi (as Bi-melts) from the early sulfarsenides and arsenides. During this remobilization the *in situ* 'lock in' of Au by Bi took place. Textural evidence also indicates the co-existence of significant Bi (Te?)-melts with hydrothermal fluids, and these melts were capable of concentrating Au transported in solution.

The formation of the Au-scavenging Bi-melts at temperatures >271ºC (or slightly less due to the presence of gold) was a result of reducing conditions resulting in the interconversion of sulfarsenides, co-precipitation of magnetite III and desulfidation (early precipitation sulfarseindes, arsenides and sulfides) of hydrothermal fluids caused by the interaction with the Fe-Ca-K altered rocks of the TLG. In addition, the temporarily associated brittle deformation created the permeability necessary to precipitate and accommodate the Au, Bi and Bi-Au-rich

phases in microveins. Such Au refining via recrystallization of sulfarsenides and arsenides (in situ 'lock in') accounts for the occurrence of Bi, Au and Au-Bi (±Te) inclusions in arsenopyrite II. Gold enrichment via direct fractionation from Au-bearing fluids (due to the presence of Bi melts) is more likely to explain the Au-Bi (±Te-Au) disseminations and microveins in the host rocks that are not associated with sulfarsenides and arsenides.

Both mechanisms can explain the Au, Bi, Au-Bi (±Te-Au) occurrence in microveins that crosscut arsenopyrite, cobaltite and loellingite, as well in the Fe-Ca amphibole-biotite-magnetite altered host rocks containing Au-rich minerals. Both Au-refining processes occurred either contemporaneously or closely associated in time. As temperature dropped and sulfur, oxygen and Cu fugacity increased, native Bi was altered to bismuthinite and emplectite (<270°C; Fig. 3.13B). The later explains the common association between bismuthinite and gold. Emplectite replaced bismuthinite along with the precipitation of chalcopyrite, chlorite, hastingsite and hematite.

In this study we have shown that in the NICO deposit Au is spatially associated with Bi, but the presence of native Bi and bismuthinite is not always linked to significant amounts of Au. This implies that the partitioning of Au into minerals and the presence of Au in the hydrothermal fluids is erratic within the deposit, but where present, Au is systematically associated with Bi (±Te). Our work suggests that the presence of Bi (±Te) melts, as predicted by the Bi collector model (cf. Tomkins et al., 2004; Ciobanu et al. 2005; Törmanën and Koski 2005; Tooth et al. 2011; Cockerton and Tomkins 2012) played a critical role in refining the Au concentrations in the NICO deposit and possibly in similar Au deposits associated with Fe-As-S-rich IOCG systems.

3.6 References

Acosta-Góngora, P., Gleeson, S.A., Samson, I.M. and Corriveau, L., in press, Trace elements in magnetite and its relationship to Cu-Bi-Co-Au-Ag-U-W mineralization in the Great Bear magmatic zone, NWT, Canada: Economic Geology.

Ashley, P.M., Creagh, C.J., and Ryan, C.G., 2000, Invisible gold in ore and mineral concentrates from the Hillgrove gold-antimony deposits, NSW, Australia: Mineralium Deposita, v. 35, p. 285-301.

Bastrakov, E.N., Skirrow, R.G., Davidson, G.J., 2007, Fluid evolution and origins of iron oxide Cu-Au prospects in the Olympic Dam District, Gawler Craton, South Australia: Economic Geology, v. 102, p. 1415-1440.

Bennett, V., and Rivers, T., 2006, U-Pb ages of zircon primary crystallization and inheritance for magmatic rocks of the southern Wopmay orogen, Northwest Territories: Northwest Territories Geoscience Office, Open File 2006-006, p. 65.

Bennett, V., Rivers, T., Jackson, V.A., 2012, A compilation of U-Pb zircon primary crystallization and depositional ages from the Paleoproterozoic southern Wopmay Orogen, Northwest Territories: NWT Open report 2012-003, 157p.

Cabri, L.J., Chryssoulis, S.L., Villiers, J.P.R., LaFlamme, J.H.G., Buseck, P.R., 1989 The nature of invisible gold in arsenopyrite: The Canadian Mineralogist, v. 27, p. 353-362.

Cepedal, A., Fuertes-Fuente, M., and Martin-Izard, A., 2008, Gold bearing As-rich pyrite and arsenopyrite from the El Valle gold deposit, Asturias, northwestern Spain: The Canadian Mineralogist, v. 46, p. 233-247.

Changkakoti, A., Morton, R.D., and Gray, J., Hydrothermal environments during the genesis of silver deposits in the Northwest Territories of Canada: Evidence from fluid inclusions: Mineralium Deposita, v. 21, p. 63-69.

Ciobanu, C.L., Cook, N.J., Utsunomiya, S., Kogagwa, M., Green, L., Gilbert, S., Wade, B. , 2012, Gold-telluride nanoparticles revealed in arsenic-free pyrite. American Mineralogist, v. 97, p. 1515-1518.

Ciobanu, C. L., Cook N. J., and Pring A., 2005, Bismuth tellurides as gold scavengers, in J. W., Mao and F. P,. Bierlein, eds., Mineral Deposit Research Meeting the Global Challenge: Springer, Berlin, p. 1383-1386.

Ciobanu, C.L., Cook, N.J., Damian, F., and Damian, G., 2006, Gold scavenged by bismuth melts: An example from Alpine shear-remobilisates in the Highiş Massif, Romania: Mineralogy and Petrology, v. 87, 351-384.

Ciobanu, C. L., Birch, W.D., Cook, N.J., Pring, A., and Grundler, P.V., 2010, Petrogenic significance of Au-Bi-Te-S-associations: The example of Maldon, central Victorian gold province, Australia: Lithos, v. 116, p. 1-17.

Cook, N.J., and Ciobanu, C.L., 2004: Bismuth tellurides and sulphosalts from the Larga hydrothermal system, Metaliferi Mts., Romania: Paragenesis and genetic significance: Mineralogical Magazine, v. 68, p. 301-321.

Cook, N.J., Ciobanu, C.L., and Mao, J., 2009, Textural control on gold distribution in As-free pyrite from the Dongping, Huangtuliang and Hougou gold deposits, north China craton (Hebei Province, China): Chemical Geology, v. 264, p. 101-121.

Cockerton, A.M.D., and Tomkins, A.G., 2012, Insights into the liquid bismuth collector model through analysis of the Bi-Au Stortmont skarn prospect, northwest Tasmania: Economic Geology, v. 107, p. 667-682.

Corriveau, L., 2007, Iron oxide-copper-gold deposits: a Canadian perspective, in Goodfellow, W.D., ed., Mineral deposits of Canada: a synthesis of major deposit-types, district metallogeny, the evolution of geological provinces and exploration method: Geological Association of Canada, Special Publication 5, p. 307-328.

Corriveau, L., Ootes, L., Mumin, H., Jackson, V., Bennett, V., Cremer, J.F., Revard, B, McMartin, I., Beaudoin, G., 2007, Alteration vectoring to IOCG (U) deposits in frontier volcanic-plutonic terrains, Canada. International Conference on Mineral Exploration, 5th, Canada, 9-12 September 2007, Proceedings, p. 1171-1177.

Corriveau, L., Williams, P.J., and Mumin A.H, 2010, Alteration vectors to IOCG mineralization from uncharted terranes to deposits, in Corriveau, L., and Mumin, A.H., eds., Exploring for iron oxide copper-gold deposits: Canada and global analogues: Geological Association of Canada, Short Course 20, p. 89-110.

Corriveau, L., Mumin, A.H., and Montreuil, J.F., 2011, The Great Bear magmatic zone: The IOCG spectrum and related deposit types: Society of Geology Applied to Mineral Deposits Biennial Meeting, 11th, Chile, 26-29 September, Abstracts, p. 524-526.

Crerar, D.A., Susak, N.J., Borcsik, M., Schwartz, S., 1978, Solubility of the buffer assemblage pyrite +pyrrhotite +magnetite in NaCl solutions from 200 to 350°C: Geochimica et Cosmochimica Acta, v. 42, p. 1427-1438.

Davis, W., Corriveau, L., van Breemen, O., Bleeker W., Montreuil, J.F., Potter, E., Pelletier, E., 2011, Timing of IOCG mineralizing and alteration events within the Great Bear Magmatic Zone: Yellowknife Geoscience Forum, 39th , Canada, 15-17 November 2011, Abstracts, p. 97.

Douglas, N., Mavrogenes, J., Hack, A. and England, R. 2000, The liquid bismuth collector model: an alternative gold deposition mechanism, in C. G., Silbeck and T. C. T., Hubble eds., Understanding planet Earth; searching for a sustainable future; on the starting blocks of the third millennium, 15th Australian Geological Convention, eds: Geological Society of Australia, Sydney, 135 p.

El-Naciri, A., Barbanson, L., Touray, J.C., 1997, Brine inclusions from the Co-As(Au) Bou Azzer district, anti-atlas mountains, Morocco: Economic Geology, v. 92, p. 360-367.

Fleet, M.E., and Mumin, A.H., 1997, Gold-bearing arsenian pyrite, marcasite and arsenopyrite from Carlin trend gold deposits and laboratory synthesis: The American Mineralogist, v. 82, p. 182-193.

Gandhi, S.S., and Lentz, D.R., 1990, Bi-Co-Cu-As and U occurrences in the metasediments of the Snare Group and felsic volcanics of the southern Great Bear magmatic zone, Lou Lake, Northwest Territories: Geological Survey of Canada, Paper 90-1C, p. 239-253.

Gandhi S.S., 1994, Geological setting and genetic aspects of mineral occurrences in the southern Great Bear magmatic zone, Northwest Territories, in Sinclair, W.D., Richardson, D.G. , eds., Studies of rare-metal deposits in the Northwest Territories: Geological Survey of Canada, Bulletin 475, p. 63-96.

Gandhi, S.S., Mortensen, J.K., Prasad, N., and van Breemen , O., 2001, Magmatic evolution of the southern Great Bear continental arc, northwestern Canadian Shield: Geochronological constraints: Canadian Journal of Earth Sciences, v. 38, p. 767-785, doi: 10.1139/cjes-38-5-767.

Gandhi, S.S., and van Breemen, O., 2005. SHRIMP U-Pb geochronology of detrital zircons from the Treasure Lake Group - new evidence for Paleoproterozoic collisional tectonics in the southern Hottah terrane, northwestern Canadian Shield: Canadian Journal of Earth Sciences, v. 42, p. 833-845.

Genkin, A.D., Bortnikov, N.S., Safonov, Y.G., Cabri, L.J., McMahon, G., Stanley, C.G., Wagner, F.E., Friedl, J., Kurzin, A.L., and Gamyanin, G.N., 1998, A multidisciplinary study of invisible gold in arsenopyrite from four mesothermal gold deposits in Siberia, Russian Federation: Economic Geology, v. 93, p. 463-487.

Goad, R.E., Mumin, A.H., Duke, N.A., Neale, K.L., Mulligan, D.L., Camier, W.J., 2000, The NICO and Sue-Dianne Proterozoic, iron oxide-hosted, polymetallic deposits, Northwest Territories: Application of the Olympic Dam model in exploration: Exploration and Mining Geology, v.9, p. 123-140.

Hem, S.K., and Makovicky, E., 2004, The system Fe-Co-Ni-As-S II. Phase relations in the (Fe,Co,Ni)As1.5S0.5 section at 650 and 500 ºC: The Canadian Mineralogist, v. 42, p. 63-86.

Hildebrand, R.S., Hoffman, P.F., and Bowring, S.A, 1987, Tectono-magmatic evolution of the1.9-Ga Great Bear magmatic zone, Wopmay orogen, northwestern Canada: Journal of Volcanology and Geothermal Research, v. 32, p. 99-118.

Hildebrand, R.S, Hoffman, P.F and Bowring, S.A., 2010a. The Calderian orogeny in Wopmay orogeny (1.9 Ga) northwestern Canadian Shield: Geological Society of America Bulletin, v. 122, p. 794-814.

Klemm, D.D., 1965, Synthesen und Analysen in den Dreiecksdiagrammen FeAsS-CoAs-NiAs und FeS2-CoS2-NiS2: Neues Jahrbuch für Mineralogie - Abhandlungen, v.103, p.205-255.

Kolb, J., Sakellaris, G.A., Meyer, F.M., 2006, Controls on hydrothermal Fe oxide-Cu-Au-Co mineralization at the Guelb Moghrein deposit, Akjoujt area, Mauritania: Mineralium Deposita, v. 41, p. 68-81.

Large, R.R., Maslennikov, V.V., Robert, F., Danyushevsky, L.V. and Chang, Z., 2007, Multistage origin of pyrite and gold in the giant Sukhoi Log deposit, Lena gold province, Russia: Economic Geology, v. 102, p. 1233-1267.

Liu, W., Stacey, J.B., Testmale, D., Etschmann, B., Hazemann, J.L., and Bugger, J., 2011, Speciation and thermodynamic properties for cobalt chloride complexes in hydrothermal fluids at 35-440 oC and 600 bar: An in-situ XAS study: Geochimica et Cosmochimica Acta, v. 75, p. 1227-1248.

Lin, J. C., Sharma, R. C., and Chang, Y. A., 1996, The Bi-S (bismuth-sulfur) system: Journal of Phase Equilibria, v. 17, p. 132-139.

Maddox, L.M., Bancroft, G.M., Scaini, M.J., and Lorimer, J.W., 1998, Invisible: comparison of Au deposition on pyrite and arsenopyrite: American Mineralogist, v. 83, p. 1240-1245.

Marshall, D. M., Diamond, L.W., Skippen, G.B., 1993, Silver transport and deposition at Cobalt, Ontario, Canada: fluid inclusion evidence: Economic Geology, v. 88, p. 837-854.

Migdisov, A.A., Zezin, D., and Williams-Jones, A.E., 2011, An experimental study of cobalt (II) complexation in H2S-bearing hydrothermal solutions: Geochimica et Cosmochimica Acta, v. 75, p. 4065-4079.

Montreuil, J.F., Corriveau, L., and Grunsky, E., 2013, A compositional data analysis of IOCG systems, Great Bear magmatic zone, Canada: To each alteration types its own geochemical signature: Geochemistry: Exploration, Environment, Analysis, doi: 10.1144/geochem2011-101.

Mumin, H., Corriveau L., Somarin, A.K., Ootes, L., 2007, Iron Oxide Copper-Gold-type Polymetallic Mineralization in the Contact Lake Belt, Great Bear Magmatic zone, Northwest Territories, Canada: Exploration and Mining Geology, v. 16, p.187-208.

Mumin, A.H., and Fleet, M.E., and Chryssoulis, S.L., 1994, Gold mineralization in As-rich mesothermal gold ores of the Bogosu-Prestea mining district of the

Ashanti Gold Belt, Ghana: remobilization of “invisible” gold: Economic Geology, v. 29, p. 445-460.

Neumayr, P., Cabri L. J., Groves D. I., Mikucki E. J. and Jackman, J. A., 1993, The mineralogical distribution of gold and relative timing of gold mineralization in two Archean settings of high metamorphic grade in Australia: The Canadian Mineralogist, v.31, p. 711-725.

Oberthür, T., Vetter, U., Schmidt Mumm, A., Weiser, T., Amanor, J.A., Gyapong, W.A. Kumi, R. and Blenkinsop, T.G., 1994, The Ashanti gold mine, Obuasi, Ghana: Mineralogical, geochemical, stable isotope and fluid inclusion studies on the metallogenesis of the deposit: Geologisches Jahrbuch, D100, p. 31-129.

Oberthür, T., and T.W., Weiser, 2008, Gold-bismuth-telluride-sulphide assemblages at the Viceroy mine, Harare-Bindura-Shamva greenstone belt, Zimbawe: Mineralogical Magazine, v. 72, 0. 953-970.

Okamoto H., and Massalski T. B, 1986, Au-Bi (gold-bismuth), in T.B., Massalski, J. L. Murray, L. H. Bennet and H., Baker, eds., Binary Alloy Phase Diagrams: Ac-Au to Fe-Rh: American Society for Metals, v. 1, p. 238-240.

Ootes, L., Goff, S., Jackson, V., Gleeson, S.A., Creaser, R.A., Samson, I.M., Samson, Evenson, N., Corriveau, L., and Mumin, H., 2010, Timing and thermochemical constraint on multi-element mineralization at the Nori/RA Cu-Mo-U prospect, Great Bear magmatic zone, Northwest Territories, Canada: Mineralium Deposita, v. 45, p. 549-566.

Pokrovski G. S., Kara S., and Roux J., 2002, Stability and solubility of arsenopyrite, FeAsS, in crustal fluids: Geochimica et Cosmochimica Acta, v. 66, p. 2361-2378.

Puritch, E., Ewert, W., Armstrong, T., Brown, F., Orava, D., Pearson, J.L., Hayes, T., Duggan, T., Holmes, G., Uceda, D., Sumners, W., Mackie, D., Rougier, M., Bocking, K., Mezei, A., Horne, B., 2012. Technical report and updated mineral reserve estimate and front-end engineering and design (FEED) study on the NICO gold-cobalt-bismuth-copper deposit, Mazenod Lake area, Northwest Territories, Canada: NI 43-101 Technical Report No. 247 prepared for Fortune Minerals Ltd., 307 p.

Qian, G., Xia, F., Brügger, J., Skinner, W.M., Bei, J., Chen, G., and Pring, A., 2011, Replacement of pyrrhotite by pyrite and marcasite under hydrothermal conditions up to 220°C: An experimental study of reaction textures and mechanisms: American mineralogist, v. 96, p. 1878-1893.

Qian, G., Brügger, J., Skinner, W.M., Chen, G., and Pring, A., 2010, An experimental study of the mechanism of the replacement of magnetite by pyrite up to 300°C: Geochimica et Cosmochimica Acta, v. 74, p. 5610-5630.

Reich, M., Kesler, S.E., Utsunomiya, S., Palenik, C.S., Chryssoulis, S.L., and Ewing, R.C., 2005, Solubility of Gold in arsenian pyrite: Geochimica et Cosmochimica Acta, v. 69, p. 2781-2796.

Rusk, B., Oliver, N., Blenkinsop, T., Zhang D, Williams, P., Cleverley, J., and Habermann, P., 2010, Physical and chemical characteristics of the Ernest Henry iron oxide copper gold deposit, australia; implications for IOCG genesis *in* Porter T. M., ed., Hydrothermal iron oxide copper-gold and related deposits: A Global Perspective PGC Publishing, Adelaide, v. 3, p. 201-218.

Sakellaris, 2004, Petrology, geochemistry, stable and radiogenic isotopy of the Guelb Moghrein iron-oxide-copper-gold-cobalt deposit, Mauritania: Unpublished PhD thesis, Rheinisch-Westfälische Technische Hochschule Aachen, 222 p.

Sidor, M., 2000, The origin of the black rock alteration overprinting iron-rich sediments and its genetic relationship to disseminated polymetallic sulfide ores, Lou Lake, Northwest Territories, Canada: Unpublished M.Sc thesis, London, The University Western Ontario, 190 p.

Simon, G., Kesles, S.E., and Chryssoulis, S., 1999, Geochemistry and textures of gold-bearing arsenian pyrite, Twin Creeks, Nevada: implications for deposition of gold in Carlin-type deposits: Economic Geology, v. 94, p. 405-421.

Skirrow, R., and Walshe, J., 2002, Reduced and oxidized Au-Cu-Bi iron oxide deposits of the Tennant Creej Inlier, Australia: An integrated geologic and chemical model: Economic geology, v. 97, p. 1167-1202.

Slack, J., 2012, Strata bound Fe-Co-Cu-Au-Bi-Y-REE deposits of Idaho Cobalt belt: multistage, hydrothermal mineralization in a magmatic-related iron oxide copper-gold system: Economic Geology, v. 107, p. 1089-1113.

Somarin, A.K., and Mumin, H.A., 2013, P-T composition and evolution of paleofluids in the Paleoproterozoic Mag Hill IOCG system, Contact Lake, Northwest Territories, Canada: Mineralium Deposita, doi 10.1007/s00126-013-0482-3.

Sung, Y.-H., Brugger, J., Ciobanu, C.L., Pring A., Skinner, W., and Nugus, M., 2009, Invisible gold in arsenian pyrite and arsenopyrite from a multistage Archean gold deposit: Sunrise Dam, Eastern Gold fields Province, Western Australia: Mineralium Deposita, v. 44, p. 765-791.

Sylvester P. J., Cabri L. J., Tubrett M. N., McMahon G., Laflamme J. H. G., and Peregoedova A., 2005, Synthesis and evaluation of a fused pyrrhotite standard reference material for platinum group element and gold analysis by laser ablation-ICPMS: 10th International Platinum Symposium, Oulu, Finland, p. 16-20.

Testemale, D., Brugger, J., Liu, W., Etschmann, B., Hazemann, J.L., 2009, In-situ X-ray absorption study of Iron (II) speciation in brines up to supercritical conditions: Chemical Geology, v. 264, p. 295-310.

Tian, Y., Etschmann, B., Liu, W., Borg, S., Mei, Y, Testemale, D., O'Neill, B., Rae, N., Sherman, D.M., Ngothai, Y., Johannessen, B., Glover, C. and Brugger, J., 2012, Speciation of nickel (II) chloride complexes in hydrothermal fluids: In situ XAS study: Chemical Geology, v. 334, p. 345-363.

Thomas, H.V., Large, R.R., Bull, S.W., Maslennikov, V., Berry, R.F., Fraser, R., Froud, S., and Moye, R., 2011, Pyrite and pyrrhotite textures and composition in sediments, laminated quartz veins and reefs at Bendigo gold mine, Australia: insights for ore genesis: Economic Geology, v. 106, p. 1-31.

Tomkins, A.G, and Mavrogenes, J.A., 2001. Redistribution of Gold within arsenopyrite and loellingite during pro- and retrograde metamorphism: application to timing of mineralization: Economic Geology, v. 96, p. 525-534.

Tomkins, A.G., and Mavrogenes, J.A., 2002, Mobilization of gold as a polymetallic melt during pelite anatexis at the Challenger deposit, South Australia: A metamorphosed Archean Gold deposit: Economic Geology, v. 97, p. 1249-1271.

Tomkins A.G., Pattinson, D. R.M., and Zaleski, W., 2004, The Hemlo gold deposit, Ontario: An example of melting and mobilization of a precious metal-sulfosalt assemblage during amphibolite facies metamorphism and deformation: Economic Geology, v. 99, p. 1063-1084.

Tooth, B., Etschmann, B., Pokrovski, G.S., Testemale, D., Hazemann, J.L., Grundler, P.V. and Brugger, J., 2013, Bismuth speciation in hydrothermal fluids: An X-ray absorption spectroscopy and solubility study: Geochimica et Cosmochimica Acta, v. 101, p. 156-172.

Tooth B., Ciobanu C. L., O'Neill B., Green L., and Brugger J., 2011, Melt formation and gold scavenging from hydrothermal fluids: an experimental study: Geochimica. Cosmochimica. Acta, v. 75, p. 5423-5443.

Tooth B., Brugger J., Ciobanu C., and Liu W., 2008, Modeling of gold scavenging by bismuth melts coexisting with hydrothermal fluids: Geology, v.36, p. 815-818.

Törmanën, T.O., and Koski, R.A., 2005, Gold enrichment and the Bi-Au association in pyrrhotite-rich massive sulfide deposits, Escanaba trough, Gorda Ridge: Economic Geology, v. 100, p. 1135-1150.

Vanhanen, E., 2001, Geology, mineralogy and geochemistry of the Fe-Co-Au-U deposits in the Paleo Proterozoic Kuusamo Schist Belt Northeastern Finland: Bulletin of Geological Survey of Finland, v. 399, p. 9-229.

Wagner, T., 2007, Thermodynamic modeling of Au-Bi-Te melt precipitation from high-temperature hydrothermal fluids: Preliminary results: Society of Geologists Applied to Mineral Deposits, 9th, Ireland, November 15-17, p. 97.

Wagner, T., and Lorenz, J., 2002, Mineralogy of complex Co-Bi-Bi vein mineralization, Bieber deposit, Spessart, Germany: Mineralogical Magazine, v. 66, p. 385-407.

Wagner, T., Klemd, R., Wenzel, T., and Mattson, B., 2007, Gold upgrading in metamorphosed massive sulfide ore deposits: direct evidence from-laser-ablation-inductively coupled plasma-mass spectrometry analysis of invisible gold: Geology, v. 35, p. 775-778.

Wells, J.D., and Mullens, T.E., 1989, Gold-bearing arsenian pyrite determined by microprobe analysis, Cortez and Carlin gold mines, Nevada: Economic Geology, v. 68, p. 187-201.

Wu, X., and Debolve, F., 1989, Hydrothermal synthesis of gold-bearing arsenopyrite: Economic Geology, v. 84, p. 2029-2032.

Zachariáš, J., Frýda, J., Paterová, B., and Mihaljevic, M., 2004, Arsenopyrite and As-bearing pyrite from Roudný deposit, Bohemian: Mineralogical Magazine, v. 68, p. 31-46.

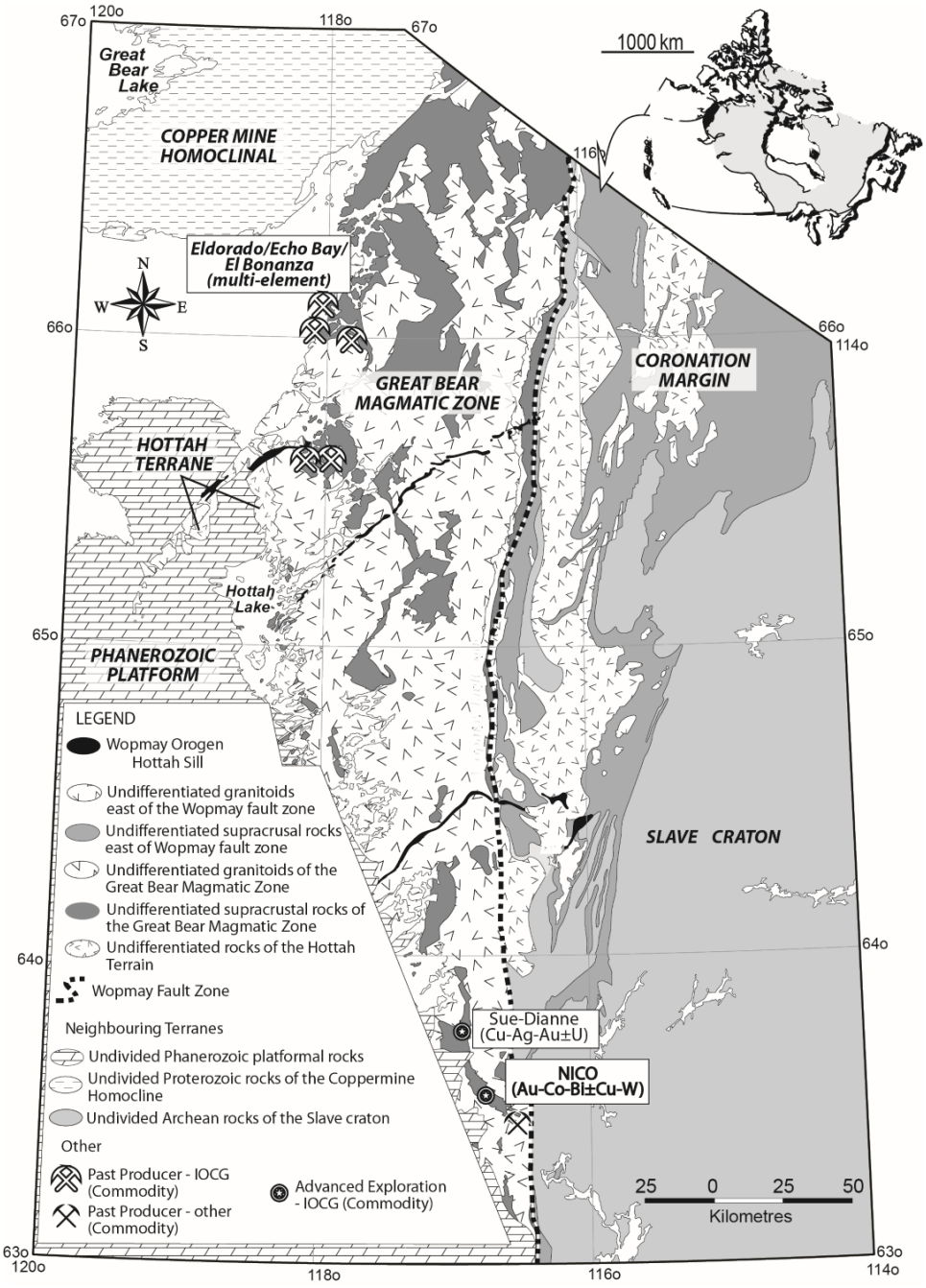

Figure. 3.1. Regional geology of the study of the GBMZ
Locations of selected past producing mines and advanced exploration projects. Modified after Ootes et al. (2010). NICO is located in the southernmost portion of the GBMZ.

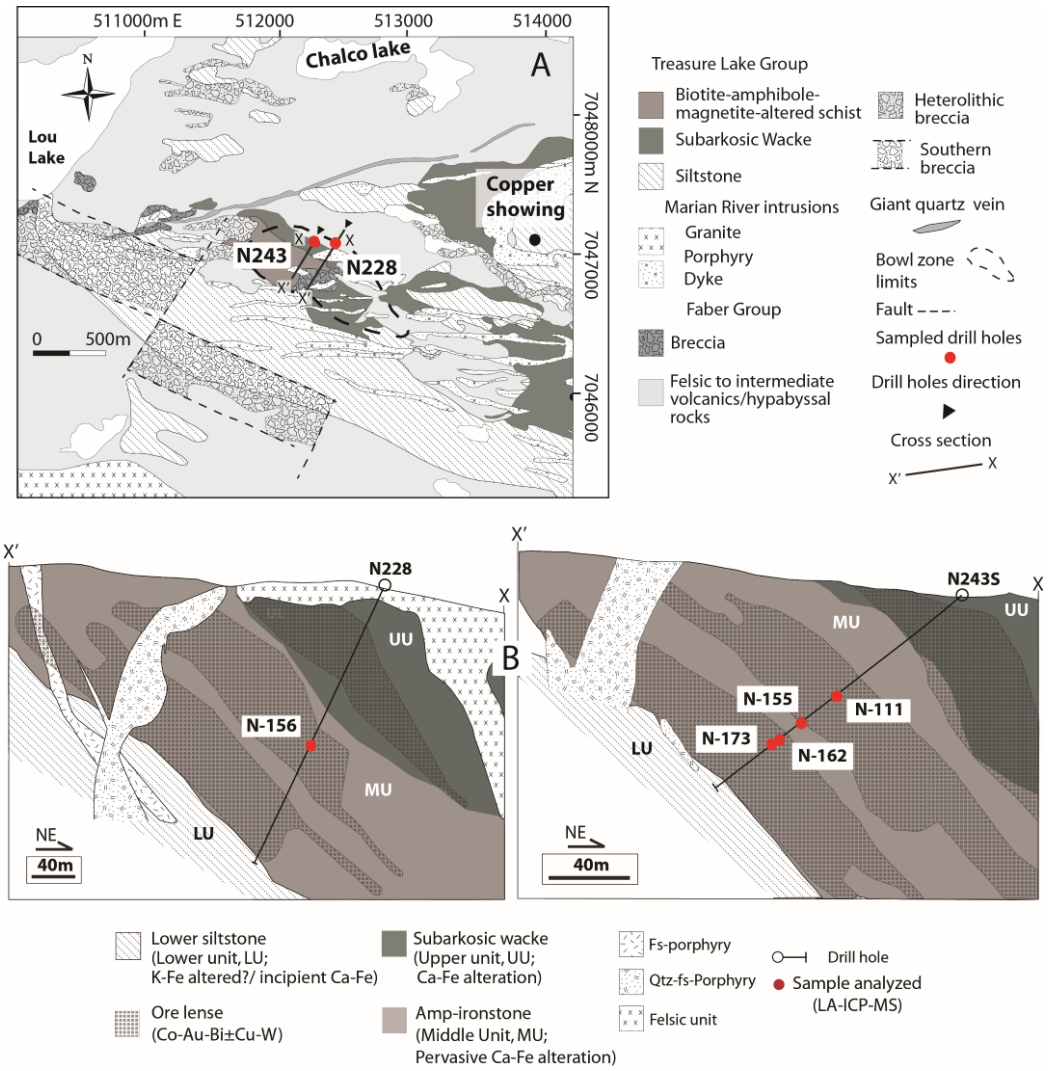

Figure. 3.2. Geology of NICO deposit and location of samples
(A) Geology of NICO deposit after Goad et al. (2000). (B) Amphibole-magnetite-biotite altered rocks of the Middle Treasure Lake Group containing the ore lenses and location of the drill core samples analyzed via LA-ICP-MS in the study.

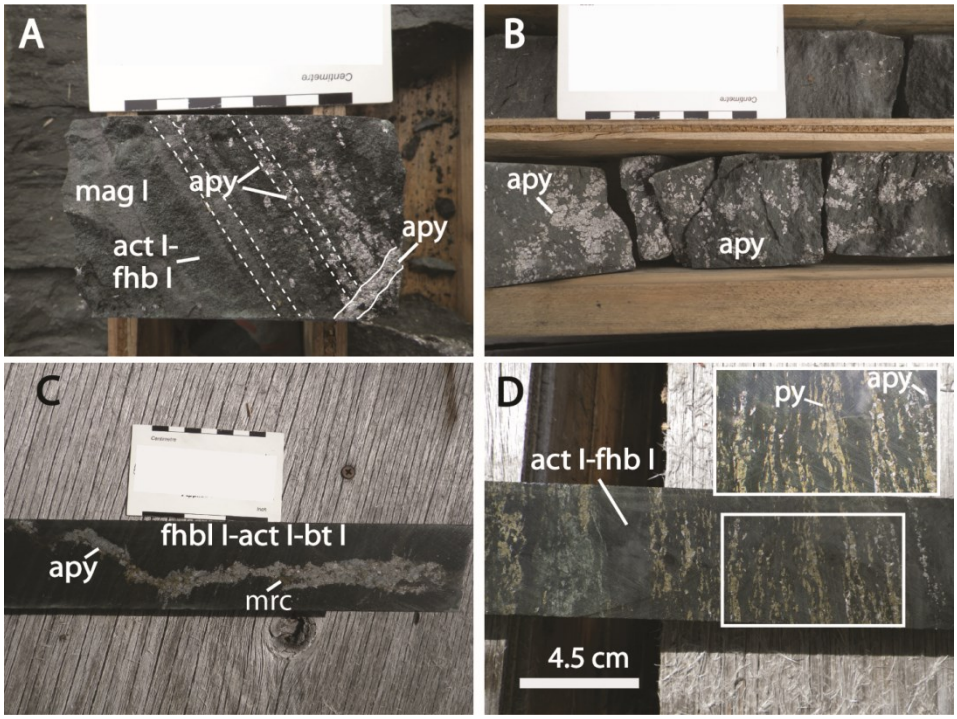

Figure 3.3. Mineralization styles at NICO deposit in the TLG.
A-D correspond with examples of the NICO mineralization hosted by the ferrohornblende (fhbl) I-actinolite (act) I-biotite (bt) I-magnetite (mag) I altered rocks (barren Ca-Fe-K alteration) from the TLG. (A) Vein hosted arsenopyrite (apy; solid line) is disseminated along the bedding (dashed line shows the bedding). (B) Arsenopyrite (apy) randomly disseminated in the host rocks and also as mineralized patches. (C) A centimeter thick arsenopyrite (apy)-pyrite (py)-marcasite (mrc) ± chalcopyrite-scheelite vein. (D) Pyrite (py) and arsenopyrite (apy) emplaced along the bedding, and partially replacing the barren Ca-Fe-K alteration silicates.

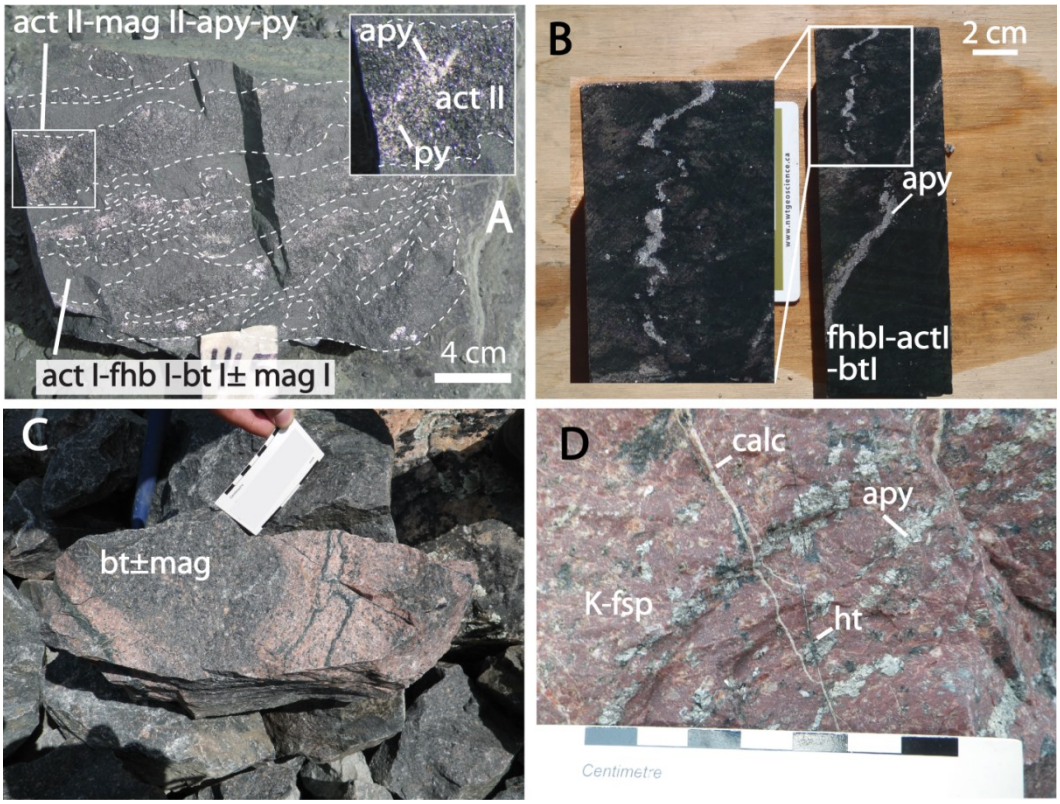

Figure 3.4. Mineralization styles in the TLG and the GBMZ porphyries
(A) Ca-Fe-K altered TLG rocks. Alteration fronts of coarse grained actinolite (act) II-ferrohornblende (fhbl) II- arsenopyrite (apy)-pyrite (py) ± biotite II-mag II alteration, crosscutting the early (barren) and finer grained Ca-Fe-K alteration. (B) Arsenopyrite (apy)-rich veins hosted by Ca-Fe-K altered rocks after ductile deformation. (C) K-altered porphyry overprinted by biotite (bt) alteration. (D) K-altered (k-fsp) porphyry hosting Co-rich arsenopyrite (apy). Late hastingsite (ht) and calcite (calc) veins crosscut the sulfarsenides.

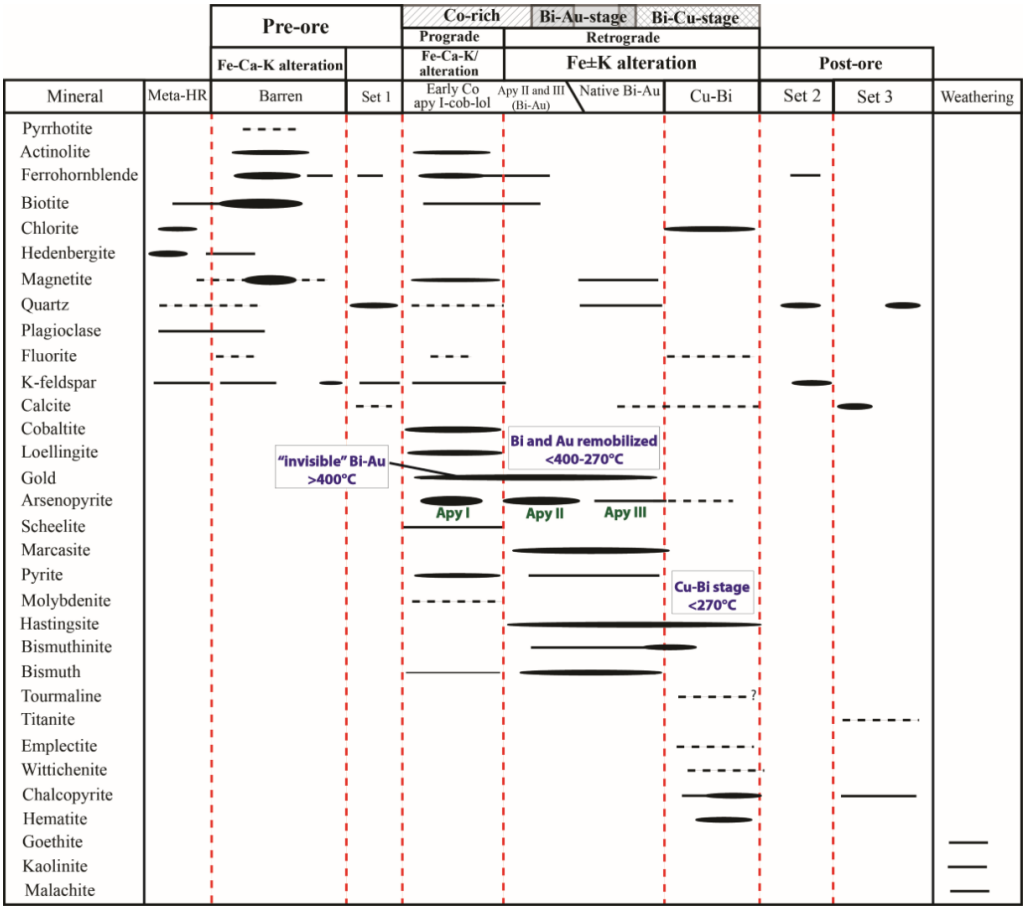

Figure 3.5. Paragenetic sequence interpreted from NICO deposit

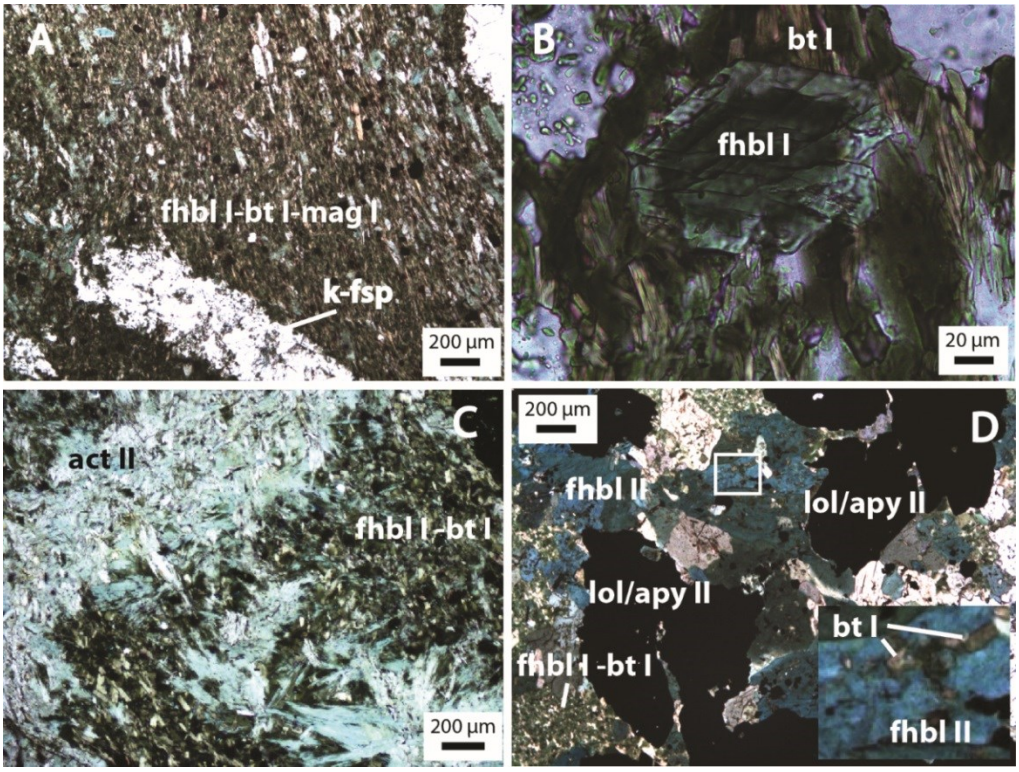

Figure 3.6. Hostrock alteration and gangue minerals
Petrography of the barren and Co-rich Fe-Ca-K alteration stages. (A) Selective replacement of the pre-ore Ca-Fe-K alteration along the bedding or foliation plane. This alteration assemblage consists of dominant fine grained biotite (bt) I-ferrohornblende (fhbl) I ± magnetite (mag I). A relict K-feldspar grain remains and is partially replaced the former minerals. (B) A close up of the fine grained barren Ca-Fe-K alteration phase showing biotite (bt) I and ferrohornblende (fhbl) I. (C) The Ca-Fe-K barren alteration overprinted by coarser grained actinolite (act) II part of the Co-rich Ca-Fe-K alteration type. (D) Co-rich Ca-Fe-K alteration minerals overprinting the barren Ca-Fe-K assemblage. Commonly the sulfarsenides like loellingite (lol) and arsenopyrite (apy) II, and ferrohornblende II have inclusions of the barren Ca-Fe-K alteration minerals (e.g., biotite, bt).

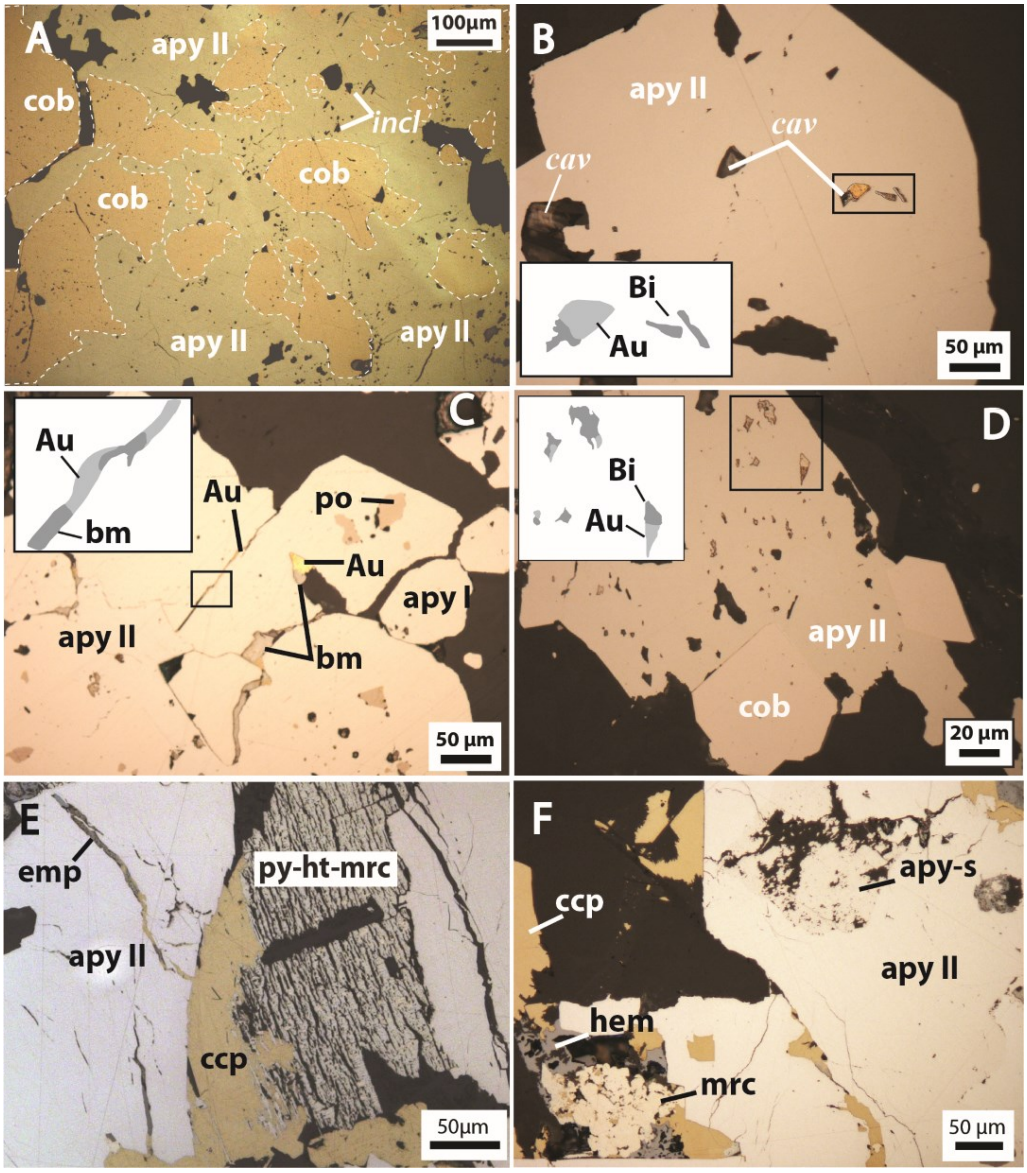

Figure 3.7. Early (Co-rich) mineralization at NICO deposit
(A) Arsenopyrite (apy) II replacing cobaltite (cob) grains. Sulfarsenides incorporate silicate inclusions (*incl*, dark spots) from the barren Ca-Fe-K alteration type during its crystallization. (B) Arsenopyrite II replacing an euhedral grain of arsenopyrite I. Arsenopyrite II contains Au and native Bi inclusions. The Au-Bi inclusion is filling up a cavity (*cav*) within the host grain. (C) Arsenopyrite (apy) II grains with pyrrhotite (po) cores crosscut by bismuthinite (bm)-Au veins. (D) Arsenopyrite (apy) II completely replaced loellingite and is coating cobaltite grains. Arsenopyrite II has abundant native Bi and Au inclusions. (E) Chalcopyrite (ccp) and emplectite (emp) crosscutting arsenopyrite (apy) II and replacing lamellae pyrite (py)-marcasite (mrc)-hastingsite (ht) intergrowths. (F) Arsenopyrite (apy) II containing apy-s (upper right corner) and a marcasite (mrc) aggregate adjacent to the arsenopyrite grains (lower left corner).

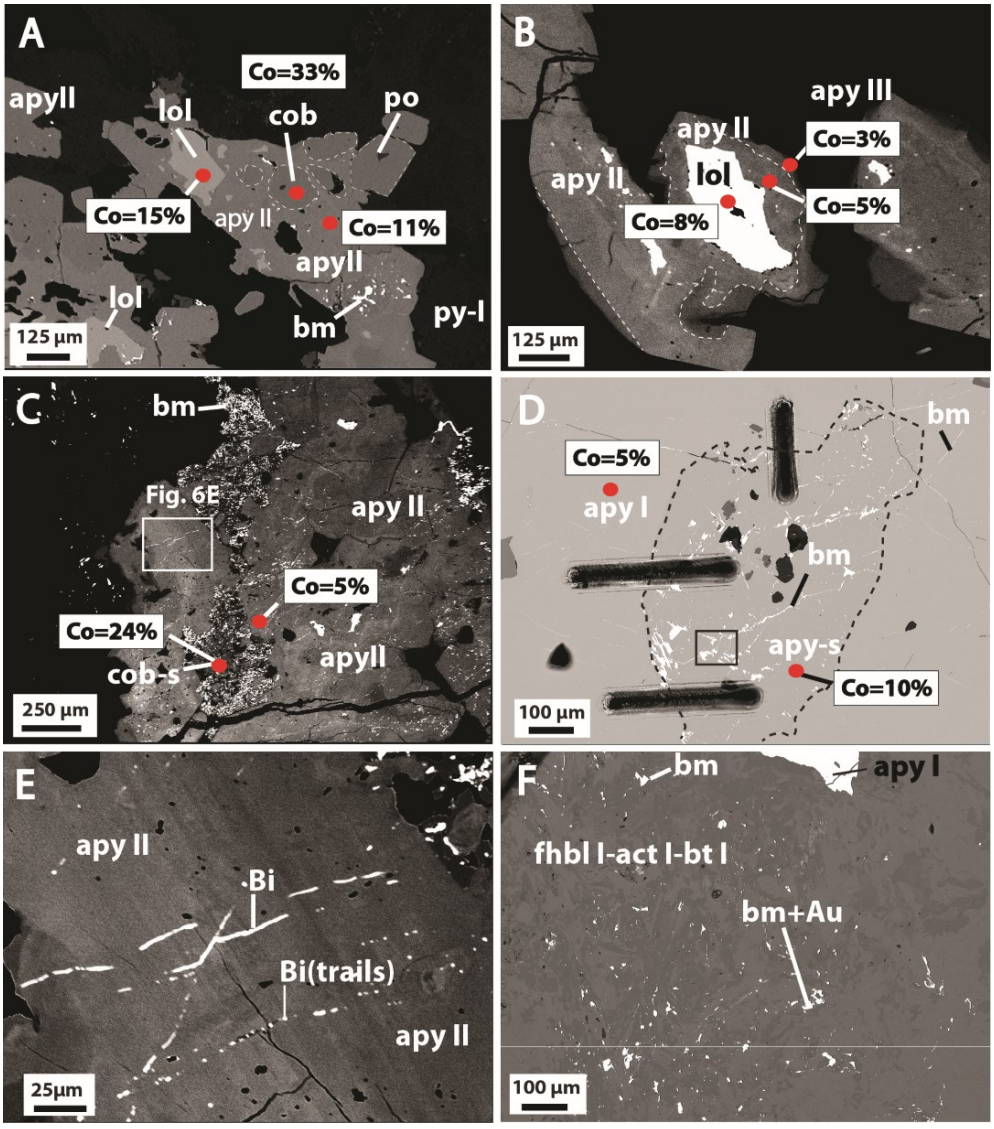

Figure 3.8. Backscattered images of the mineralization at NICO

Backscattered (BSE) images. (A) Arsenopyrite (apy) II replacing loellingite (lol) and partially replacing cobaltite (cob). Loellingite (lol) remnants are distributed in arsenopyrite II grains as inclusions. Cobaltite grains have rounded shapes due to arsenopyrite II alteration. Porous zones of arsenopyrite are filled with bismuthinite (±Au). Cobalt contents (mol. %) of arsenopyrite (apy II), loellingite (lol) and cobaltite (cob) obtained from EMPA analyses are labeled. (B) Arsenopyrite (apy) II with a loellingite (lol) core. A well-defined concentric rim of arsenopyrite (apy) III is recognized at the edge of these grains. The Co contents are depleted from the core to the outer rim. (C) Recrystallized arsenopyrite (apy) II with irregular ('patchy') zoning; darker zones indicate higher amounts of Co. The cob-s alteration fronts go into this grain. Bismuthinite and native bismuth partially replace the cob-s (light color). The white box shows a higher magnification in in Fig. 6E. (D) The Co-rich sieve-textured arsenopyrite (apy-s) contained within a larger Co-bearing arsenopyrite (apy I) grain. Both are crosscut by native Bi microveins. (E) Close up from C. Bi-rich microveins and linear trails of globular shaped Bi crosscutting arsenopyrite. (F) Disseminations and microveins of bismuthinite (bm) and Au overprinting the Ca-Fe-K altered host rocks.

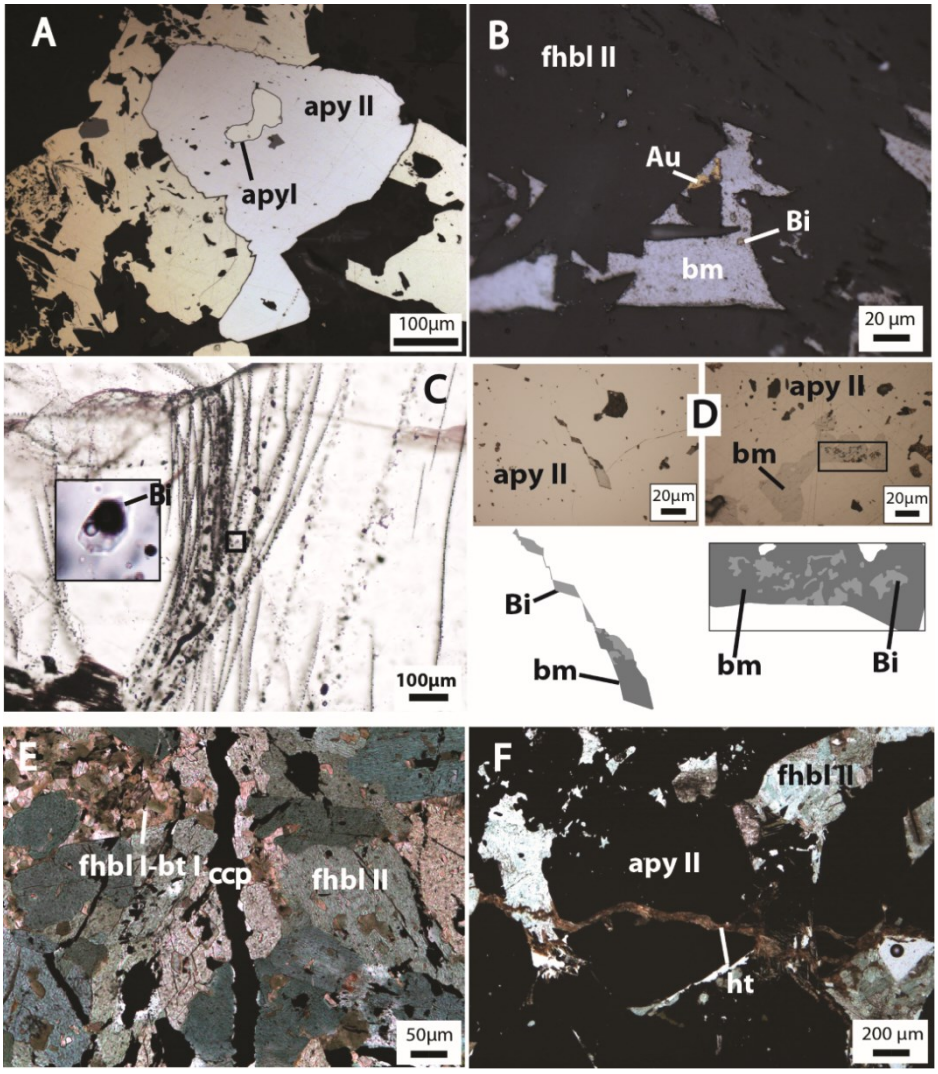

Figure 3.9. Retrograde alteration/mineralization at NICO deposit
(A) Euhedral arsenopyrite (apy I) replaced by late arsenopyrite (apy) II. Massive pyrite (py-m) coats the former grain. (B) Ca-Fe-K alteration with late bismuthinite-gold disseminations. Au and Bi are contained within bismuthinite. (C) Linear and arcuate trails of native bismuth and associated fluid inclusions in quartz (qtz) from the set 1 veins. Native bismuth occurs within two phase fluid inclusions (inset). (D) The left side shows an arsenopyrite grain with a brittle shear and filled up with native Bi and bismuthinite (bm) (sketch). The right side exhibits native Bi almost completely replaced by bismuthinite and is better portrayed by the sketch below. (E) Chalcopyrite micro vein crosscuting earlier ferrohornblende (fhbl) I-II and biotite (bt) I (F) Arsenopyrite (apy) II and ferrohornblende (fhbl) II crosscut and partially replaced by late hastingsite (ht).

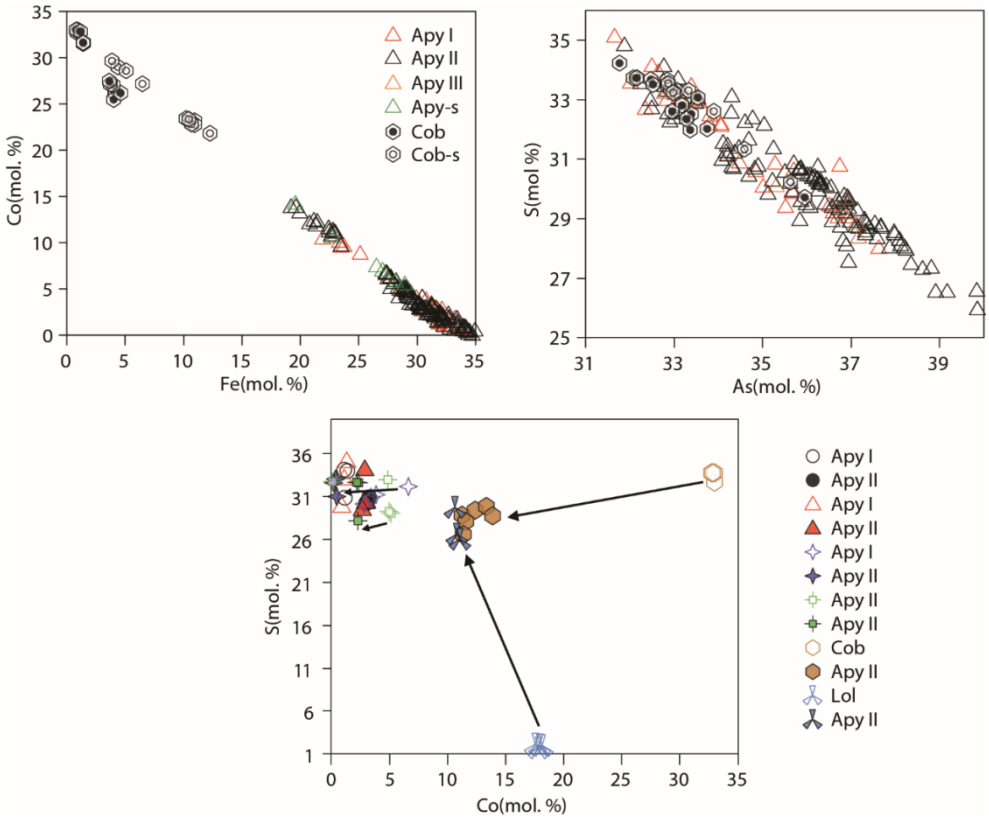

Figure 3.10. Major element chemistry of sulfarsenides and arsenides Major element distributions. (A) The Fe vs Co plot shows an inverse correlation between these two elements in arsenopyrite (apy I, II, III), cobaltite (cob) and loellingite (lol). (B) A similar inverse correlation is also displayed by As and S in arsenopyrite. (C) Selected pairs of sulfarsenides where loellingite (lol), cobaltite (cob) and arsenopyrite (apy) I are replaced by arsenopyrite (apy) II. Arrows go from the original Fe-Co-As-S mineral to the resulting arsenopyrite II.

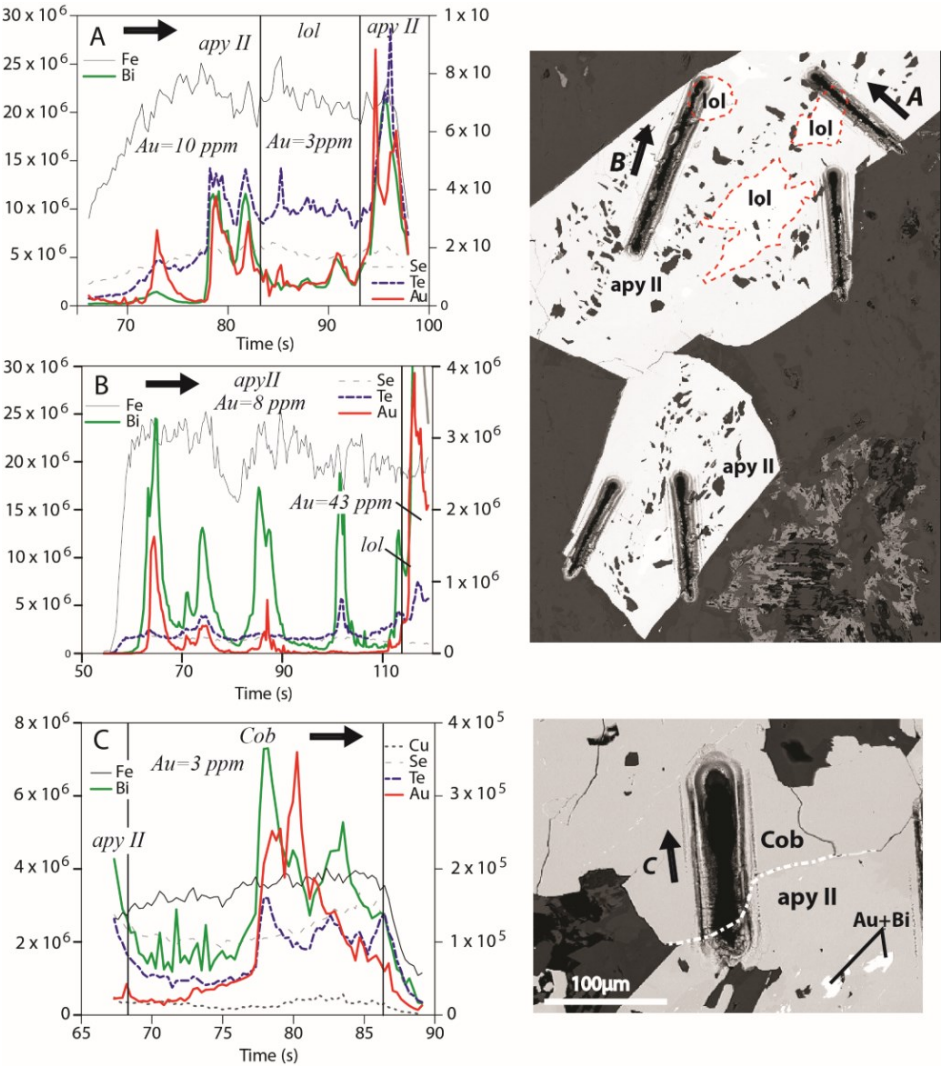

Figure 3.11. Spectra and trace element geochemisty of ore minerals (A) Spectrum of Au and Bi shows these elements occurring as inclusions within arsenopyrite (apy) II and as structurally-bound and invisible inclusions in loellingite (lol). The highest counts per second are recorded at the contact between both mineral phases. (B) Traverse on arsenopyrite (apy) II replacing loellingite (lol). Gold and Bi exhibit analogous trends either in arsenopyrite and loellingite. Higher amounts of gold were obtained as the laser approaches loellingite (Au= 43 ppm). (C) Distribution of Bi, Au and Te in cobaltite (cob), either in solid solution or in invisible nanoparticles have similar trends. The pictures adjacent to the ablation profiles show the analyzed grains. The red and white dashed line shows the contour of the loellingite grains before the analysis, and the boundary between cobaltite and arsenopyrite II.

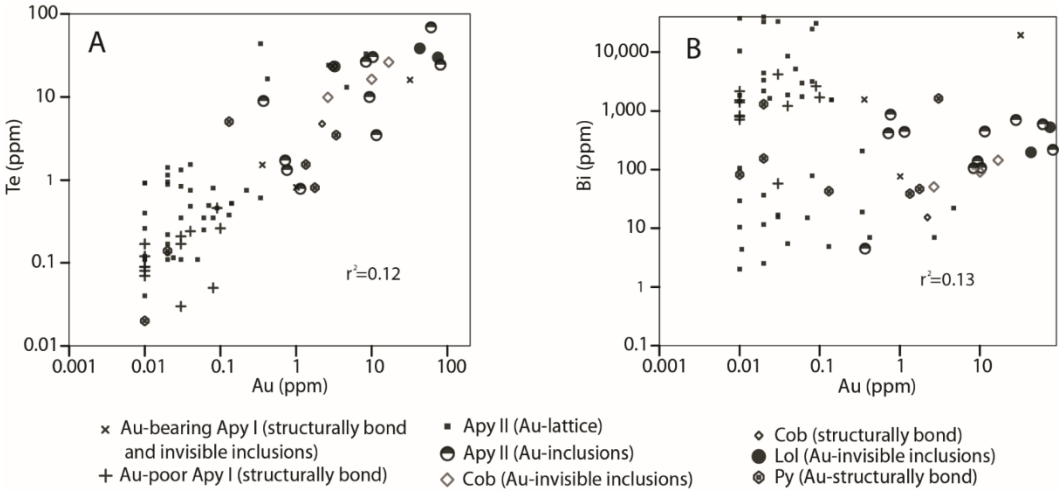

Figure 3.12. Au-Bi-Te plots
(A) Cobaltite, loellingite and Au-inclusion rich arsenopyrite have the highest gold contents (>1 to 91 ppm). Structurally bound gold frequently has values <1 ppm. (B) Despite the analogous trends displayed in Au-rich traverses between Au and Bi, these two elements show no correlation.

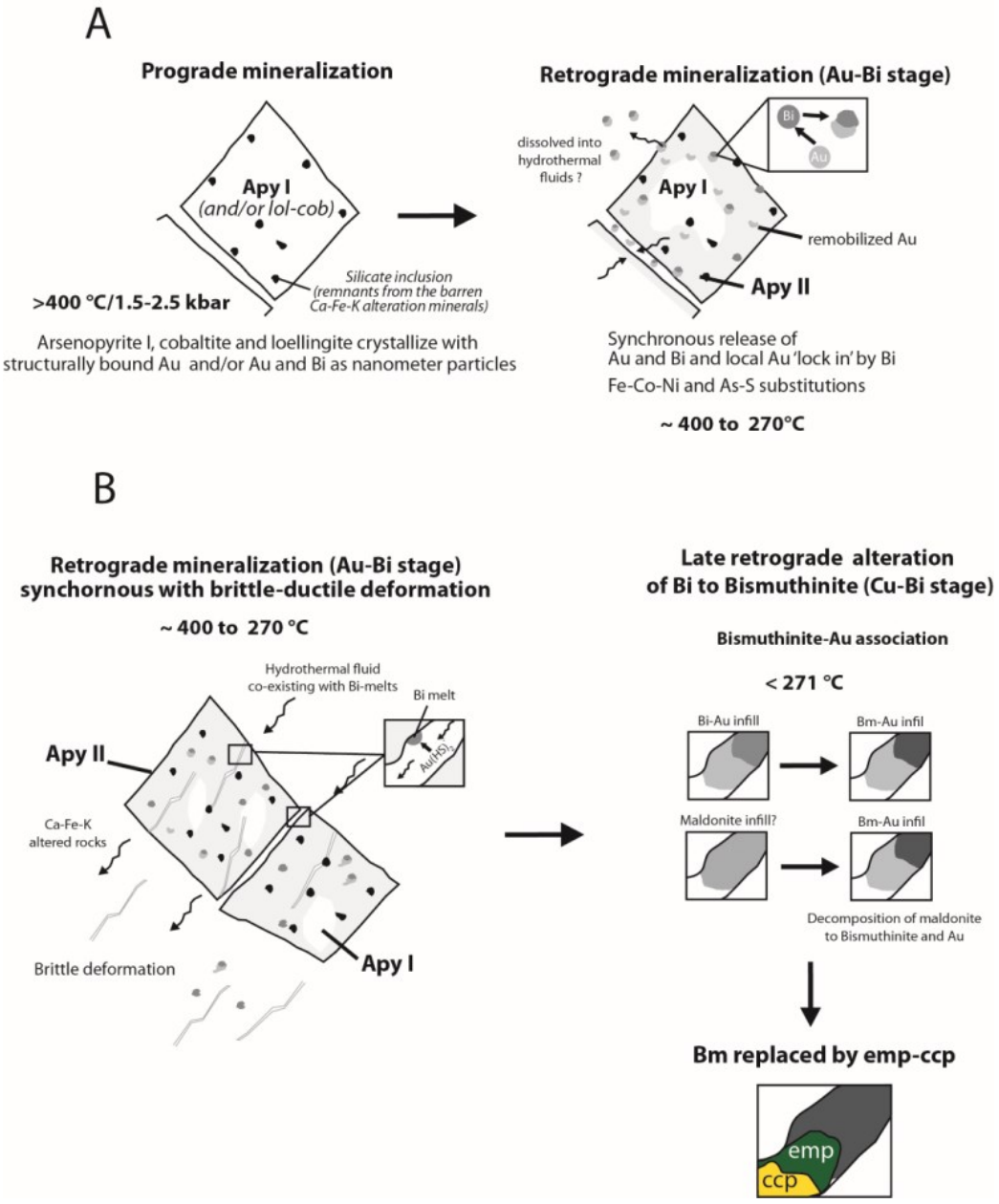

Figure 3.13. Mechanisms of Au refining

(A) Structurally bound Au and nanoparticles of Au ('invisible gold')and Bi are contained by the pro-grade (>400°C /1.5-2.5 kbar) cobaltite (cob), arsenopyrite (apy) I and loellingite (lol). The initial stages of retrograde metasomatism (~400 to 270°C) remobilized the Au and Bi as arsenopyrite (apy) II was formed. Also during this process Fe-Co-Ni substitutions took place and Bi droplets 'locked in' adjacent gold particles. (B) Retrograde metasomatism is contemporaneous with brittle-ductile regimes creating the permeability necessary (fractures) for the deposition of native Bi droplets. These melts fixed Au from the hydrothermal solutions, which resulted in Bi and Au infillings in fractures, intergranular spaces and cavities within arsenopyrite. At later, and lower temperature stages, of the retrograde metasomatism (<270°C) an increase of sulfur fugacity caused the native Bi to be transformed to bismuthinite (bm). On the other hand, the Au-bismuthinite assemblage can also result from the breakdown of maldonite to Au and bismuthinite. The latest mineralization stages probably took place at temperatures much lower than 270°C and comprise the replacement of bismuthinite by emplectite and chalcopyrite.

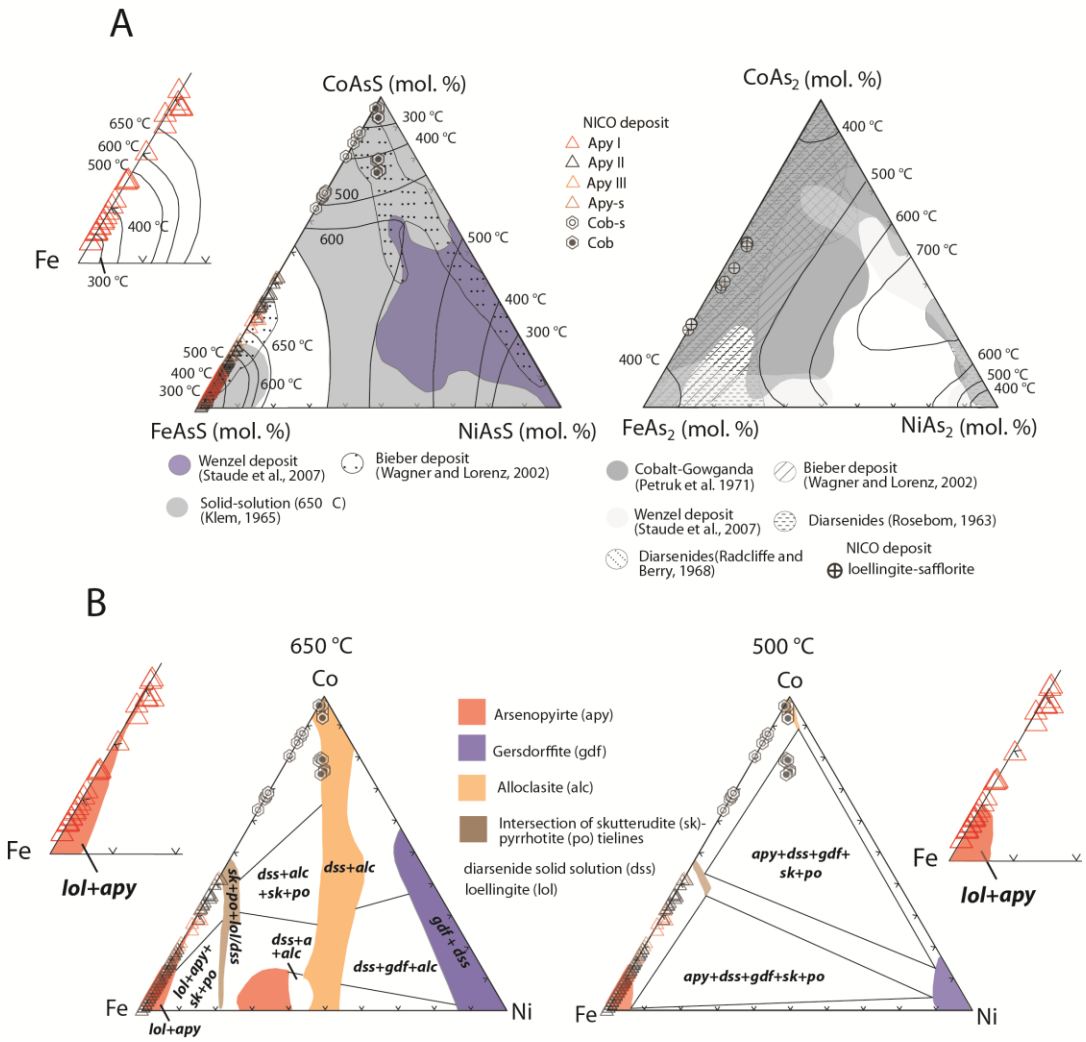

Figure 3.14. Fe-Co-Ni compositions

Fe-Co-Ni compositions. (A) NICO data plotted on Klemm (1965) geothermometers. Data from other deposits also overlap that of NICO. (B) NICO data plotted on the Hem and Mackoviky (2004) stability fields for (Fe, Co, Ni)$As_{1.5}S_{0.5}$ at 500°C and 650°C (data given in apfu).

Table 3.1. Standards and conditions of the EMPA analysis

Standard	Element	Line	Crystal	Counting times (s)	
				Peak	Background
Sphalerite	S	Kα	PET	20	10
Arsenopyrite	As	Lα	TAP	20	10
Bi-metal	Bi	Mα	PETH	20	10
Sb-metal	Sb	Lα	PET	20	10
Pyrite	Fe	Kα	LIFH	20	10
Te-metal	Te	Lα	PET	20	10
Diopside	Si	Kα	TAP	20	10
PbS	Pb	Mα	PETH	20	10
Sn-metal	Sn	Lα	PET	20	10
Co-metal	Co	Kα	LIFH	40	20
Chromite	Cr	Kα	PET	20	10
MoS2	Mo	Lα	PET	20	10
NiAs2	Ni	Kα	LIFH	20	10
Cu-metal	Cu	Kα	LIFH	20	10

Table 3.2. Representative major elements concentrations (mol. %) of the sulfarsenides, arsenides and sulfides.

Sample/*in-situ* analysis	Mineral	S	Fe	As	Bi	Pb	Co	Ni	Empirical formula
N243-111/1	Apy I	28.5	29.1	37.3	<0.2	<0.2	5.1	<0.3	$(Fe_{0.8}, Co_{0.2})As_{1.1}S_{0.9}$
N243-111/3	Apy I	31.7	29.2	34.7	<0.2	<0.2	4.4	<0.3	$(Fe_{0.9}, Co_{0.1})As_{1.0}S_{1.0}$
N243-111/4	Apy II	28.3	33.9	36.8	<0.2	<0.2	1.0	<0.3	$(Fe_{1.0}, Co_{0.0})As_{1.1}S_{0.9}$
N243-111/5	Apy II	33.3	32.2	32.8	<0.2	<0.2	1.7	<0.3	$(Fe_{1.0}, Co_{0.1})As_{1.0}S_{1.0}$
N243-162.3/1	Apy-s	32.1	23.7	34.1	<0.2	<0.2	9.6	0.5	$(Fe_{0.7}, Co_{0.3})As_{1.0}S_{1.0}$
N243-162.3/2	Apy-s	32.2	23.4	34.1	<0.2	<0.2	9.6	0.7	$(Fe_{0.7}, Co_{0.3})As_{1.0}S_{1.0}$
N243-173/1	Apy II	28.8	33.9	36.8	<0.2	<0.2	0.5	0.0	$(Fe_{1.0}, Co_{0.0})As_{1.1}S_{0.9}$
N243-173/2	Apy II	33.0	33.2	33.2	0.4	<0.2	0.6	0.0	$(Fe_{1.0}, Co_{0.0})As_{1.0}S_{1.0}$
N243-173/3	Apy I	29.5	30.2	36.9	<0.2	<0.2	3.5	0.0	$(Fe_{0.9}, Co_{0.1})As_{1.1}S_{0.9}$
N243-173/4	Apy I	29.6	30.1	36.9	<0.2	<0.2	3.4	0.0	$(Fe_{0.9}, Co_{0.1})As_{1.1}S_{0.9}$
N228-156/1	Apy I	29.7	20.8	36.9	<0.2	<0.2	12.1	0.5	$(Fe_{0.6}, Co_{0.4})As_{1.1}S_{0.9}$
N228-156/2	Apy II	28.5	23.5	38.0	<0.2	<0.2	9.7	0.3	$(Fe_{0.7}, Co_{0.3})As_{1.1}S_{0.9}$
N228-156/3	Apy II	28.8	21.3	37.5	<0.2	<0.2	11.9	0.4	$(Fe_{0.6}, Co_{0.4})As_{1.1}S_{0.9}$
N228-156/4	Apy II	28.0	27.5	38.2	<0.2	<0.2	6.2	<0.3	$(Fe_{0.8}, Co_{0.2})As_{1.2}S_{0.8}$
N228-156/5	Lol	2.0	20.2	63.6	<0.2	<0.2	13.3	0.9	$(Fe_{0.6}, Co_{0.4})As_{1.9}S_{0.1}$
N228-156/6	Lol	2.6	19.8	63.4	<0.2	<0.2	13.5	0.7	$(Fe_{0.6}, Co_{0.4})As_{1.9}S_{0.1}$
N228-156/7	Lol	2.6	19.2	63.5	<0.2	<0.2	13.8	0.9	$(Fe_{0.6}, Co_{0.4})As_{1.9}S_{0.1}$
N228-156/8	Lol	2.3	17.6	63.7	<0.2	<0.2	15.3	1.0	$(Fe_{0.5}, Co_{0.5})As_{1.9}S_{0.1}$
N205-88.50/1	Co-s	30.2	11.0	35.6	<0.2	<0.2	23.2	NA	$(Co_{0.7}, Fe_{0.3})As_{1.1}S_{0.9}$
N205-88.50/2	Co-s	33.4	11.0	32.9	<0.2	<0.2	22.8	NA	$(Co_{0.7}, Fe_{0.3})As_{1.0}S_{1.0}$
N228-156/9	Cob	29.7	4.1	35.9	<0.2	<0.2	26.2	4.1	$(Co_{0.8}, Fe_{0.1}, Ni_{0.1})As_{1.1}S_{0.9}$
N228-156/10	Cob	32.0	4.1	33.7	<0.2	<0.2	26.2	3.9	$(Co_{0.8}, Fe_{0.1}, Ni_{0.1})As_{1.0}S_{1.0}$
N228-156/11	Cob	33.1	4.0	33.5	<0.2	<0.2	25.5	3.9	$(Co_{0.8}, Fe_{0.1}, Ni_{0.1})As_{1.0}S_{1.0}$
N228-156/12	Cob	32.0	4.6	33.4	<0.2	<0.2	26.2	3.9	$(Co_{0.8}, Fe_{0.1}, Ni_{0.1})As_{1.0}S_{1.0}$
N243-111/5	Py-m	66.1	33.6	0.2	<0.2	<0.2	0.1	<0.3	$(Fe_{1.0}, Co_{0.0})(S_{2.0}, As_{0.0})$
N243-111/6	Py-m	66.0	33.7	0.3	0.2	<0.2	0.1	<0.3	$(Fe_{1.0}, Co_{0.0})(S_{2.0}, As_{0.0})$
N243-111/7	Py-m	66.2	33.5	0.3	<0.2	<0.2	0.1	<0.3	$(Fe_{1.0}, Co_{0.0})(S_{2.0}, As_{0.0})$
N243-111/8	Py-m	66.1	33.5	0.4	<0.2	<0.2	0.0	<0.3	$(Fe_{1.0}, Co_{0.0})(S_{2.0}, As_{0.0})$

Abbreviations. Cob, cobaltite; lol, loellingite; arsenopyrite, apy; py-m, massive pyrite.
NA, not analyzed

Table 3.3. Trace elements concentrations (ppm) of the sulfides, sulfarsenides and arsenides from NICO deposit. Average major element (*Fe, Co, As, S*) concentrations (mol. %) per sample are given for comparison.

Mineral	Sample/analysis	*Fe*	*Co*	*As*	*S*	Ni	Cu	Se	Ag	Sn	Sb	Te	Pb	Au	Bi	Au occurrence	Comment
Apy I-Au poor	N243-173/A	31.4	2.3	36.0	32.3	510	16.5	81.1	6.5	0.9	244	0.3	2.5	0.1	1691	Au-SB*	Apy randomly disseminated.
Apy I-Au poor	N243-173/B	31.4	2.3	36.0	32.3	712	NG	60.4	5.9	0.4	284	0.5	4.2	0.1	2625	Au-SB*	Apy randomly disseminated
Apy I-Au poor	N243-173/C	31.4	2.3	36.0	32.3	363	21.0	76.5	3.1	1.0	167	0.1	1.4	0.0	1631	Au-SB*	Apy randomly disseminated
Apy I-Au-bearing	N243-111/A	29.6	4.4	36.7	29.3	13009	0.4	290	0.7	0.3	394	16.0	0.8	32.3	19608	Au-SB* and inv-incl	Apy disseminated along the bedding
Apy I-Au-bearing	N243-111/B	29.6	4.4	36.7	29.3	810	9.0	121	0.3	0.4	721	0.8	0.5	1.0	76.8	Au-SB* and inv-incl	Apy disseminated along the bedding
Apy II	N243-162/A	28.2	4.1	37.2	29.1	523	26.5	125	0.2	0.3	246	0.1	0.8	0.0	1138	Au-SB*	Apy vein. Au-structurally bound
Apy II	N243-162/B	28.2	4.1	37.2	29.1	477	2.3	112	0.3	0.3	239	0.0	0.3	0.0	101	Au-SB*	Apy vein. Au-structurally bound
Apy II	N243-162/C	28.2	4.1	37.2	29.1	1007	NG	150	0.7	0.4	624	0.9	2.4	0.0	37602	Au-SB*	Apy vein. Au-structurally bound
Apy II	N243-162/D	28.2	4.1	37.2	29.1	844	2.4	147	0.3	0.4	480	0.3	0.7	0.0	10409	Au-SB*	Apy vein. Au-structurally bound
Apy II	N243-162/E	28.2	4.1	37.2	29.1	535	1.3	107	0.0	0.3	242	0.0	0.2	<0.01	146	Au-SB*	Apy vein. Au-structurally bound
Apy II	N243-162/F	28.2	4.1	37.2	29.1	558	7.1	118	1.0	0.4	260	0.1	0.5	0.0	1845	Au-SB*	Apy vein. Au-structurally bound
Apy II	N228-156/A	22.3	11.0	37.9	28.5	1422	0.3	52.0	0.4	0.2	550	68.8	0.7	61.0	587	Au-v-incl	Apy disseminated along the bedding.
Apy II	N228-156/B	22.3	11.0	37.9	28.5	316	1.1	38.3	0.1	0.2	401	10.0	2.1	9.4	137	Au-v-incl	Apy disseminated along the bedding.
Apy II	N228-156/C	22.3	11.0	37.9	28.5	1093	0.5	57.1	0.1	0.3	622	24.5	0.7	81.2	217	Au-v-incl	Apy disseminated along the bedding.
Apy II	N228-156/D	22.3	11.0	37.9	28.5	387	0.2	38.4	0.0	0.2	354	8.9	0.2	0.4	4.5	Au-v-incl	Apy disseminated along the bedding.

Apy II	N228-156/E	22.3	11.0	37.9	28.5	1479	0.5	51.1	0.1	0.4	567	30.0	1.0	10.3	107	Au-v-incl	Apy disseminated along the bedding.
Apy II	N243-111/B	32.8	1.4	35.5	31.6	347	0.3	95.2	0.1	0.4	571	1.7	0.1	0.7	414	Au-v-incl	Apy disseminated along the bedding.
Apy II	N243-111/C	32.8	1.4	35.5	31.6	410	2.2	107	2.9	1.6	555	3.5	4.2	11.5	445.4	Au-v-incl	Apy disseminated along the bedding.
Apy II	N243-111/D	32.8	1.4	35.5	31.6	1497	1.6	61.3	0.1	0.5	686	26.4	2.6	8.4	105	Au-v-incl	Apy disseminated along the bedding.
Cob	N243-156/A	4.0	26.5	33.4	32.1	36975	1.9	137	0.0	0.3	195	9.9	1.1	2.7	50.9	Au-lattic*	Cob disseminated along the bedding.
Cob	N243-156/B	4.0	26.5	33.4	32.1	18521	0.5	85.1	0.1	1.3	142	4.7	0.4	2.2	15.3	Au-lattice*	Cob disseminated along the bedding.
Cob	N243-111/E	4.0	26.5	33.4	32.1	32569	2.1	125	0.1	0.4	176.7	16.4	1.0	10.0	90.6	Au-inv-incl	Apy disseminated along the bedding.
Lol	N228-156	19.2	13.4	63.5	2.38	1109	1.3	49.9	0.0	0.4	494	29.9	2.1	75.5	527.	Au-inv-incl	Lol disseminated along the bedding.
Lol	N228-156	19.2	13.4	63.5	2.38	2567	0.1	34.4	0.1	0.3	363	38.5	0.7	43.4	197	Au-inv-incl	Lol disseminated along the bedding.
Py-m	N243-155	33.8	0.1	0.1	63.1	309	722	19.9	38.1	0.4	299	<0.18	174	0.0	154	Au-SB	Py disseminated along the bedding.
Py-m	N243-155	33.8	0.1	0.1	63.1	312	11.6	240	3.0	0.5	487	0.8	3.6	1.8	46.8	Au-SB	Py disseminated along the bedding.
Py-m	N243-111/P1	33.5	0.1	0.3	66.1	364	11.1	298	1.9	1.2	619	1.5	2.0	1.3	39.1	Au-SB	Py disseminated along the bedding.
Py-m	N243-111/P2	33.5	0.1	0.3	66.1	4.0	7.6	266	1.4	0.4	2.9	5.1	1.9	0.1	43.1	Au-SB	Py disseminated along the bedding.
Py-m	N243-111	33.5	0.1	0.3	66.1	278	10.2	177	1.7	0.4	297	23.4	3.0	3.1	1627	Au-SB	Py disseminated along the bedding.

Abbreviations. Cob, cobaltite; lol, loellingite ; apy, arsenopyrite; py-m, massive pyrite.
Au-SB*, Au structurally bound and evenly disseminated in the apy grain.
Au-inv-incl, Au occurring as invisible inclusions (<0.1 μm) in the grain..
Au-v-incl, Au occurring as visible inclusions (>2 μm) after re-crystallization.

4 The formation of the Iron-Oxide-Cobalt-Gold-Bismuth NICO deposit, Northwest Territories, Canada: evidence from isotope geochemistry and fluid inclusions

4.1 Introduction

The similarities between iron oxide-dominated polymetallic ore deposits, such as Olympic Dam, La Candelaria, and Ernest Henry, have led to the development of the iron oxide copper-gold (IOCG) ore deposits model (Hitzman et al. 1992; Corriveau, 2007). Despite these similarities, deposits in the IOCG class have many disparate features, such as tectonic setting, metal budgets, salinity sources, mineralization style, fluid source, alteration assemblages, age, and nature of the host rocks (e.g., Oreskes and Einaudi, 1992; Hitzman et al., 1992; Pollard, 2006; Benavides et al., 2007; de Haller and Fontboté, 2009; Richards and Mumin, 2013; Gleeson and Smith, 2012). The Paleoproterozoic Great Bear magmatic zone, in northwest Canada, shares a number of similarities with well-known IOCG deposits in Australia and elsewhere (e.g., Oreskes and Einaudi, 1992; Gandhi, 1994; Skirrow and Walshe 2002; Rusk et al., 2010). Recent studies have characterized the types of alteration and mineralization associated with prospects and advanced exploration projects in the Great Bear magmatic zone (e.g., Sue Dianne, NICO, Contact Lake; Gandhi, 1994; Goad et al., 2000; Corriveau, 2007; Mumin et al., 2007; Potter et al., 2013; Acosta-Góngora et al., in press; Montreuil, et al. 2013). The largest system discovered to date is the Au-Co-Bi (±W-Cu-Mo) NICO deposit that is hosted within heavily altered Treasure Lake Group (TLG) metasedimentary rocks. The extensive amphibole-biotite-magnetite alteration and its association with Co and Bi mineralization resembles other magnetite members of the IOCG family, such as the Au-Cu-Bi Tennant Creek district (Huston et al., 1993; Skirrow, 1993; Skirrow

and Walshe, 2002), the Co-Cu-Au-Bi-Y-REE Idaho Cobalt belt (Slack, 2012) and the Au-Cu-Co-Bi-Te-Ag Guelb deposit (Sakellaris, 2007). At NICO, mapping and geochemical data have been used to suggest that ore deposition was associated with intense metasomatism of the metasedimentary sequence during the emplacement of the Great Bear volcanic arc (Sidor 2000, Goad et al. 2000). This is also supported by U-Pb geochronological dating carried out by Davis et al. (2011). Other key aspects necessary to understand the origin of this deposit, such as sources of metals and ore-forming elements like As and S, the geochemistry of the fluids, and their relationship to tectonic events, have not been fully explored. This study documents the age of the mineralization (Re-Os), stable isotope data ($\delta^{34}S$, $\delta^{13}C$, $\delta^{18}O$), fluid inclusion results, and host-rock geochemical data and provide a genetic model for the formation of the NICO deposit.

4.2 Geological Setting

The Wopmay orogen is a Paleoproterozoic mobile belt that lies on the western margin of the Archean Slave craton in northwest Canada. The Wopmay orogen consists of the Paleoproterozoic Coronation margin in the east, and the 1875 to 1850 Ma Great Bear magmatic zone (GBMZ) and its >1950 to 1890 Ma basement, the Hottah terrane, in the west (Fig. 4.1); Hildebrand et al., 2010a, b; Ootes et al., 2013). The Wopmay fault zone separates the GBMZ and Hottah basement from the Slave craton and the Coronation margin. In the southern GBMZ, the oldest exposed bedrock is the <1885 Ma Treasure Lake Group (TLG) metasedimentary rocks that are unconformably overlain by 1875 to 1850 Ma felsic volcanic rocks and intruded by felsic to intermediate plutons of the GBMZ (Goad et al., 2000; Gandhi et al. 2001; Gandhi and van Breemen, 2005; Bennett and Rivers, 2006; Ootes et al., 2010).

The TLG hosts the NICO IOCG deposit, and therefore a brief overview of this group is necessary. The TLG has been deformed and metamorphosed to upper greenschist to amphibolite facies. Field observations show that the regional metamorphism is synchronous with a steeply-dipping foliation that predates the emplacement of the Great Bear volcanic and plutonic rocks (L. Corriveau and J.F.

Montreuil, pers. comm.). The type section of the TLG (Figs. 4.2, 4.3) is exposed 10 km southeast of the NICO property where it consists of a shallowing upward sequence that is separated into four units, T1-T4 (Fig. 4.2); Gandhi and van Breemen, 2005; Acosta-Góngora, in press; this study). The T1 Lower Siltstone is an approximately one kilometer thick quartzo-feldspathic unit, bedded on a centimeter scale, including weakly to strongly magnetic argillaceous beds. Localized zones of potassic alteration (orthoclase and biotite) are present, and in the upper part of the sequence, incipient amphibole alteration occurs as micro-veins and as individual grains or aggregates disseminated along bedding planes. Near its upper contact, the siltstone is interlayered with carbonate-rich beds, and minor scapolite is preserved. The T2 Carbonate unit overlies T1, is approximately 100 m thick, and has bedding from 0.1 to tens of centimeters thick. Thrust faults are present in this unit, such that the true stratigraphic thickness is not fully constrained. T2 is dominated by marble (calcitic ± dolomitic), but also includes calcareous argillite and calc-silicate beds, and thin, magnetite-amphibole rich layers and elongate lenses (Gandhi and van Breemen, 2005; Fig. 4.4A). Potassic alteration (orthoclase and microcline) locally overprints the bedding, and selective replacement of quartz, orthoclase, and calcite by an assemblage comprising chlorite-epidote-garnet ± tourmaline ± scapolite is common, and is manifested as stratabound alteration zones. The T2 unit pinches out rapidly to the northwest at the NICO deposit, where an amphibole-biotite-magnetite-altered siltstone-argillite subunit occurs at the same stratigraphic level. The top of T2 is interfingered with Quartz arenite unit (T3). T3 is 300 to 500 m thick, and varies from centimeter to >1m beds of moderately to well-sorted quartz arenite to subarkosic wacke. Quartz is the dominant mineral in the clastic portion (55-65 %) along with minor K-feldspar (microcline and orthoclase). T3 grades upward into a zone of thin to thick-bedded T4 Upper siltstone unit, which mainly comprises a biotite-rich, magnetite-bearing argillite, with arkose and carbonate-rich interbeds. Although T4 was previously reported to be >300 m thick, a reconnaissance traverse failed to confirm such a significant thickness, but instead found abundant granitic sills and some quartz arenite exposures in an area.

The GBMZ is exposed along a strike length of 450 x 100 km, where plutons intrude and volcanic rocks overly the Hottah terrane and TLG. The volcanic rocks are assigned to the MacTavish Supergroup and are formally and informally divided into various groups. From oldest to youngest these are the ca. 1875 to 1870 Ma LaBine and Dumas Groups, and the younger Sloan Group in the north (Hoffman and McGlynn, 1977; Hoffman, 1980; Bowring, 1984; Hildebrand et al., 1987; Fig. 4.3). In the south, all volcanic rocks are assigned to the Faber Group, which may include flows temporally equivalent to the LaBine or Sloan Groups (Gandhi et al., 2001). Notably, the LaBine Group hosts the past producing Terra, Norex, Silver Bay, El Dorado, Bonanza, and Contact Lake mines (vein-hosted Ag-Ni-Co-Bi-U-Cu; Fig. 4.1), polymetallic vein prospects (U-Cu-Co-Au-Ag-Bi), and a series of magnetite-apatite bodies (Robinson 1971; Badham 1973, 1975; Hildebrand, 1986; Mumin et al. 2007).

The Faber Group consists of several assemblages of calc-alkaline to shoshonitic rhyolite to andesite flows and pyroclastic units (Gandhi et al., 2001). It is the Faber Group that unconformably overlies the TLG in the southern GBMZ, and both are intruded by a series of calc-alkaline to shoshonitic porphyritic intrusions and felsic plutons (e.g., Gandhi et al., 2001). These intrusions range in age from 1873 ± 2 Ma to 1866 ± 2 Ma (Gandhi et al., 2001; Bennett and Rivers, 2006). Rapakivi-textured granite, emplaced at 1856 +3/-2 Ma, constitutes the youngest magmatic suite in the GBMZ (Gandhi et al., 2001).

The Dumas Group is bimodal and occurs on the east side of the GBMZ, is thought to be equivalent in age to the LaBine Group, and forms a narrow basin that tapers southward (Hildebrand et al., 1987; Jackson and Ootes, 2012). The Sloan Group consists of multiple dacite-rhyodacite-rhyolite flows and ignimbrites with minor mafic volcanic rocks (Hoffman and McGlynn, 1977; Hildebrand et al., 1987). Although defined by relationships in the north of the belt, it is likely that Sloan Group volcanic rocks are variably preserved throughout the GBMZ, for example, a ca. 1862 Ma ignimbrite that overlies the Sue-Dianne IOCG deposit (Gandhi et al., 2001).

4.3 The NICO deposit

4.3.1 Bowl Zone

The NICO Au-Co-Bi±Cu-W deposit (Fig. 4.6) is currently the most significant mineralized discovery in the region, with reserves of 33 Mt grading 1.02 g/t Au, 0.112 % Co, 0.14 % Bi, and 0.04 % Cu (Puritch et al., 2012). The bulk of the mineralization at NICO is within the Bowl Zone and is hosted in stratabound ore lenses in the T2 unit of the TLG, below an unconformity with the overlying Faber Group volcanic rocks (Fig. 4.6; middle unit of Sidor, 2000). Minor mineralization also occurs at the unconformity with potassic altered porphyries, and overlying rhyolites of the Faber Group. The middle unit is laminated on the millimeter-scale, with rare centimeter-thick layers, but underwent considerable Ca-Fe-K alteration prior to mineralization (Fig. 4.4B). This alteration is stratabound and consists of veins, massive-replacements, or breccia cements composed of Ca-Fe amphibole (actinolite I, ferrohornblende I), green brown biotite I, and magnetite I ± orthoclase-hedenbergite-plagioclase (Fig. 4.4B); Sidor, 2000; Acosta-Góngora et al., in press). Due to the pervasive Ca-Fe amphibole-magnetite alteration assemblage, these rocks are commonly referred to as ironstones. The alteration is crosscut by quartz ± ferrohornblende-orhoclase-calcite veins (S1), which also precede ore deposition (Acosta-Góngora et al., in revision; Figs. 4.4C-E). Feldspar (plagioclase-perthite) ± quartz-amphibole porphyries intruded the TLG, mainly on the east side of the deposit, and are moderately to pervasively K-altered in the Bowl Zone (Figs. 4.5A, B). Like the unconformity, the porphyries contain minor amounts of mineralization (Fig. 4.5B; Acosta-Góngora et al., in revision). Uranium-lead zircon geochronology of two sub-volcanic porphyries, one hosting mineralization and the other crosscutting the ore lenses, constrain the timing of mineralization to ~1870 Ma (Davis et al., 2011).

The mineralization is divided in prograde and retrograde assemblages (Sidor, 2000; Acosta-Góngora et al., in revision). The prograde assemblage consists of locally Au-bearing cobaltite, Co-rich loellingite, Co-rich arsenopyrite

I, magnetite II, ferrohornblende II, actinolite II, green brown biotite II, and minor, scheelite, quartz and orthoclase. Molybdenite is scarce and localized within the NICO system, although, textural relationships suggests that this sulfide pre-dates the retrograde assemblage. The retrograde assemblage occurs mostly as replacement textures and microveins that crosscut the Co-rich Ca-Fe- K altered host rocks, the S1 veins, and the prograde mineralization. The retrograde mineral assemblage consists of stages II and III arsenopyrite, with variable amounts of Co. This occurs along with marcasite-pyrite-magnetite-hastingsite intergrowths, native Bi and Au, along with magnetite, bismuthinite, and quartz. Some of the arsenopyrite-bearing veins are ductily deformed (Acosta-Góngora et al., in revision). The last retrograde stage comprises a chalcopyrite-bismuthinite-hematite-hastingsite-chlorite ± emplectite-whittichenite assemblage. Fine-grained centimeter-thick quartz ± amphibole-feldspar veins (S2) (Fig. 4.5C) crosscut the retrograde mineralization. Coarse-grained epithermal veins (S3) of quartz ± potassic feldspar-calcite-dolomite ± chalcopyrite also post-date mineralization. S3 crosscut the ironstones (Fig. 4.5D), and the altered porphyries and overlying volcanic rocks. A lack of crosscutting relationships between S2 and S3 limits the determination of a conclusive paragenetic relationships between them.

4.3.2 Southern Breccia

Mapping has demonstrated that the NICO system extends south of the Bowl Zone into the "Southern Breccia zone", a 3 x 0.5 km breccia with localized U ± Cu-Mo mineralization (Corriveau et al., 2011, Montreuil et al., accepted; Fig. 4.6). The uraninite ± molybdenite-chalcopyrite assemblage is contained in the magnetite-K-feldspar ± biotite-cement of brecciated albite-rich host rocks. The breccia is a result of post-metamorphic brittle-ductile deformation, similar to deformation of arsenopyrite-rich veins in the Bowl Zone (Acosta-Góngora et al., in revision). Overall, this demonstrates that a post-mineralization deformation event affected the NICO system (Acosta-Góngora et al., in revision).

4.4 Analytical Techniques

4.4.1 Bulk Rock geochemistry

Major and trace element analyses were carried out on least-altered TLG samples from the type section. All the analytical work was done by Activation Laboratories, Canada. The major elements were determined by X-ray fluorescence (XRF) on a Panalytical Axios Advanced wavelength dispersive XRF. The concentrations of the elements of interest such as As, Bi, Co, Cu, Cr, Ni and Ag, were obtained by using ICP-MS and ICP-OES methods. A sodium peroxide fused blank was run in triplicate for every 22 samples, duplicates were run every 10 samples, and the instrument was recalibrated every 44 samples. Every 10^{th} sample was analyzed in duplicate and a blank was run every 30 samples. Au was determined by instrumental neutron activation analysis (INAA). For both methods, XRF and INAA the analytical precision is 5 % (or better), except for elements with low concentrations which may have higher errors.

4.4.2 X-ray diffraction

X-ray diffraction (XRD) of magnetite, quartz, and bulk rock was conducted at the University of Alberta, using a Rigaku Ultima IV instrument. In the case of quartz and magnetite, the XRD analyses were performed to ensure the purity of the mineral separates for subsequent oxygen stable isotopes studies. The bulk rocks were subject to XRD analysis to determine the presence of sulfur bearing phases on the TLG rocks not recognized via petrographic studies. Diffraction patterns were matched to specific minerals using the Joint Committee on Powder Diffraction Standards (JCPDS) database published by the International Center for Diffraction Data (ICDD).

4.4.3 Fluid inclusions

Fluid inclusions were analyzed using an Olympus BX50 microscope and a Linkham THMSG600 microthermometric stage at the Fluid Inclusion Laboratory at the University of Alberta. Fluid inclusions were cooled to -134°C, and phase changes were recorded upon reheating until the total homogenization temperature (Th) was reached. Sequential freezing (Haynes, 1985) was used to determine the

presence of Cl-bearing phases and salinity concentrations. Calibration was carried out before and after the study using pure CO_2 and H_2O standards. Temperature measurement precision is estimated to be ± 0.1°C below 0°C, ± 1°C between 0° and 300°C, and ± 2°C at higher temperatures.

4.4.4 Stable isotopes

Sulfur: Sulfur isotope compositons ($\delta^{34}S_{V\text{-}CDT}$) were determined from sulfide minerals exposed in ~2 mm thick polished rock slabs. Analyses were undertaken at the Geological Survey of Canada, Ottawa, in the Light Stable Isotope Laboratory, using an in situ fluorination micro laser extraction technique (MILES; Beaudoin and Taylor, 1994; Taylor, 2004). Each sample was degassed overnight at ~80ºC in the sample chamber. The purified SF_6 gas was collected and sealed in a 0.25-in OD Pyrex® tube for offline isotopic analysis using the microvolume inlet of a Finnigan MAT 252 mass spectrometer. The reaction pits created by the micro laser have a width between 100 and 130 μm. Measurement precision is 0.1‰. The $\delta^{34}S_{VCDT}$ values were determined on powdered whole rock samples at the Isotope Science Laboratory of the University of Calgary via Elemental Analysis Isotopic Ratio Mass Spectrometry (EA-IRMS). Measurement precision was 0.3‰.

Oxygen and Carbon: Oxygen isotope compositions ($\delta^{18}O_{V\text{-}SMOW}$) were determined from magnetite separates at the University of Alberta, and from quartz and calcite separates at Queen's University Facility for Isotopic research (QFIR). Results were calibrated using the NBS-28 standard. Measurement accuracy is reported at ± 0.1‰. The carbon isotopic composition ($\delta^{13}C_{VPDB}$) of calcite separates was determined at QFIR. Results are reported at ± 0.1‰.

4.4.5 Re-Os dating

Two molybdenite-bearing samples from the Bowl Zone and the Southern Breccia were selected for Re^{187}-Os^{187} dating (as per Stein et al., 2001). The samples were crushed in a ceramic shatterbox and a molybdenite separate was prepared by gravity separation methods. Approximately 20-30 mg of molybdenite was produced from each sample, and the ^{187}Re and ^{187}Os concentrations in

aliquots of molybdenite from these separates were determined by isotope dilution mass spectrometry at the University of Alberta Radiogenic Isotope Facility, Alberta, using the analytical protocol of Selby and Creaser (2001a, b, 2004). The decay constant used for ^{187}Re was 1.666×10^{-11} $year^{-1}$ (Smoliar et al., 1996). All uncertainties are reported at 2σ levels, and model ages include an uncertainty of 0.31% in the value of the decay constant (λ) for ^{187}Re.

4.5 Results

4.5.1 Major and trace element compositions of the TLG

Fifteen samples of least-altered outcrop samples from the TLG type section were analyzed for major and trace elements (Table 4.1). Only elements relevant to this contribution are discussed below and presented in Table 4.1. Iron concentrations range from 4-10% in the T1 lower siltstone, 2-9% in the T2 carbonate, 2-3% in the T3 quartz arenite, and 3-15% in the T4 upper siltstone. The Ca contents are high for T2 (17%) and lower (<4%) in T1, T3, and T4. Silicon has by far the highest concentrations in T3 (up to 39%).

As the NICO deposit contains significant concentration of Co, S, Bi, As, Au, Cu, these elements are relevant to this study, and are generally low in the least-altered background rocks from the type section (Table 4.1). In particular, Bi in all the samples is below the detection limits. Only 6 samples have detectable gold contents (5 to 7 ppb; Table 4.1). All Co and most Cu values are <20 ppm, except for two samples from T4 (>30 ppm) (Table 4.1). Arsenic concentrations range from <5 to 36 ppm, with one outlier at 95 ppm (Table 4.1). Sulfur concentrations are variable, and range from <0.01 to 1900 ppm. The T2 Carbonate unit is the most enriched in S, with an average of 1310 ppm, whereas the most depleted is the T3 quartz arenite unit (150 ppm), with some values <100 ppm. There is a positive correlation between the Ca and the S concentrations in T2 and an inverse correlation between S and Si (Figs. 4.7A, B).

4.5.2 Stable isotopes

A total of 85 sulfur isotope analyses using the MILES technique were carried out on 12 sulfide-rich samples from the ore lenses in the Bowl Zone. Two

of these samples (NC-1 and NC-42) were collected from waste material close to the Discovery showing road. The $\delta^{34}S$ values of the NICO sulfides range from -3 to 11‰ (mode at ~5‰), with no consistent relationship between $\delta^{34}S$ and location or depth in the deposit (Figs. 4.8A, 4.9A-D; Table 4.2). Petrographic studies demonstrate that arsenopyrite I grains were re-crystallized to form arsenopyrite II and III, and that these newly formed arsenopyrite grains form micrometer irregular zones (30-60 μm) and concentric rims (3-10 μm wide; Acosta-Góngora et al., in revision) (Fig. 4.8B). Due to the relatively large beam diameter used during MILES analyses (~115 μm), individual paragenetic stages for arsenopyrite were not resolved. The latter means that the individual $\delta^{34}S$ values given in this study represent a mixture between arsenopyrite I, II and III. These bulk results indicate that most of the arsenopyrite grains have $\delta^{34}S$ near 5‰, and the variation within a single sample is usually <2‰ (Figs. 4.9A-E). Porphyry-hosted arsenopyrite has the lowest (-3‰) and highest (11‰) $\delta^{34}S$ values of the entire suite analyzed (NC-1 and NC-42; Table 4.2). In NC-1, $\delta^{34}S$ values vary from -3 to 6‰, whereas NC-42 has a relatively homogenous arsenopyrite signature at ~5‰, with one outlier at 11‰. Pyrite and chalcopyrite have a narrower range of isotopic compositions, varying from 4 to 6‰ (Fig. 4.9, Table 4.2) with a mode at 4‰. Whole rock $\delta^{34}S$ analysis only yielded data for 3 samples from the T1 lower siltstone unit, which ranged from -2 to 6‰ (Table 4.2; Fig. 4.8A). Samples of the T2 carbonate were analyzed, but failed to yield any data, likely because the S in the sample resides in scapolite, consistent with correlation between Ca and S in these samples (Fig. 4.7A).

The oxygen isotopic compositions were determined for quartz mineral separates from the pre-ore S1 and the post-mineralization S2 and S3 vein sets, for magnetite from the barren and Co-rich (vein-hosted arsenopyrite) Ca-Fe-K alteration, and for three calcite grains, one from an S1 vein and two from S3 veins (Table 4.2). The $\delta^{18}O$ values from the quartz in S1 and S2 range in composition from 10 to 13‰, with one outlier at 19‰ (Fig. 4.10B). Quartz in the coarse quartz-calcite S3 veins have $\delta^{18}O$ values from 9 to 17‰ (Fig. 4.10B; Table 4.2). Magnetite $\delta^{18}O$ values have a narrow range from -0.9 to 2‰. The barren Ca-Fe ±

K alteration-hosted magnetite varies from -0.5 to 1‰, and similar values were obtained from vein-hosted magnetite (-0.9 to 2‰; Fig. 4.10A). Calcite from S1 has a $\delta^{13}C$ value of -4‰ and a $\delta^{18}O$ value of 11 ‰. The calcite from the S3 veins have $\delta^{13}C$ values of -6 and -15.5‰ and $\delta^{18}O$ values of 13 and 9‰, where the former calcite grains are from veins hosted by the amphibolitic ironstones and the latter by K-altered feldspar porphyry (Fig. 4.10C).

4.5.3 Fluid inclusions

A total of 175 fluid inclusions from nine samples from vein sets S1, S2, and S3 were analysed. All but the coarse grained S3 vein sample were from drill core. The S3 sample is from debris material close to the Discovery showing. Most of these were quartz-hosted, but a lesser number of calcite-hosted inclusions were analyzed. In general, there was a lack of fluid inclusion-bearing gangue minerals that are clearly co-precipitated with the ore minerals, there were limited examples of clearly primary fluid inclusions, and the inclusions identified and analyzed have complex compositions and physical properties (see descriptions below).

The measured inclusions ranged in size from 5 to 15 μm, with rare inclusions up to 35 μm in diameter. Fluid inclusion assemblages (FIA) were characterized and classified according to their origin as primary, secondary or pseudosecondary (Roedder, 1984, Goldstein, 2003). Primary inclusions occur within re-crystallization zones around quartz grains (Figs. 4.11B, C). Pseudosecondary inclusions were trapped in trails or bands terminated at a growth zone (Fig. 4.11A, B; 4.12A). Secondary inclusions occur along trails crosscutting two or more grains (Fig. 4.11A). Inclusions that do not occur along healed fractures (trails) nor in growth zones, are classified as “unknown” in origin. They occur as clusters within the host grain (Fig. 4.11D), are not contained in growth zones, and/or associated trails as expected for primary, pseudosecondary and secondary inclusions.

Vein set S1: Fluid inclusions measured in these vein set were classified as primary, pseudosecondary, secondary and unknown. The section describes the FIA from the oldest to youngest fluid inclusions in the samples.

Pseudosecondary and secondary: The oldest fluid inclusions in these veins are hosted by quartz and the FIA are trapped in pseudosecondary trails that terminate at growth zones, and also in secondary linear arrangements contained in host grains and terminated at grainn boundaries. The FIA comprise liquid-vapor inclusions (LV-C), which have a dark appearance, and constant L/V ratios, where the vapor phase occupies a 15 vol%. of the host inclusions. These inclusions are CO_2-rich (solid CO_2 melts at -56.6) and the temperature of homogenization of the CO_2 phase (Th_{CO2}) ranges between 30 and 31ºC (Table 4.3). The formation of ice was not observed in these inclusions.

Liquid-vapor-solid inclusions (LVS) occur as separate bands and/or trails. These inclusions are never trapped with the LV-C inclusions and the relative timing between the two inclusion types is not known. LVS inclusions with a single solid are labeled as LVS-1. Those with two or more solids are classified as LVS-2 (Fig. 4.12A). The solids have cubic and/or rounded to elongated shape and are white to greenish in colour. Inclusions from LVS-1 FIA have vapor and solid phases occupying a 5-10 vol. % and 6-10 vol. % of the inclusions, respectively. The vol. % occupied by the vapor phase in a single LVS-2 FIA was constant, but varied between 5 to15 vol. % between different FIA. The vol. % occupied by the solid phases is more variable within assemblages, e.g., in a single assemblage the vol.% of the solids could vary from 10 to 30 vol. %. Occasionally, in the same assemblage LVS-1 and LVS-2 co-exist.

It was noticed that upon freezing that some of these inclusions form brown solids (possibly antarcticite; e.g. Shepherd, 1985; Molnár et al., 1999). Homogenization of the vapor and liquid phases ($T_{l\text{-}v}$) occurred in the ranges 148-224ºC (LVS-1) and 182-228ºC (LVS-2) (Table 4.3). The LVS (-1 and -2) inclusions commonly stretcted and/or leaked after reaching $T_{l\text{-}v}$. The stretching was recognized as a sudden increase of the vol. % of the vapor phase (up to 3 times its original size) as the inclusion approached the total homogenization temperature (Th). In some cases, the development of fractures around the inclusion during the analyses was also observed. The volume change or partial decrepitation of these inclusions occurred between 191 and 350 ºC, such that solid

(halite) dissolution (Tm_h) (i.e., *Th)* was only recorded in a few inclusions (Fig. 4.13A). In these inclusions, salinities were calculated using Tm_h and the solubility of halite using the equations of Sterner et al. (1988). Salinities of LVS-1 inclusions range from 37 to 40 wt. % NaCl equiv., and those of LVS-2 are >32 wt. % NaCl equiv. (Fig. 4.13C).

"Unknown" inclusions: These are the least common type of inclusion and are single phase carbonic inclusions (L-C). Some of these nucleated a vapor phase upon freezing. All these inclusions formed solid CO_2, which melted upon heating at -56.9ºC. Where a vapor phase nucleated, the Tm_{CO2} homogenization occurred in the range between -21.1 and -11.7ºC. Ice formation was not observed.

Overgrowth Primary inclusions: Grains hosting LV-C, LVS (-1 and -2) and L-C inclusions have re-crystallized rims that host primary inclusions (to that growth phase). These primary inclusions have only one visible phase interpreted to be a liquid (L) (Figs. 4.11B, C). These inclusions did not freeze or change in appearance upon cooling to -134°C, suggesting that they may contain low melting point volatiles e.g., N_2, or CH_4.

Secondary inclusions: Trails and/or, less commonly, bands of globular shaped native Bi crosscut quartz hosting L, L-C, LV-C and LVS-1 and -2 FIA (Fig. 4.11A). In some cases the Bi trails contain fluid inclusions, and occasionally these inclusions contain native Bi. These inclusions can be sub-classified on the basis of their visible phases. Inclusions with visible LV phases are referred as LV-Bi (Fig. 4.12B), and those containing LVS phases are classified as LVS-Bi (Figs. 4.12C, D). Within LVS-Bi inclusions, two subdivisions are made depending on the number of solids present: LVS-Bi-1 (single solid) and LVS-Bi-2 (multisolids) (Figs. 4.12C, D). In some cases, the FIA from both, the LV-Bi and LVS-Bi, contain very small (<8 μm) inclusions, so that only one or two measurements (inclusions >10 μm) per FIA were done. Another important constraint for the microthermometric analysis of these inclusions is the elevated vol. % (up to 60 vol.% in times), occupied by the Bi solid in the inclusions, so it can could mask the presence of other vapor and/or solid phases (see description below).

The LV-Bi FIA have constant L/V ratios where the vapor phase occupies 5 to 10 vol. % of the inclusion. When present, the size of the native Bi solids can be highly variable and can occupy between 10 to 60 vol. % of the host inclusion. The LV-Bi inclusions freeze to form ice and hydrates with a brown and green (Table 4.3) appearance. Upon heating, first melting temperatures (*T*e) vary between -85 and -56 ºC. When recognized, the brown hydrate phase (possibly antarcticite) melts at temperatures between -61 and -45°C. A high relief transparent to bright green hydrate interpreted to be hydrohalite (e.g., Shepherd et al., 1985), was occasionally recognized in these inclusions and had higher final melting temperatures (Tm_{hh}) varying between -47 and 12°C. The LV-Bi inclusions have final ice melting (Tm_i) temperatures that range from -41 to -7 ºC (Fig. 4.13D). The large deviations from the expected final melting temperatures for antarcticite and hydrohalite (Tm_{ant} = -49.8 and Tm_{hh} = -21.1°C) limits our capacity to calculate their salinity values and suggest the presence of complex brines containing significant amounts of other Li-Mg-Fe-Bi chloride phases (Shepherd et al., 1985). No CO_2 or clathrate formation was observed in these inclusions. The *T*h of these inclusions range from 137 to 216°C (Fig. 4.13D). In occasions, the LV-Bi will contain two bismuth solids, and it was noticed that at 271.3°C the Bi solids melted and re-combine in a single solid phase. Equations from Steele-MacInnis et al. (2011) were used to calculate the salinity where possible and total salinity (S_T) ranges from 17-27% (wt.% NaCl equiv + wt.% $CaCl_2$ equiv). The wt. % NaCl equiv and wt.% $CaCl_2$ equiv values are 0.4 to 10 and 8 to 22, respectively (Figs. 4.13B, C). The former equations do not allow salinity to be calculated for inclusions with metastable hydrohalite (Tm_{hh}> 0°C). A single LV-Bi FIA did not freeze or change in appearance upon cooling and has a very low range in homogenization temperatures of 98-122ºC (Fig. 4.13A).

The LVS-Bi-1 and -2 inclusions have uniform L/V ratios (vapor phase occupies 5-8 vol.% of the inclusion). Nevertheless, in some cases the vol. % of solids within the inclusions of the same assemblage varies up to 10%. Usually, LVS-Bi-1 and -2 co-exist in the same assemblage. However, in places, they are also associated with the presence of large Bi solids, and it is possible that other

solid phases could be masked by the Bi opaques. These inclusions form brown solids upon freezing that could be interpreted as a calcium hydrate phase (antarcticite). The LVS-Bi-1 inclusions have $T_{l\text{-}v}$ values ranging from 152-220ºC and for the LVS-Bi-2 inclusions, the range is from >159-198 ºC. The $T\text{m}_{\text{h}}$ for LVS-Bi-1 range between 192 to 287ºC (Fig. 4.13A; Table 4.3). Most of the LVS-Bi inclusions were also found to stretch and/or leak during heating, and for this reason, we only provide $T\text{m}_{\text{h}}$ data from inclusions that do not appear to have any visible physical change (e.g., change of the L/V ratio) when cooled down to room temperature after total homogenization. Leaking and stretching occurred at temperatures as low as 159 ºC and up to 350 ºC. The calculated salinity range of the LVS-Bi-1 and -2 FIA is 32 to 37 and >34 wt.% NaCl equiv, respectively (Figs. 4.13B, C; Sterner et al., 1988).

Vein set S2: Liquid and vapor bearing (LV-S2) secondary FIA are common in these quartz grains. Individual inclusions within a single FIA have uniform L/V ratios (vapor phase occupies 5-10 vol%. of the inclusion). These inclusions freeze to form ice and a bright-green phase interpreted to be hydrohalite. Occasionally, a brown colored phase also formed (possibly antarcticite). The $T\text{e}$ vary between -44 and -30 ºC, with $T\text{m}_{\text{hh}}$ values in the range -24 to -21ºC, and five $T\text{m}_{\text{ant}}$ were measured at -35ºC. Values of $T\text{m}_{\text{i}}$ vary from -22 to -2ºC, and $T\text{h}$ ranges between 138 and 205ºC (Figs. 4.13A). Calculated salinity values range between 5 and 23 wt. % (wt. % NaCl equiv + wt. % $CaCl_2$ equiv), with $CaCl_2$ contents of 1 to 7 wt. % and NaCl contents of 5 to 18 wt. % (Fig. 4.13B, C).

Vein set S3: Quartz from S3 veins contains LV pseudosecondary FIA (LV-S3) that have uniform L/V in individual FIA, where the vapor phase occupies 5 to 10 vol.%. The inclusions form ice and a bright green phase (hydrohalite) upon freezing. Values of $T\text{e}$ vary between -67 and -59ºC. Hydrohalite melting temperatures are well constrained between -24 and -25ºC, and $T\text{m}_{\text{i}}$ values lie between -16 and -24ºC. The $T\text{h}$ ranges between 122 and 187ºC (Fig. 4.13A, D). Total salinity (S_t) ranges from 20 to 24 wt. %, and the calculated concentrations

for NaCl and $CaCl_2$ are 10 to 14 wt. % and 5 to 14 wt. %, respectively $CaCl_2$ (Figs. 4.13B, C).

Pressure correction: There is no evidence of boiling in single FIA, and therefore a pressure correction must be applied to the *T*h values (Roedder and Bodnar, 1980). It has been suggested that the globular shaped Bi solids trapped in fluid inclusions originated as Bi melts (Acosta-Góngora et al., in revision). The minimum entrapment temperature for the Bi-bearing inclusions is therefore the melting point of Bi at 271.4ºC (Okamoto and Massalki, 1986). The Zhang and Frantz (1987) equation of state allows isochores to be calculated based on the wt. % $CaCl_2$ equiv and wt. % NaCl equiv and the *T*h of the LV-Bi inclusions, and thus, to estimate a pressure correction for the system. The calculated minimum trapping pressures vary from 1.5 to 2.4 kbars. This is equivalent to 4.9 to 8.1 km depth (Table 4.4).

4.5.4 Molybdenite occurrence in NICO and Re-Os dating

The molybdenite-bearing sample taken from the bulk-sample was extracted from the decline across the NICO ore zone. The molybdenite is hosted by amphibole-altered siltstones that have been overprinted by K-feldspar-amphibole alteration fronts, and minor calcite. The molybdenite grains are deformed (Fig. 4.14A), and in textural equilibrium with coarse-grained ferrohornblende II. A few grains of arsenopyrite appear to be in textural equilibrium with amphibole. Fine-grained bismuthinite occurs disseminated in the host rock, along molybdenite cleavage planes, and as microveins crosscutting and partially replacing molybdenite (Fig. 4.14A). Fine-grained native gold is contained within the bismuthinite grains that are disseminated in the wallrock. A chalcopyrite-carbonate vein crosscuts the alteration. Re-Os analysis of the molybdenite yields a model age of 1865 ± 9 Ma (Table 5; 2σ uncertainty, including 0.31% uncertainty in the decay constant).

Molybdenite from the Southern Breccia occurs as undeformed, fine-grained (~35 μm) euhedral laths that co-precipitated with uraninite-ilmenite ± pyrite-chalcopyrite within a magnetite-K-feldspar ± biotite-cemented breccia (Montreuil et al., accepted) (Fig. 4.14B). Molybdenite from the Southern Breccia

yields a Re-Os model age of 1877 ± 8 Ma (Table 5; 2σ uncertainty, including 0.31% uncertainty in the decay constant).

4.6 Discussion

4.6.1 Timing of mineralization

The IOCG systems and many other polymetallic deposits in the GBMZ have been shown to be temporally associated with the onset of Great Bear magmatism (e.g., Gandhi et al., 2001; Ootes et al. 2010; Davis et al., 2011) (Fig. 4.14C). Davis et al. (2011) reported crystallization ages of ~1872 and 1873.8 ± 1.2 Ma for intrusions associated with multiple IOCG alteration assemblages and breccia zones in the Echo Bay district and the Terra mine area. Crystallization ages of ca.1866 and ca.1867 Ma were obtained from porphyry dykes that crosscut amphibole-biotite-magnetite alteration assemblages, and thus correspond to the minimum age of the alteration in the Grouard and Faber Lake areas (Davis et al. 2011). The Nori/RA Cu-Mo-U prospect is hosted by undefined TLG siltstones and mineralization and alteration have been dated by Re-Os molybdenite and Ar-Ar biotite at ca.1874 Ma (Ootes et al., 2010). In the southern GBMZ, north of Dianne Lake, a 1867.9 +2.9/-2.4 Ma rhyodacite porphyry (Gandhi et. al., 2001) is interpreted to be representative of the mineralizing event at the Sue Dianne deposit (Camier, 2002; Ootes et al., 2010). At NICO, the timing of mineralization is constrained by a ca.1872 mineralized K-altered granite and ca. 1869 Ma post-ore porphyry dyke, providing a ca. 1870 Ma estimate for the timing of mineralization (Davis et al., 2011).

The two new Re-Os dates of 1865 ± 9 Ma and 1877 ± 8 Ma are statistically indistinguishable and in agreement with the latter U-Pb dates. Molybdenite from the Bowl Zone sample is crosscut by bismuthinite micro-veins, indicating that the Bi-Cu mineralization is part of a younger mineralizing event. The mineralogy of the molybdenite-bearing sample from the Southern Breccia cannot be related to the with the Bowl Zone prograde or retrograde mineralization assemblages. However, in IOCG deposits, the presence of extensively albitized rocks (Na-alteration) is commonly associated with relatively early, deep, and high

temperature parts of the hydrothermal system (e.g., Corriveau et al., 2010). Montreuil et. al. (accepted) has proposed that differential uplift and even exhumation occurred at NICO during the build-up of the Ca-Fe-K and Na alteration types. Hence, the presence of extensive Na-alteration affecting the protolith to the Southern Breccia might indicate that this alteration/mineralization corresponds to an early formed, deep extension of the NICO system that has been subsequently uplifted. Therefore, although these two parts of the NICO system evolved synchronously, they are spatially separated, and may have been subjected to different physiochemical regimes, which would also account for their mineralogical differences. Overall, the timing of the NICO mineralization and formation of other IOCG and polymetallic deposits coincides with the initial ca. 1873 Ma LaBine Group intermediate arc magmatism and its transition to the more evolved ca. 1868 Ma Faber group felsic volcanism (Bowring, 1984; Hildebrand et al., 1987; Gandhi et al., 2001; Davis et al., 2011).

In the northern GBMZ, this transition of the arc geochemistry is temporally associated with the generation of dioritic, granodioritic, and monzonitic intrusions, roughly syngenetic to the mineralization at the Echo Bay district and the Terra mine (e.g., Hildebrand, 1986; Mumin et al., 2007; Davis et al., 2011). The occurrence of elements like Co and Ni in these deposits supports a mafic contribution to their mineralizing systems. Possible alternatives for the introduction of such metals could be either magma mixing or/and assimilation of older mafic units at depth (Acosta-Góngora et al., in press) by more evolved (intermediate to felsic) up-welling magmas.

4.6.2 Sources of S, O and C

The relatively narrow range of $\delta^{34}S$ values from early Co-rich arsenopyrite and pyrite and the later chalcopyrite suggest a common source (or sources) of sulfur for the sulfarsenides, arsenides, and sulfides at the NICO deposit (Table 4.2). The significant grain scale $\delta^{34}S$ values in arsenopyrite crystals and crystal aggregates in sample NC-1 might be indicative of multiple growth and/or partial re-equilibration during re-crystallization of early arsenopyrite to arsenopyrite II and III. Pokrovski et al. (2002) have shown that replacement or recrystallization

of sulfarsenides derive in a relatively more reducing environment. Thus, the variability in $\delta^{34}S$ results could reflect isotopic fractionation in response to grain size scale changes of redox conditions during arsenopyrite recrystallization. In the case of NC-42, there is only minimal isotopic variation across the analyzed grains, with the exception of one outlier value of 11‰. Pyrite and chalcopyrite $\delta^{34}S$ values are relatively homogeneous (4‰-6‰), and overlap the arsenopyrite values. Most $\delta^{34}S$ values at NICO are <5‰, but there is a range from -3‰ to 11‰. This is consistent with a magmatic source of sulfur, but the elevated values could be indicative of non-magmatic sulfur contributions.

The Terra and Echo Bay mineralized systems have $\delta^{34}S$ values with an average of 4‰, whereas the data from Norex has an average of 0.5‰ (Badham, 1973; Robinson, 1971). These values are consistent with the results from NICO, which also overlap with other magnetite-dominated IOCG deposits hosted by meta-volcanic and/or -sedimentary rocks in the Cloncurry district (e.g., Ernest Henry deposit; Mark et al. 2005), Tennant Creek district (Huston et al., 1993; Skirrow, 1993), the Idaho Cobalt belt (Johnson et al., 2012), and the Guelb deposit (Sakellaris, 2007) (Fig. 4.8A). In all these locations it has been suggested that the sulfur is derived from hydrothermal magmatic and crustal sources (mostly metasedimentary).

As stated, the non-magmatic end member of the S isotope data for NICO could be derived from a metasedimentary source. The T2 Carbonate Unit contains high amounts of S (700-1900 ppm) and Ca compared to the T1, T3, and T4 units (Table 4.1). Petrographic and XRD analysis on the carbonate-rich samples demonstrate the presence of scapolite. No other sources of sulfur (e.g., sulfides) were recognized in this unit. In many IOCG systems sulfur from evaporitic sequences ($\delta^{34}S$ >10‰) is argued to be an important non-magmatic S source (e.g. Barton and Johnson, 1996). Evaporites have not been discovered in the GBMZ, and in general the NICO mineralization has $\delta^{34}S$ <10‰, with the exception of one outlier. So, although scapolite may indicate that gypsum was originally present in T2, it was likely minor. Neverthless, the data from the T1 samples, with $\delta^{34}S$

values of -1‰ to 6‰, may indicate that some sulfur in the NICO system was derived from hydrothermal fluids that equilibrated with the TLG (Fig. 4.8A).

The fractionation factor for the magnetite-water system (Friedman and O'Neill, 1977) and estimated temperature data (>400-600 ºC; Sidor, 2000; Acosta-Góngora et al., in press) were used to calculate the $\delta^{18}O$ values of the fluids for three magnetite bearing samples hosted in arsenopyrite veins and in textural equilibrium with this sulfarsenide. The results indicate the precipitating fluid had $\delta^{18}O$ values of between 6 and 8‰, consistent with magmatic waters or metamorphic fluids (Taylor, 1979; Sheppard, 1986). The $\delta^{18}O$ values of magnetite and quartz from the NICO deposit overlap those of minerals derived from magmatic reservoirs and magmatic hydrothermal deposits (e.g., IOCG, porphyry, and epithermal) (Figs. 410A, B). The $\delta^{18}O$ and $\delta^{13}C$ values for two out of three of the carbonate-rich samples are consistent with a magmatic CO_2 source (Fig. 4.10C). The third sample has a similar $\delta^{18}O$ value, but the lower $\delta^{13}C$ value (-15‰) indicates input from a more reduced carbon source, possibly organic matter in the TLG. Although organic matter has not been recognized in the TLG, it cannot be ruled out.

The stable isotope compositions determined from the NICO deposit support a model in which: i) S, O, and C have a magmatic-hydrothermal source, similar to other IOCG related magmatic-hydrothermal systems in the northern GBMZ, ii) magmatic S and C has mixed with a non-magmatic source of S and C, probably the TLG, iii) sulfur from early and late stages of mineralization have analogous sources, and iv) grain size scale variations in the $\delta^{34}S$ values of the arsenopyrite are consistent with local growth zones and/or partial re-equilibration during formation of arsenopyrite II and III.

4.6.3 Fluid chemistry

Paragenetically, the S1 quartz-hosted LV-C (CO_2-rich) and L-C and LVS inclusions are pre-ore, and constitute the earliest fluid inclusions identified in this study. The co-existence of these brines is common in other IOCG systems (see below). The LVS inclusions have on average the highest *T*h (~314 ºC) and salinity (>37 NaCl wt.%) of all the fluid inclusion assemblages. The formation of

brown solids upon freezing in some of these, suggests that $CaCl_2$ could be an important contributor to the high salinity.

These S1 LVS FIA are cross-cut by fluid inclusions associated with native Bi trails, which constitute the only information on the fluid composition of the ore-bearing stage at the NICO deposit. The data indicate that the Bi-mineralizing fluids were complex Ca-Na-Cl fluids. These fluids can be roughly separated into high (LVS-Bi-1 and -2) and moderate to low (LV-Bi) salinity end members. Although, the variation of the solids vol. %, and the co-existence of single and multisolid inclusions in single LVS-Bi FIA, might also suggest that, in some of these inclusions the solids were accidentally trapped and are not true daughter crystals. The LVS-Bi inclusions from the halite saturated brine generally have higher *T*h values compared to those of the LV-Bi inclusions. The LVS-Bi inclusions have salinities (~38 NaCl wt. %) that are similar to the pre-ore LVS inclusions. Some of the LVS-Bi inclusions form brown solids upon cooling, indicating that $CaCl_2$ may exist in these fluids. The presence of multisolid-bearing inclusions associated with mineralization is typical of other IOCG systems. For example hyper-saline and multi-solid bearing fluid inclusions with halite, calcite, and ferropyrosmalite daughter minerals, salinities of up to 52 wt.% NaCl., and *T*h up to 610ºC is characteristic of Olympic Dam (Bastrakov et al., 2007), Starra (Rotherham et al., 1998), Lightning Creek (Perring et al. 2000) and Ernest Henry (Mark et al. 2005).

A roughly positive correlation between the Tm_i and *T*h of the LV-Bi FIA indicates compositional and temperature changes of these fluids with time (Fig. 4.13D). They evolve from a high temperature and less saline to a lower temperature highly saline fluid (or vice versa) (Fig. 4.13D). In general, these inclusions contain >10 wt.% $CaCl_2$ equiv, with respect to the late S2 and S3 (<10 wt.% $CaCl_2$ equiv) post-ore veins. The presence of FIA with metastable hydrohalite might suggest that these inclusions were originally halite saturated, but halite failed to nucleate crystals as temperature dropped. The overall constrained Tm_i and *T*h, and the few salinity values obtained for the individual assemblages does not support the occurrence of significant fluid mixing between

the different Bi-rich fluids. However, this positive correlation of Tm_i and *T*h could indicate fluids mixing on a grander scale that has not been recorded by localized individual pulses represented by individual FIA. In any case, the data imply an evolving multi-pulse build-up of the Bi-mineralization.

Other fluid inclusions studies have been carried out in the northern GBMZ at Mag Hill, Echo Bay district (Somarin and Mumin, 2013). Here, the fluids responsible for the polymetallic mineralization, and hosted in epithermal veins have the presence of brines with multiple chloride species (e.g., $CaCl_2$, KCl, MgCl) and up to 38 wt% NaCl. These are interpreted to result from low-temperature boiling (~120 ºC) (Somarin and Mumin 2013). However, the data in our study does not indicate fluid boiling related to the Bi mineralization at NICO. At the Tennant Creek district and Lightning Creek IOCG deposits, two phase (LV) $CaCl_2$-rich inclusions have similar compositional characteristics (e.g., Lightning Creek, 3-7 wt% NaCl and 15-28% $CaCl_2$: Perring et al., 2000) to those of the NICO deposit. At Tennant Creek, Bi-rich inclusions have also been recognized (Skirrow, 1993; Skirrow et al. 2002); however, the *T*h and salinities reported by Skirrow (1993) are higher (~270 ºC) and lower (<10 wt. % NaCl equiv + wt. % $CaCl_2$ equiv), than those obtained at NICO. In contrast to NICO, fluid mixing between a higher salinity (up to 35%) Ca-Na-Cl brine and lower salinity Bi-Au bearing fluid is inferred, where the former brine is responsible for the formation of the ironstones hosting the deposit (Skirrow and Walshe, 2002). Unfortunately, the absence of gangue minerals hosting fluid inclusion material in the amphibolitic ironstones at NICO deposit renders it impossible to determine the composition of the Fe-rich fluids that altered those rocks. With respect to the depth of formation (4.9 to 8.1 km) of NICO, this overlaps the depth estimated for other Australian IOCG deposits (<4-10 km; Skirrow, 1993; Perring et al. 2000; Rusk et al., 2010). The relatively high T and P that this depth of formation implies, might explain the elevated decrepitation rate of the LVS and LVS-Bi inclusions.

The co-existence of carbonic (e.g., L-C and LV-C) and high salinity brines (e.g., LVS) pre-, syn- and post-dating main IOCG mineralization, such as those

from NICO deposit, has been recorded in multiple IOCG systems worldwide, e.g., like Igarapé Bahia (Brazil; Dreher et al., 2008), Norrbotten (Sweden, Smith et al. 2013), Kolari (Finland; Niiranen et al., 2007), Lightning Creek (Australia; Perring et al., 2000) and Starra (Australia, Rotherham and Blake, 1998). The true cause of such phenomenon is still poorly understood. However, a common mechanism suggested for the latter is the unmixing of H_2O- CO_2-NaCl-$CaCl_2$-bearing fluids due to changes in pressure and temperature (e.g., Perring et al., 2000; Niiranen et al., 2007; Smith et al., 2013). Pollard (2006) has shown that such a phase separation is associated with the emplacement of oxidized alkali-rich granitoids (Pollard, 2006). For example, in Lightning Creek, Perring et al. (2000) have suggested that during the emplacement of granitic intrusions, H_2O-NaCl-$CaCl_2$-bearing hypersaline brines and CO_2-rich fluids could have been formed by liquid-gas phase separation of an initially supercritical fluid of moderate salinity as shown by Heinrich et al. (2004). Although is not possible to confirm that NICO fluids were formed by this process, the intense metasomatic alteration (comparable to e.g., Lightning Creek and Kolari) and the occurrence of calc-alkaline felsic magmatism associated with the latter, could support this hypothesis.

Alternatively, the source of Ca of the pre- and syn-ore fluids in the NICO deposit could be the carbonate-rich Middle unit of the TLG. As Ca-Fe-K alteration took place, carbonates were dissolved and some Ca was used to form Ca-Fe bearing amphibole. However, a portion of this Ca could have stayed in solution with the remnant fluids after the early ironstone development. These Ca-rich fluids might have subsequently equilibrated with the later upwelling polymetallic-depositing fluid providing the salinity observed. Another option is a lateral input of Ca from fluids in equilibrium with a portion of non- or poorly Ca-Fe-K metasomatized rocks of the Carbonate unit located closer to the type section. It is also possible that some Ca was recycled from the previous Ca-Fe amphibole alteration.

The later S2 and S3 LV inclusions have similar T_h (~165 ºC) to those of the LV-Bi, but the salinity is mostly dominated by NaCl over $CaCl_2$ (~10 NaCl

wt.%). This constitutes an important difference between the ore-forming fluids and the later hydrothermal stages.

4.6.4 Metal budget of the Treasure Lake Group

It has been suggested that shales and in particular carbonaceous shales and their metamorphosed equivalents, can be the source of economic metals like Au, Cu, Bi, Pb, Zn and Ag in sedimentary hosted Au deposits (e.g., Large et al. 2011). These carbonaceous shales can be up to 20 times more enriched in Au, S, and As, than the average upper crust, felsic and mafic igneous rocks, metamorphic rocks, and limestones or dolostones (Large et al., 2011). The majority of TLG rocks contain < 1 ppb Au. An average value of 1.4 ppb was calculated for the TLG. This average was obtained by giving a value of 0.9 ppb Au to those samples with Au <1 ppb. The average Au content of the upper crust is 1.5 ppb, and of marine shales is 2 ppb, whereas felsic and mafic volcanic rocks and granites have average concentrations ranging between 2 and 6 ppb (Turekian and Wedepohl, 1961; Crocket et al., 1991; Li and Schoonmaker, 2003; Hu and Gao, 2008). Carbonaceous shales contain an average of 6.7 ppb Au (Crocket et al., 1991). Other elements in the TLG, such as Cu (average 12 ppm) and Co (average 10 ppm), have similar concentrations to average upper crust, or are depleted with respect to that reservoir. In the case of Bi, the detection limit (2 ppm) in this study is well above the average upper continental crust (0.16 ppm), oceanic crust (0.1 ppm), and shale (0.43 ppm). Hence, it is difficult to evaluate whether or not Bi is anomalous in the TLG.

Arsenic concentrations in the upper continental crust average 4.8 ppm (Rudnick and Gao, 2003), and range from 1 to 4 ppm in felsic and mafic igneous rocks, although As rich S- and I-type granites with 5 to 9 ppm have been documented (Chappell, 2010). Shales typically have higher As concentrations, with, on average, 13 to 15 ppm, and up to 29 ppm (Quinby-Hunt et al., 1989). These shale As values are on the order of four times higher than the bulk crustal values (Boyle and Jonasson, 1973; Li and Schoonmaker, 2003). The TLG has variable As contents (Table 4.1). The T3 and T4 units have values that overlap average continental crust, with two samples with higher As (14 and 15 ppm). The

T1 unit has, on average, 11 ppm As and T2 has 25 ppm As; concentrations that are well above average crustal values but similar to shales and carbonaceous shales (Fig. 4.7C). Arsenic concentrations in GBMZ felsic porphyries, dacite and rhyolite volcanic rocks range from <1 to 4 ppm (Acosta-Góngora et al., in revision; L. Ootes unpublished data). The T2 Carbonate unit contains on average 1310 ppm S, which is comparable to average carbonate-rich rocks (1200 ppm; Turekian and Wedepohl, 1961), and is at least 2.5 times higher than bulk continental crust (Fig. 4.7C; Rudnick and Gao, 2003).

The data indicate that the TLG contain, average Au, Cu and Co concentrations that are similar to, or lower than, those of the upper continental crust (Fig. 4.7C). In principle, these data could suggest that the TLG is not a likely source of these metals to the NICO deposit. However, mass balance calculations are needed to address this. The elevated concentrations of As and S in the T2, and of As in the T1 unit, indicates that they could have been potential sources of these components in the NICO system. Although, an As-rich magmatic source cannot be ruled out, the existing data for the GBMZ felsic rocks do not readily support this.

4.6.5 Alteration and ore precipitation

Calcium-Fe-K altered TLG host the NICO ore lenses. Co-rich sulfarsenides and arsenides are the most common ore minerals and normally crosscut these rocks as veins and/or replace the alteration minerals along the bedding planes or in localized patches. In other metasediment-hosted IOCG systems worldwide, the host rocks were subjected to magnetite ± amphibole-Fe-rich phyllosilicates-Fe-rich chlorite alteration that generally occurred in shear zones, and which developed during regional metamorphism (e.g., Skirrow and Walshe, 2002; Kouvervaara; Vanhanen, 2000; Slack, 2012). These early and ubiquitous Ca-Fe ± K alteration assemblages in sediment-hosted IOCG deposits are likely indicating ground preparation for the subsequent ore mineral precipitation. In the former deposits, and at NICO, the interaction of the polymetallic-rich fluids with the heavily altered protolith may have enhanced the precipitation of the ore minerals from hydrothermal fluid phase.

Arsenic is mainly transported as As^{3+} in the form of $As(OH)_3^0$ in hydrothermal solutions and volatile phases from 300 to 450 ºC; 100 to 1000 bar, even in the presence of H_2S and HCl (Pokrovski et al., 1996; 2002). These conditions are similar to those that characterize hydrothermal fluids associated with intermediate to felsic magmas and Au-Cu-Sn-W deposits (Pokrovski et al., 2002). The stability of this species reaches a maximum at near neutral pH values between 6 and 8 (Pokrovski et al., 1996; 2002) and is not significantly affected by temperature changes. As pH increases, $As(OH)_3^0$ deprotonizes and forms the charged $AsO(OH)_2^-$ species. Therefore, the $As(OH)_3^0$ complex is less stable in aqueous solutions at alkaline conditions (pH>8; Prokrovski et al. 2002) and such conditions cause the precipitation of As-rich minerals from $As(OH)_3^0$ and formation of $AsO(OH)_2^-$. Borisova et al. (2010) have shown that hydrous silicate melts may be important transporting media for As in shallow magmatic-hydrothermal settings due to their high affinity for the water and hydroxide ligand ($AsO(OH)_2^-$, $As(OH)_3^0$).

The overall alkaline conditions coincide with the stability fields calculated for magnetite precipitated from seawater solutions (Glasby and Schultz, 1999) and forming the ironstones (magnetite>hematite-stilpnomelane) in the Tennant Creek district (e.g., Skirrow and Walshe, 2002). Chemical and mass transfer modeling of reactions between a reducing ore fluid and magnetite-rich ironstones indicates that highly efficient Au and native Bi precipitation occurs in response to desulfidation and oxidation of the fluid resulting in the destabilization of $AuHS^0$, $Au(HS)^-_2$ and $Bi_2S_2(OH)^0_2$ complexes (Skirrow and Walshe, 2002). Moreover, in that study, chalcopyrite was mainly precipitated due to a pH increase (Skirrow and Walshe, 2002). Recently, a study made by Tooth et al. (2011) argues that fluid-rock equilibration can trigger precipitation of Bi^0 if the fluid interacts with reduced phases like pyrrhotite and graphite causing them to oxidize to CO_2 and magnetite, respectively. Another mechanism to exsolve Bi is the precipitation of Fe^{+3} bearing phases (e.g., magnetite), because Fe is mostly transported in hydrothermal solutions as Fe^{+2} (Bell and Simon, 2011), and thus, important

precipitation of Fe^{+3} will consequently lead to an overall reduction of the remaining fluid (Cockerton and Tomkins, 2012).

In the NICO deposit, the Bi-bearing fluids are precipitated later with respect to the early Co-rich sulfarsenides. Hence, one can argue that interaction of these late fluids with reducing phases such as cobaltite, arsenopyrite and loellingite might have precipitated native Bi (Acosta-Góngora et al, in revision). However, oxidation of such reduced minerals temporally associated with the native Bi occurrence is not well constrained. Alternatively, decoupling of Bi from its parental solution could have taken place as coeval magnetite precipitated. This is indicated by the presence of native Bi with magnetite±bismuthinite in micro veins crosscutting Fe-As-S-Co mineral phases (Acosta-Góngora et al., in press; in revision).

Collectively, the latter suggests that if an initially reducing and acidic to neutral hydrothermal magmatic ore fluid interacts with Ca-Fe-K altered rocks at relatively low fluid-rock ratios, this process will most likely increase the pH of the solutions carrying the $As(OH)_3^0$ complexes. The latter will promote the precipitation of the sulfarsenides. Consequently, this will also provoke the desulfidation of the remnant fluids (increase of fO_2), and further precipitation of magnetite might also favor the decoupling of Bi (and Au?) as a melt phase from hydrothermal fluids.

4.7 NICO genetic model

The IOCG and polymetallic mineral deposits in the GBMZ have been interpreted to be part of a continuum of magmatic-hydrothermal pulses derived from the emplacement of alkaline to calc-alkaline granitic intrusions generated during arc magmatism (Badham 1973, 1975, 1976; Mumin et al. 2007). The formation of the NICO deposit is the result of several factors associated with the development of shear zones during regional metamorphism, and the subsequent emplacement of magmatic phases of the Great Bear arc. The pervasive Ca-Fe- K alteration of the carbonate-rich rocks from the T2 unit of the TLG served as a sink for Au-Co-Bi ± Cu-W mineralization.

The approximate timing of regional metamorphism of the TLG is synchronous with the arrival of the Hottah terrane adjacent to the Slave craton at ca. 1882 Ma (~1882 Ma; Bowring and Grotzinger, 1992). During this event, the TLG was tilted and folded, with the formation of associated penetrative fabrics, including major shear zones (Fig. 4.15A). The emplacement of the GBMZ by ca. 1875 Ma resulted in the reactivation of some of these shear zones, creating secondary permeability that was capable of focusing Fe-K-(Ca?)-rich metasomatic fluids. The Ca-Fe-K metasomatic alteration pervasively overprinted the T2 unit to form the early and barren Ca-Fe-amphibole-biotite-magnetite alteration assemblage between ~1875 to 1870 Ma (Fig. 4.15B). This alteration may have occurred at low fluid/rock ratios and pressures >1.2 kbar, which are similar conditions to those reported for the formation of other IOCG-related ironstones (e.g., Skirrow and Walshe, 2002). These rocks at NICO are crosscut by the S1 vein set, which host highly saline ($CaCl_2$-bearing) brines (~38 NaCl wt.%) with *T*h= ~325 ºC and less abundant CO_2-rich fluids.

The Co-Au-Bi ± Cu-W ore fluid was generated at ca. 1870 Ma (Fig. 4.15C), as regional magmatism evolved from mafic/intermediate to a more felsic composition. This magmatic evolution might have been important for the introduction of mafic-related elements such as Co to the NICO system, and Co-Ni in the northern GBMZ (Mumin et al., 2007; Somarin and Mumin, 2013). Equilibration of the ore fluids with the ironstones may have triggered the precipitation of the sulfarsenides as a pH increase destabilized the $As(OH)_3^0$ complexes. The $\delta^{34}S$, $\delta^{18}O$, and $\delta^{13}C$ values mostly support a magmatic origin for these components. In principle, the trace element analysis of the least altered TLG samples indicates that this package of rocks is not a likely source of Co, Au, and Cu. However, the absence of appropriate mass balance calculations also constrains the latter assumption. The relatively high concentrations S and As in the T2 Carbonate unit and its bulk rock $\delta^{34}S$ values suggest that some S and As could have been derived by these host rocks to the deposit. In the same way, the high Ca content of the fluids might reflect interaction of the ore-bearing fluids with this unit.

The earlier stages of mineralization correspond with a prograde assemblage (>400°C/1.5-2.5kbar; Sidor, 2000; Acosta-Góngora et al., in revision) characterized by the precipitation of Co-rich sulfarsenides (and Fe-Ca-K-rich associated gangue minerals) that locally have significant amounts of Au and Bi in solid solution (Acosta-Góngora et al., in revision). The retrograde mineralization is characterized by the recrystallization of the early sulfarsenides into arsenopyrite II and II, along with the release and remobilization of Au and Bi from their former hosts to fractures and other low strain sites (~400 to 270°C; Acosta-Góngora et al., in revision). Acosta-Góngora et al. (in revision) suggested that in this retrograde fluid, Bi was exsolved from the hydrothermal phase at temperatures over 270 ºC, and occurred as co-existing native Bi-melts. The Bi exsolution could have resulted in response to desulfidation of the remnant fluids as Fe-S-As-Co minerals precipitated, equilibration of Bi-rich fluids with those sulfarsenides and/or co-precipitation of magnetite. In any case, the decoupling of the Bi melts eventually led to further Au-concentration in the NICO deposit (Acosta-Góngora et al., in revision). In the present study we have shown that the hydrothermal fluids carrying native Bi (and possibly Au) are complex $CaCl_2$-NaCl-H_2O brines, and that the Bi(-Au?) mineralization occurred as a series of magmatic-hydrothermal pulses (at >4 km depth), in which generally $CaCl_2$ was an important component of the fluid. As the temperature started to drop (<270 ºC), and fO_2 and fS_2 increased, Cu-Bi sulfides, chalcopyrite, hastingsite, chlorite and hematite replaced the host rock silicates and the Bi-bearing phases (Acosta-Góngora et al., in revision). Finally late-stage quartz- (S2) and quartz-carbonate-rich (S3) barren veins were emplaced after the main mineralization, which were formed by $CaCl_2$-NaCl-bearing (T_h= ~160 ºC) fluids, where NaCl was dominant over $CaCl_2$.

4.8 References

Acosta-Góngora, P., Gleeson, S.A., Samson, I.M., Corriveau, L., Taylor, B., Ootes, L., and Creaser, R., Mechanisms of gold refining at the Au-Co-Bi±Cu-W iron oxide dominated NICO deposit, NWT, Canada: Economic Geology. In revision.

Acosta-Góngora, P., Gleeson, S.A., Samson, I.M., Corriveau, and L., Ootes, L., Trace element geochemistry of magnetite and its relationship to Cu-Bi-Co-Au-Ag-U-W mineralization in the Great Bear magmatic zone, NWT, Canada Economic Geology. In press.

Badham, J.P.N., and Morton, R.D., 1976, Magnetite-apatite intrusions and calc-alkaline magmatism, Camsell River, N.W.T: Canadian Journal of Earth Sciences, v. 13, p. 348-354.

Badham, J.P.N., 1975, Mineralogy, paragenesis and origin of the Ag-Ni-Co arsenide mineralization, Camsell River, N.W.T. Canada: Mineralium Deposita, v. 10, p. 153-175.

Badham, J.P.N., 1973, Calc-alkaline volcanism and plutonism from the Great Bear batholith, N.W.T: Canadian Journal of Earth Sciences, v. 10, p. 1319-1328.

Baker, T., Perkins C, Blake K.L., Williams, P.J., 2001, Radiogenic and stable isotope constraints on the genesis of the Eloise Cu-Au deposit, Cloncurry district, northwest Queensland: Economic Geology, v. 96, p.723-742.

Barton, M.D., and Johnson, D.A., 1996, Evaporitic-source model for igneous-related Fe oxide-(REE-Cu-Au-U) mineralization: Geology, v. 24, p.259-262.

Bastrakov, E.N., Skirrow, R.G., Davidson, G.J., 2007, Fluid evolution and origins of iron oxide Cu-Au prospects in the Olympic Dam District, Gawler Craton, South Australia: Economic Geology, v. 102, p. 1415-1440.

Beaudoin, G., and Taylor, B.E., High precision and spatial resolution sulfur analysis using MILES laser mircroprobe: Geochimica et Cosmochimica Acta, v. 58, p. 5055-5063.

Bell, A.S., and Simon, A., 2011, Experimental evidence for the alteration of the Fe 3+/SFe of silicate melt caused by the degassing of chlorine-bearing aqueous volatiles: Geology, v. 39, p. 499–502.

Benavides, J., Kyser, T.K., Clark, A.H., Oates, C.J., Zamora, R., Tarnovschi, R., Castillo, B., 2007, The Manto Verde Iron-oxide-Copper-Gold district, III Región, Chile: the role of regionally derived, nonmagmatic fluids in chalcopyrite mineralization: Economic Geology v.102, p. 415-440.

Bennett, V., and Rivers, T., 2006, U-Pb ages of zircon primary crystallization and inheritance for magmatic rocks of the southern Wopmay orogen, Northwest Territories: NWT Open File 2006-006, 65 p.

Bindeman, I.N., and Valley, J.W., Rapid generation of both high- and low-δ18O, large-volume silicic magmas at the Timber Mountain, Oasis Valley caldera: Geological Society of America Bulletin, v. 115, p. 581-595.

Borisova, A.Y., Pokrovskim G.S., Pichanvant, M., Freydier, R., Canaudap, F., 2010, Arsenic enrichment in hydrous peraluminous melts: Insights from femtosecond laser ablation-inductively coupled plasma-quadropole mass spectrometry, and in in-situ X-ray absorption fine structure spectroscopy: American Mineralogist, v. 95, p. 1104-2010.

Bowring, S.A., 1984, U-Pb zircon geochronology of Early Proterozoic Wopmay orogen, N.W.T. Canada: An example of rapid crustal evolution: Unpublished Ph.D. thesis, Lawrence, Kansas, University of Kansas, 148 p.

Bowring, S.A., and Grotzinger, J.P. 1992, Implications of new chronostratigraphy for tectonic evolution of Wopmay Orogen, northwest Canadian Shield: American Journal of Science, v. 292, p. 1–20.

Boyle, R.W., and Jonasson, I.R., 1973, The geochemistry of arsenic and its use as an indicator element in geochemical prospecting: Journal of Geochemical Exploration, v. 2, p. 251−196.

Calagari, A.A., 2003, Stable isotopes (S, O, H and C) studies of the phyllic and potassic-phyllic alteration zones of the porphyry copper deposit at Sungun, East Azarbaidjan, Iran: Journal of Asian Earth Sciences, v. 21, p. 767-780.

Camier, W.J., 2002, Geology of the Sue-Dianne Proterozoic Cu-Ag-Fe oxide breccia complex, Mazenod Lake district, Northwest Territories: Unpublished M.Sc. thesis, London, University of Western Ontario, 210 p.

Chappell, B.W., 2010, A chemical database for the New England batholith: New England Orogen Conference, University of New England, Armidale, NSW, Proceedings, p. 119−123.

Cockerton, A.M.D., and Tomkins, A.G., 2012, Insights into the liquid bismuth collector model through analysis of the Bi-Au Stortmont skarn prospect, northwest Tasmania: Economic Geology, v. 107, pp. 667-682.

Corriveau, L., 2007, Iron oxide-copper-gold deposits: A Canadian perspective, in Goodfellow, W.D., ed., Mineral deposits of Canada: A synthesis of major deposit-types, district metallogeny, the evolution of geological provinces and exploration methods: Geological Association of Canada, Special Publication 5, p. 307-328.

Corriveau, L., Mumin, A.H., Setterfield, T., 2010, IOCG environments in Canada: Characteristics, geological vectors to ore and challenges, in Porter, T.M., ed., Hydrothermal iron oxide copper-gold and related deposits: A global perspective, Advances in the understanding of IOCG deposits. PGC Publishing, Adelaide, v.4, p. 311-343.

Crocket, J.H., 1991, Distribution of gold in the Earth's crust, in Foster, R.P., eds., Gold metallogeny and exploration: London, New York, NY, Chapman and Hall, p. 1-36.

Davis, W., Corriveau, L., van Breemen, O., Bleeker W., Montreuil, J.F., Potter, E., Pelletier, E., 2011, Timing of IOCG mineralizing and alteration events within the Great Bear Magmatic Zone: Yellowknife Geoscience Forum , 39th , Canada, 15-17 November 2011, Abstracts, p. 97.

De Haller, A., and Fontboté, L., 2009, The Raúl-Condestable iron oxide copper-gold deposit, central coast of Peru: ore related hydrothermal alteration, sulfur isotopes, and thermodynamic constrainst: Economic Geology, v. 104, p. 365-384.

Deines, P., 1980, Stable isotope variations in carbonatites, in Bell, K., ed., Carbonatites, genesis and evolution: London, Unwin Hyman, p. 301-359.

Dreher, A.M., Xavier, R.P., Taylor, B.E., and Martini, S., 2008, New geologic, fluid inclusion and stable isotope studies on the controversial Igarapé Bahia Cu-Au deposit, Carajás Province, Brazil: Mineralium Deposita, v. 43, p. 162-184.

Ganino, C., Harris, C., Arndt, N.T., Prevec, S.A., Howarth, G.H., 2013, Assimilation of carbonate country rock by parent magma of the Panzhizhua Fe-Ti-V deposit (SW China): Evidence from stable isotopes: Geoscience Frontiers, v. 4, p. 547-554.

Friedman, I. and O'Neil, J.R., 1977, Compilation of stable isotope fractionation factors of geochemical interest, in Fleischer, M., ed., Data of Geochemistry: United States Geological Survey, Professional Paper, 440-KK.

Gandhi, S.S., 1994, Geological setting and genetic aspects of mineral occurrences in the southern Great Bear magmatic zone, Northwest Territories, in Sinclair, W.D., Richardson, D.G., eds., Studies of rare-metal deposits in the Northwest Territories: Geological Survey of Canada, Bulletin 475, p. 63-96.

Gandhi, S.S., Mortensen, J.K., Prasad, N., and van Breemen, O., 2001, Magmatic evolution of the southern Great Bear continental arc, northwestern Canadian Shield: Geochronological constraints: Canadian Journal of Earth Sciences, v. 38, p. 767-785.

Gandhi, S.S., and van Breemen, O., 2005, SHRIMP U-Pb geochronology of detrital zircons from the Treasure Lake Group - new evidence for Paleoproterozoic collisional tectonics in the southern Hottah terrane, northwestern Canadian Shield: Canadian Journal of Earth Sciences, v. 42, p. 833-845.

Glasby, P.G., and Shultz, H.D., 1999, Eh, pH diagrams for Mn, Fe, Co, Ni, Cu and As under seawater conditions: application of two new types of Eh, pH diagrams to the study of specific problems in marine geochemistry: Aquatic Geochemistry, v. 5, p. 227-248.

Gleeson, S.A. and Smith, M.P., 2009, The sources and evolution of mineralising fluids in iron oxide-copper-gold systems, Norrbotten, Sweden: Constraints from stable Cl isotopes of fluid inclusion leachates: Geochimica Cosmochimica Acta, v. 73, p. 5658-5672.

Goad, R.E., Mumin, A.H., Duke, N.A., Neale, K.L., Mulligan, D.L., Camier, W.J., 2000, The NICO and Sue-Dianne Proterozoic, iron oxide-hosted,

polymetallic deposits, Northwest Territories: Application of the Olympic Dam model in exploration: Exploration and Mining Geology, v.9, p. 123-140.

Goldstein, R.H., 2003, Petrographic analysis of fluid inclusions, in Samson, I., Anderson, A., and Marshall, D., eds., Fluid inclusions: Analysis and interpretation: Mineralogical Association of Canada, Short Course Handbook, v. 32, p. 9-53.

Hangari, K.M., Ahmad, S.N., and Perry, E.C., Jr., 1980, Carbon and oxygen isotope ratios in the diagenetic siderite and magnetite from the upper Devonian ironstone, Wadi Shatti, district, Lybia: Economic Geology, v. 75, p. 538-545.

Haynes, F.M., 1985, Determination of fluid inclusion compositions by sequential freezing: Economic Geology, v. 80, p. 1436-1439.

Heck, P.R., Huberty, J.M., Kita, N.T., Ushikubo, T., Kozdon, R., Valley, J.W., SIMS analyses of silicon and oxygen isotope ratios for quartz from Archean and Paleoproterozoic banded iron formations: Geochimica et Cosmochimica Acta, v. 75, p. 5879-5891.

Heinrich, C.A., Driesner, T., Stefansson, A., and Seward, T., 2004, Magmatic vapor contraction and the transport of gold from the porphyry environment to epithermal ore deposits: Geology, v. 32, p. 761-764.

Hildebrand, R. S., 1986, Kiruna-type deposits: their origin and relationship to intermediate subvolcanic plutons in the Great Bear magmatic zone, Northwest Canada: Economic Geology, v. 81, p. 640-659.

Hildebrand R.S., Hoffman, P.F., Bowring, S.A., 1987, Tectono-magmatic evolution of the1.9-Ga Great Bear magmatic zone, Wopmay orogen, northwestern Canada: Journal of Vulcanology and Geothermal Research, v. 36, p. 32:99-118.

Hildebrand, R.S., Hoffman, P.F., and Bowring, S.A., 2010a, The Calderian orogeny in Wopmay orogeny (1.9 Ga) northwestern Canadian Shield: Geological Society of America, Bulletin 122, p. 794-814.

Hildebrand, R.S., Hoffman, P.F., Housh, T., and Bowring, S.A., 2010b, The nature of volcano-plutonic relations and shapes of epizonal plutons of

continental arcs as revealed in the Great Bear magmatic zone, northwestern Canada: Geosphere, v. 6, p. 812-839.

Hitzman, M., Oresekes, N., and Einaudi, M.T., 1992, Geological characteristics and tectonic setting of the Proterozoic iron oxide (Cu-U-Au-REE) deposits: Precambrian Research, v. 58, p. 241-287.

Hoffman, P.F., and McGlynn, J.C., 1977, Great Bear batholith: A volcano-plutonic depression, in Baragar, W.R.A , Colemean, L.C. and Hall, J.M., eds., Volcanic regimes in Canada: Geological Association of Canada, Special Paper 16, p. 170-192.

Hoffman, P.F., 1980, Wopmay orogen: A Wilson cycle of Early Proterozoic age in the northwest of the Canadian Shield, in Strangway, D.W., ed., The continental crust and its mineral deposits: Geological Association of Canada, Special Paper 20, p. 523–549.

Hu, Z., and Gao, S., 2008, Upper crustal abundances of traces elements: A revision and update: Chemical Geology, v. 253, p. 205-221.

Huston, D.L., Bolger, C., and Cozens, G., 1993, A comparison of mineral deposits at the Gecko and White Devil Deposits: Implications for ore genesis in the Tennant Creek district, Northern Territory, Australia: Economic Geology, v. 88, p. 1198-1225.

Jackson, V.A., and Ootes, L., 2012, Preliminary geologic map of the south-central Wopmay orogen, results from 2008 to 2011: NWT Open File 2012-04, http//www.nwtgeoscience.ca.

Johnson, C.A., Bookstrom, A.A., Slack, J.F., 2012, Sulfur, carbon, hydrogen, and oxygen isotope geochemistry of the Idaho Cobalt belt: Economic Geology, v. 107, p. 1207-1221.

Large, R.R., Bull, S.W., and Maslennikov, V.V., 2011, A carbonaceous sedimentary source-rock model for Carlin-type and orogenic gold deposits: Economic Geology, v. 106, p. 331-358.

Li, Y.H., and Schoomaker, J.E., 2003, Chemical composition and mineralogy of marine sediments, in F.T., Holland, D.H., and Turekian, K., eds., Treatise of Geochemistry: Elsevier, London, 35 p.

Li, X., and Sasaki, M., 2007, Hydrothermal alteration and mineralization of middle Jurassic Dexing porphyry Cu-Mo deposit, southeast China: Resource geology, v. 57, p. 409-426.

Mandernack, K.W., 1999, Oxygen and iron isotope studies of magnetite produced by magnetotactic bacteria: Science, v. 285, p. 1892-1896.

Marin, J., Chaussidon, M., Robert, F., 2010, Microscale oxygen isotope variation in 1.9 Ga Gunflint cherts: Assessments of diagenesis effect and implications for oceanic paleotemperature reconstructions: Geochimica et Cosmochimica Acta, v. 74, p. 116-30.

Mark G, Williams, P.J., Oliver, N.H.S., Ryan, C. and Mernagh, T., 2005, Fluid inclusion and stable isotope geochemistry of the Ernest Henry Fe oxide-Cu-Au deposit, Queensland, Australia: Society of Geology Applied to Mineral Deposits Biennial Meeting , 8th, China, August 18-21, Abstracts, p. 785-788.

Mark G, Williams, P.J., Oliver, N.H.S., Ryan, C. and Mernagh, T., 2005, Fluid inclusion and stable isotope geochemistry of the Ernest Henry Fe oxide-Cu-Au deposit, Queensland, Australia: Society of Geology Applied to Mineral Deposits Biennial Meeting , 8th, China, August 18-21, Abstracts, p. 785-788.

Marschik, R., and Fontboté, L., 2001, The Candelaria-punta del Cobre iron oxide Cu-Au(-Zn-Ag) deposits, Chile: Economic Geology, 96, p.1799-1826.

Montreuil, J.F., Corriveau, L., and Potter, E. (accepted), Albitite-hosted uranium development within IOCG systems: The southern breccia, Great Beat magmatic zone, Northwest Territories, Canada: Mineralium Deposita.

Montreuil, J.F., Corriveau, L., and Grunsky, E., 2013, A compositional data analysis of IOCG systems, Great Bear magmatic zone, Canada: To each alteration types its own geochemical signature: Geochemistry: Exploration, Environment, Analysis, doi: 10.1144/geochem2011-101.

Mumin, A.H., Corriveau L., Somarin, A.K., and Ootes, L., 2007, Iron Oxide Copper-Gold-type polymetallic mineralization in the Contact Lake Belt, Great Bear magmatic zone, Northwest Territories, Canada: Exploration and Mining Geology, v. 16, p.187-208.

Niiranen, T., Poutiainen, M. and Mänttäri, I., 2007, Geology, geochemistry, fluid inclusion characteristics, and U-Pb age studies on iron oxide-Cu-Au deposits in the Kolari region, northern Finland: Ore Geology Reviews, v. 30, p. 75-105.

Okamoto H. and Massalski T. B, 1986, Au-Bi (gold-bismuth), in T.B., Massalski, J. L. Murray, L. H. Bennet and H., Baker, eds., Binary Alloy Phase Diagrams: Ac-Au to Fe-Rh: American Society for Metals, v. 1, p. 238-240.

Ootes, L., Davis, W.J., and Jackson, V.A., 2013, Whence came Hottah Terrane?: Geological Association of Canada/Mineralogical Association of Canada Annual Meeting, Winnipeg, MN, 22-24 May 2013, p. 154.

Ootes L., Goff, S., Jackson, V., Gleeson, S.A, Creaser, R., Samson, I.M., Evensen, N., Corriveau, L., and Mumin, H. , 2010, Timing and thermochemical constraints on multi-element mineralization at the Nori/RA Cu-Mo-U prospect, Great Bear magmatic zone, Northwest Territories, Canada: Mineralium Deposita, v. 45, p.549-566.

Oreskes, N., and Einaudi, T., 1992, Origin of hydrothermal fluids at Olympic Dam: preliminary results from fluid inclusions and stable isotopes: Economic Geology, v. 87, p.64-90.

Perring, C.S., Pollard, P.J., Dong, G., Nunn, A.J., and Blake, K.L, 2000: The Lightning Creek sill complex, Cloncurry district, northwest Queensland: A source of fluids for Fe oxide-Cu-Au mineralization and sodic-calcic alteration: Economic Geology, v. 95, p. 1067-1089.

Pokrovski, G.S., Gout, R., Zotov, A., Schott, J., Harrichoury, J.C., 1996: Thermodynamic properties and stoichiometry of the arsenic (III) hydroxide complexes at hydrothermal conditions: Geochimica et Cosmochimica Acta, v. 60, p. 737-749

Pokrovski G. S., Kara S., and Roux J., 2002, Stability and solubility of arsenopyrite, FeAsS, in crustal fluids: Geochimica et Cosmochimica Acta: v. 66, p. 2361-2378.

Pollard, P.J., 2006, An intrusion-related origin for Cu-Au mineralization in iron-oxide-copper-gold (IOCG) provinces: Mineralium Deposita, v. 41, p. 179-187.

Potter, E.G., Montreuil, J.-F., Corriveau, L., and DeToni, A., 2013, Geology and hydrothermal alteration of the Fab Lake region, Northwest Territories: Geological Survey of Canada, Open File 7339.

Puritch, E., Ewert, W., Armstrong, T., Brown, F., Orava, D., Pearson, J.L., Hayes, T., Duggan, T., Holmes, G., Uceda, D., Sumners, W., Mackie, D., Rougier, M., Bocking, K., Mezei, A., Horne, B., 2012, Technical report and updated mineral reserve estimate and front-end engineering and design (FEED) study on the NICO gold-cobalt-bismuth-copper deposit, Mazenod Lake area, Northwest Territories, Canada: NI 43-101 Technical Report No. 247 prepared for Fortune Minerals Ltd., 307 p.

Quinby-Hunt, M.S., Wide, P., and Berry, W.B.N., 1989, Element geochemistry of low calcic black shales-statistical comparison with other shales: U.S Geological Survey, Circular 1037, p. 8−15.

Richards, J.P., and Mumin, H., 2013, Magmatic-hydrothermal processes within an evolving earth: Iron oxide-copper-gold and porphyry Cu±Mo±Au deposits: Geology, v. 41, p. 767-770.

Robinson, B.W., 1971, Studies on the Echo Bay silver deposit, NWT: Unpublished PhD thesis, Alberta, Canada, University of Alberta, 256 p.

Roedder, E., 1984, Fluid inclusions, in P.H., Ribbe, ed., Reviews in Mineralogy: Mineralogical Society of America, v. 12, 644 p.

Rotherham, J.F., Blake, K.L., Cartwright, I. and Williams, P.J., 1998, Stable isotope evidence for the origin of Mesoproterozoic Starra Au-Cu deposit, Conclurry district, Northwest Queenland: Economic Geology, n. 93, v.1435-1449.

Roedder, E., and Bodnar, R.J., 1980, Geologic pressure determinations from fluid inclusion studies: Annual Review of Earth and Planetary Sciences, v.8, p. 263-301.

Rudnick, R.L. and Gao, S., 2003, The composition of the continental Crust, in, eds, Holland and K.K., Turekian Rudnick, Treatise on Geochemistry: Elsevier-Pergamon, Oxford, p. 1-64.

Rusk, B., Oliver, N., Blenkinsop, T., Zhang D, Williams, P., Cleverley, J., and Habermann, P., 2010, Physical and chemical characteristics of the Ernest Henry iron oxide copper gold deposit, australia; implications for IOCG genesis *in* Porter T. M., ed., Hydrothermal iron oxide copper-gold and related deposits: A Global Perspective PGC Publishing, Adelaide, v.3, p. 201-218.

Santos, R.V., de Alvarenga, C.J.S., Dardenne, A.N. Sial, Ferreira, V.P., 2000, Carbon and oxygen profiles across Meso-Neoproterozoic limestones from from central Brazil: Bambuí and Paranoá groups: Precambrian Research, v. 104, p. 107-122.

Sakellaris, G.A., 2007, Petrology, Geochemistry, stable and Radiogenic isotopy of Guelb Moghrein Iron oxide-Copper-Gold deposit, Mauritania: Unpublished Ph.D thesis, Aachen, Germany, Rheinisch-Westfälischen Technischen Hochschule Aachen, 222 p.

Selby D., Creaser, R.A., 2001, Re-Os geochronology and systematics in molybdenite from the Endako porphyry molybdenum deposit, British Columbia, Canada: Economic Geology, v. 96, p.197-204.

Selby, D., Creaser, R.A., 2001b, Late and mid-Cretaceous mineralization in the northern Canadian Cordillera: constraints from Re-Os molybdenite dates: Economic Geology, v. 96, p. 1461-1467.

Selby, D., Creaser, R.A., 2004, Macroscale NTIMS and microscale LAMC-ICP-MS Re-O isotopic analysis of molybdenite: testing spatial restrictions for reliable Re-Os age determinations, and implications for the decoupling of Re and Os within molybdenite: Geochimica et Cosmochimica Acta, v. 68, p. 3897-3908.

Sheppard, S.M.F., 1986, Characterization and isotopic variations in natural waters: Reviews in Mineralogy, v. 16, p. 165-183.

Sheppard, S.M.F., Nielsen, R.L., and Taylor, H.P., 1971, Hydrogen and oxygen isotope ratios in minerals from porphyry copper deposits: Economic geology, v. 66, p. 515-542.

Sidor, M., 2000, The origin of the black rock alteration overprinting iron-rich sediments and its genetic relationship to disseminated polymetallic sulfide

ores, Lou Lake, Northwest Territories, Canada: Unpublished M.Sc thesis, London, Canada, University Western Ontario, 190 p.

Simard, M., Beaudoin, J., Bernard, J., Hupé, A., 2006, Metallogeny of the Mont-de-l'Aigle IOCG deposits, Gaspé Peninsula, Québec, Canada: Mineralium Deposita, v. 41, v. 607-636.

Skirrow, R.G., 1993, The genesis of gold-copper-bismuth deposits, Tennant Creek, Northern Territory: Unpublished Ph.D. thesis, Canberra, Australian National University, 158 p.

Skirrow, R.G., and Walshe, J.L., 2002, Reduced and oxidized Au-Cu-Bi iron oxide deposits of the Tenant Creek Inlier, Australia: an integrated geologic and chemical model: Economic Geology, v. 97, p. 1167-1202.

Slack, J., 2012, Strata bound Fe-Co-Cu-Au-Bi-Y-REE deposits of Idaho Cobalt belt: multistage, hydrothermal mineralization in a magmatic-related iron oxide copper-gold system: Economic Geology, v. 107, p. 1089-1113.

Smith, M.P., Gleeson, S.A., Yardley, B.W.D., Hydrothermal evolution and metal transport in the Kiruna district, Sweden: Constrasting metal behavior in aqueous and aqueous-carbonic brines: Geochimica et Cosmochima Act, v. 102, p. 89-112.

Smoliar, M.I., Walker, R.J., Morgan, J.W., 1996: Re-Os ages of Group IIA, IIIA, IVA, and IVB iron meteorites: Nature, v. 271, p. 1099-1102.

Stein, H.J., Markey, R.J., Morgan, J.W., Hannah, J.L., Scherstén, A., 2001: The remarkable Re-Os molybdenite chronometer in molybdenite: how and why it works: Terra Nova, v. 13, p. 479-486.

Steele-Maclnnis. M., Bodnar, R.J., and Naden, J., 2011, Numerical model to determine the composition of H2O-NaCl-CaCl2 fluid inclusions based on microthermometric and microanalytical data; Geochimica et Cosmochimica Acta, v. 75, p. 21-40.

Sterner, S.S., Hall, D.L., and Bodnar, R.J., 1988, Synthetic fluid inclsuions. V. Solubility relations in the system NaCl-KCl-H2O under vapor-saturated conditions: Geochemica et Cosmochimica Acta, v. 52, p. 989-1005.

Somarin, A.K., and Mumin, H.A., 2013, P-T composition and evolution of paleofluids in the Paleoproterozoic Mag Hill IOCG system, Contact Lake, Northwest Territories, Canada: Mineralium Deposita, doi 10.1007/s00126-013-0482-3.

Taylor, H.P., 1979, Oxygen and hydrogen isotope relationships in hydrothermal mineral deposits, in Barnes, H.L., ed., Geochemistry of Hydrothermal Ore Deposits, New York, p. 236–277.

Taylor, B.E., 2004, Biogenic and thermogenic sulfate reduction in the Sullivan Pb-Zn-Ag deposit, British Columbia (Canada): Evidence from microisotopic analysis of carbonate and sulfide in bedded ores: Chemical Geology, v. 204, p. 215-236.

Tichimorowa, M., Grosche, G., Götze, J., Belyatsky, B.V., Savva, E.V., Keller, J., and Todt, W., 2006, The mineral isotope composition of two Precambrian carbonatite complexes from the Kola Alkaline province-Alteration versus primary magmatic signatures: Lithos, v. 91, p. 229-249.

Thorne, W., Hagemann, S., Vennemann, T., Oliver, N., 2009, Oxygen isotope compositions of iron oxides from high-grade BIF-hosted iron ore deposits of the central Hamersley province, Western Australia: constraints on the evolution of hydrothermal fluids: Economic Geology, v. 104, p. 1019-1035.

Tooth B., Ciobanu C. L., O'Neill B., Green L., and Brugger J., 2011, Melt formation and gold scavenging from hydrothermal fluids: an experimental study: Geochimica. Cosmochimica. Acta, v. 75, p. 5423-5443.

Turekian, K.K., and Wedephol, K.H., 1961, Distribution of elements in some major units of the Earth's crust: Geological Society of America Bulletin, 72, p. 175-192.

Vahanen, E., 2000, Geology, mineralogy and geochemistry of the (Fe-Co-Au-U) deposits in the Paleoproterozoic Kuusamo Schist Belt Northeastern Finland: Bulletin of Geological Survey of Finland, v. 399, p. 9-229.

Zhang, Y.G., and Frantz, J.D. 1987, Determination of homogenization temperatures and densities of supercritical fluids in the system NaCl-KCl-

CaCl2-H2O using synthetic fluid inclusions: Chemical Geology, v. 64, p. 335-350.

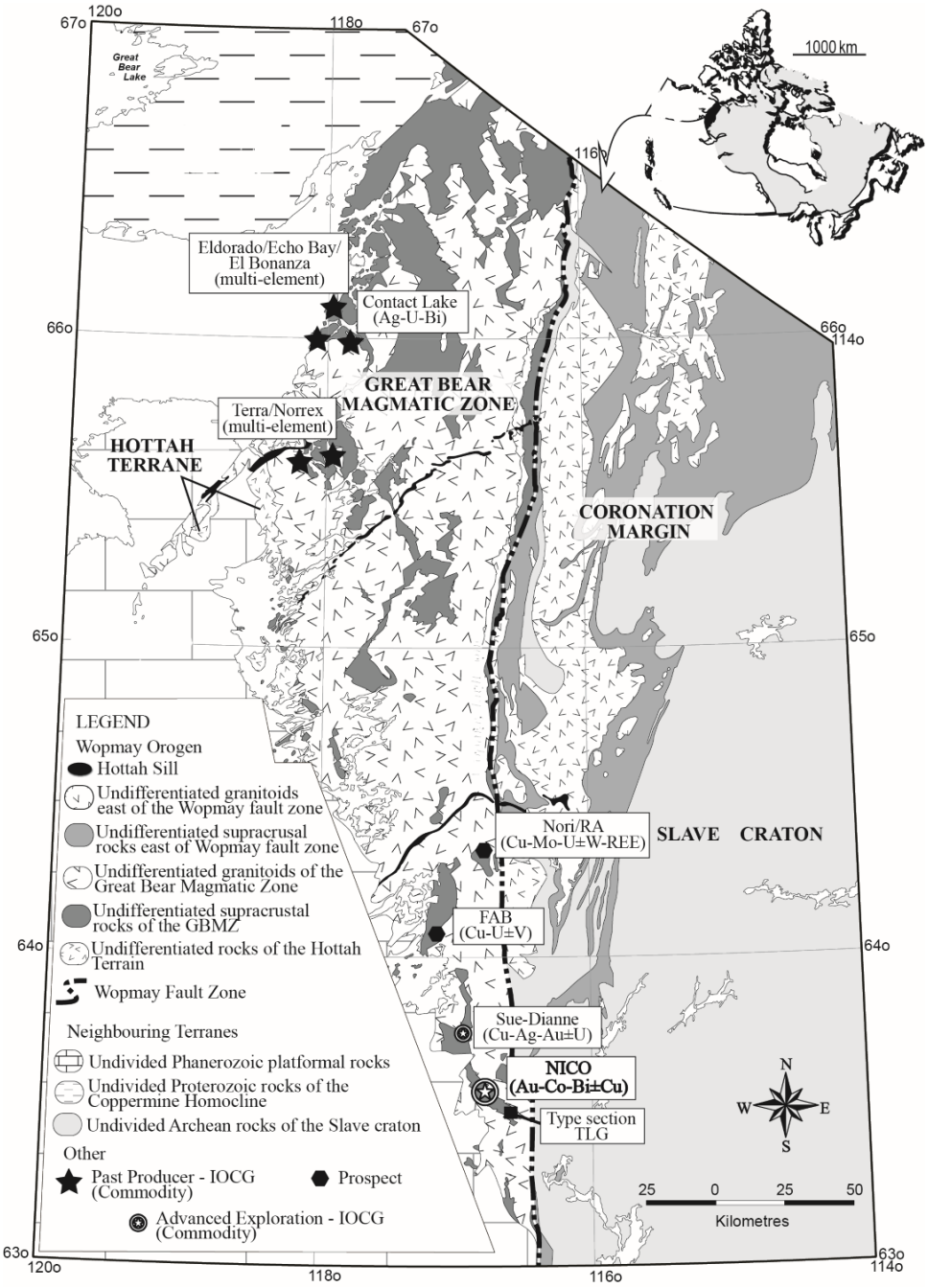

Figure 4.1. Regional Geology of the Wopmay orogen
Geology of the Great Bear Magmatic Zone and the Hottah Terrane is shown, along with selected prospects, past producing mines and advanced exploration projects. Modified after Ootes et al. (2010).

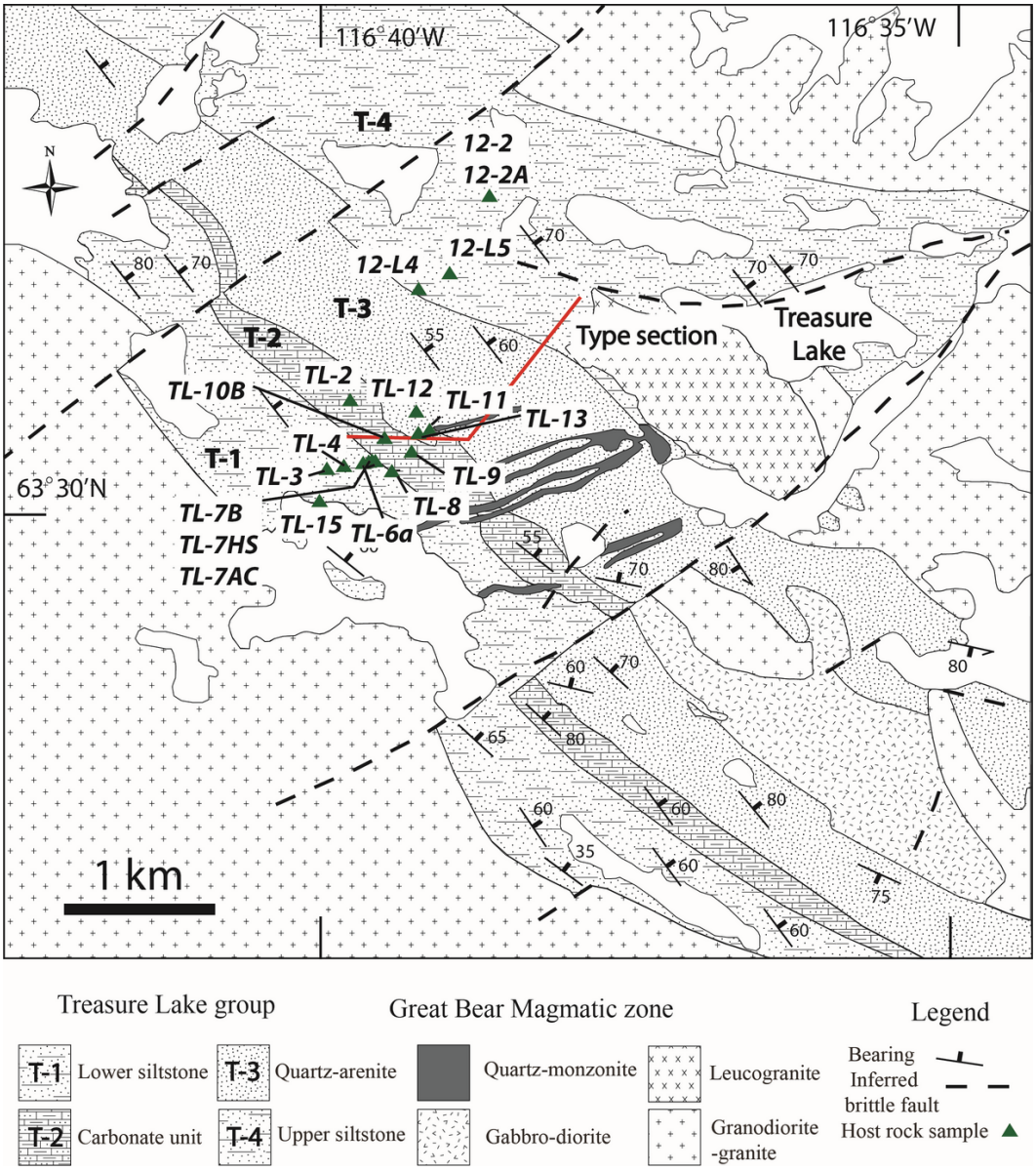

Figure 4.2. Geology of the TLG type section.
Geology of Treasure Lake Group type section after Gandhi and van Breemen (2005). Locations of the bulk rock samples analyzed for trace elements are given.

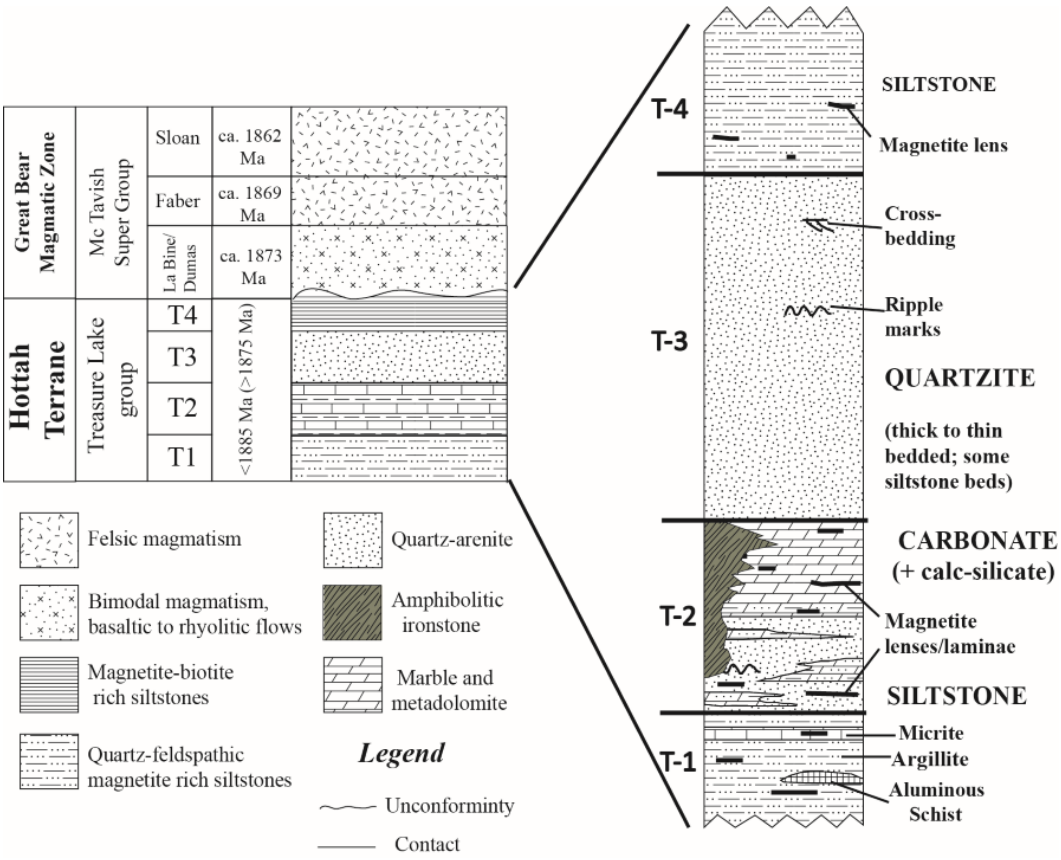

Figure 4.3. Chronostratigraphy of the upper Hottah terrane and the GBMZ Chronostratigraphic column of the GBMZ and the upper Hottah Terrane modified from Acosta-Góngora et al. (in press). Geochronological data from Hildebrand et al. (1987, 2010b), Reichenbach (1991), and Gandhi et al., (2001).

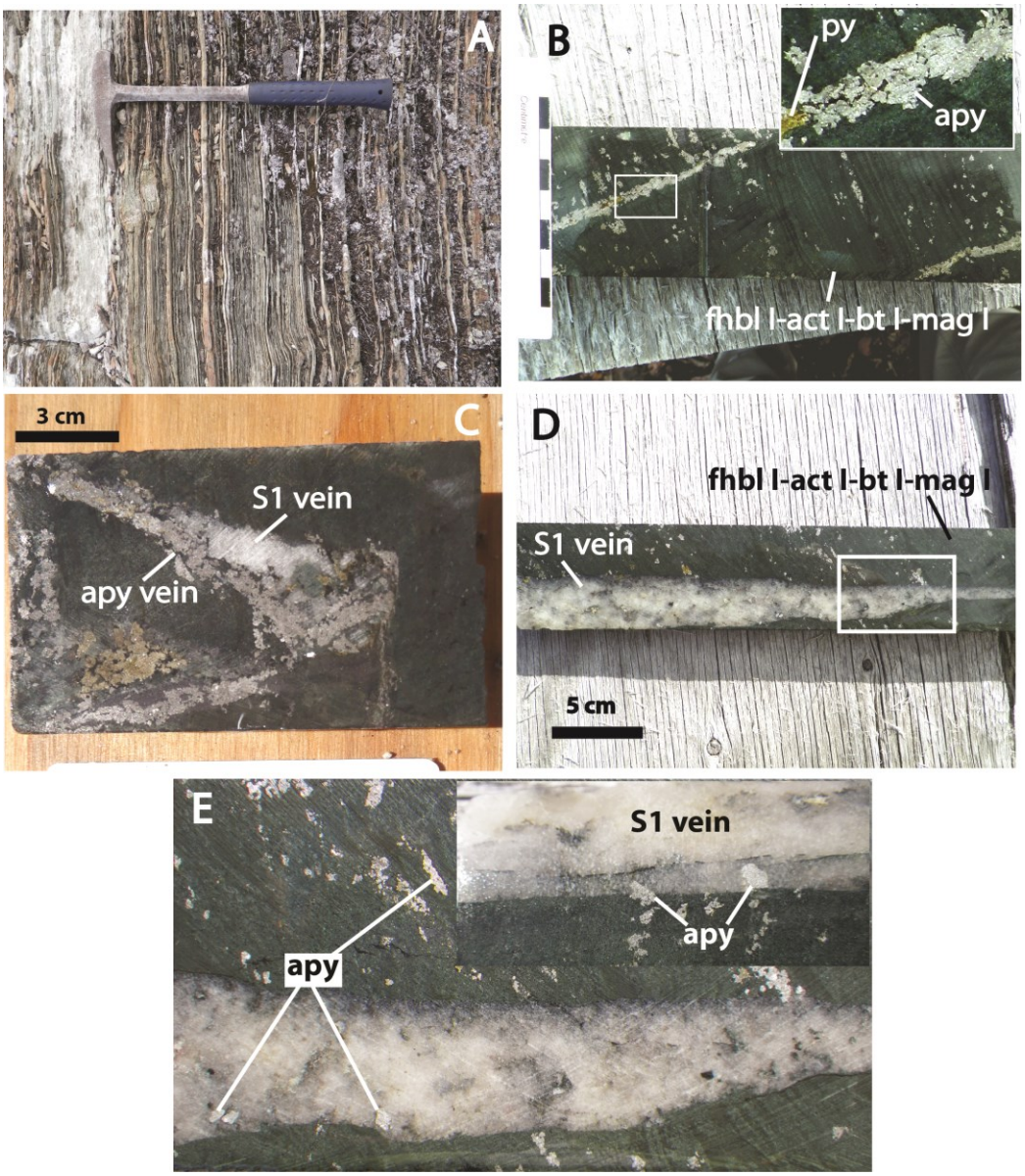

Figure 4.4. The T2 unit of the TLG and occurrence of S1 veins in NICO
(A) Bedded T2 Carbonate unit of the TLG type section. (B) Early stratabound Ca-Fe-K alteration assablage comprised by ferrohornblende (fhbl) I, biotite (bt) I, actinolite (act) I, and magnetite (mag) I. The assemblage is crosscut by Co-rich arsenopyrite (apy)-pyrite (py) veins. (C) Quartz vein (S1) crosscutting Ca-Fe-K alteration and overprinted by later arsenopyrite vein. (D) Disseminated arsenopyrite (apy) hosted by Ca-Fe-alteration and S1 veins. (E) Inset from D. Arsenopyrite (apy) occurs within the S1 vein. The inset in the upper right corner clearly shows how arsenopyrite is overprinting the S1 vein.

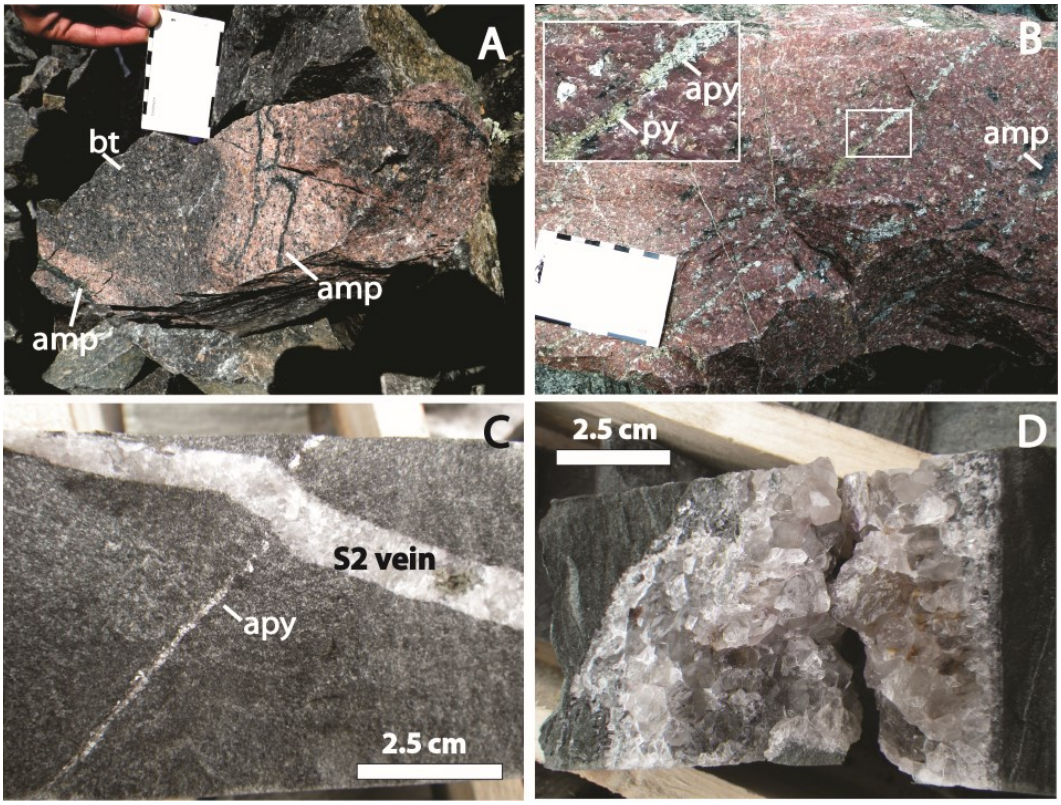

Figure 4.5. Alteration/mineralization in porphyries and S2 and S3 vein sets
(A) Potassically altered porphyry overprinted by a biotite±magnetite alteration front. (B) Potassically altered porphyry hosting Co-rich arsenopyrite mineralization. (C) Arsenopyrite microvein crosscut by a S2 post-ore barren quartz vein. (D) Coarse grained S3 vein set crosscutting the Ca-Fe-K altered TLG.

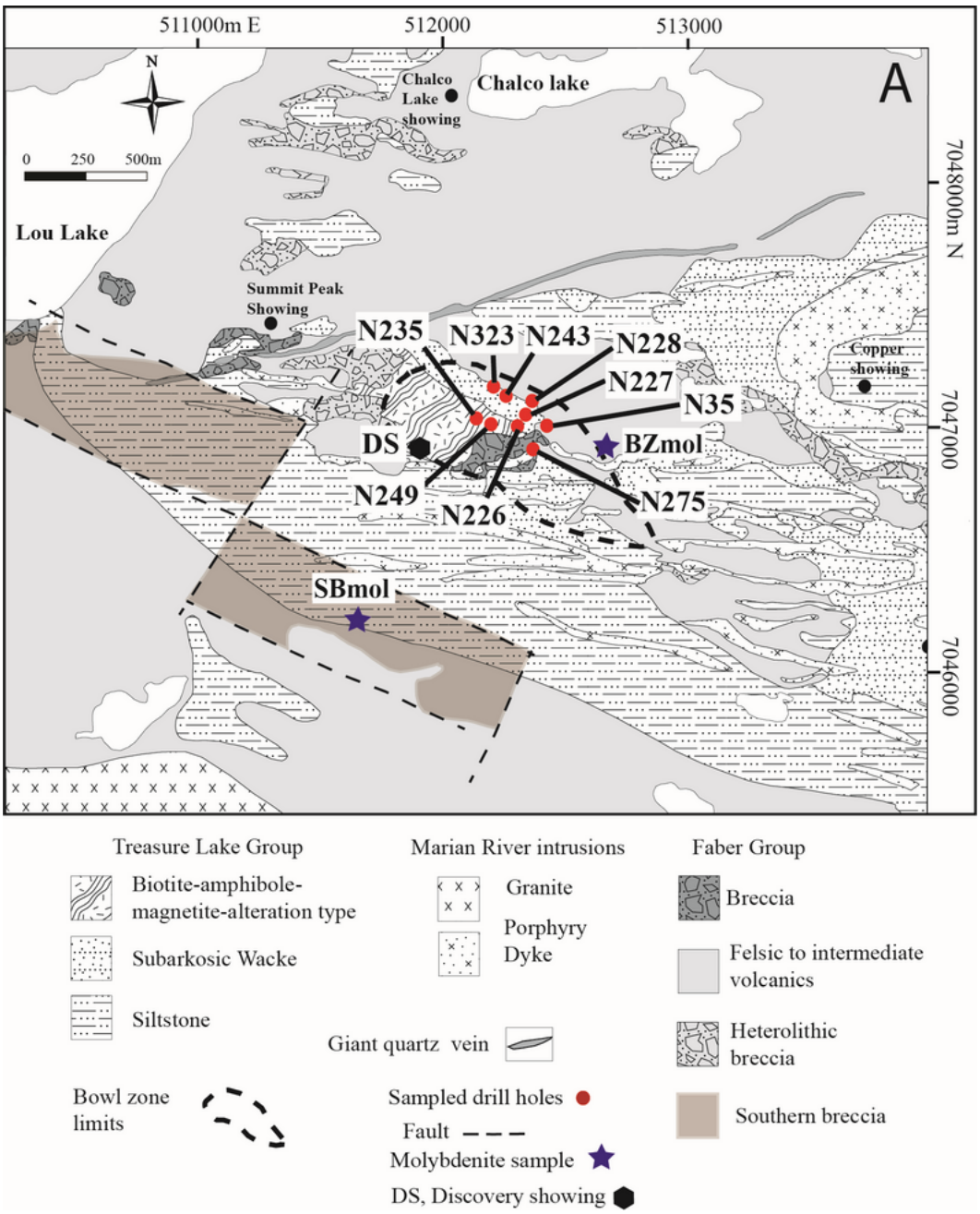

Figure 4.6. Geology of the NICO deposit
Geology after Goad et al. (2000). Drill-hole sampled for S isotopes, fluid inclusions and locations of the molybdenite samples used for Re-Os dating are given.

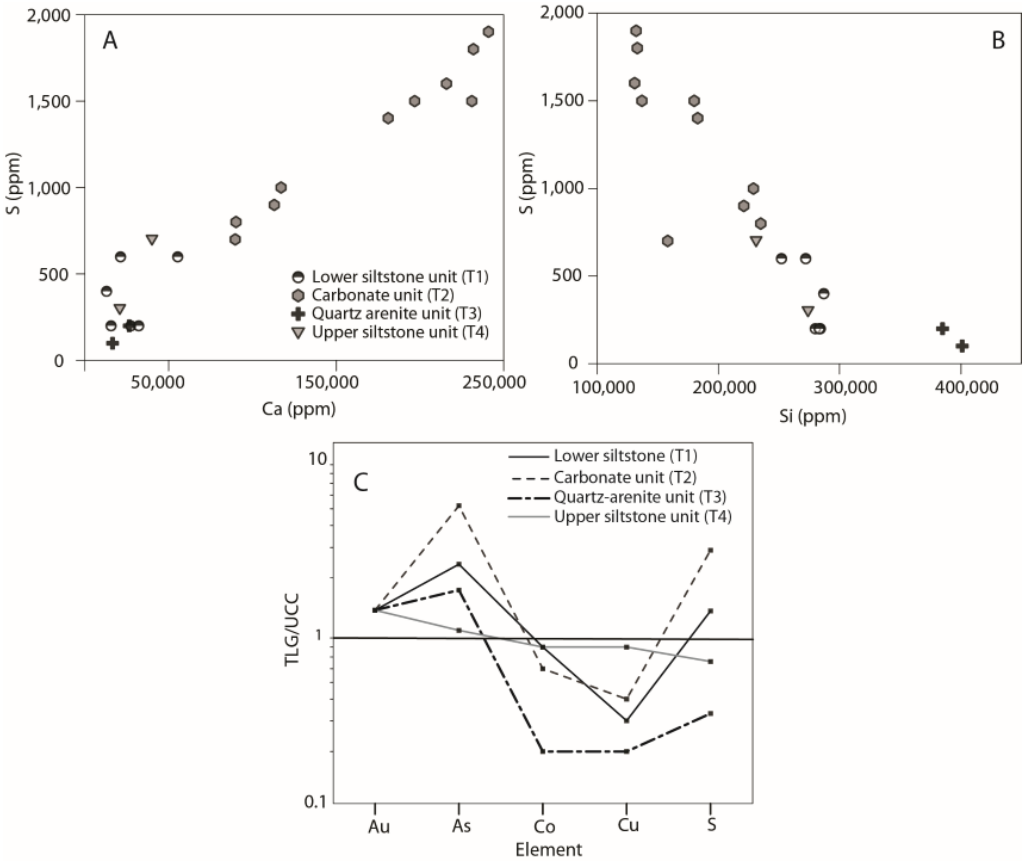

Figure 4.7. Major and trace element plots from the TLG
(A) Correlation between Si and Ca in the TLG and (B) correlation between S and Si. (C) Relative abundance of Au, As, Co, Cu, and S of the TLG compared to the that of the upper continental crust (UCC). Ratios >1 represent a relative enrichment of the TLG over UCC, and values <1, the opposite. Upper continental crust values (Rudnick and Gao, 2003).

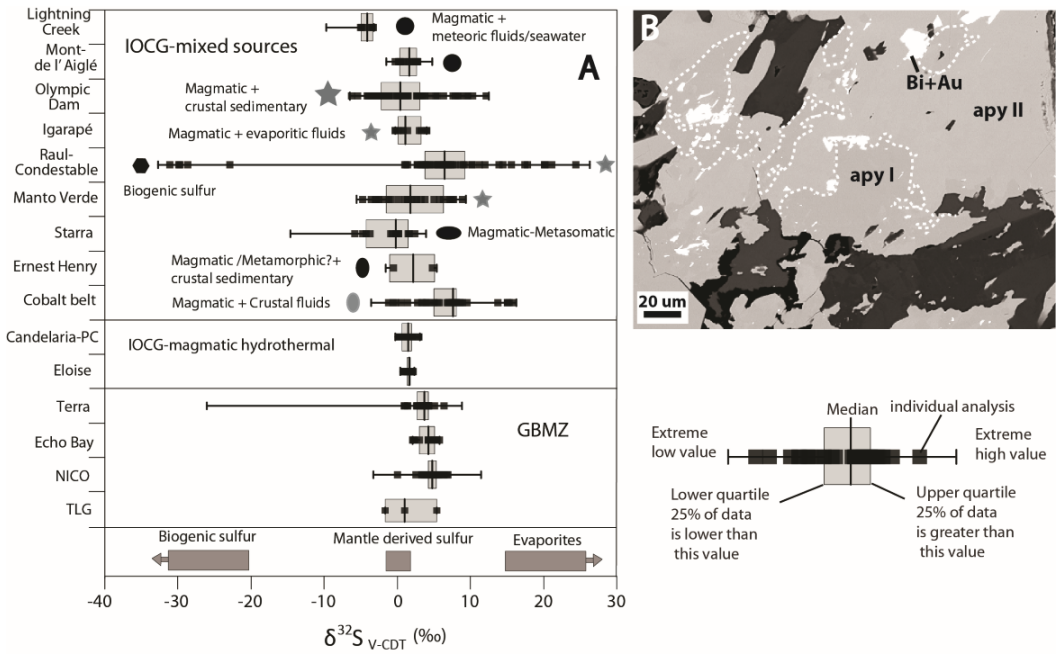

Figure 4.8. Distribution of S isotopes in different IOCG systems
(A) Comparison of the $\delta^{34}S$ values from the NICO deposit with other IOCG deposits from Peru, Australia, and Brazil. Symbols indicate inferred fluid sources in deposits where fluid mixing is proposed. Data from Robinson (1971), Badham (1973), Skirrow (1993), Rotherham et al. (1998), Perring et al. (2000), Baker et al. (2001), Marschik and Fontboté (2001), Mark et al. (2005), Simard et al. (2006), Bastrakov et al. (2007), Benavides et al. (2007), Dreher et al. (2008) and de Haller and Fontboté (2009), Johnson et al. (2012). (B) Occurrence of irregular zoning as arsenopyrite I is replaced by arsenopyrite II (dashed line highlights zones of apy).

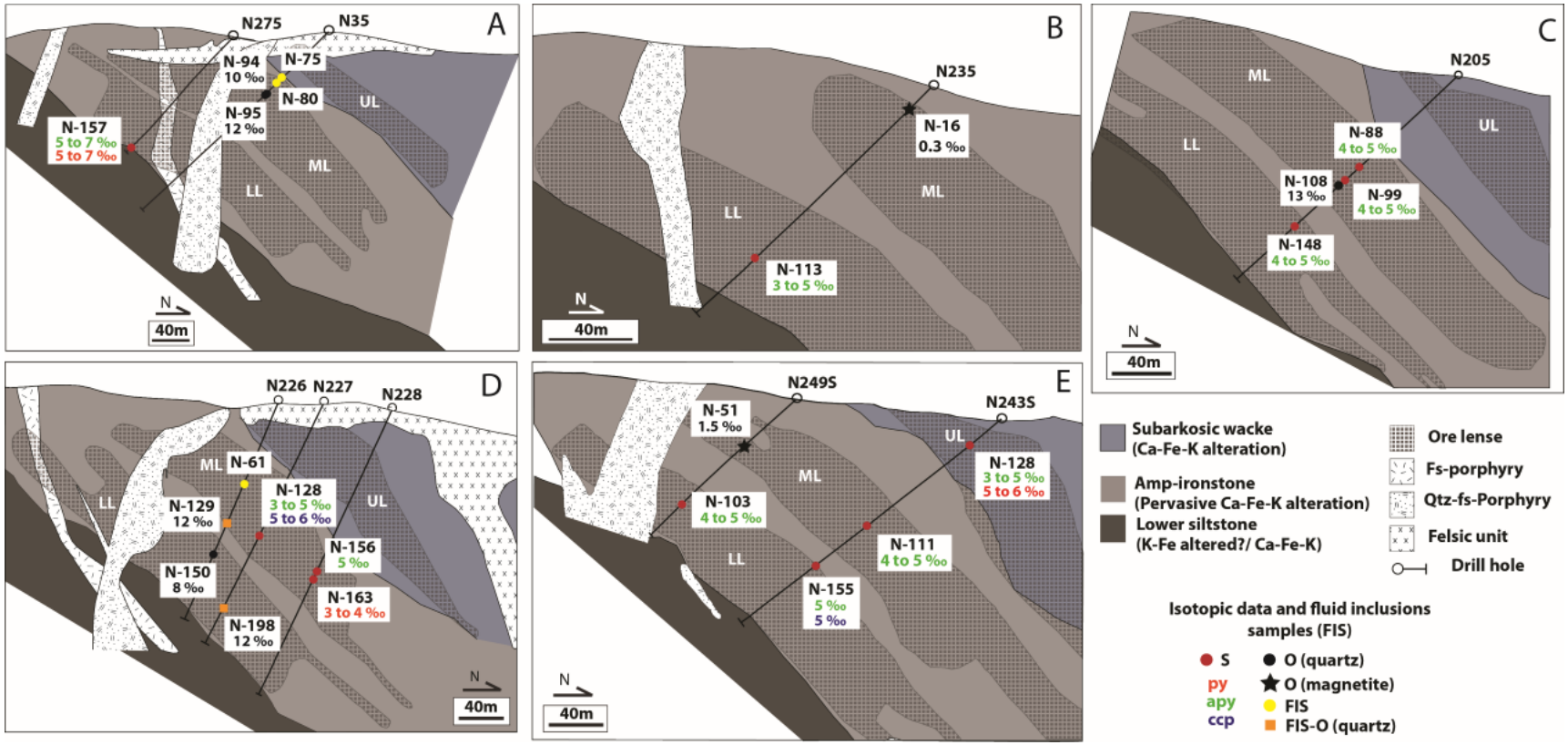

Figure 4.9. Location of the drill-hole samples analyzed for S, C and O isotopes and fluid inclusions studies in cross-section.

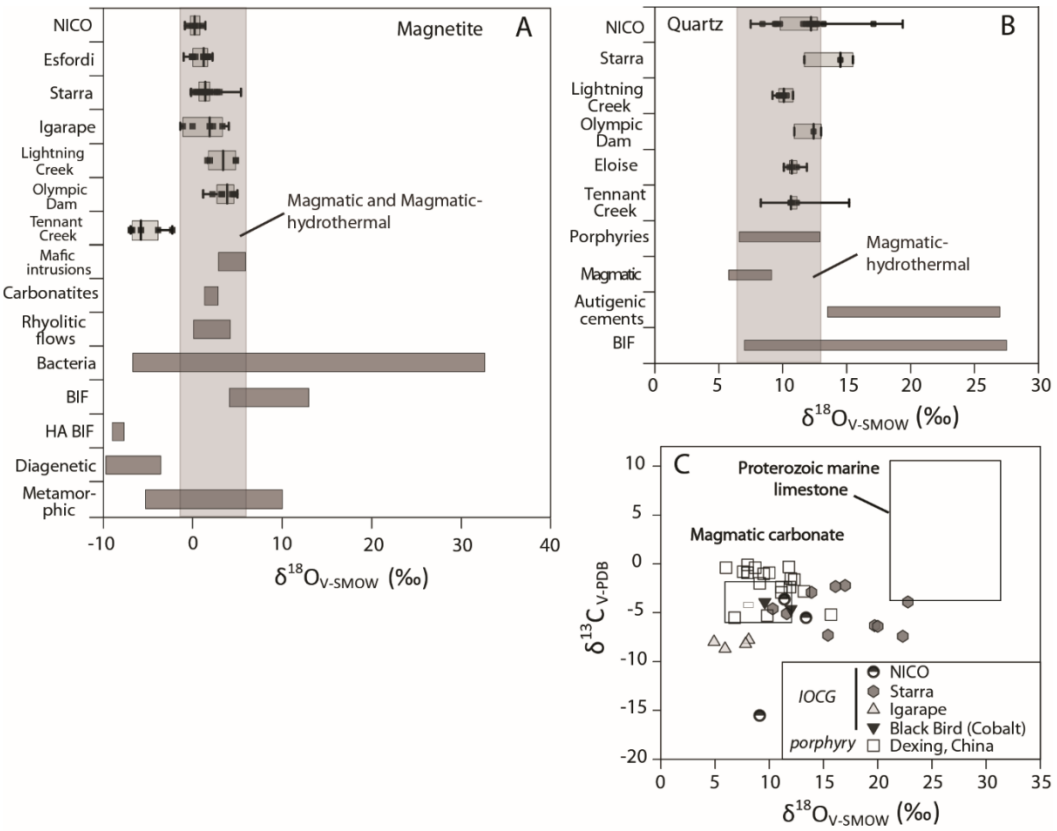

Figure 4.10. Isotopic data (O and C) from NICO and other IOCG deposits
(A) Comparison of magnetite $\delta^{18}O$ values in the NICO deposit with other IOCG deposits from Australia and Brazil, and magnetite from other geological settings. Data from Hangari et al. (1980), Skirrow (1993), Rotherham et al. (1998), Mandernack et al. (1999), Dreher et al. (2008), Perring et al. (2000), Bindeman and Valley (2003),Tichomirowa et al. (2006), Bastrakov et al. (2007), Morteza et al. (2007), Thorne et al. (2009), Ganino et al. (2013). (B) Comparison of quartz $\delta^{18}O$ values in the NICO deposit with other IOCG deposits from Australia and Brazil and quartz from other geological settings. Sheppard et al. (1971), Skirrow (1993), Rotherham et al. (1998), Perring et al. (2000), Bindeman and Valley (2003), Bastrakov et al. (2007), Marin et al. (2010), Heck et al. (2011). (C) Comparison of the $\delta^{18}O$ and $\delta^{13}C$ values of NICO calcite with other IOCG and porphyry calcites. Data from Rotherham et al. (1998), Dreher et al. (2008), Li and Sasaki (2007) and Calagari (2003). Fields of the Proterozoic limestones and magmatic carbon from Santos et al. (2000) and Deines (1980).

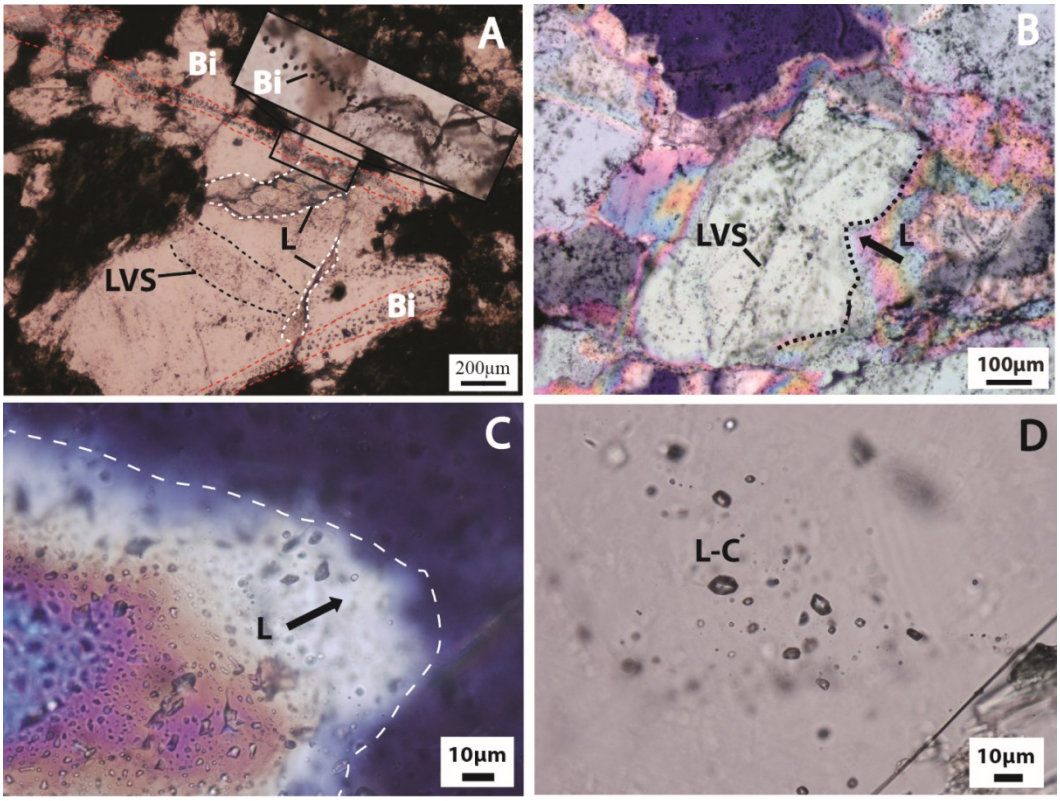

Figure 4.11. Summary of fluid inclusions types in S1veins
Quartz from the S1 veins. (A) Paragenetic relationships between the pre-ore LVS and L and the Bi-trails containing LV- and LVS-Bi. (B) Recrystallization rim containing L inclusions overgrowing secondary LVS inclusions. (C) Zoom in of the L inclsuions. (D) Unknown CO_2 rich L-C inclusions.

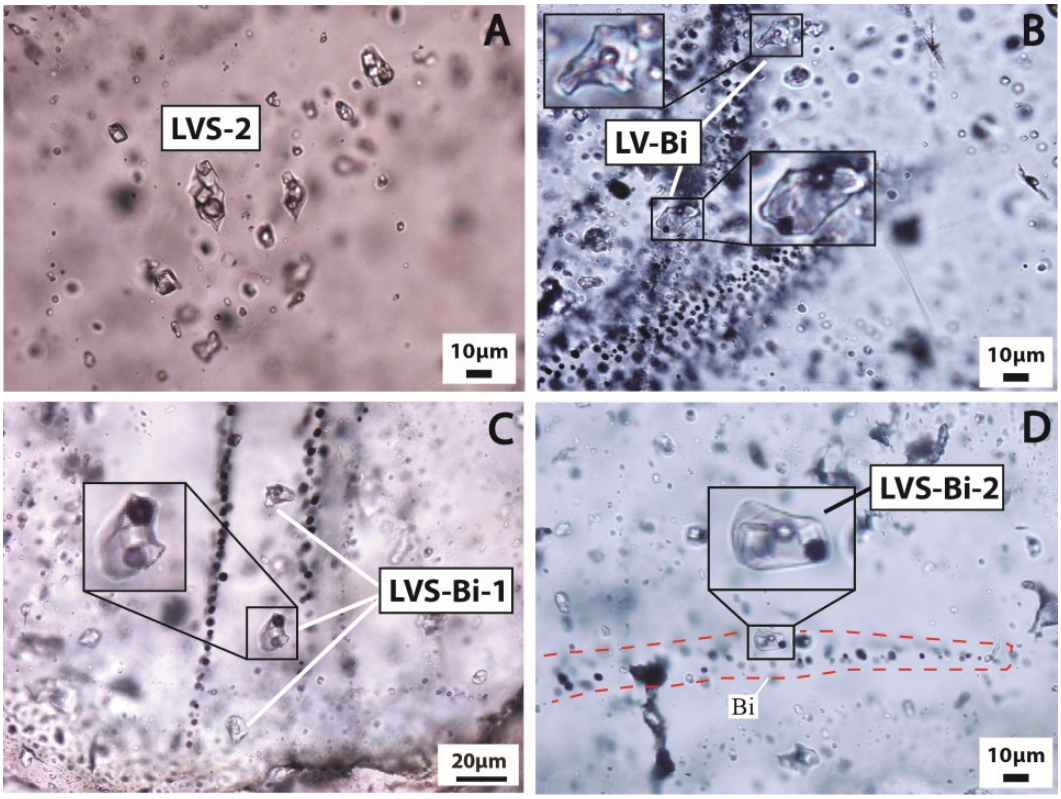

Figure 4.12. Summary of LVS and Bi-bearing fluid inclusions types in S1 Quartz from the S1 veins. (A) LVS-2 inclusions, pre-dating the Bi-mineralization. (B) Native Bi trails having LV-Bi fluid inclusions, where some of these contain native Bi. (C) Native Bi trails having LVS-Bi-1 inclusions. In some cases native Bi occurs within these inclusions. (D) Secondary multisolid Bi-bearing inclusions (LVS-Bi-2).

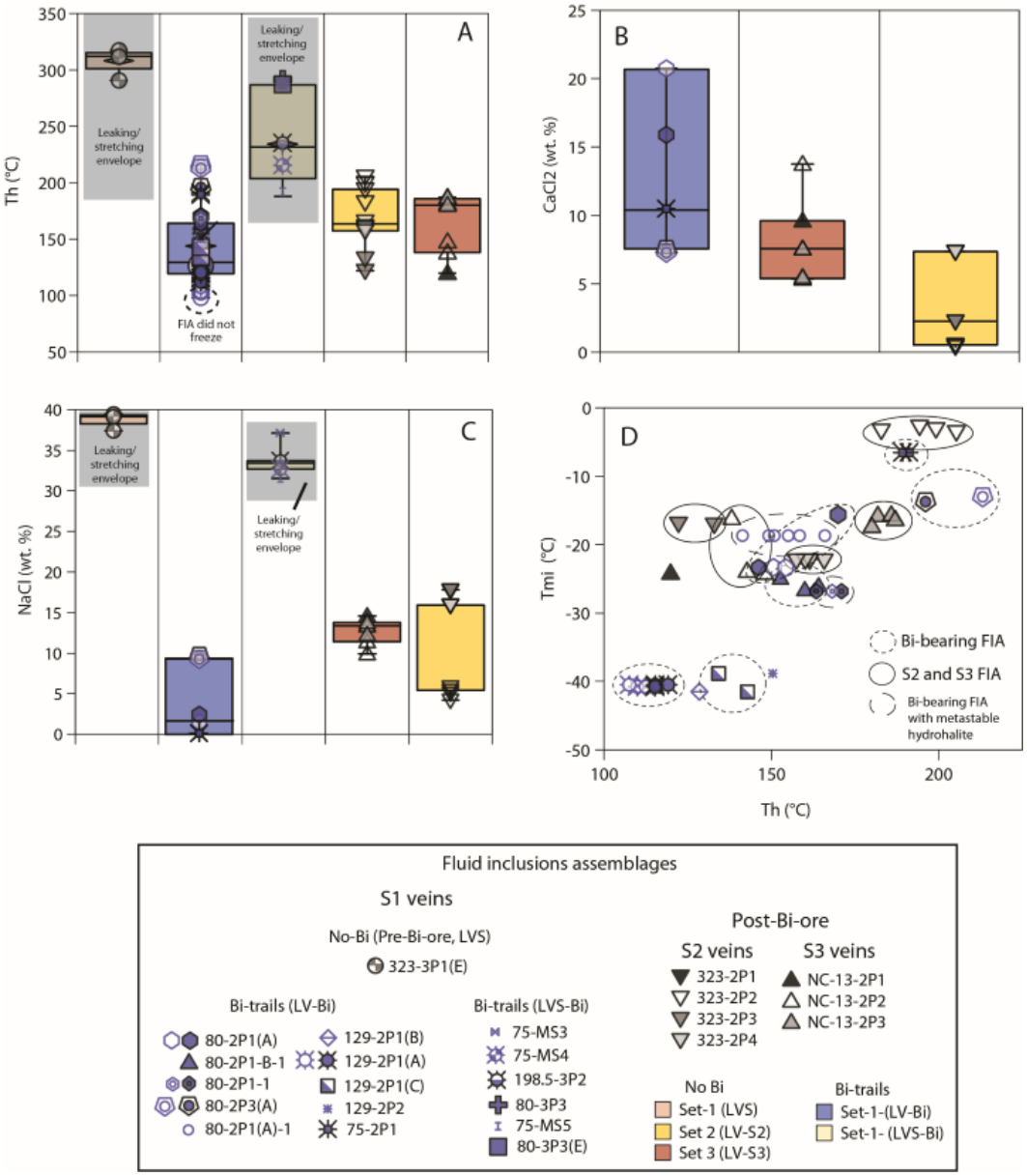

Figure 4.13. Fluid inclusion data from the NICO deposit
(A) Distribution of *T*h. for S1, S2 and S3 fluid inclusions, (B) Salinity of inclusions in terms of wt. % NaClequiv. (C) Salinity of S1 (Bi-rich), S2 and S3 LV inclusions in terms of wt. % $CaCl_2$ equiv. (D) Positive correlation of the LV-Bi inclusions, suggesting multiple magmatic-hydrothermal pulses, changing in composition and temperature with time. Open blue symbols represent inclusions in the same Bi trail, but not having Bi solids.

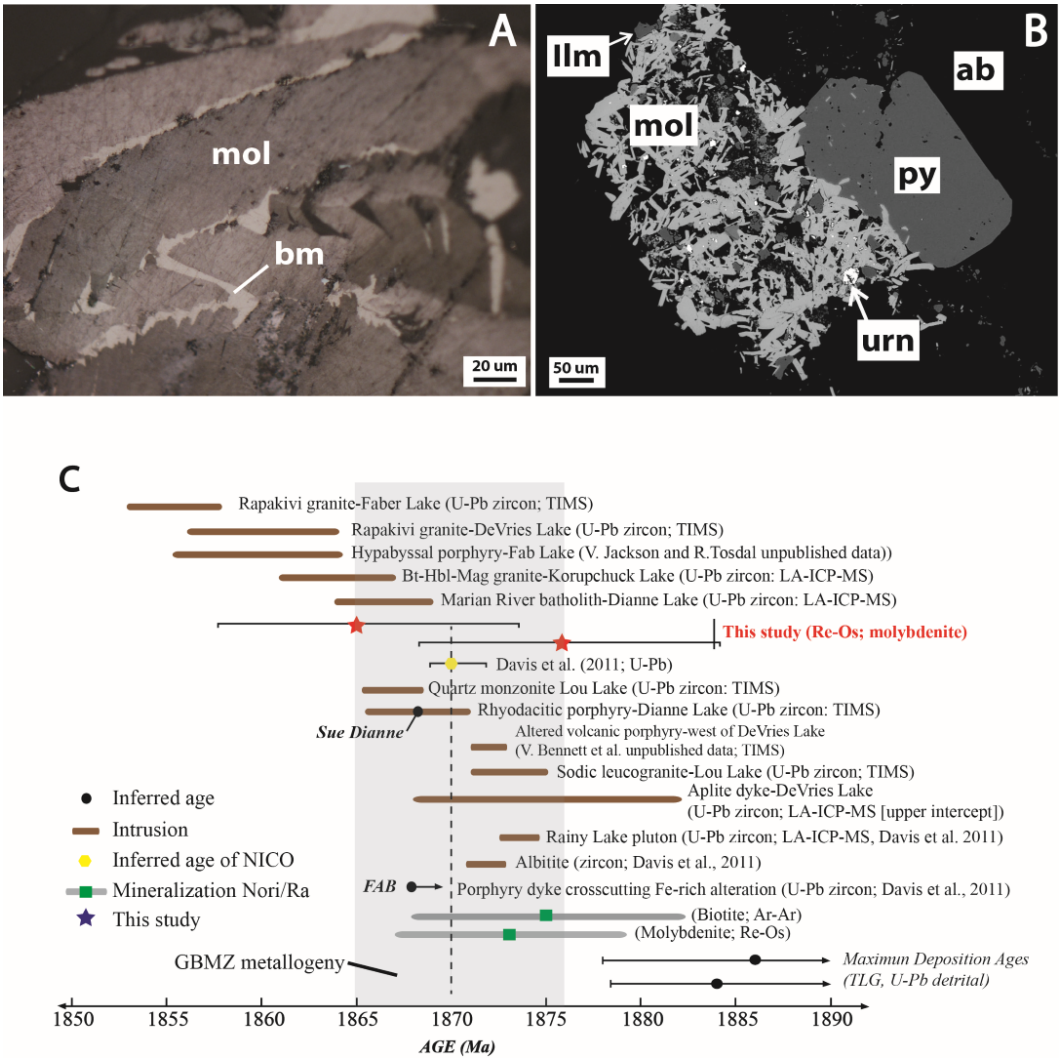

Figure 4.14. Molydenite dating and metallogeny of the GBMZ IOCG systems (A) Deformed molybdenite from the Bowl Zone replaced along the cleavage in bismuthinite. (B) Molybdenite in textural equilibrium with uraninite and pyrite at the Southern Breccia zone. (C) Summary of geochronological constraints in the GBMZ and new Re-Os molybdenite ages from the Bowl Zone and Southern Breccia (modified after Ootes et al., 2010). The U-Pb data is from Gandhi et al. (2001) and Bennett and Rivers (2006), unless otherwise cited.

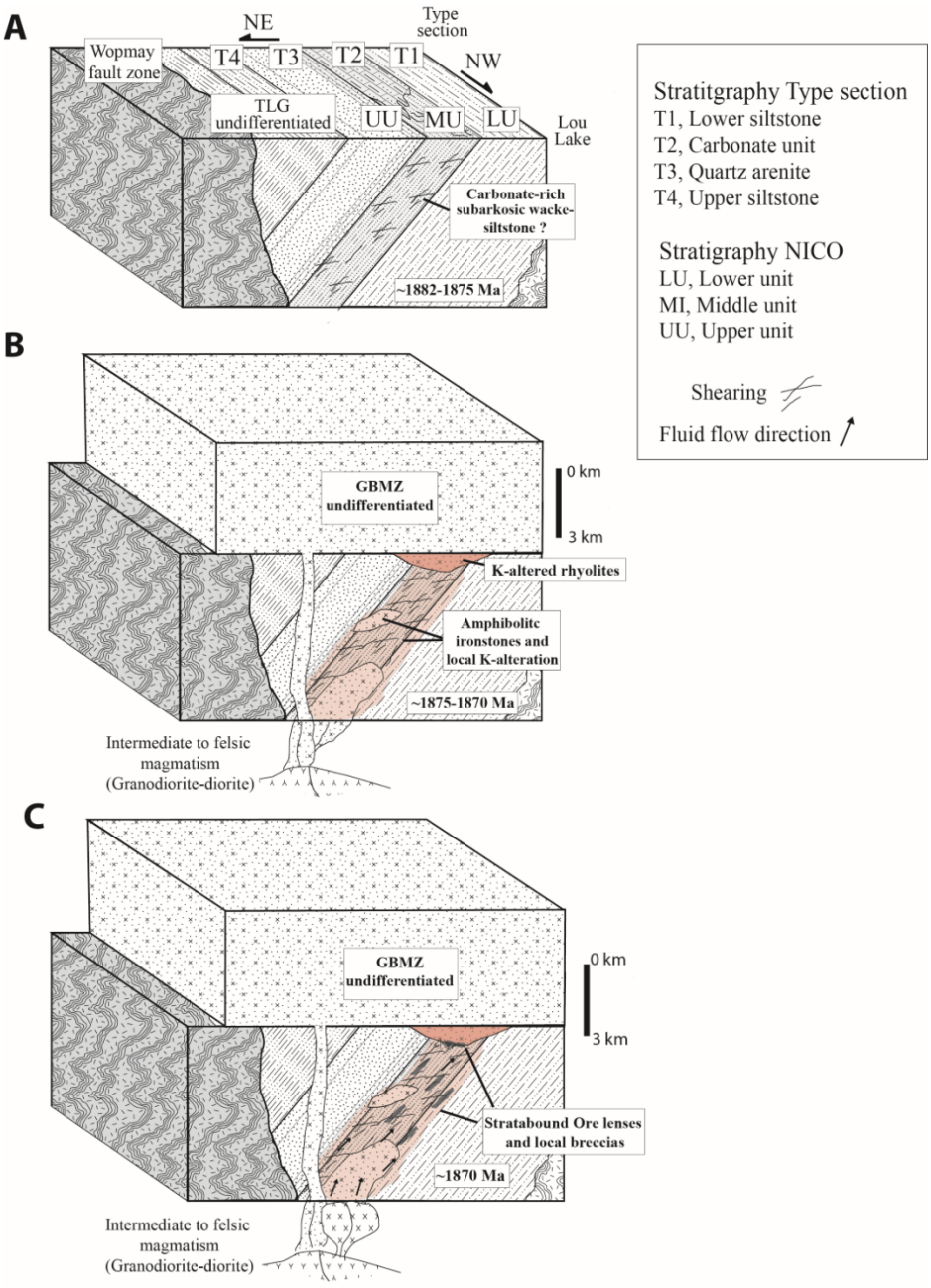

Figure 4.15. Genetic model of NICO deposit

(A) Schematic distribution of the TLG units at the type section and the Lou Lake, before the emplacement of the GBMZ. Foliation and localized shear zones probably developed during regional metamorphism. **(B)** Genetic model of the NICO deposit showing early and pervasive Ca-Fe-K alteration associated with emplacement of Great Bear magmatic rocks resulted in the formation of the amphibolitic ironstones. **(C)** Ore-bearing fluids interacting with the amphibolitic ironstones (~7 km depth) triggered the emplacement of the prograde Co-rich Ca-Fe-K alteration (pro-grade mineralization), followed by the Bi-Au-Cu rich retrograde event.

Table 4.1. Whole rock geochemistry data from the TLG type section

Sample	Alteration	Fe(wt. %)	Ca(wt. %)	K(wt. %)	Si(wt. %)	Co* (ppm)	S (ppm)	As (ppm)	Bi* (ppm)	Cu (ppm)	Au (ppb)	Unit
TL-15	Incipient K-Fe (bt-k-fsp-mag)	10.1	1.29	2.6	28.7	18.1	400	< 5	< 2	4	< 1	Lower siltstone unit (T1)
TL-3	Incipient K-Fe (bt-k-fsp-mag)	5.78	2.12	4.3	27.2	18.7	600	7	< 2	19	< 1	Lower siltstone unit (T1)
TL-4	Incipient amp	3.18	2.73	6.2	28.4	10.4	200	9	<2	2	<1	Lower siltstone unit (T1)
TL-6A	Advanced K (k-fsp), Ep-Grt	3.69	1.56	5.2	28.3	12.1	200	9	< 2	7	5	Lower siltstone at the T1-T2 contact
TL-7B	Moderate Ep, K (k-fsp), ±Tur	2.08	24.1	2.6	13.2	7.8	1900	25	< 2	3	6	Carbonate unit at the T1-T2 contact
TL-7HS	Moderate Ep, K (k-fsp), ±Tur	2.32	23.2	2.3	13.3	8.4	1800	36	< 2	3	< 1	Carbonate unit at the T1-T2 contact
TL-7AC	Moderate Ep, K (k-fsp), ±Tur	2.42	23.1	2.2	13.7	8.7	1500	36	< 2	3	< 1	Carbonate unit (T2)
TL-2A	Moderate Ep, K (k-fsp), ±Tur	1.92	19.7	3	18	8.4	1500	25	< 2	15	6	Carbonate unit (T2)
TL-8	Moderate Ep, K (k-fsp), ±Tur	7.14	11.7	2	22.9	16.1	1000	32	<2	5	<1	Carbonate unit (T2)
TL-9A	Advanced Ep-Grt, Ca-Fe (amph)	2.79	18.1	2.7	18.3	9.3	1400	26	< 2	2	7	Carbonate unit (T2)
TL-10B	Advanced K (k-fsp),Ca-Fe (amp-mag)	8.96	11.3	5.2	22.1	4.6	900	95	< 2	3	6	Carbonate unit (T2)
TL-13	Moderate K-Fe (bt-k-fsp-cpx)	1.91	21.6	2.7	13.1	4.4	1600	18	<2	3	< 1	Carbonate unit (T2)
TL-11	Incipient K(k-fsp)	2.37	2.65	3.3	38.5	2.9	200	14	< 2	3	< 1	Quartz arenite unit (T3)
TL-12	Incipient K(k-fsp)	1.86	1.64	2.5	40.1	3.2	100	15	< 2	3	5	Quartz arenite unit (T3)
12-L4b	Moderate mag-chl	3.2	0.25	3.5	38.5	2.8	<100	< 5	< 2	9	< 1	Quartz arenite unit (T3-T4 contact)
12-L2a	Incipient amp-k-fsp?	8.68	2.07	3.4	27.4	30	300	< 5	< 2	33	< 1	Upper siltstone (T4)
12-L2	Incipient amp-k-fsp?	15.2	4	3.1	23.1	5.6	700	< 5	< 2	39	< 1	Upper siltstone (T4)

12-L5	Moderate K(k-fsp-bt)	7.65	0.65	3.9	26.7	11.3	<100	< 5	< 2	8	< 1	Upper siltstone (T4)

Abbreviations. Amphibole = amp, biotite = bt, calcite = calc, clinopyroxene = cpx; chlorite = chl, epidote = ep, garnet =grt, magnetite,= mag, potassic feldspar = k-fsp, tourmaline = tur

Incipient: alteration overprinted <5% of the precursor hostrock

Moderate: alteration overprinted >5% to 15% of the precursor rock

Advanced: alteration has overprinted >15% to 30% of the precursor host rock

Data for Co and Bi taken from Acosta et al. (in press)

Table 4.2. Representative stable isotope data (‰) from NICO deposit

Sample	Mineral	Host rock	$\delta^{18}O$	$\delta^{32}S$	$\delta^{13}C$	Comment
CQA-D	MagI	Amp-ironstone	0.3			Pre-ore replacement along the bedding
CQA-F	Mag I	Amp-ironstone	1.1			Pre-ore replacement along the bedding
CQA-F1	Mag I	Amp-ironstone	0.6			Pre-ore mag vein
CQA-G2	Mag I	Amp-ironstone	-0.5			Pre-ore replacement along the bedding
CQA-G	Mag I	Amp-ironstone	-0.8			Pre-ore mag vein (mag I)
128-N222	Mag II	Amp-ironstone	0.0			Apy vein
16-N235 *(N-16)*	Mag II	Amp-ironstone	0.3			Apy vein
51-N249 *(N-51)*	Mag II	Amp-ironstone	1.5			Apy vein
NC-29	Calcite	Amp-ironstone	13.4		-5.5	Coarse grained qz-calc-vein (S3)
NC-7-11	Calcite	K-altered porphyry	9.1		-15.5	Coarse grained qz-calc-vein (S3)
NC-226 *(N-129)*	Calcite	Amp-ironstone	11.4		-3.6	Qz±amp-ksp vein pre-apy (S1)
108-N205	Qz	Amp-ironstone	12.7			Qz±amp vein pre-apy (S1)
NC-28	Qz	K-altered porphyry	12.2			coarse grained vein (S3)
NC-108 *(N-108)*	Qz	Biotite altered quartz-arenite	13.2			Qz crosscutting apy vein (S2)
NC-105	Qz	Biotite altered quartz-arenite	19.4			Qz vein crosscuting apy (S2)
NC-23	Qz	K-altered porpyry	11.6			Qz-calc coarse grained vein (S3)
NC-11	Qz	K-altered porpyry	9.4			Qz-calc coarse grained vein (S3)
NC-29	Qz	Amp-ironstone	17.1			Qz-calc coarse grained vein (S3)
N-148/9	Apy	Amp-ironstone		4.6		Apy vein, minor ccp and py
N-148/12	Apy	Amp-ironstone		5.4		Apy vein, minor ccp and py
N-99/4	Apy	Amp-ironstone		4.2		Apy disseminated along the bedding. Minor py and po
N-99/3	Apy	Amp-ironstone		4.6		Apy disseminated along the bedding. Minor py and po
NC-42/3	Apy	K-altered volcanics		11.4		Apy disseminated. Minor py
NC-1/4	Apy	K-altered porpyry		-3.3		Apy disseminated. Minor py
N-103/7	Apy	Amp-ironstone		5.0		Disseminated in patches. Minor native Bi
N-103/8	Apy	Amp-ironstone		3.9		Disseminated in patches. Minor native Bi
N-111/6	Apy	Amp-ironstone		4.1		Apy disseminated along the bedding. Minor ccp, py, native Bi and Au
N-111-9	Apy	Amp-ironstone		4.8		Apy disseminated along the bedding. Minor Bi, ccp and py
N-156/8	Apy	Amp-ironstone		4.8		Apy vein (2.5 cm thick). Minor scheelite, py, ccp, Bi
N-24/8	Py	Biotite altered quartz-arenite		5.1		Apy vein (1 cm thick). Minor ccp and py
N-24/7	Py	Biotite altered quartz-arenite		4.5		Apy vein (1 cm thick). Minor ccp and py
N-163/9	Py	Amp-ironstone		4.3		Deformed apy vein (0.5 cm), minor py,
N-163/8	Py	Amp-ironstone		3.9		Deformed apy vein (0.5 cm), minor py,
N-129/4	Ccp	Amp-ironstone		5.0		Apy vein (2.5 cm thick). Minor scheelite, py, ccp, Bi
N-148/10	Ccp	Amp-ironstone		5.3		Apy vein, minor ccp and py
N-155	Ccp	Amp-ironstone		4.4		Apy disseminated along the bedding. Minor ccp and py

TL-6	BR	Lower siltsone	-1.6	Close to the contact with T2
TL-15	BR	Lower siltsone	5.5	Base of the unit
TL-4	BR	Lower siltsone	1.1	Intermediate portion of T1

Amphibole= Amp, quartz=qz, calcite= calc, magnetite=mag, arsenopyrite=apy, chalcopyrite=ccp, pyrite=py, bulk rock= BR

Samples with the label e.g., N-129/8, refers to sample N-129 and in-situ analysis number 8.

In parenthesis are given the samples names used in Figure 8. For sample N-129, only $\delta^{18}O$ is given map.

Table 4.3. Summary of FIA data from the NICO deposit

Mineral /vein set	Assemblage /n	Age	Type	Te (°C)	Tm_i (°C)	$T_{l\text{-}v}$ (°C)	Th (°C)	Salinity[1] (wt.% NaCl equiv)	Salinity[2] (wt.% $CaCl_2$ equiv)	Comments
Quartz/S1	323-3P1(A)-1/ n=4	PS	LVS-2	n.m.	n.d.	191-208	n.d	>30	n.c.	Leaking/strectching occurred between 191 °C and 350 °C
Quartz/S1	323-3P1(B)-1/ n=3	PS	LVS-2	n.m.	n.d	191-228	n.d	>30	n.c.	Leaking/strectching occurred between 207 °C and 350 °C
Quartz/S1	323-3P1(D)-1/ n=3	PS	LVS-2	n.m.	n.d	182-203	n.d	>30	n.c.	Leaking/strectching occurred between 315 °C and 350 °C
Quartz, S1	323-3P1(A)-2 n=3	PS	LVS-1	n.m.	n.d	148-188	n.d	>30	n.c.	One inclusion leaked at 191 °C
Quartz/S1	323-3P1(B)-2/ n=6	PS	LVS-1	n.m.	n.d	191-207	n.d	>30	n.c.	
Quartz/S1	323-3P1(D)-2 n=3	PS	LVS-1	n.m.	n.d	198-224	n.d	>30	n.c.	One inclusion leaked at 322 °C
Quartz/S1	323-3P1(E) n=6	PS	LVS-1	n.m.	n.d.	194, 210	311, 317	39, 40	n.c.	Two inclusions did not reach Th at 350 °C. Other two inclusions presented changes in L/V ratios after Th_i was reached
Quartz/S1	323-3P1(C)/ n=4	PS	LVS-1	n.m.	n.d.	181-204	>293	>38	n.c.	Inclusions fractured at 293
Quartz/S1	80-CO(A) n=7	Unk	LV-C	n.m.	n.d.	n.m.	24-31	n.c.	n.c.	
Quartz/S1	80-CO(B) n=5	Unk	LV-C	n.m.	n.d.	n.m	30-31	n.m.	n.m.	
Quartz/S1	61-2P1 n=3	S	LV-Bi	n.m.	n.m.	n.m.	98-104	n.c	n.c	Inclusions do not freeze at -134 °C
Quartz/S1	61-2P2 n=5	S	LV-Bi	n.m.	n.m.	n.m.	127-129	n.c	n.c	Inclusions do not freeze at -134 °C
Quartz/S1	60-2P3 n=7	S	LV-Bi	n.m.	n.m.	n.m.	119-126	n.m.	n.m.	Inclusions do not freeze at -134 °C
Quartz/S1	80-2P1(A)/ n=4	S	LV-Bi	-76	-15- to -23	n.m.	146-169	1-2	16-21	Brownish solids formed, and melted by -59 to- -60
Quartz/S1	80-2P1(B)-1/ n=3	S	LV-Bi	-62 to -56	-27 to -25	n.m.	152-164	n.c.	n.c.	Brownish solids formed and melted by -45 °C
Quartz/S1	80-2P1-1/ n=3	S	LV-Bi	-72	-26	n.m.	163-170	n.c	n.c	Brownish solids formed and melted by -60
Quartz/S1	80-2P3(A) n=3	S	LV-Bi	-75	-13.to -14	n.m.	196-216	3-10	8-22	
Quartz/S1	129-2P1(A)/ n=7	S	LV-Bi	-85 to -82	-41	n.m.	107-120	n.c	n.c	Brownish-greenish solids formed and melted by -70
Quartz/S1	129-2P1(C)/ n=2	S	LV-Bi	-60	-41 to -39	n.m.	134, 142	n.c	n.c	Brownish solids formed and melted by -65

Calcite/S1	75-2P1 n=2	S	LV-Bi	-74	-6.50	n.m.	189, 191	0.1	11	Brownish solids formed
Quartz/S1	80-3P3(E) n=1	S	LVS-Bi-1	n.m.	n.m.	220	287	37	n.c	
Quartz/S1	198.5-3P3 n=1	S	LVS-Bi-1	n.m.	n.m.	220	228.	33	n.c	Brownish solids formed and melted by -65
Calcite/S1	75-MS1(A) n=1	S	LVS-Bi-1	n.m.	n.m.	152	n.g.	>30	n.c	
Calcite /S1	75-MS3 n=1	S	LVS-Bi-1	n.m	n.m.	179	286	37	n.c	Brownish solids formed under freezing
Calcite /S1	75-MS5 n=1	S	LVS-Bi-1	n.m.	n.m.	181	192	32	n.c	Brownish solids formed under freezing
Calcite /S1	75-MS1 n=2	S	LVS-Bi-1	n.m	n.m	152-159	n.g	>30	n.c	Brownish solids formed under freezing. Stretched inclusions
Calcite/S1	75-3P1/ n=2	S	LVS-Bi-2	n.m.	n.m.	>159, 198	>243	>34	n.c	Brown solids formed during heating. Leaking occurred at 159 ºC and 243º C.º
Quartz/S2	323-2P2 n=4	PS	LV	-32 to -30	-2 to- -4	n.m.	194-205	4-6	0.4-0.6	
Quartz/S2	323-2P3 n=2	PS	LV	-44	-17	n.m.	122, 133	18	2	
Quartz/S2	323-2P4 n=4	PS	LV	-44	-22	n.m	158-166	16	7	
Quartz/S3	NC-13-2P2 n=2	PS	LV	-59 to -67	-24 to -16.1	n.m.	138, 148	10-11	7-13	Solids with slight brownish tint formed
Quartz/S3	NC-13-2P3 n=4	PS	LV	-66 to -67	-17 to -16	n.m	180-187	13	5	Solids with slight brownish tint formed

n, number of inclusions measured per assemblage; n.d., not determined; n.m., not measured; n.c., not calculated
Series 61, 75, 80, 129 and 198 correspond with samplesN-61, N-75, N-80, N-129, and N-198 in Figure 8.

Table 4.4. Pressure correction on LV-Bi inclusions

FIA /flinc number	wt. % NaCl equiv	wt.% CaCl2 equiv	NaCl (M)	$CaCl_2$ (M)	Th	Bars	Depth (km)
80-2P1(A)/7	1.5	20.7	0.4	3.0	150.6	2424.2	8.1
80-2P1(A)/14	2.4	15.9	0.7	2.3	169.9	2028.7	6.8
80-2P1-1/6	15.7	11.6	4.3	1.7	163.4	2269.1	7.6
80-2P1-1/5	15.8	11.6	4.3	1.7	170.0	2099.6	7.0
80-2P1-1/7	9.7	7.5	2.6	1.1	168.1	2037.6	6.8
75-2P1/1-2	0.1	10.5	0.0	1.5	190.0	1478.5	4.9

The isochores used for the pressure correction were calculated by using Zhang and Frantz (1987) equations
M, molality
FIA, Fluid inclusion assemblage

Table 4.5. Results of Re-Os of molybdenite of NICO deposit

Location/ *sample*	Re (ppm)	±2σ	^{187}Re (ppb)	±2σ	^{187}Os (ppb)	±2σ	Model Age (Ma)	±2σ absolute	Reported Age
Bowl Zone/*CQA*	47.7	0.13	29986	83.7	946.4	1.76	1865	9	1865±9
Souther Breccia/ *SB(11)*	26.66	0.08	18645	48	592.4	0.4	1877	8	1877±8

Coordinates: SB(11), 7046031.250 mN, 51640.625 mE and CQA, 7046594,00 mN, 512478,00 mE (Zone 11, NAD 83).

[a]Includes 0.31% uncertainity in decay constant

5 Constraints on the origin of polymetallic (Cu-Au-Co-Bi-U±Ag) iron-oxide-dominated systems in the Great Bear magmatic zone

5.1 Introduction

In the Paleoproterozoic Great Bear magmatic zone (GMBZ), Northwest Territories, Canada, a number of iron oxide-dominated systems host polymetallic mineralization (Fig. 5.1). It has been suggested that these mineralized and heavily altered systems are analogous to Iron Oxide-Copper-Gold deposits in Australia and South America (e.g., Olympic Dam, Ernest Henry, and Tennant Creek district, La Candelaria, Manto Verde; Williams, 1998; Oreskes and Einaudi, 1990; Marschik and Fontboté, 2001; Skirrow and Walshe, 2002). Since the pioneering work of Gandhi (1994), the composition and distribution of the Great Bear IOCG systems has received considerable attention (e.g., Goad et al., 2000; Mumin et al., 2007; Corriveau et al., 2010a,b; Ootes et al., 2010; Montreuil et al., 2013; Potter et al., 2013; Somarin and Mumin, 2013; Acosta-Góngora et al., in press; in revision). However key questions, regarding the nature of the mineralization, such as source of metals and sulfur, and the nature of the ore forming fluids remain poorly constrained.

In the southern GBMZ, geochronology of the NICO and Sue Dianne deposits and the Nori/RA prospect indicate that these mineralizing events are temporally associated with the emplacement of the Great Bear arc between 1875 and 1865 Ma (Gandhi et al., 2001; Ootes et al., 2010; Davis et al., 2011; Acosta-Góngora et al., in prep.). It has been suggested that O, C, and S in the polymetallic mineralization was derived from a magmatic-hydrothermal source (Robinson, 1971; Badham, 1973; Acosta-Góngora et al., in prep.), although, other ore-forming components such as S and As (±C) could have been derived, at least in part, from host rocks (Acosta-Góngora et al., in prep.). Fluid inclusion analyses suggest that complex $CaCl_2$-NaCl-H_2O brines were responsible for the

polymetallic mineralization (Somarin and Mumin, 2013; Acosta-Góngora et al., in prep.). In this contribution fluid inclusion, stable isotope (S, O, C and Cu), and whole rock geochemical data, along with mass balance calculations, are used to argue that the IOCG and related deposits and prospects in the GBMZ are derived from magmatic-hydrothermal fluids that could have acquired some elements (S, Co, Cu, Au and Ag) from the local country rocks. Finally, the data are placed into a regional context, providing further insights into the metallogenic evolution of the GBMZ.

5.2 Geological setting

The GBMZ and underlying Hottah Terrane form the western component of the Wopmay orogen, which is separated from the Coronation margin by the Wopmay fault zone (Fig 5.1). In the southern GBMZ, the <1885 Ma Treasure Lake Group (TLG) metasedimentary rocks predate Great Bear magmatism (Gandhi and van Breemen, 2005) and host the polymetallic NICO deposit and the Nori/RA prospect (Goad et al., 2000; Ootes et al., 2010). All the other deposits and prospects are hosted in Great Bear felsic volcanic rocks and porphyries, in particular the LaBine Group in the north and Faber Group in the south (Hildebrand et al., 1987; Gandhi et al., 2001; Mumin et al., 2007). The oldest Great Bear plutonic phase is a 1873 ± 2 Ma leucogranite that intruded the TLG in the southern magmatic zone (Gandhi et al., 2001). Quartz monzonite and subvolcanic porphyry were emplaced at ca. 1867 and predate the extensive 1866 ± 2 Ma Marian River quartz-monzonitic to monzogranitic batholith (e.g., Gandhi et al., 2001; Bennett and Rivers, 2006). The 1856 +3/-2 Ma Rapakivi-textured granite constitutes the youngest magmatic suite in the GBMZ (Gandhi et al., 2001).

5.3 Mineralization

5.3.1 Nori/RA prospect

The Nori/RA (Cu-Mo-U ± W, REE) prospect is hosted by deformed and metamorphosed biotite-K-feldspar ± magnetite-quartz siltstones of the TLG (Fig.

5.2A; 5.3A, B; Gandhi, 1994; Bennett and Rivers, 2006; Ootes et al., 2010; Acosta-Góngora et al., in press). The main mineralization at Nori/RA occurs in up to one meter thick deformed hydrothermal veins containing molybdenite and uraninite that were co-precipitated with biotite, tourmaline, and K-feldspar, with minor amounts of magnetite and pyrite (Figs. 5.3A, 5.4A; Ootes et al., 2010; Acosta-Góngora et al., in press). Minor Mo-Cu mineralization occurs in later, deformed quartz and K-feldspar veins, with lesser amounts of chalcopyrite, pyrite, magnetite and molybdenite (Fig. 5.3B; Ootes et al., 2010; Acosta-Góngora et al., in press). The veins have coarse biotite selvages which varies from 1 mm to 2 cm thick that has been dated by ^{40}Ar-^{39}Ar to be 1873.5 $\pm$ 6.1 Ma. In addition, vein hosted molybdenite has yielded a 1875 $\pm$ 8 Ma Re-Os model age (Ootes et al., 2010). Primary fluid inclusions in tourmaline suggest that the parental ore fluid was Ca- and CO_2-rich, with homogenization temperatures of >260ºC, and possibly as high as 400 ºC (Ootes et al., 2010).

5.3.2 NICO deposit

The NICO deposit is located in the southern GBMZ and is mostly hosted by Ca-Fe altered TLG rocks (Fig. 5.2B). Minor mineralization is also found within K-Fe altered porphyries and felsic volcanic rocks of the GBMZ (Goad et al., 2000; Acosta-Góngora et al., in press; in revision). The barren Ca-Fe alteration stage is crosscut by a pre-ore quartz±calcite-amphibole-K-feldspar vein set (S1) (Acosta- Góngora et al., in revision).

The mineralization at NICO (Fig. 5.3C) is contained within stratabound ore lenses (Figs. 5.5A-C) and can be broadly divided into prograde and retrograde assemblages (Acosta-Góngora et al., in revision). The prograde assemblage (Co-rich Ca-Fe-K alteration) consists of Co-rich arsenopyrite I, loellingite, cobaltite, magnetite I, amphibole (actinolite II-ferrohornblende II) and biotite II (Fig. 5.4B). Locally, these sulfarsenides have nanometer-sized Au-Bi inclusions. Retrograde metasomatism consists of intergrowths of marcasite, pyrite, hastingsite and magnetite, and is associated with the re-crystallization of arsenopyrite I to arsenopyrite types II and III (Fig. 5.4B). This recrystallization led to the release and remobilization of Au and Bi from the early sulfarsenides and arsenides.

Further refining of Au, by Bi melts, also took place in contemporaneous Bi-rich hydrothermal fluids that carried Bi in a molten state, as per the liquid Bi collector model (Douglas, 2000; Acosta-Góngora et al., in revision). The latest part of the mineralization history at NICO is dominated by an increase of sulfur and oxygen fugacity, in association with the introduction of Cu to the system (Acosta-Góngora et al., in revison). Emplectite ($CuBiS_2$) and chalcopyrite are the dominant ore minerals in the latest phase, and were co-precipitated locally with hematite, hastingsite, chlorite, and minor calcite (Fig. 5.4B). A quartz ± amphibole-K-feldspar vein set (S2) crosscuts the arsenopyrite veins, and a coarse grained quartz-calcite±amphibole-chalcopyrite vein set (S3) occurs at shallower levels in the deposit (Acosta-Góngora et al., in revision; in prep.). The Southern Breccia zone may be an extension of the NICO mineralized system and consists of uraninite± molybdenite-chalcopyrite contained in magnetite-K-feldspar ± biotite-cemented breccias (Montreuil et al., accepted). At both, NICO and the Southern Breccia, textural evidence supports that brittle-ductile deformation was post-metamorphic and syn- to post-mineralization (Montreuil et al., accepted).

Geochronological constraints suggest that ore deposition took place at ~1870 Ma, consistent with the emplacement of the Great Bear volcanic rocks (Davis et al., 2011; Acosta- Góngora et al., in prep.). Stable isotope (S, C, O) and trace element data suggest a magmatic origin. However, Acosta-Góngora et al. (in prep.) suggest that some S and As (±C) might have been dissolved from the TLG. Microthermometric studies have demonstrated that the Bi (and possibly the Au) mineralization was the result of multiple hydrothermal pulses, of fluids with variable homogenization temperatures and compositions including complex $CaCl_2$-NaCl-H_2O fluids. These fluids have estimated Na and Ca contents ranging from 1 to >40 wt. % NaCl equiv. and 7 to 20 wt. % $CaCl_2$ equiv. Calculated depths of formation of NICO deposit, based on fluid inclusion data range from 4.9 to 8.1 km (Acosta-Góngora, et al., in prep.)

5.3.3 DAMP prospect

The DAMP prospect (Fig. 5.6A) comprises Cu-U-Co-V ± Zn-Pb mineralization hosted in rhyodacitic ignimbrites (Gandhi and Prasad, 1995;

Acosta et al., 2011). The ore minerals occur in a breccia zone where the volcanic rocks are albitized and, to a lesser extent, potassically altered (Fig. 5.3D). The breccia matrix contains abundant hematite (var. specularite) and magnetite, along with minor pyrite, K-feldspar, quartz and calcite. The dominant ore minerals are chalcopyrite, with minor carrollite ($CuCo_2S_4$) and bornite that occur in microveins crosscutting early pyrite and magnetite, and as micro-scale alteration fronts with epidote and hematite that overprint calcite (Figs. 5.4C-E; Acosta-Góngora et al., in press). Minor amounts of secondary covellite and chalcocite replace the former Co-Cu sulfides where hematite is more abundant than magnetite, or magnetite has been extensively martitized (Acosta et al., 2011; Acosta-Góngora et al., in press).

5.3.4 Sue-Dianne deposit

The Sue Dianne deposit has resources of 8.4 Mt @ 0.8 % Cu, 0.07 g/t Au, 3.2 g/t Ag; (Hennessey and Puritch, 2008). This deposit is located at the intersection of the Mar and Dianne faults (Fig. 5.6B), and is hosted by a Faber group rhyodacitic ignimbrite sequence (Gandhi et al., 2001; Fig. 5.6B). The mineralization is principally hosted by an iron oxide breccia zone (Figs. 5.6B; 5.7A; 5.8A-C), interpreted as a volcanic diatreme, that is approximately 600 x500 m and 350 m deep (Gandhi, 1989; Goad et al., 2000). Within the breccia, the ignimbritic clasts are strongly potassically altered (K-feldspar), and partially replaced by hematite and magnetite (Goad et al., 2000; Acosta-Góngora et al., in press). Early magnetite and hematite along with fluorite and epidote are the major components of the breccia matrix (Fig. 5.7A); fluorite and magnetite are more dominant at greater depths and hematite at shallower depths (Camier, 2002; Acosta-Góngora et al., in press).

Ore minerals include chalcopyrite and lesser amounts of bornite, covellite, chalcocite, emplectite, wittichenite (Cu_3BiS_3), and carrollite (Gandhi, 1989; Goad et al., 2000; Camier, 2002; Acosta-Góngora et al. in press). Carrollite is scarce in the system, and it was co-precipitated with the early iron-oxide-epidote-fluorite alteration stage (Acosta-Góngora et al., in press). On the other hand, chalcopyrite, bornite, and wittichenite occur mostly interstitially to minerals of the latter assemblage (Fig. 5.9A). Covellite and chalcocite, are commonly found at

shallower levels of the systems (hematite dominated) replacing chalcopyrite and bornite (Camier, 2002; Acosta-Góngora et al., in press). Uranium enrichment is recognized peripheral to the copper enrichment and occurs as pitchblende, or its weathered products, in micro-veins (0.5 cm to <1 mm thick) (Goad et al., 2000; Camier, 2002). No significant uranium has been detected at depth in the deposit (Camier, 2002). The iron oxide-rich breccia complex is bounded and overprinted by a brittle shear zone with quartz-epidote and quartz stockworks and breccias (Figs. 5.7B, 5.8A-C). Byron et. al (2009) has classified this silica-flooded zone as one of the giant quartz veins recognized across the GBMZ.

5.3.5 FAB prospect

The FAB prospect (Fig. 5.6C) hosts Cu-U mineralization in K-Fe altered felsic volcanic rocks and porphyries (Gandhi, 1988, 1994; Azar, 2007). The mineralization is contained within K-feldspar, magnetite/hematite-biotite veins, alteration fronts and minor breccias (Fig. 5.7C; Potter et al., 2013; Acosta-Góngora et al., in press). The mineralized veins and matrix to the breccias mostly contain pyrite, chalcopyrite, and magnetite, and subordinate hematite (Acosta-Góngora et al., in press). Within the mineralization, pitchblende and fluorite commonly occur as veinlets and fracture fillings, and small amounts of apatite and actinolite are present (Gandhi, 1994). Most of the chalcopyrite occurs as microveins crosscutting and/ or interstitial to pyrite and magnetite in veins and breccias (Fig. 5.9B) and disseminated in the host rocks adjacent to the veins or breccias (Fig. 5.9B). Less commonly, chalcopyrite occurs as inclusions in magnetite grains (Acosta-Góngora et al., in press).

5.4 Analytical techniques

5.4.1 Fluid inclusion samples and methodology

Fluid inclusion analyses were undertaken using an Olympus BX50 microscope and a Linkham THMSG600 microthermometric stage in Dr. J. Richards Microthermometry Laboratory, at the University of Alberta. The inclusions were cooled to –138°C, and phase changes were recorded upon reheating until the total homogenization temperature (*T*h) was reached. Sequential

freezing (Haynes, 1985) was used to determine phase changes, which allowed salinity to be calculated. Calibration was carried out before and after the experiments using pure CO_2 and H_2O-bearing fluid inclusion standards. The accuracy of temperature measurements is estimated to be ± 0.1°C below 0°C, ±1°C between 0° and 300°C, and ± 2°C at higher temperatures.

5.4.2 Stable isotopes

Sulfur isotopes: The sulfur isotope analyses were carried out *in situ* on sulfide minerals in polished rock slabs (~2 mm thick) at the Geological Survey of Canada, Ottawa, in the Light Stable Isotope Laboratory, using a fluorination micro laser extraction technique (MILES; Beaudoin and Taylor, 1994; Taylor, 2004). In a single slab, multiple sulfide phases can be contained.The samples were degassed overnight (at ~80ºC) in the sample chamber. The purified SF_6 gas was collected and sealed in a 0.25-in OD Pyrex® tube for offline isotopic analysis using the microvolume inlet of a Finnigan MAT 252 mass spectrometer. Measurement accuracy is ±0.1‰ and results are reported in ‰ notation relative to the Canyon Diablo Troilite (V-CDT) standard.

Oxygen and Carbon isotopes: Oxygen isotope analyses of quartz and calcite and carbon isotope analyses of calcite were carried out at the Queen's Facility for Isotopic research (QFIR), Queen's University, Ontario. Results were calibrated using the NBS-28 standard. Measurement accuracy is ± 0.1‰ and are relative to Vienna Standard Mean Ocean Water (V-SMOW) for oxygen and Vienna-Pee Dee Belemnite (V-PDB) for carbon.

Hydrogen isotopes: Hydrogen isotope analysis of biotite was carried out at the QFIR using a high-temperature reduction method (Sharp et al., 2001) via elemental analysis continuous-flow isotope ratio mass spectrometry (CF-IRMS). Analyses were carried out with a Finnigan MatDelta XL Plus gas source mass spectrometer. Precision (1σ) was found to be better than ±3‰. The hydrogen isotope data are reported relative to V-SMOW.

Copper isotopes: In situ Cu isotopic measurement by LA-MC-ICP-MS was carried out on chalcopyrite grains in ~2 mm thick polished rock slabs and 100μm thick thin sections at the Geological Survey of Canada. A New Wave

Research UP213 laser ablation system was operated with an in-house built sample cell and coupled to a Nu Plasma multi collector ICP-MS. The setup of the system and analytical conditions are similar to those of Li et al. (2010), except as described below. A Nu Instruments DSN-100 membrane desolvation system was used to mix into the sample carrier gas stream (He) an aerosol of a laboratory Zn standard (in Ar) for mass bias correction. Chalcopyrite from the Bougainville porphyry Cu deposit was used as a standard due to its homogeneous isotopic composition (δ^{65}Cu = 0.40±0.06‰; 2σ, *n*=8) relative to NIST Cu isotope standard SRM 976. Individual spot analyses on chalcopyrite grains have a nominal diameter of 40µm. The data were acquired using the time resolved analysis (TRA) software of the Nu Plasma instrument. For each analysis, an off-peak background signal was collected for 30 s before the beginning of ablation. The Bougainville standard was analyzed twice before and after every 2 chalcopyrite analyses.

Data were corrected for mass bias using the instrument's NICE software using an in-house determined value for ^{66}Zn/^{64}Zn and the exponential mass bias law. For correction of any uncorrected drift in mass bias and isotopic fractionation introduced by laser sampling processes (e.g., Jackson and Günther, 2003; Kuhn et al., 2007), the mass bias-corrected Cu isotope ratios were corrected off-line by application of the sample-standard bracketing procedure (cf., Li et al. 2010). All data were then recalculated relative to NIST SRM 976. The analytical precision (2σ) of the δ^{65}Cu analyses is ca. 0.1‰.

5.5 Results

5.5.1 Fluid inclusions

Fluid inclusion analyses were undertaken on four outcrop samples from the Nori/RA and DAMP prospects. Fluid inclusion assemblages (FIA) in calcite (DAMP) and quartz (Nori/RA) were identified and characterized according to their origin (primary, secondary, or unknown) following Roedder (1984) and Goldstein (2003) (Table 3). Individual inclusions were classified on the basis of their phase relationships at room temperature as liquid-vapor (LV) and liquid-

vapor-solid (LVS). The measured inclusions have a size range of 5 to 10 μm, with rare larger inclusions (up to 30 μm).

Nori/RA: The quartz-bearing samples from Nori/RA are from Cu-Mo-bearing quartz-feldspar veins. The FIA comprise both LV and LVS types and occur in irregular inclusion-rich zones in the cores (Figs. 5.10A, C) and close to the rims of quartz crystals (Figs. 5.10A-D). These zones are neither associated with trails or with re-crystallization rims of the crystals, however, they cannot be unequivocally demonstrated to be primary in origin and so have been classified as "unknown". Of these two inclusion types, the LV are more abundant than the LVS inclusions.

The vapor phase occupies 5 to 10 vol. % of LV inclusions. First melting (*T*e) and final ice melting (Tm_i) temperature ranges from -78 to -76ºC and -18 to -35 ºC, respectively (Figs. 5.11A, B). Upon freezing, high relief (relative to ice) brownish and greenish colored solids formed in some inclusions, which were interpreted as $CaCl_2$ (antarcticite) and NaCl (hydrohalite) hydrate phases, respectively (e.g. Shepherd et al. 1985; Molnár et al. 1999). Disappearance of the $CaCl_2$- and NaCl-hydrates occurred between -48 ºC and -50 ºC and -51 ºC to -47 ºC, respectively. Homogenization temperatures (*T*h) range from 105 to 207 ºC (Fig. 5.11D). The total salinity was calculated only in a few inclusions where the NaCl and $CaCl_2$ hydrated phases nucleated and their temperatures were measured. The salinity values for these inclusions ranges from 20 to 27 wt.% (NaCl + $CaCl_2$ equiv) where $CaCl_2$ is the dominant solute (19-24 wt.%) and NaCl is less abundant (1-2 wt.%) (Steele-Maclnnis et al., 2011; Fig. 5.11E). The LVS inclusions contain light green to transparent solids with cubic morphologies were interpreted to be halite (Fig. 5.10D). These FIA have uniform L/V ratios, where the vapor phase occupies approximately 10 vol.% of the inclusions. The V/S ratios are more variable within single FIA as in some cases the halite varies from <5 to 10 vol. %. The LVS inclusions have liquid vapor-homogenization temperatures *T*h(LV→L) that range between 128 to 141 ºC and total homogenization temperatures (*T*h(LS→L)) ranging from 151 to 206 ºC (Fig. 5.11D). Salinities of 31 to 32 wt. % NaCl equiv. for these inclusions (Fig. 5.11E)

were calculated using the equation of Sterner et al. (1988). Further inspection at room temperature of both types of inclusions show that the degree of fill of the inclusions changed during the heating and cooling runs, suggesting some modification of the inclusions during microthermometry. Usually, the vapor phase increased by ~5 vol. %, and less commonly, the halite solid will not nucleate back at room temperature. Therefore, we only present data from those inclusions that preserved the same phase relationships before and after heating.

DAMP: The calcite-bearing samples from DAMP are in breccia-matrix material that pre-date the Cu-mineralization and contain 'possible' primary and secondary LV inclusions. The 'possible' primary (pp) FIA are contained between cleavage planes in three dimensional arrays, that are not associated with healed fracture planes (Figs. 5.12A, B), and thus, as these inclusions are not directly associated with growth zones, they cannot be conclusively interpreted as primary inclusions. Secondary FIA occur in healed fractures crosscutting or within calcite grains (Fig. 5.12C, D). Both, possibly secondary and secondary FIAs have constant L/V ratios in which the vapor phase occupies between 5 to 10 vol. % of the fluid inclusion.

The pp LV inclusions have *T*e values between -76 and -67ºC and Tm_i ranging from -33 to -16 ºC; in some of these inclusions brown solids formed (antarcticite?). However, due to their small size (~8 µm) it was difficult to estimate the final melting temperatures of antarcticite and/or hydrohalite Homogenization temepratures *T*h (LV→L) vary from 128 to 174ºC, with most values between 140 and 170 ºC (Fig. 5.11 C, D). The secondary FIA have *T*e values from -77 to -63ºC and Tm_i values of -19 to -43ºC. During freezing only the $CaCl_2$ hydrate was recognized and melted at temperatures between -43.6 and -50.2. The total salinity (S_t) calculated, varies from 19 to 29 wt.% (NaCl + $CaCl_2$ equiv.), and the data indicate that fluids are Ca-rich (20-27 $CaCl_2$ wt.% and 0.1 to 2 NaCl wt.%; Fig. 5.11E) (Steele-Maclnnis et al. 2011). Homogenization temperatures are more variable in the secondary inclusions than in pp, as the former range from 95 to >244 ºC, but most of the data have values between 120 and 180 ºC (Fig. 5.11D).

5.5.2 Stable isotopes

A total of 55 in-situ $\delta^{34}S$ analyses of sulfides were carried out from the Sue Dianne deposit and the DAMP, Nori/RA, and FAB propects (Tables 5.1 and 5.2; Fig. 5.13A). Isotopic zoning in sulfide grains was not observed in any of the samples. Chalcopyrite from the Sue Dianne deposit has the most negative $\delta^{34}S$ values (down to -8‰), with most data lying between -6 and -2‰. The majority of the samples have an internal variation of ~2‰ (Figs. 5.8A-C), and three samples (SD-21, SD-137 and SD-140) have higher internal variations (from 4 to 7‰; Fig. 5.10A). These internal variations in the $\delta^{34}S$ signature do not correlate with textural and mineralogical character, or with depth in the deposit. The $\delta^{34}S$ data for pyrite from the DAMP shows significant variability in the two samples analyzed (3523A, py= 5 to 6‰; 3523B, py= -0.1 to 2‰). Conversely, DAMP chalcopyrite shows a tight range in $\delta^{34}S$ values from -4 ‰ to -3‰. Pyrite and molybdenite from Nori/RA have a restricted range in isotopic values; 2-4‰ and 3‰, respectively. FAB pyrite has slightly lower values that range from -1‰ to 3‰.

Copper isotope analyses were carried out on chalcopyrite from NICO, Sue Dianne, DAMP, and FAB (Tables 5.1, 5.2). The entire $\delta^{65}Cu$ data set ranges from -1.2 to -0.3‰ and internal variability within a single sample is <0.2‰. Sue Dianne has the largest range and most negative values (-1.2 to -0.8‰; Fig. 5.13B; Table 5.2). The $\delta^{65}Cu$ data from the NICO deposit is between -1.0 and -0.3‰, and values for individual samples vary by <0.2‰ (Figs. 5.5A-C). The FAB and DAMP values are mostly restricted to -0.8 and -0.6‰.

Two breccia-hosted calcite samples from the DAMP prospect have $\delta^{13}C$ values of -3‰ and -2‰, and $\delta^{18}O$ values of 10‰ (both samples). Quartz from the late barren veins at the Sue Dianne deposit have $\delta^{18}O$ values that range from 8 to 11‰. Quartz from the Nori/RA veins have similar $\delta^{18}O$ values (10-12‰). Similarly, at Nori/RA, four samples of the coarse-grained biotite alteration associated with the mineralized veins have $\delta^{18}O$ values from 6 to 8‰ and δD values that range from -5 to +75‰.

5.5.3 Mass balance

In this section we present the results of a simple mass balance calculation in which we used the trace element compositions of the TLG and felsic host rocks from the Great Bear arc and calculated what minimum volume of host-rock would have been required to provide the metals to form the deposits at NICO and Sue Dianne (Table 5.4). Details of the mass balance calculation are given in the Appendix.

For this calculation, two data sets were used, and each will be discussed in turn. Firstly, the mass (in tonnes) of Cu, Au, Co and Bi contained in the NICO deposit and of Cu, Au and Ag in the Sue Dianne deposit was obtained using published resource and reserves data from Fortune Minerals (Hennessey and Puritch, 2008; Puritch et al., 2012). Secondly, trace element data were collected from the least altered rock samples from the TLG type section (Acosta-Góngora et al., in press; in prep.) and from the least-altered to unaltered granitoids and felsic volcanics from the Dianne Lake area and other locations in the Great Bear arc (Gandhi 1989; Camier, 2002; Azar 2007; Acosta-Góngora et al., in press). The assumption made here is that these values are of the metal concentrations in the host-rocks deposits before Ca-Fe-K- (NICO) and K (Sue Dianne)-alteration occurred. In the particular case of Au, only six out of seventeen samples from the TLG have Au concentrations (5-7 ppb) above the detection limit (1 ppb). A mean Au concentration (2 ppb) was obtained for the TLG by assuming a concentration of 0.9 ppb for those samples with Au <1 ppb. In the same way, a mean value of Au for the felsic rocks from the La Bine and Faber Groups (3 ppb) was calculated by giving a value of 0.9 ppb to samples with Au<1 ppb. In these felsic rocks only one in 8 samples have detectable Ag (>0.1 ppm). Thus, a maximum concentration of 0.1ppm for Ag is assigned to the rocks of these groups. Bismuth in all the TLG samples was below the detection limit (2 ppm), and therefore, we used 1.99 ppm as a maximum Bi concentration for the TLG in the mass balance calculation. Median values for Cu (TLG, 4 ppm; La Bine and Faber Groups, 10 ppm), and Co (TLG, 9) were used to represent the concentrations of those elements in the TLG

and the felsic rocks as this value is less affected by the extreme low and high concentrations of the outlier data.

We also calculated an approximate TLG rock volume of 1882 km^3 from the outcrop area given on the map of Gandhi and van Breemen (2005), and a minimum thickness calculated using the reported bedding orientation measurements and the outcrop distribution at the type section (also provided by these authors). The volume of the Faber group igneous host rocks around the Dianne Lake could not be accurately calculated, as it is not possible to estimate the thickness of these rocks. However, it can be conservatively estimated, based on felsic rock outcrop extent and distribution in the Dianne lake area that the volume of those rocks is at least an order of magnitude greater than that of the TLG.

It is estimated that a cube of TLG rocks with a side of 1.8 km and a volume (v) of 5.8 km^3 would have been required to provide the mass of Au found in the NICO deposit. In the case of Co, Bi and Cu, sides and volumes of the cubes are 1.1 km (v = 1.5 km^3), 2.1 km (v = 9.1 km^3) and 1.1 km (v = 1.4 km^3), respectively. For the Sue Dianne deposit, cubes of the felsic rocks with sides and volumes 1.4 km (v = 2.9 km^3), 0.5 km (v = 0.1 km^3) and 0.5 (v = 0.1 km^3), respectively, would have been required to provide the necessary masses of Cu, Au and Ag. These are all minimum volumes however, and are based on the assumptions that the metal concentration in the rock package is homogeneous throughout, the use of a maximum metal concentrations (Au, Ag and Bi) when data were below detection limits, and a 100 % leaching capacity of the hydrothermal fluids.

5.6 Discussion

5.6.1 The TLG and GBMZ, a possible source of metals

The S, O and C isotopic analyses constrain the possible sources of those elements in hydrothermal fluids, but they cannot tell us much about the source of metals such as Cu, Au, Co, Bi and Ag. In this section we will discuss if the host TLG and the felsic rocks of the LaBine and Faber Groups of the GBMZ could

have contributed Cu, Au, Co, Bi and Ag to the NICO and Sue Dianne systems, or if conversely, the metal budget of these units is very limited and, these elements are more likely to have been introduced by magmatic-hydrothermal fluids, as has been suggested in other IOCG deposits.

Cubes of host rock with sides between 1 and 2 km, which represent volumes of 2 to 9km^3 can account for the total amounts of Cu, Au, Co and Bi contained in the NICO deposit according to the mass balance calculations. These volumes only represent a small fraction (0.1 to 0.4%) of the minimum volume calculated for the TLG in the study area (~1882 km^3). The latter suggests that, even if these rocks have equal to lower concentrations of these metals (Acosta-Góngora et al., in prep) compared to the average continental crust (Au, 2 ppb; Co, 17 ppm; Bi, 0.16 ppm; Cu, 28 ppm; e.g., Rudnick and Gao, 2003), they can still be a potential source of metals. Similar results were obtained for Sue Dianne, where cube sides for Cu, Au and Ag vary from 0.5 to 1 and their volumes from 0.1 to 2.9 km^3. As with the TLG, the GBMZ felsic rocks are not especially enriched in Cu, Au and Ag when compared to the average continental crust values. Despite this, the mass balance suggests these rocks could be a possible source of metals.

The issue of how much metal can be recycled from the host rocks versus how much is directly supplied from a magmatic source is an important question in the genesis of IOCG deposits (or any other magmatic hydrothermal deposits). This is particularly important in IOCG deposits, which are well known for having extensive high temperature (350-400 ºC) alteration zones (1 to ≥ 7 km; e.g., Richards and Mumin et al. 2012).

Mass balance studies in the Iron Springs district (USA) have shown that the total Fe in the limestone hosted iron-rich ore bodies can be accounted for by the decomposition (Fe release) of amphibole and biotite at the selvages of underlying quartz monzonite intrusions (Barker, 1995). Geochemical modelling on the IOCG district of the Eastern Mount Isa (Australia) suggests that during albitization (Na-alteration), fluids are progressively enriched in K, Fe, Pb and Zn as these metals were leached from calc-silicate host-rocks (Oliver et al. 2004).

Moreover, the concentrations of those elements in the fluids are analogous to those in equilibrium with magnetite and biotite (subsequent K-Fe alteration) from Cu-Au deposits (Oliver et al. 2004). Recent studies on the IOCG alteration in the GBMZ have also demonstrated that during early Na-alteration metals are leached, and in subsequent mineralization-bearing Ca-Fe and K-Fe alteration assemblages, elements like Co, Ni and V are enriched (Montreuil et al. 2013; Montreuil et al. accepted). In the Swedish IOCG deposits (Norrbotten) it has been suggested that Cl has a crustal source on the basis of Cl-isotope data (Gleeson and Smith, 2009). In these deposits, hydrothermal-magmatic fluids could have incorporated additional Cl from either evaporites (meta- evaporites), and/or granitic pegmatites along the flow path (Gleeson and Smith, 2009).

We acknowledge that the mass balance calculation is conceptually simple, and should be applied with care. Nevertheless, this estimation shows in general terms, that the TLG and the GBMZ host-rocks contain a mass of Cu, Au, Co, Bi and Ag that is several orders of magnitude greater than that which was required to form the NICO and Sue Dianne deposits. Thus, they could have been a feasible source of these elements if the permeability was such that the high temperature IOCG fluids might be able to mobilize and concentrate the contained metals. The following sections will discuss the data and assess the likelihood of such processes.

5.6.2 Fluid chemistry

The fluid inclusion study has important limitations that greatly constrain our knowledge of the mineralizing fluid chemistry of the Nori/RA and DAMP prospects. At DAMP, there is a lack of gangue minerals that are clearly co-precipitated with copper mineralization. Only pre-ore calcite contains fluid inclusions and their abundance and distribution is limited. In the case of Nori/RA, the quartz that is co-precipitated with molybdenite and chalcopyrite contains relatively few fluid inclusions, and those that do exist have physical properties indicating that some of them may have been modified during analysis.

Nori/RA: The fluids that formed the vein-hosted Cu-Mo-U mineralization at the Nori/RA prospect are trapped in tourmaline-hosted, primary, fluid inclusions (Ootes et al., 2010). These inclusions indicate the fluids were calcium-rich and CO_2-bearing and trapped at a temperature of >260ºC (Ootes et al. 2010). That study also recognized the presence of pseudosecondary and secondary LVS inclusions in quartz from the quartz-K-feldspar veins that correspond to a lower temperature event (174 to 194ºC; ~31 NaCl wt.%). The LVS "unknown" inclusions analyzed in this study have similar ranges of temperature and total salinity to those reported by Ootes et al. (2010), and thus, might represent the same fluid. The Tm_i results obtained for the LV FIAs is consistent with hydrothermal pulses of brines with variable salinities, where the most saline end member is dominated by $CaCl_2$-rich brines (Fig. 5.11B). The relationship between the LV and LVS inclusions from this study is unknown, however, the formation of antarcticite (?) in some of the LVS inclusions during freezing experiments could indicate that both fluids are Ca-bearing and may be genetically linked. The lack of CO_2 and lower *T*h obtained for the "unknown" LV and LVS inclusions indicates that these fluids represent a different hydrothermal stage to that of the main mineralization hosted in the tourmaline-biotite veins. Thus, the fluids that formed the quartz-K-feldspar veins may have been responsible for later remobilization of the main Mo-U±Cu mineralization.

The isotopic composition of fluids in equilibrium with quartz from the K-feldspar-quartz veins was calculated using the range of temperatures of the more abundant LV inclusions (105 to 207ºC) and the fractionation factor for the quartz-water system from Meheut et al. (2007). These yield $\delta^{18}O_{fluid}$ values ranging between -12 to 1‰, suggesting the fluid is derived from meteoric water, and has interacted with the wall rocks, shifting its isotopic composition. No pressure correction was applied to this *T*h value so it just a minimum trapping temperature. The application of a pressure correction will result on a higher *T*h, and in consequence higher $\delta^{18}O_{fluid}$ values (e.g., at a *T*h of 220ºC, the $\delta^{18}O_{fluid}$ values range from 1 to 2‰). This still suggests that the fluids were meteoric in origin and have undergone water-rock interaction. The calculated $\delta^{18}O$ (Zheng 1993) of the

fluid that precipitated the biotite (using a minimum trapping temperature of 260 ºC ; Ootes et al. 2010), yields values from 6 to 8‰, consistent with a magmatic-hydrothermal origin. The abnormally high δD values might suggest the presence of significant amounts of F in biotite that affected the isotopic ratio analysis (Table 5.2).

DAMP: The pp and secondary inclusions in samples from the DAMP prospect have overlapping $T m_i$ and *T*h ranges (Fig. 5.11C). The few pp and secondary inclusions where salinity values could be calculated suggest that these are $CaCl_2$-rich fluids (> 12 wt. % $CaCl_2$; Fig. 5.11D). Similar fluids at NICO are interpreted to represent a magmatic brine (Acosta-Góngora, et al., in prep.). 'Possible' primary and secondary FIAs have large $T m_i$ variations (e.g., -36 to -16°C; Fig. 5.12B) suggesting fluid mixing between lower (possibly meteoric) and higher salinity (possibly magmatic) fluids (Fig. 5.11C).

The $\delta^{18}O$ values of the fluids ($\delta^{18}O_{fluid}$) in equilibrium with this calcite were calculated using the pp FIAs measured range of *T*h (128 and 174ºC) and fractionation factors for the calcite-water system given by Kim and O'Neil (1997). The calculated values range from -2 to 2‰, and these data suggest again, that the fluid was originally meteoric water which has partially equilibrated with the host-rocks. However, the $\delta^{18}O_{fluid}$ values must be interpreted carefully, in the absence of a pressure correction to the Th values. If a pressure correction was applied, there would be an increase in the calculated $\delta^{18}O_{fluid}$ values e.g., if the temperature of trapping was 210ºC, a corresponding range of 4 to 5‰ in $\delta^{18}O_{fluid}$ values would be obtained. Therefore, the resulting $\delta^{18}O_{fluid}$ values will approach those of magmatic fluids (6-10‰; Taylor, 1979; Sheppard, 1986). Calcites from DAMP have $\delta^{13}C$ and $\delta^{18}O$ values that are consistent with a magmatic source (Fig. 5.13C), which is also in agreement with the expected $\delta^{18}O_{fluid}$ shift after the application of a pressure correction.

GBMZ hydrothermal fluids: The mixing of meteoric and magmatic waters, as suggested by the DAMP data, has been recognized in other systems in the GBMZ, such as Sue Dianne (giant quartz veins), Echo Bay and Camsell River districts (Changkakoti, 1986; Byron et al., 2009; Somarin and Mumin 2013). In

the northern GBMZ (Echo Bay and Camsell River districts), polymetallic mineralization is mostly hosted by epithermal veins that have intermediate to moderate *T*h values, with most data between 105 and 350 ºC (Changkakoti, 1986; Somarin and Mumin, 2013). In those systems, boiling and fluid mixing was interpreted to have occurred at the time of mineralization, such that the *T*h values represent the original entrapment temperature of the fluids (Somarin and Mumin, 2013). The salinities of the ore-bearing fluids in the northern GBMZ are quite variable (3 to 37 wt. % NaCl equiv.; Changkakoti, 1986; Somarin and Mumin, 2013). LVS inclusions with multiple solids (hyper-saline inclusions) are rare in the pre-ore alteration and/or the ore deposition stages. In deeper systems such as the NICO deposit (5-8 km depth; Acosta-Góngora et al., in prep) and Nori/RA (tourmaline-biotite veins; Ootes et al., 2010), the *T*h range of ore-bearing fluids is similar, with a higher proportion of inclusions >260 ºC. In NICO, the presence of Bi solids that have been trapped as a melt phase in ore-related fluid inclusions suggest that their minimum trapping temperature was ≥ 271.3 ºC (Bi melting point; Okamoto et al., 1986). Moreover, in NICO and Nori/RA, the occurence of pre- and syn-ore hyper-saline $CaCl_2$ enriched inclusions are more common (typical of IOCGs), where Ca is a major component (Ootes et al. 2010; Acosta-Gongora et al., in prep.). As stated above, in the Nori/RA prospect, later saline hydrothermal fluids represented by the quartz-K-feldspar veins could have remobilized some of the main mineralization. Such a phenomenon was also described by Byron (2010) to explain the occurrence of brines associated with minor mineralization in the giant quartz veins of the GBMZ. In Sue Dianne deposit, the $\delta^{18}O_{qtz}$ values (9 to 11‰) of the post-ore quartz veins and stockworks are in agreement with those of other giant quartz veins from the GBMZ ($\delta^{18}O_{qtz}$ = 8 to 11‰), which are interpreted to have a meteoric origin ($\delta^{18}O_{fluid}$= -6 to -17‰) (Byron et al. 2009; Byron, 2010).

In summary, the presence of complex $CaCl_2$-$NaCl_2$-H_2O fluids associated with mineralization in the GBMZ is consistent with other IOCG mineralized systems worldwide (e.g., Tennant Creek, Skirrow and Walshe, 2002; Olympic Dam, Bastrakov and Skirrow, 2007; Norrbotten, Smith et al. 2013). The northern

portion of the GBMZ is dominated by shallower ore-bearing deposits (e.g., epithermal systems, Echobay and Camsell River districts, and a breccia-hosted system, DAMP), where mixing of magmatic and meteoric waters and boiling is indicated by the fluid inclusions. These fluids are also characterized by a fluid chemistry dominated by NaCl (with or without $CaCl_2$) and temperatures commonly <260 ºC. In contrast, the southern and metasedimentary-hosted systems like NICO and Nori/RA were formed at greater depths, and are characterized by fluids with generally higher temperatures (>260 ºC), fluid chemistry characterized by $CaCl_2$ and NaCl, and the presence of hyper-saline brines. In the southern portion of the GBMZ, the Sue Dianne deposit represents a shallow brecciated system associated with a volcanic diatreme (<~1 km depth) where post-ore fluids could have had a meteoric origin.

5.6.3 Sources of S and Cu

Sulfur: Pyrite and molybdenite have higher $\delta^{34}S$ values than chalcopyrite. In the DAMP, FAB, and Nori/RA prospects, most of the data cluster around 2‰, which is consistent with a magmatic-hydrothermal origin (Fig. 5.13A). The slightly higher $\delta^{34}S$ values of pyrite from DAMP (3 to 5‰) are in agreement with the signature of accessory sulfides from oxidized magnetite series intrusions (e.g., see compilation in Taylor, 1987). However, the bulk rock $\delta^{34}S$ values of the TLG range from -1 to 6‰ (Acosta-Góngora et al., in prep.) and may indicate that some of the S could have also been dissolved from this metasedimentary sequence. Overall though, $\delta^{34}S$ values of pyrite in these prospects are similar to the $\delta^{34}S$ values in sulfides from other polymetallic systems in the GBMZ, such as the Terra-Norex region, Echo Bay district, and the NICO deposit, all of which have been interpreted to have a magmatic-hydrothermal origin (Badham, 1973; Mumin et al. 2007; Acosta-Góngora et al., in prep.; Fig. 5.13A).

Sue Dianne and DAMP chalcopyrite was formed from a late Cu-bearing fluid that post-dated early magnetite±pyrite deposition. The more negative $\delta^{34}S$ values of the chalcopyrite may be a result of multiple factors, such as temperature variation and redox changes during mineralization (e.g. Ohmoto, 1972; Ohmoto, 1979), and/or interaction with the metasedimentary package.

Copper isotopes: Changes in redox conditions, temperature, pH, phase changes and salinity can result in copper isotope fractionation (e.g. Larson et al., 2003; Markl et al., 2006; Asael et al., 2007; Li et al., 2010; Maher et al., 2011; Rempel et al., 2012; Mathur et al., 2013). Magmatic-hydrothermal, magmatic, and supergene sulfides, as well as sediment hosted and meteoritic material have significant overlaps in δ^{65}Cu values (e.g., Zhu et al., 2000; Larson et al., 2003; Luck et al., 2003; Rouxel et al., 2004; Graham et al., 2004; Mathur et al., 2005; Asael et al., 2007; Li et al., 2010; Bishop et al., 2011; Fig. 5.13B). In the majority of these systems the δ^{65}Cu values are centered at 0‰ (Li et al., 2010) and the absolute δ^{65}Cu values are not representative of a particular process, or Cu source. Hence, an interpretation of the data is better applied on a local to more regional scale. In general, larger δ^{65}Cu variations (>1‰) are more common in low-temperature redox processes, compared to the smaller fractionations (<1‰) in high temperature, ore-related systems (e.g., Larson et al. 2003; Mathur et al. 2005; Markl et al., 2006; Li et al., 2010).

Despite the lack of well defined Cu reservoirs, it has been suggested that hypogene copper has a δ^{65}Cu signature of 0±1‰ (e.g., Larson et al., 2003; Graham et al., 2004; Li et al., 2010; Ikheata et al., 2011; Ikheata and Hirata, 2012; Mathur et al., 2012, 2013). However, most of these studies analyzed mineral separates (e.g., chalcopyrite) and mineralized rock samples. Therefore, the latter data represents either an average δ^{65}Cu value for several single-sulfide (e.g., chalcopyrite) generations, or a mixture of multiple Cu-bearing phases (e.g., sulfides and oxides). *In-situ* grain analyses done on hypogene chalcopyrite from porphyries and VMS deposits by Li et al. (2010) and Ikheata and Hirata (2012) respectively, and on non-altered peridotite-hosted native Cu by Ikheata et al. (2011), give a δ^{65}Cu range of -1.6 to +0.8‰. However, most of the data in these systems is closely clustered at -0.4 and +0.4‰ (Fig. 5.13B).

The δ^{65}Cu data from chalcopyrite in the NICO and Sue Dianne deposits, and the DAMP and FAB prospects have a range of values (-1.2 to -0.4‰; Fig. 5.13B) that are generally isotopically lighter than most of the data from magmatic and magmatic-hydrothermal systems data (-0.4 to 0.4%). Although, the low

GBMZ $\delta^{65}Cu$ values overlap with the overall *in-situ* hypogene $\delta^{65}Cu$ range (-1.6 to +0.8‰), and might indicate that further fractionation of copper isotopes resulted from phase separation (Li et al., 2010; Rempel et al., 2012) and redox changes (e.g., Markl et al., 2006; Ikheata et al., 2011) (see discussion below).

Experimental work has demonstrated that in Cl- and S-bearing hydrothermal fluids (450 ºC; 400 bar) phase separation between vapor and liquid favors the fractionation of the lighter Cu isotope into the vapor phase (via Rayleigh fractionation), and hence, the residual liquid has higher $\delta^{65}Cu$ values (Rempel et al., 2012). Li et al. (2010) has suggested that the lower $\delta^{65}Cu$ values (< -0.4‰) in the margins of the Northpakes porphyry systems could be explain by this mechanism. Phase separation has not been recognized in any of the studied GBMZ systems, although, it can not be discarded that such a phenomenon takes place at deeper levels. Low temperature redox process that take place during weathering can also fractionate the Cu isotopes significantly (e.g., Markl et al., 2006, Mathur et al. 2010; Ikheata et al.,2011). Studies from these authors have demonstrated that oxidation of Cu-rich sulfides preferentially enriches the solution in the isotopically heavier ^{65}Cu, and hence the residual phase preferentially retains the ^{63}Cu. In DAMP outcrop samples, martitization and replacement of chalcopyrite by covellite and bornite (Acosta-Góngora et al., in press) is common, and suggests that some degree of supergene enrichement (weathering) might account for the relatively negative $\delta^{65}Cu$ values of the residual chalcopyrite. The NICO and Sue Dianne chalcopyrites are less likely to be affected by weathering processes as their samples were taken from deeper parts of the system. Alternatively, their ^{63}Cu-rich values could also result from leaching Cu from igneous/metamorphic rocks that later reprecipitates as Cu-sulfides (e.g., Asael et al., 2007). In the Timna Valley sedimentary hosted copper deposits (Israel), Asael et al. (2007) have suggested that Cu leached from the igneous Precambrian basement rocks ($\delta^{65}Cu$, 0±0.5‰) undergoes a negative fractionation as $Cu(II)_{aq}$ is reduced to form later Cu-sulfides (-3.5 to -1.6‰).

Thus, the GBMZ data suggests that chalcopyrite with $\delta^{65}Cu$ data closer to -0.4‰ is consistent with a magmatic-hydrothermal source. Conversely, values < -

0.4‰ could imply that Cu derived from magmatic-hydrothermal fluids underwent phase changes or that hypogene Cu-sulfides were significantly weathered. Alternatively, the low δ^{65}Cu values can also be achieved if Cu is recycled from igneous/metamorphic rocks (e.g., GBMZ felsic volcanics) and re-precipitated as Cu-sulfides.

5.6.4 IOCG metallogeny of the GMBZ

The mass balance results suggest that some of the metals forming the NICO and Sue Dianne deposits could have been leached from their host rocks, and this is partially supported by the Cu and S isotopic data (see below). However, compositions of most of the components in the mineralizing systems suggest a magmatic source. The IOCG metallogenic evolution in the GBMZ has been constrained to between ca. 1875 to 1865 Ma (Gandhi et al. 2001; Ootes et al. 2010; Davis et al. 2011; Acosta-Góngora et al, in prep.), consistent with the emplacement of the calc-alkaline arc-like volcanic stage of the magmatic zone (Hildebrand et al., 1987; Gandhi et al., 2001; Ootes et al., 2013). This period of time is coeval with the early ca. 1873 Ma LaBine Group intermediate arc magmatism (e.g., monzodiorites, diorites, granodiorites), which subsequently evolved to the more felsic volcanism of the Faber Group at ca. 1868 Ma (Bowring, 1984; Hildebrand et al., 1987; Gandhi et al., 2001; Davis et al. 2011). The occurrence of elements like Co and Ni, typical of mafic sources, in association with Bi, U, Mo and W, which are characteristic of more felsic magmatism, in the GBMZ supports a mafic contribution to these mineralizing systems (Acosta-Góngora et al., in prep). Magma mixing or/and incorporation of older mafic units at depth by younger intermediate to felsic up-welling magmas could account for the enrichment of these elements (Acosta-Góngora et al., in prep).

Carbon isotopic data from DAMP and the $\delta^{18}O_{fluid}$ value calculated for the Nori/RA biotite, support a magmatic-hydrothermal source of mineralization (Acosta-Góngora et al., in prep.; this study). Conversely, the $\delta^{18}O_{fluid}$ calculated for calcite and quartz from DAMP and Nori/RA suggests a meteoric fluid input, although, this interpretation is limited by the absence of a pressure correction on

fluid inclusions from those locations. Fluid inclusion data from DAMP indicate fluid mixing between a more saline magmatic-hydrothermal fluid and a less saline meteoric fluid. Barton and Johnson (1996) have suggested that S and other salinity components, principally NaCl and $CaCl_2$ in IOCG deposits, are derived from evaporitic sequences. In the GBMZ, evaporitic rocks have not been recognized and the S isotopic data indicates a magmatic-hydrothermal source of S (Robinson et al. 1971; Badham et al. 1973; Acosta-Góngora et al., in prep.; this study). However some S and As at the NICO deposit could have been stripped from the TLG by hydrothermal fluids. Similarly, the Cu isotopes data signal a magmatic-hydrothermal fluid source, that may have recycled some Cu from host felsic rocks. Overall, we consider these deposits to be magmatic-hydrothermal in origin.

5.7 References

Acosta-Góngora, P., Gleeson, S.A., Samson, I.M., Corriveau, L., Taylor, B., Ootes, L., Creaser, R., The formation of the Iron-Oxide-Cobalt-Gold-Bismuth NICO deposit, Northwest Territories, Canada: evidence from isotope geochemistry and fluid inclusions Canada. In preparation.

Acosta-Góngora, P., Gleeson, S.A., Samson, I.M., Corriveau, L., Taylor, B., Ootes, L., and Creaser, R., Mechanisms of gold refining at the Au-Co-Bi±Cu-W iron oxide dominated NICO deposit, NWT, Canada. In revision.

Acosta-Góngora, P., Gleeson, S.A., Samson, I.M. and Corriveau, L., in press, Trace elements in magnetite and its relationship to Cu-Bi-Co-Au-Ag-U-W mineralization in the Great Bear magmatic zone, NWT, Canada: Economic Geology. In press.

Acosta-Góngora, P., Gleeson S.A., Ootes, L., Jackson, V.A., Lee, M.D., and Samson, I., 2011, Preliminary observations on the IOCG mineralization at the DAMP, Fab, and Nori showings and Terra-Norex mines, Great Bear Magmatic Zone: NWT Open File 2011-01, 11p.

Asael, D., Matthews Butler I., Rickard A. D., Bar-Matthews, M. and Halicz, L., 2006, $^{65}Cu/^{63}Cu$ fractionation during copper sulphide formation from iron sulphides in aqueous solution: Geochimica Cosmochimica Acta, v. 70, A23.

Azar, B., 2007, The lithogeochemistry of volcanic and subvolcanic rocks of the FAB Lake area, Great Bear magmatic zone, Northwest Territories, Canada: Unpublished B.Sc. thesis, Toronto, University of Toronto, 96 p.

Badham, J.P.M., 1973, Volcanogenesis, orogenesis and metallogenesis, Camsell River area, N.W.T.: Unpublished Ph.D., thesis, Edmonton, University of Alberta, 332 p.

Baker, T., Perkins C, Blake K.L., Williams, P.J., 2001: Radiogenic and stable isotope constraints on the genesis of the Eloise Cu-Au deposit, Cloncurry district, northwest Queensland: Economic Geology, v. 96, p.723-742.

Barker, D.S., 1995, Crystallization and alteration of monzonite, Iron Springs mining district, Utah: relation to associated iron deposits: Economic Geology, v. 90, p. 2197-2217.

Barton, M.D., and Johnson, D.A., 1996, Evaporitic-source model for igneous-related Fe oxide-(REE-Cu-Au-U) mineralization: Geology, v. 24, p.259-262.

Bastrakov, E.N., Skirrow, R.G., Davidson, G.J., 2007, Fluid evolution and origins of iron oxide Cu-Au prospects in the Olympic Dam District, Gawler Craton, South Australia: Economic Geology, v. 102, p. 1415-1440.

Beaudoin, G., and Taylor, B.E., 1994 High precision and spatial resolution sulfur analysis using MILES laser mircroprobe: Geochimica et Cosmochimica Acta, v. 58, p. 5055-5063.

Benavides, J., Kyser, T.K., Clark, A.H., Oates, C.J., Zamora, R., Tarnovschi, R., Castillo, B., 2007, The Manto Verde Iron-oxide-Copper-Gold district, III Región, Chile: the role of regionally derived, nonmagmatic fluids in chalcopyrite mineralization: Economic Geology v.102, p. 415-440.

Bennett, V., and Rivers, T., 2006, U-Pb ages of zircon primary crystallization and inheritance for magmatic rocks of the southern Wopmay orogen, Northwest Territories: NWT Open File 2006-006, 65 p.

Bowring, S.A., 1984, U-Pb zircon geochronology of Early Proterozoic Wopmay orogen, N.W.T. Canada: An example of rapid crustal evolution: Unpublished Ph.D. thesis, Lawrence, Kansas, University of Kansas, 148 p.

Bishop, M.C., Moyner, F., Weinstein, C., Fraboulet, J.G.,Wang, K., and Foriel, J., 2012, Meteoric and Planetary Science, doi: 10.1111/j.1945-5100.2011.01326.x.

Byron, S., Giant quartz veins of the Great Bear magmatic zone, Northwest Territories, 2010, Canada: Unpublished M.Sc. thesis, Edmonton, University of Alberta, 146 p.

Byron, S.J., Gleeson, S.A., Muehlenbachs, K., Ootes, L., Jackson, V.A., and Samson, I.M., 2009, Giant quartz veins in the Great Bear Magmatic Zone, Northwest Territories, Canada: biennial Society of Geology Applied to Mineral deposits, 10th meeting, Australia, 17-20 August, p. 156-159.

Caligari, A.A., 2003, Stable isotopes (S, O, H and C) studies of the phyllic and potassic-phyllic alteration zones of the porphyry copper deposit at Sungun, East Azarbaidjan, Iran: Journal of Asian Earth Sciences, v. 21, p. 767-780.

Camier, W.J., 2002, Geology of the Sue-Dianne Proterozoic Cu-Ag-Fe oxide breccia complex, Mazenod Lake district, Northwest Territories: Unpublished M.Sc. thesis, London, University of Western Ontario, 210 p.

Changkakoti, A., Morton, R.D., Gray, J., Yonge, C.J., 1986, Oxygen, hydrogen, and carbon isotopic studies of the Great Bear Lake silver deposits, Northwest Territories: Canadian Journal of Earth Sciences v. 23, p. 1463-1469

Corriveau, L., Mumin, A.H., and Setterfield, T., 2010a, IOCG environments in Canada: Characteristics, geological vectors to ore and challenges, in Porter, T.M., ed., Hydrothermal iron oxide copper-gold & related deposits: A global perspective: Adelaide, PGC Publishing, v. 4, p. 311-343.

Corriveau L., Williams, P.J., and Mumin A.H, 2010b, Alteration vectors to IOCG mineralization from uncharted terranes to deposits, in Corriveau, L., and Mumin, A.H., eds., Exploring for iron oxide copper-gold deposits: Canada and global analogues: Geological Association of Canada Short Course 20, p. 89–110.

Davis, W., Corriveau, L., van Breemen, O., Bleeker W., Montreuil, J.F., Potter, E., and Pelletier, E., 2011, Timing of IOCG mineralizing and alteration events within the Great Bear magmatic zone: Yellowknife Geoscience Forum , 39th , Canada, 15-17 November 2011, Abstracts, p. 97.

De Haller, A., and Fontboté, L., 2009, The Raúl-Condestable iron oxide copper-gold deposit, central coast of Peru: ore related hydrothermal alteration, sulfur isotopes, and thermodynamic constrainst: Economic Geology, v. 104, p. 365-384.

Deines, P., 1980, Stable isotope variations in carbonatites, *in* Bell, K., ed., Carbonatites, genesis and evolution: London, Unwin Hyman, p. 301-359.

Douglas, N., Mavrogenes, J., Hack, A. and England, R. 2000, The liquid bismuth collector model: an alternative gold deposition mechanism, in C. G., Silbeck and T. C. T., Hubble eds., Understanding planet Earth; searching for a sustainable future; on the starting blocks of the third millennium, 15th Australian Geological Convention, eds: Geological Society of Australia, Sydney, 135 p.

Dreher, A.M., Xavier, R.P., Taylor, B.E., and Martini, S., 2008, New geologic, fluid inclusion and stable isotope studies on the controversial Igarapé Bahia Cu-Au deposit, Carajás Province, Brazil: Mineralium Deposita, v. 43, p. 162-184.

Gandhi, S.S., 1994, Geological setting and genetic aspects of mineral occurrences in the southern Great Bear magmatic zone, Northwest Territories, in Sinclair, W.D., and Richardson, D.G., eds., Studies of rare-metal deposits in the Northwest Territories: Geological Survey of Canada Bulletin 475, p. 63-96.

Gandhi, S.S, 1989, Rhyodacite ignimbrites and breccias of the Sue-Dianne and Mar Cu-Fe-U deposits, southern Great Bear magmatic zone, Northwest Territories: Geological Survey of Canada Paper 89-1C, p. 263-273.

Gandhi, S.S., 1988, Volcano-plutonic setting of U-Cu bearing magnetite veins of FAB claims, southern Great Bear magmatic zone, Northwest Territories: Geological Survey of Canada Paper 88-1C, p. 177-187.

Gandhi, S.S., and Lentz, D.R., 1990, Bi-Co-Cu-As and U occurrences in the metasediments of the Snare Group and felsic volcanics of the southern Great Bear magmatic zone, Lou Lake, Northwest Territories: Geological Survey of Canada Paper 90-1C, p. 239-253.

Gandhi, S., and Prasad, N., 1995, Geological setting of Bode copper and Damp polymetallic prospects, central Great Bear magmatic zone, Northwest Territories: Northwest Territories Geoscience Office, Open File 1995-C, p. 201-212.

Gandhi, S., and Prasad, N., 1993, Regional metallogenic significance of the Cu, Mo, and U occurrences at the DeVries Lake, southern Great Bear magmatic zone, Northwest Territories: Geological Survey of Canada Paper 93-1C, p. 29-39.

Gandhi, S.S., and van Breemen, O., 2005, SHRIMP U–Pb geochronology of detrital zircons from the Treasure Lake Group – new evidence for Paleoproterozoic collisional tectonics in the southern Hottah terrane, northwestern Canadian Shield: Canadian Journal of Earth Sciences, v. 42, p. 833-845.

Gandhi, S.S., Mortensen, J.K., Prasad, N., and van Breemen, O., 2001, Magmatic evolution of the southern Great Bear continental arc, northwestern Canadian Shield: Geochronological constraints: Canadian Journal of Earth Sciences, v. 38, p. 767–785.

Gleeson, S.A. and Smith, M.P., 2009, The sources and evolution of mineralising fluids in iron oxide-copper-gold systems, Norrbotten, Sweden: Constraints from stable Cl isotopes of fluid inclusion leachates: Geochimica Cosmochimica Acta, v. 73, p. 5658-5672.

Goad, R.E., Mumin, A.H., Duke, N.A., Neale, K.L., Mulligan, D.L., and Camier, W.J., 2000, The NICO and Sue-Dianne Proterozoic, iron oxide-hosted, polymetallic deposits, Northwest Territories: Application of the Olympic Dam model in exploration: Exploration and Mining Geology, v. 9, p. 123–140.

Goldstein, R.H., 2003, Petrographic analisys of fluid inclusions, in Samson, I., Anderson, A., and Marshall, D., eds., Fluid inclusions: Analysis and

interpretation: Mineralogical Association of Canada, Short Course Handbook, v. 32, p. 9-53.

Graham S., Pearson, N., Jackson, S., Griffin, W. and O'Reilly, S. Y., 2004, Tracing Cu and Fe from source to porphyry: in situ determination of Cu and Fe isotope ratios in sulfides from the Grasberg Cu–Au deposit: Chemical Geology, v. 207, p. 147–169.

Haynes, F.M., 1985, Determination of fluid inclusion compositions by sequential freezing: Economic Geology, v. 80, p. 1436-1439.

Hennessey, T., and Putrich, E., 2008, New resource estimate for Sue-Dianne copper-silver deposit: Press Release, 22nd February 2008: http://www.fortuneminerals.com/News/Press-Releases.

Hildebrand, R.S., Hoffman, P.F., and Bowring, S.A., 1987, Tectono-magmatic evolution of the 1.9-Ga Great Bear magmatic zone, Wopmay orogen, northwestern Canada: Journal of Volcanology and Geothermal Research, v. 32, p. 99–118.

Ikehata, K., and Hirata, T., 2012, Copper isotope characteristics of copper-rich minerals from the Horoman peridotite complex, Hokkaido, Northern Japan: Economic Geology, v. 107, p. 1489-1497.

Ikehata, K., Notsu, K., and Hirata, T., 2011, Copper isotope characteristics of copper-rich minerals from Besshi-type volcanogenic massive sulfide deposits, Japan, determined using a femtosecond LA-MC-ICM-MS: Economic Geology, v. 106, p. 307−316.

Jackson, V.A., 2008, Preliminary geologic map of part of the southern Wopmay orogen (parts of NTS 86B and 86C; 2007updates); descriptive notes to accompany 1:100,000 scale map: NWT Open File 2008-007, http://www.nwtgeoscience.ca.

Jackson, S.E. and Günther, D., 2003, The nature and sources of laser induced isotopic fractionation in laser ablation-multicollector-inductively plasma spectrometry: Journal of Analytical Atomic Spectrometry, v. 18, p. 205-212.

Johnson, C.A., Bookstrom, A.A., Slack, J.F., 2012, Sulfur, carbon, hydrogen, and oxygen isotope geochemistry of the Idaho Cobalt belt: Economic Geology, v. 107, p. 1207-1221.

Kim, S.T., and O'Neil, J. R., 1997, Equilibrium and nonequilibrium oxygen isotope effects in synthetic carbonates: Geochimica et Cosmochimica Acta, v. 61, p. 3461-3475.

Kühn H. R., Pearson, N. J. and Jackson, S. E., 2007, The influenceof the laser ablation process on isotopic fractionation of copper in LA-MC-ICP-MS: Journal of Analytical Atomic Spectrometry, v. 22, p. 547-552.

Larson, P. B., Maher, K., Ramos, F. C., Chang, Z. S., Gaspar, M. and Meinert, L. D., 2003, Copper isotope ratios in magmatic and hydrothermal ore-forming environments: Chemical Geology, v. 201, 337-350.

Li, W., Jackson, S.E., Pearson, N.J. and Graham, S., 2010, Copper isotopic zonation in the Northpakes porphyry Cu-Au deposit, SE Australia: Geochimica et Cosmochimica Acta, v.74, p. 4078-4096.

Li, X., and Sasaki, M., 2007, Hydrothermal alteration and mineralization of middle Jurassic Dexing porphyry Cu-Mo deposit, southeast China: Resource Geology, v. 57, p. 409-426.

Luck, J. M., Othman, D. B., Barrat, J. A., and Albarede, F., 2003, Coupled ^{63}Cu and ^{16}O excesses in chondrites: Geochimica et Cosmochimica Acta, v. 67, p.143–151.

Maher, C., Kierran, Jackson, S., Mountain, B., 2010, Experimental evaluation of the fluid-mineral fractionation of Cu isotopes at 250 ºC and 300 ºC: Chemical Geology, v. 286, p. 229-239.

Mark G, Williams, P.J., Oliver, N.H.S., Ryan, C. and Mernagh, T., 2005, Fluid inclusion and stable isotope geochemistry of the Ernest Henry Fe oxide-Cu-Au deposit, Queensland, Australia: Society of Geology Applied to Mineral Deposits Biennial Meeting , 8th, China, August 18-21, Abstracts, p. 785-788.

Markl, G., Lahaye, Y. and Schwinn,G., 2006, Copper isotopes as monitors of redox processes in hydrothermal mineralization: Geochimica Cosmochimica Acta v.70, p. 4215–4228.

Marschik, R., and Fontboté, L., 2001, The Candelaria-punta del Cobre iron oxide Cu-Au(-Zn-Ag) deposits, Chile: Economic Geology, v. 96, p.1799-1826.

Mason, T. F. D., Weiss, D. J., Chapman, J. B., Wilkinson, A. J.,Tessalina, V. G., Spiro, A., Horstwood, A. S. A., Spratt, O. and Coles, A. J., 2005, Zn and Cu isotopic variability in the Alexandrinka volcanic-hosted massive sulphide (VHMS) ore deposit, Urals, Russia: Chemical Geology v. 221, p. 170–187.

Mathur, R., Munk, L., Nguyen, M., Gregory, M., Annell, H., and Lang, J., 2013, Modern and paleofluids pathways revealed by Cu isotope compositions in surface waters and ores of the Pebble porphyry Cu-Au-Mo deposit, Alaska: Economic Geology, v. 108, p. 529-541.

Mathur, R., Ruiz, J., Casselman, M.J., Casselman, Megaw, P., van Egmond, R., 2012, Use of Cu isotopes to distinguish primary and secondary Cu mineralization in the Cañarico Norte porphyry copper deposit, Northern Peru: Mineralium Deposita, v. 47, p. 755-762.

Mathur, R., Dendas, M., Titley, S., Phillips, A., 2010, Patterns in the copper isotope composition of minerals in porphyry copper deposits in Southwestern United States: Economic Geology, v. 105, p. 1457–1467.

Mathur, R., Ruiz, J., Titley, S., Liermann, L., Buss, H., and Brantley, S., 2005,
Cu isotopic fractionation in the supergene environment with and without
bacteria: Geochimica et Cosmochimica Acta, v. 69, p. 5233−5246.

Mathur, R., Ruiz, J., Titley, S., Gibbins, S. and Margotomo, W., 2000, Different crustal sources for Au-rich and Au-poor ores of the Grasberg Cu–Au porphyry deposit: Earth Planet Science Letters v. 183, p. 7–14.

Meheut, M., Lazzeri, M., Balan, E., and Mauri, F., 2007, Equilibrium isotopic fractionation in the kaolinite, quartz, water system: Prediction from first-principles density-functional theory. Geochimica et Cosmochimica Acta, v. 71, p. 3170-3181.

Molnár, F., Watkinson, D.H., Everest, J.O., 1999, Fluid-inclusion characteristics of hydrothermal Cu-Ni-PGE veins in granitic and metavolcanic rocks at the contact of the Little Stobie deposit, Sudbury, Canada: Chemical Geology, v. 154, p. 279-301.

Montreuil, J.F., Corriveau, L., and Potter, E. (accepted), Albitite-hosted uranium development within IOCG systems: The southern breccia, Great Beat magmatic zone, Northwest Territories, Canada: Mineralium Deposita.

Montreuil, J.F., Corriveau, L., and Grunsky, E., 2013, A compositional data analysis of IOCG systems, Great Bear magmatic zone, Canada: To each alteration types its own geochemical signature: Geochemistry: Exploration, Environment, Analysis, doi: 10.1144/geochem2011-101.

Mumin, A.H., Corriveau L., Somarin, A.K., and Ootes, L., 2007, Iron oxide copper-gold-type polymetallic mineralization in the Contact Lake belt, Great Bear magmatic zone, Northwest Territories, Canada: Exploration and Mining Geology, v. 16, p. 187-208.

Ohmoto, H., 1972, Systematics of sulfur and carbon isotopes in hydrothermal ore deposits: Economic Geology, v. 67, p. 551-578.

Ohmoto H, Rye, R.O., 1979, Isotopes of sulfur and carbon, *in* Geochemistry of Hydrothermal Ore Deposits, eds, Barnes, H.L.: New York, J Wiley and Sons, p 509-567.

Okamoto, H., and Massalski, T.B., 1986, Au-Bi (gold-bismuth), *in* TB., Massalski, J. L. Murray, L. H. Bennet and H., Baker, eds., Binary Alloy Phase Diagrams: Ac-Au to Fe-Rh: American Society for Metals, v. 1, p. 238-240.

Oliver, N., Cleverly, JS., Mark, G., Pollard, P.J., Bin F., Marshall, Rubenach, M.J., Williams, P.J., Baker, T., 2004, Modelling the role of sodic alteration in the genesis of iron oxide-copper-gold deposits, Eastern Mount Isa Block, Australia: Economic Geology, v. 99, p. 1145-1176.

Ootes, L., Davis, W.J., and Jackson, V.A., 2013. Whence came Hottah Terrane?: Geological Association of Canada/Mineralogical Association of Canada Annual Meeting, Winnipeg, MN, May 2013.

Ootes, L., Goff, S., Jackson, V., Gleeson, S.A., Creaser, R.A., Samson, I.M., Evenson, N., Corriveau, L., and Mumin, H., 2010, Timing and thermochemical constraint on multi-element mineralization at the Nori/RA Cu-Mo-U prospect, Great Bear magmatic zone, Northwest Territories, Canada: Mineralium Deposita, v. 45, p. 549-566.

Oreskes, N. and Einaudi, M.T., 1992, Origin of Hydrothermal Fluids at Olympic Dam: Preliminary Results from Fluids Inclusions and Stable Isotopes: Economic Geology, v.87, p. 64-90.

Perring, C.S., Pollard, P.J., Dong, G., Nunn, A.J., and Blake, K.L, 2000: The Lightning Creek sill complex, Cloncurry district, northwest Queensland: A source of fluids for Fe oxide-Cu-Au mineralization and sodic-calcic alteration: Economic Geology, v. 95, p. 1067-1089.

Potter, E.G., Montreuil, J.-F., Corriveau, L., and DeToni, A., 2013, Geology and hydrothermal alteration of the Fab Lake region, Northwest Territories: Geological Survey of Canada, Open File 7339.

Puritch, E., Ewert, W., Armstrong, T., Brown, F., Orava, D., Pearson, J.L., Hayes, T., Duggan, T., Holmes, G., Uceda, D., Sumners, W., Mackie, D., Rougier, M., Bocking, K., Mezei, A., and Horne, B., 2012, Technical report and updated mineral reserve estimate and front-end engineering and design (FEED) study on the NICO gold-cobalt-bismuth-copper deposit, Mazenod Lake area, Northwest Territories, Canada: NI 43-101 Technical Report No. 247 prepared for Fortune Minerals Ltd., 307 p.

Rempel, K.U., Liebscher, A., Meixner, A., Romer, R.L., Heinrich, W., 2012, An experimental study of the elemental and isotopic fractionation of copper between aqueous vapor and liquid to 450 ºC and 400 bar in the CuCl-NaCl-H_2O and CuCl-NaHS-NaCl-H_2O systems: Geochimica et Cosmochimica Acta, v. 94, p. 199-216.

Robinson, B.W., Studies on the Echo Bay silver deposit, NWT, 1971, Unpublished PhD thesis, Alberta, Canada, University of Alberta, 256 p.

Roedder, E., 1984, Fluid inclusions, in P.H., Ribbe, ed., Reviews in Mineralogy: Mineralogical Society of America, v. 12, 644 p.

Rotherham, J.F., and Blake, K.L., 1998, Stable isotope evidence for the origin of Mesoproterozoic Starra Au-Cu deposit, Conclurry district, Northwest Queenland: Economic Geology, n. 93, v.1435-1449.

Rouxel O., Fouquet Y. and Ludden J. N., 2004, Copper isotope systematics of the Lucky Strike, Rainbow, and Logatchev seafloor hydrothermal fields on the

Mid-Atlantic Ridge: Economic Geology Bulletin Society of Economic Geology, v.99, p.585–600.

Rudnick, R.L. and Gao, S., 2003, The composition of the continental Crust, in, eds, Holland and K.K., Turekian Rudnick, Treatise on Geochemistry: Elsevier-Pergamon, Oxford, p. 1-64.

Santos, R.V., de Alvarenga, C.J.S., Dardenne, A.N. Sial, Ferreira, V.P., 2000, Carbon and oxygen profiles across Meso-Neoproterozoic limestones from from central Brazil: Bambuí and Paranoá groups: Precambrian Research, v. 104, p. 107-122.

Sharp, Z.D., Atudorei, V., Durakiewicz, T., 2001, A rapid method for the determination of hydrogen and oxygen isotope ratios from water and hydrous minerals: Chemical Geology, v. 178, p. 197-210.

Sheppard, S.M.F., 1986, Characterization and isotopic variations in natural waters: Reviews in Mineralogy, v. 16, p. 165-183.

Shepherd t., Rankin A. H. and Alderton D. H. M., 1985, A Practical Guide to Fluid Inclusion Studies: Blackie, London, 239 p.

Sidor, M., 2000, The origin of the black rock alteration overprinting iron-rich sediments and its genetic relationship to disseminated polymetallic sulfide ores, Lou Lake, Northwest Territories, Canada: Unpublished M.Sc. thesis, London, University Western Ontario, 190 p.

Simard, M., Beaudoin, J., Bernard, J., Hupé, A., 2006, Metallogeny of the Mont-de-l'Aigle IOCG deposits, Gaspé Peninsula, Québec, Canada: Mineralium Deposita, v. 41, v. 607-636.

Skirrow, R., and Walshe, J., 2002, Reduced and oxidized Au-Cu-Bi iron oxide deposits of the Tennant Creej Inlier, Australia: An integrated geologic and chemical model: Economic geology, v. 97, p. 1167-1202.

Skirrow, R.G., 1993, The genesis of gold-copper-bismuth deposits, Tennant Creek, Northern Territory: Unpublished Ph.D. thesis, Canberra, Australian National University, 158 p.

Smith, M.P., Gleeson, S.A., Yardley, B.W.D., Hydrothermal evolution and metal transport in the Kiruna district, Sweden: Constrasting metal behavior in

aqueous and aqueous-carbonic brines: Geochimica et Cosmochima Act, v. 102, p. 89-112.

Somarin, A.K., and Mumin, H.A., P-T composition and evolution of paleofluids in the Paleoproterozoic Mag Hill IOCG system, Contact Lake, Northwest Territories, Canada: Mineralium Deposita, doi 10.1007/s00126-013-0482-3.

Steele-Maclnnis. M., Bodnar, R.J., and Naden, J., 2011, Numerical model to determine the composition of H2O-NaCl-CaCl2 fluid inclusions based on microthermometric and microanalytical data; Geochimica et Cosmochimica Acta, v. 75, p. 21-40.

Sterner, S.S., Hall, D.L., and Bodnar, R.J., 1988, Synthetic fluid inclsuions. V. Solubility relations in the system NaCl-KCl-H2O under vapor-saturated conditions: Geochemica et Cosmochimica Acta, v. 52, p. 989-1005.

Taylor, B.E., 2004, Biogenic and thermogenic sulfate reduction in the Sullivan Pb-Zn-Ag deposit, British Columbia (Canada): Evidence from microisotopic analysis of carbonate and sulfide in bedded ores: Chemical Geology, v. 204, p. 215-236.

Taylor, B. E., 1997, Stable isotope geochemistry of ore-forming fluids, *in* Kyser, T. K., ed, Short Course in Stable Isotope Geochemistry of Low Temperature Fluids: Mineralogical Association of Canada, v. 13, p. 337-445.

Taylor H.P., 1979, Oxygen and hydrogen isotope relationships in hydrothermal mineral deposits, in Barnes, H.L., ed., Geochemistry of Hydrothermal Ore Deposits, New York, p. 236–277.

Williams P.J., 1998, An introduction to the metallogeny of the McArthur River-Mt Isa-Cloncurry minerals Province: Economic Geology, v. 93, p. 1120-1131.

Zheng Y.F., 1993, Calculation of oxygen isotope fractionation in hydroxyl-bearing silicates: Earth Planetary Scientific Letters, v. 120, p. 247-263.

Zhu X. K., O'Nions, R. K., Guo, Y., Belshaw, N. S. and Rickard, D., 2000, Determination of natural Cu-isotope variation by plasma-source mass spectrometry: implications for use as geochemical tracers: Chemical Geology, v.163, p. 139–149.

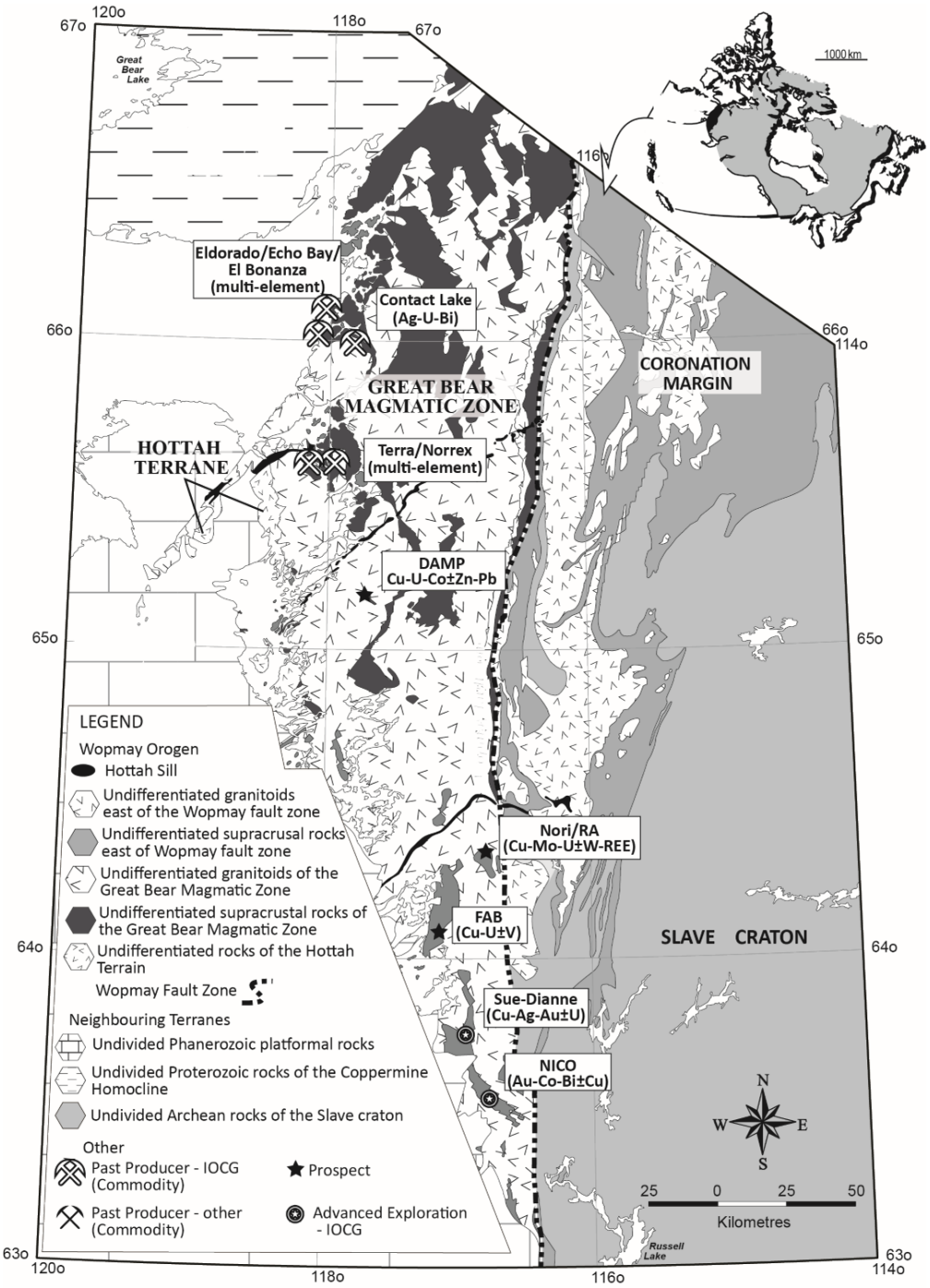

Figure 5.1. Regional geology of the study area
Geology of the GBMZ and the Hottah Terrane is shown, along with selected prospects, past producing mines and advanced exploration projects. Modified after Ootes et al. (2010).

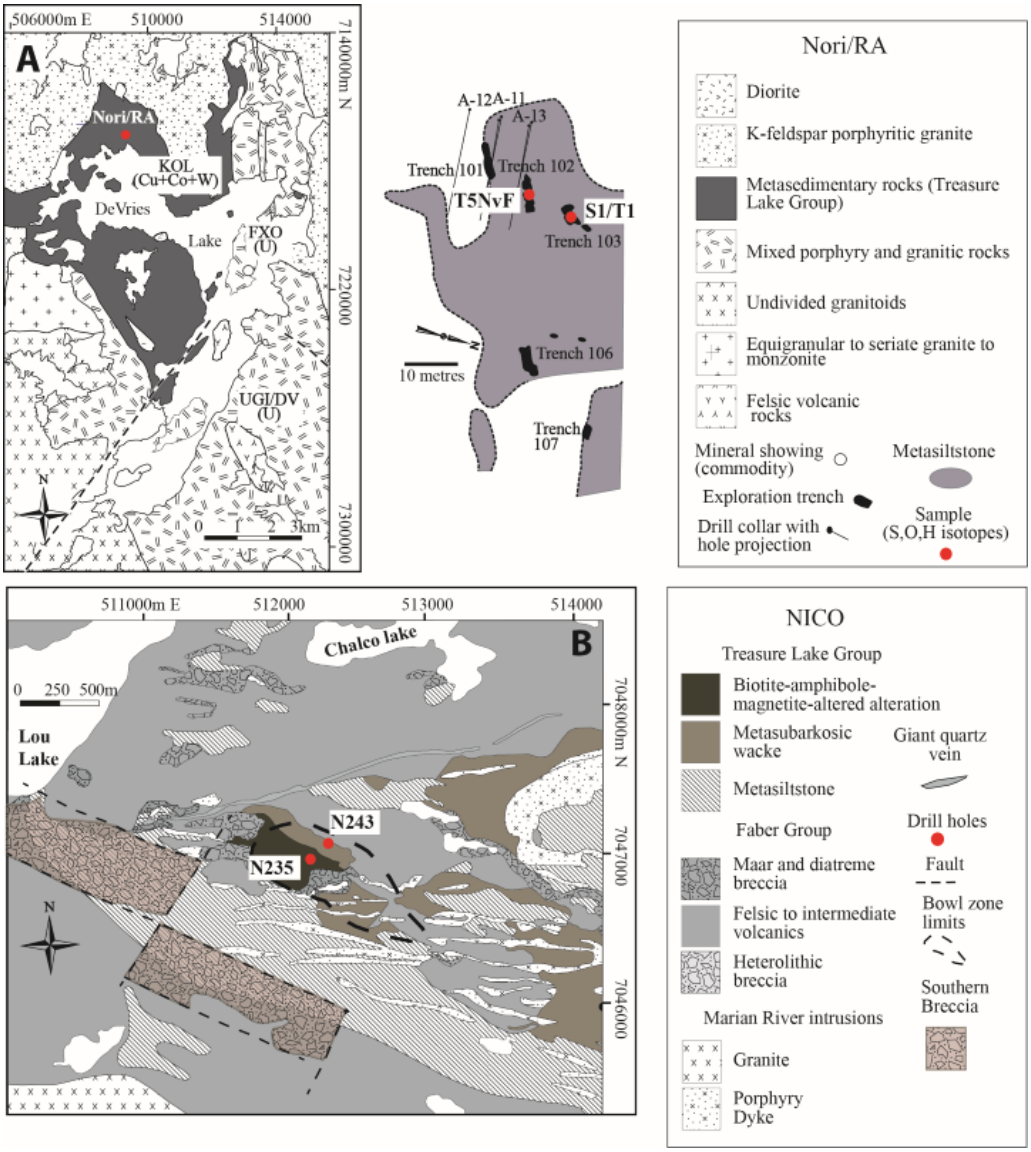

Figure 5.2. Local geology Nori/Ra prospect and the NICO deposit.
(A) Geology of the DeVries Lake area and location of the Nori/RA prospect and other mineralized zones. Geology is modified from Gandhi and Prasad (1993) and Jackson (2008). Outcrop map modified from Ootes et al. (2010) of the Nori/RA prospect depicting location of trenches and drill collar and the magnetite sample location. (B) Geology of the Lou Lake area and the Bowl Zone from the NICO deposit modified from Goad et al. (2000). The location of the drill holes are shown.

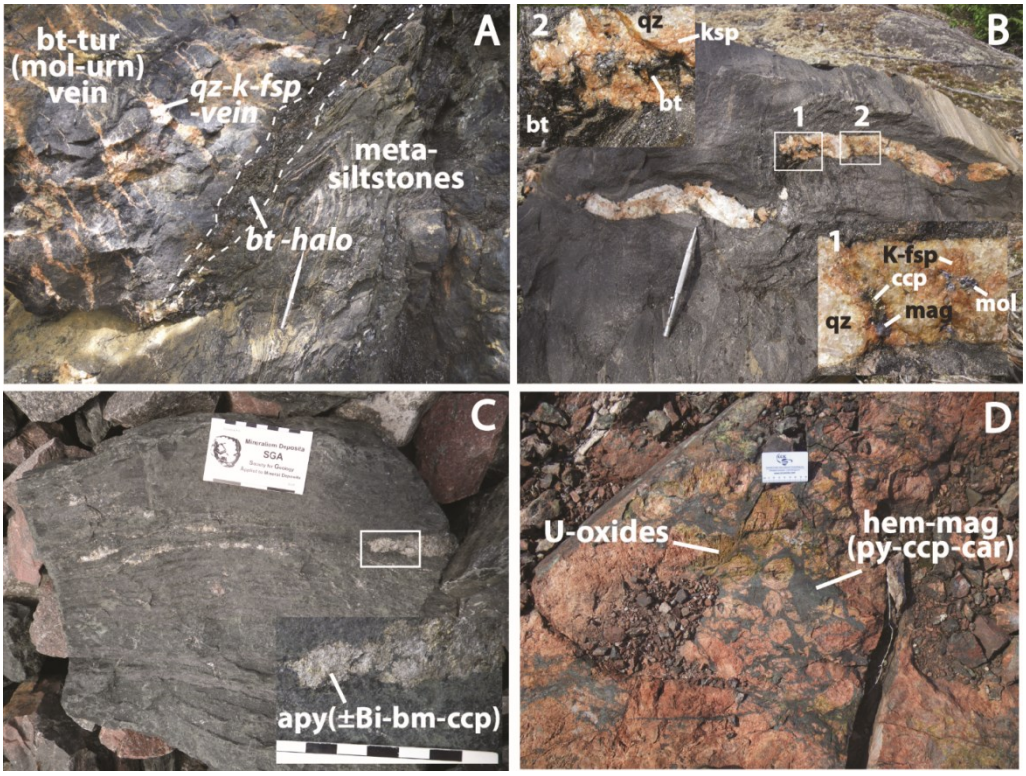

Figure 5.3. Outcrop view of NICO, Nori/RA and DAMP systems
Nori/Ra prospect (A-B). (A) Tourmaline-biotite-molybdenite-uraninite veins, containing the K-feldspar-quartz (±chalcopyrite-molybdenite) veins (tension gashes). A biotite halo is well developed at the vein-host rock contact. The host metasiltstones have been ductily deformed. (B) The deformed veins crosscutting the metasiltstones and containing minor amounts of chalcopyrite (ccp) and molybdenite (mol; insets 1 and 2). Irregular biotite alteration halos are also formed at the vein-host rock interphase. (C) Ca-Fe-K altered rocks of the TLG hosting stratabound mineralization at NICO deposit. Arsenopyrite, pyrite, bismuthinite and chalcopyrite are the most common ore minerals, and commonly spatially associated. (D) Breccia mineralization at the DAMP showing. The breccia matrix is mostly comprised of magnetite (mag) and hematite (hem), with minor disseminated pyrite (py), chalcopyrite, bornite, and carrollite (car). Weathered uranium oxides are localized within the prospect.

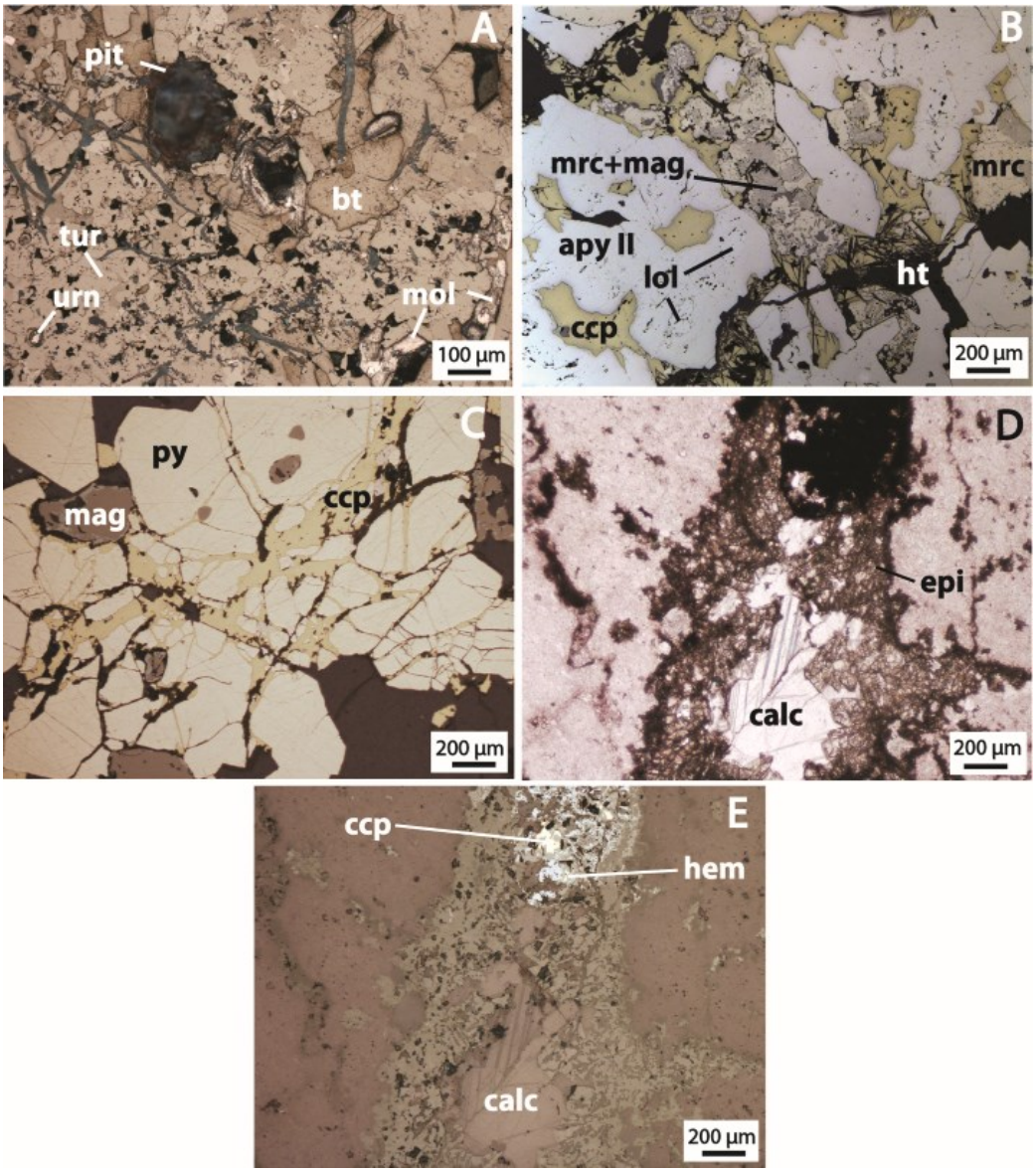

Figure 5.4. Petrography of the Nori/RA, NICO and DAMP systems
(A) Nori prospect. Tourmaline (tur) and biotite (bt) co-precipitated with uraninite (ur) and molybdenite (mol). A pit from the sulfur isotopes in-situ isotopic analysis is also shown. (B) NICO deposit. Loellingite (lol) replaced by arsenopyrite (apy) II. Marcasite (mrc) and magnetite (mag) occur as intergrowths that are later replaced by chalcopyrite. In addition, arsenopyrite (apy) II is also partialy replaced by this sulfide. (C) DAMP prospect. Early magnetite and pyrite (py) pre-dating the emplacement of late chalcopyrite (ccp). (D) Calcite vein overprinted by epidote (epi) and specular hematite (hem) alteration that serves as host to chalcopyrite (ccp). (E) Same as (D), showing the occurrence of hematite (hem) and chalcopyrite (ccp)

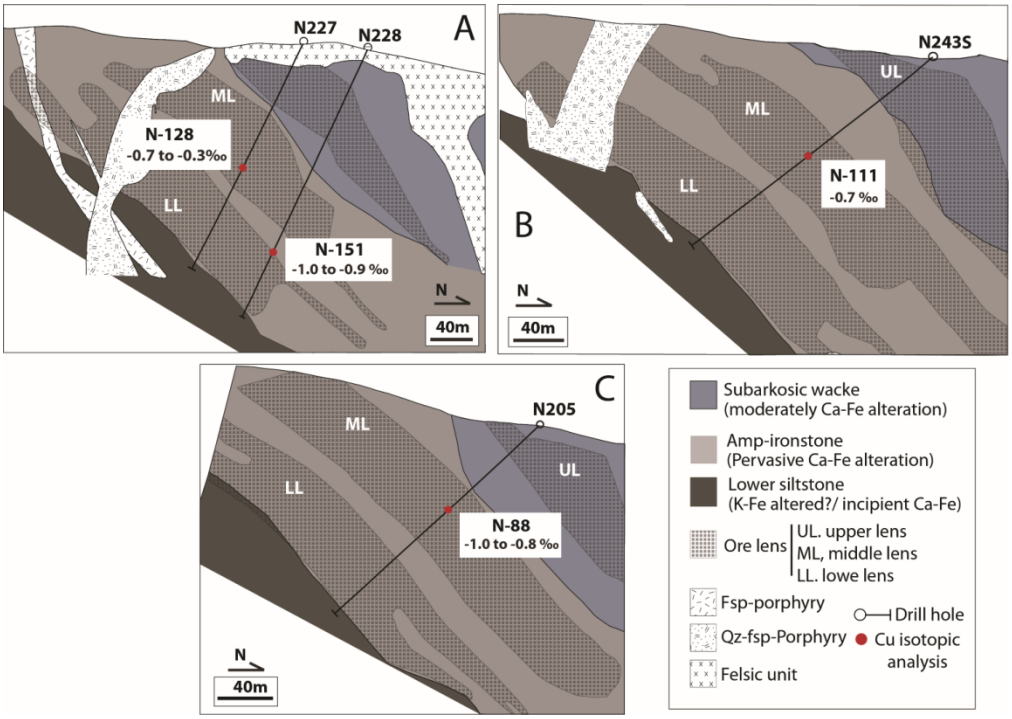

Figure 5.5. Cross sections of the drill holes in NICO deposit
Locations of samples in drill holes N227, N228, N243 and N205. The $\delta^{65}Cu$ data are given in the boxes.

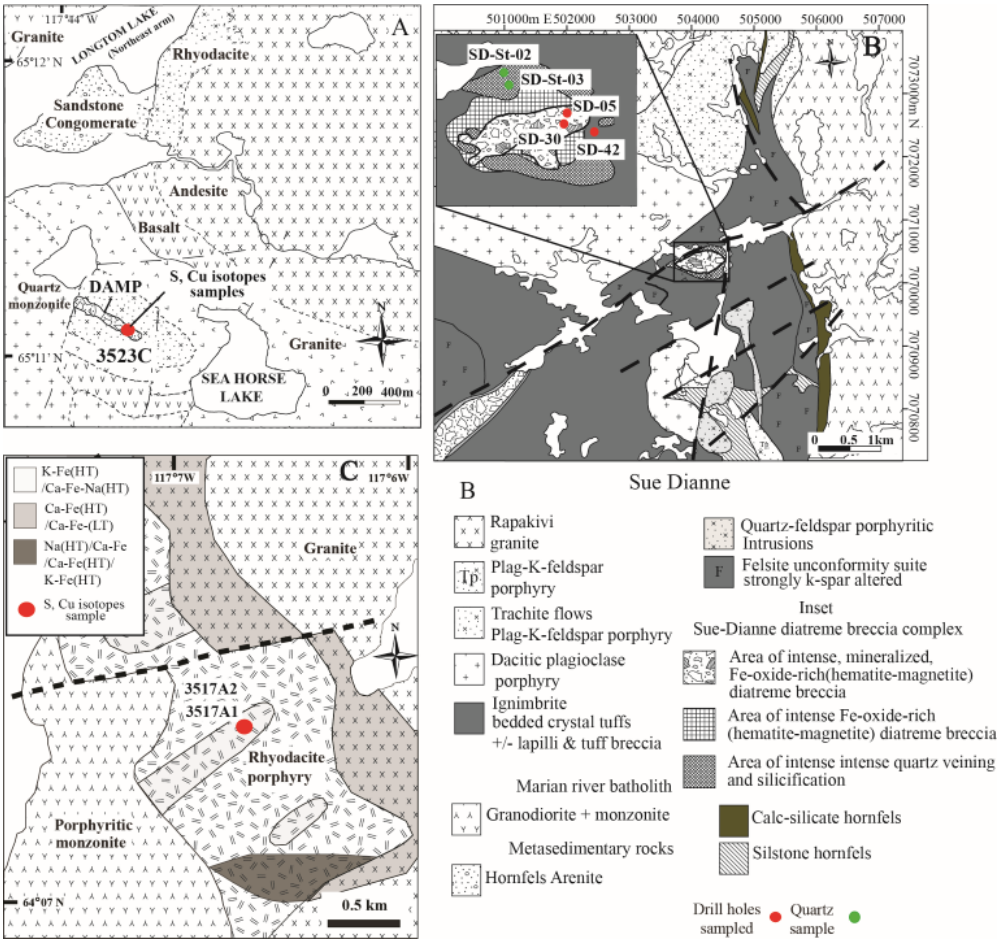

Figure 5.6. Geology of DAMP, FAB and Sue Dianne

(A) Geology of the northeast section of the Longtom Lake area, after from Gandhi and Prasad (1995). (B) Geology of the Dianne Lake area after Goad et al. (2001). (C) Geology and alteration map of the FAB prospect ater Potter et al. (2013). The alteration assemblages are refered as high (HT) and low (LT) temperature.

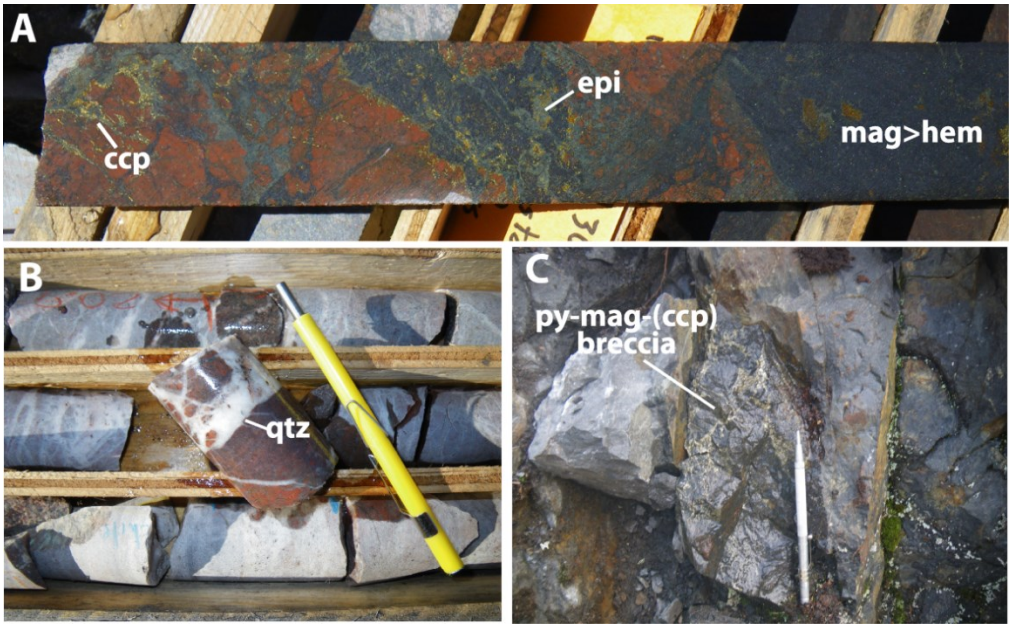

Figure 5.7. Outcrop views from Sue Dianne and FAB systems
(A) Sue-Dianne deposit. Potassic altered rhyodacites-ignimbrites from the Dianne Lake, overprinted by the dominant magnetite (mag)-hematite (hem)-epidote (epi)-fluorite (fl) alteration. Disseminated chalcopyrite and bornite (bn) are contained within the later alteration assemblage. (B) Late quartz (qtz) stockworks crosscutting the K-altered rocks and also post-dating the mineralization at the Sue Dianne system. (C) Rhyodacites-dacites from the FAB prospect hosting magnetite (mag)-pyrite (py) dominated veins and local breccias containing chalcopyrite (ccp).

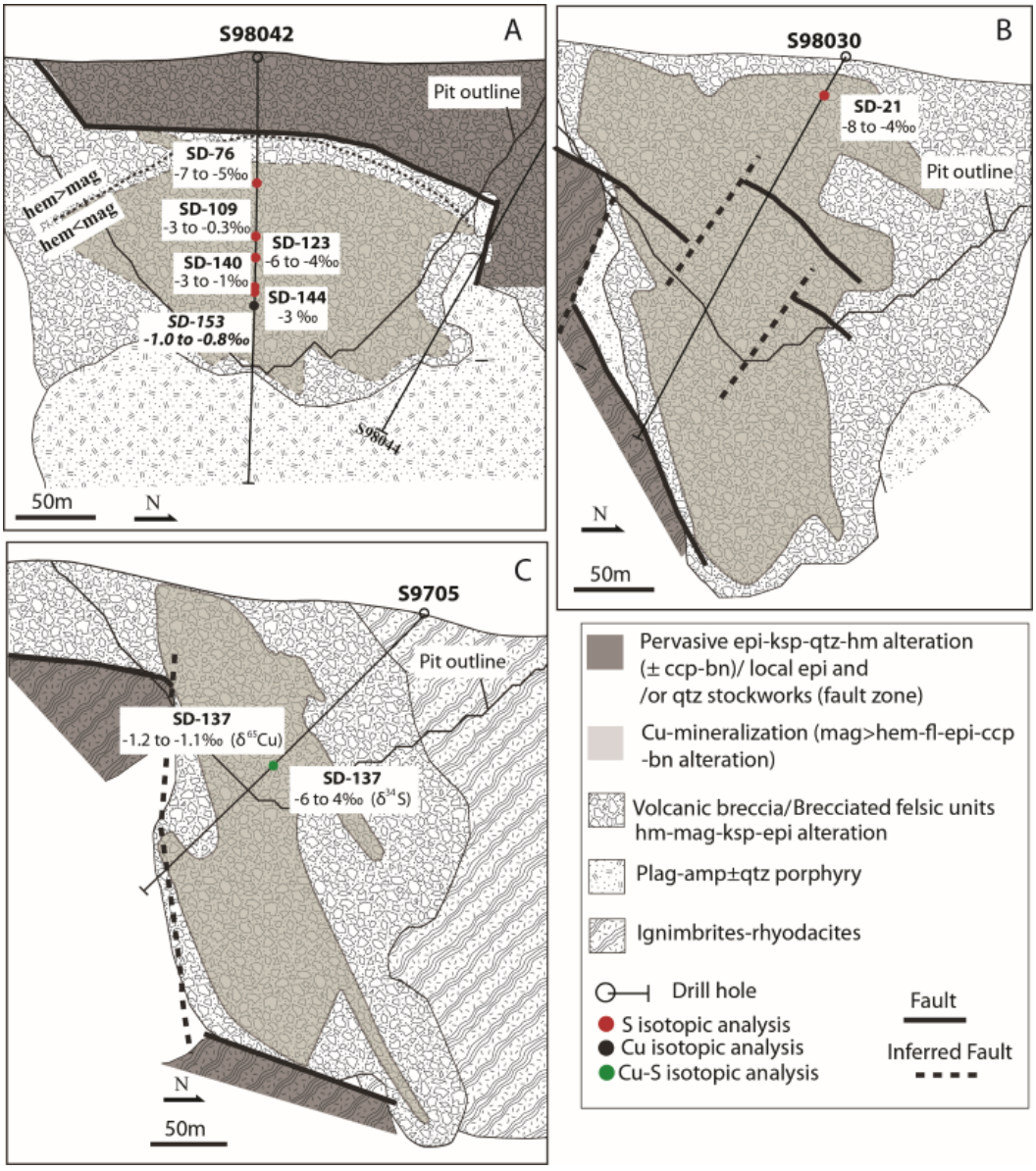

Figure 5.8. Cross sections from the Sue Dianne deposits
Cross sections of the drill holes SD09830, SD09842 and SD9705 containing chalcopyrite.

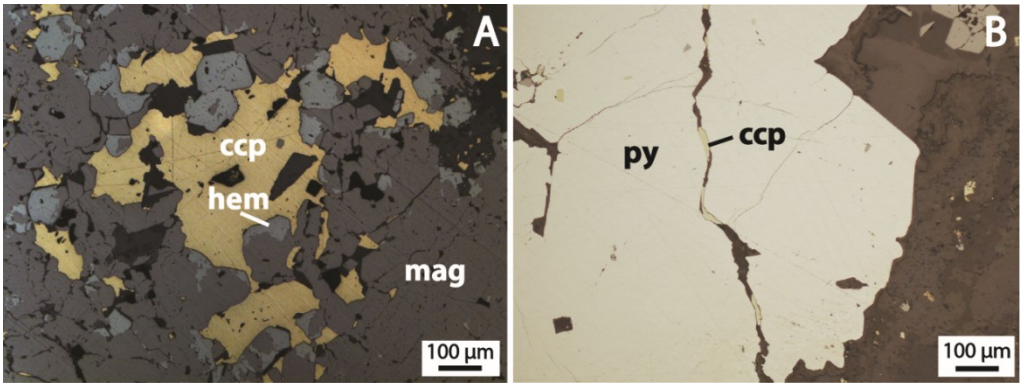

Figure 5.9. Petrography of the Sue Dianne and FAB systems
(A) Sue Dianne deposit. Chalcopyrite (ccp) intergranular to magnetite (mag) alteration. Magnetite moderately replaced to hematite (hem) (martitized). (B) Pyrite (py) emplaced in veins and crossscut by chalcopyrite (ccp). Also peripherally chalcopyrite (ccp) is disseminated on the wallrock.

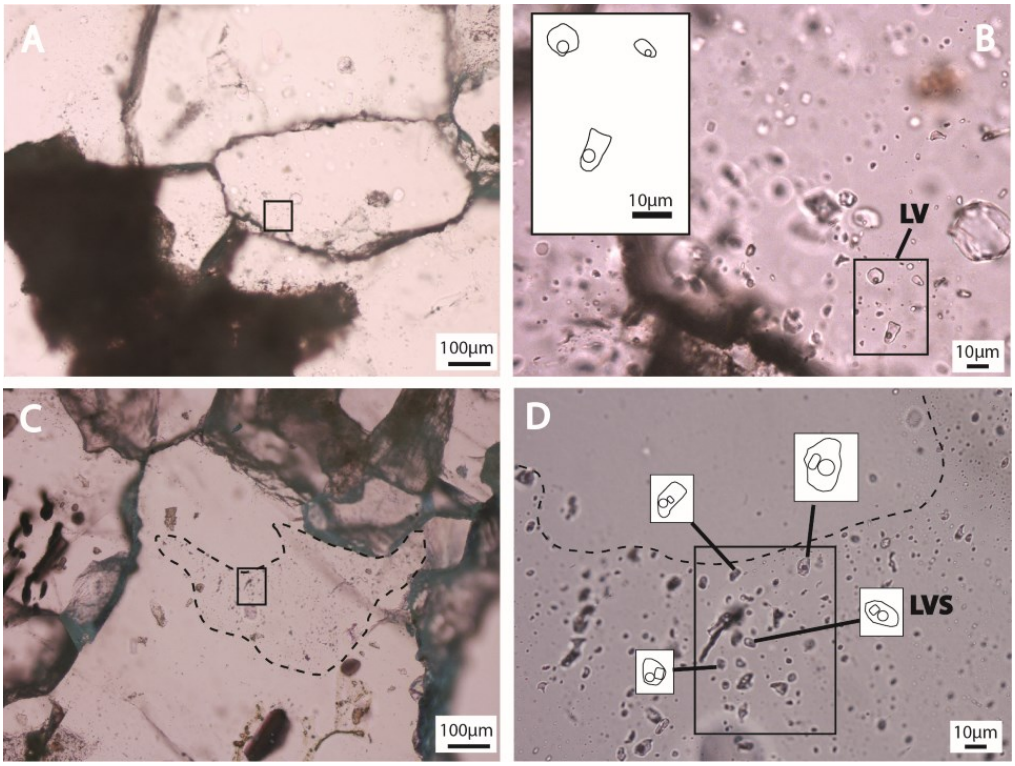

Figure 5.10. Fluid inclusion types in the Nori/Ra prospect
(A) Quartz grain containing LV fluid inclusions. The black box shows the location these inclusions. (B) Inset from E showing an assemblage of LV inclusions. (C) Quartz grain containing an irregular fluid inclusions-rich zone. The black box shows the location of LVS inclusions. (D) Inset from G showing an assemblage of LVS inclusions.

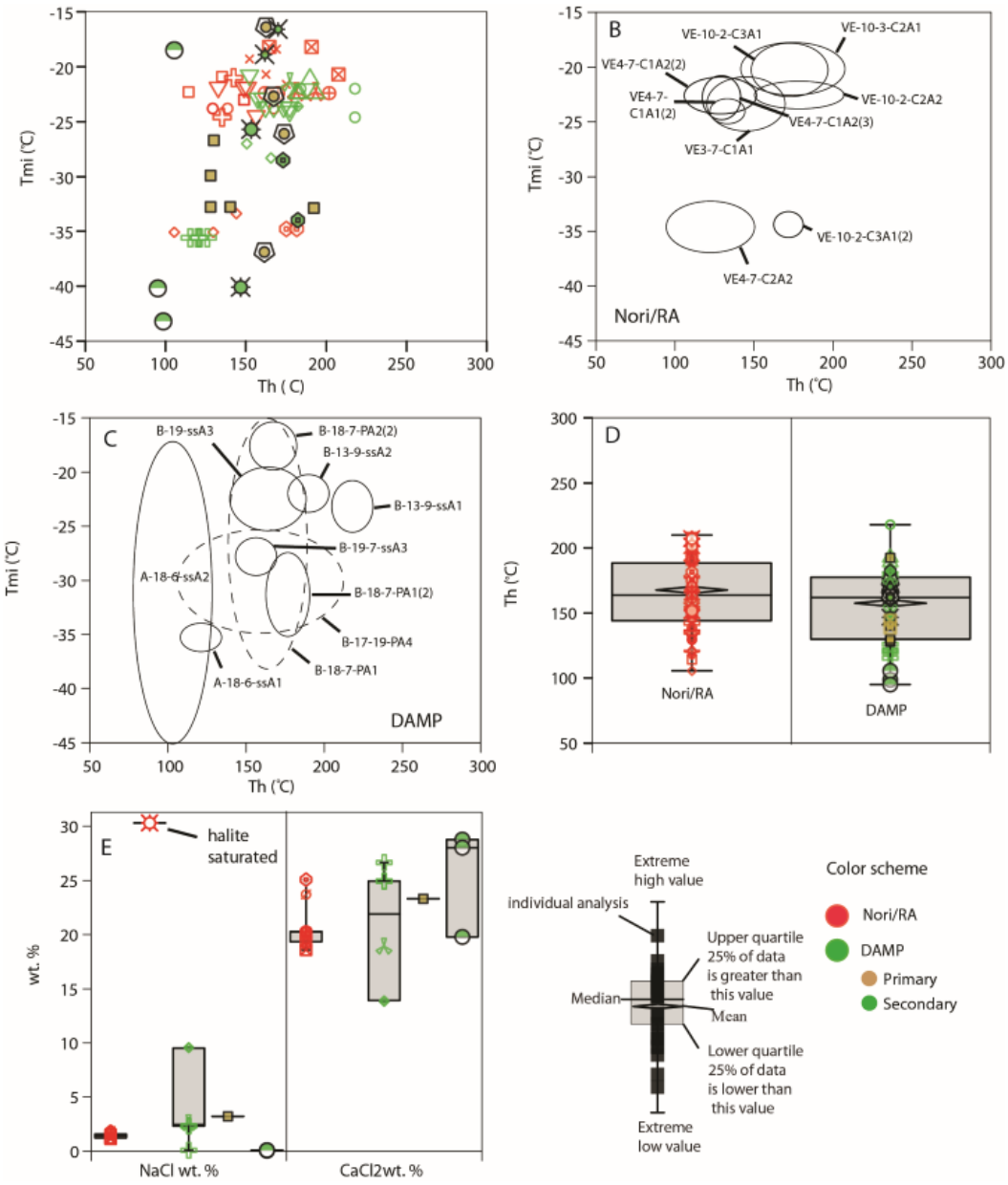

Figure 5.11. Fluid inclusion data from the Nori/RA and DAMP prospects
(A) Scatter plot of the *T*h vs Tm_i from DAMP and Nori/RA. (B) The distribution of FIA from Nori/RA prospect is consistent with multiple fluid pulses. (C) Distribution of DAMP FI showing individual fluid pulses and possible fluid mixing. (D) Distribution of *T*h in both locations. (E) Salinity of the Nori/RA and DAMP fluid inclusion assemblages.

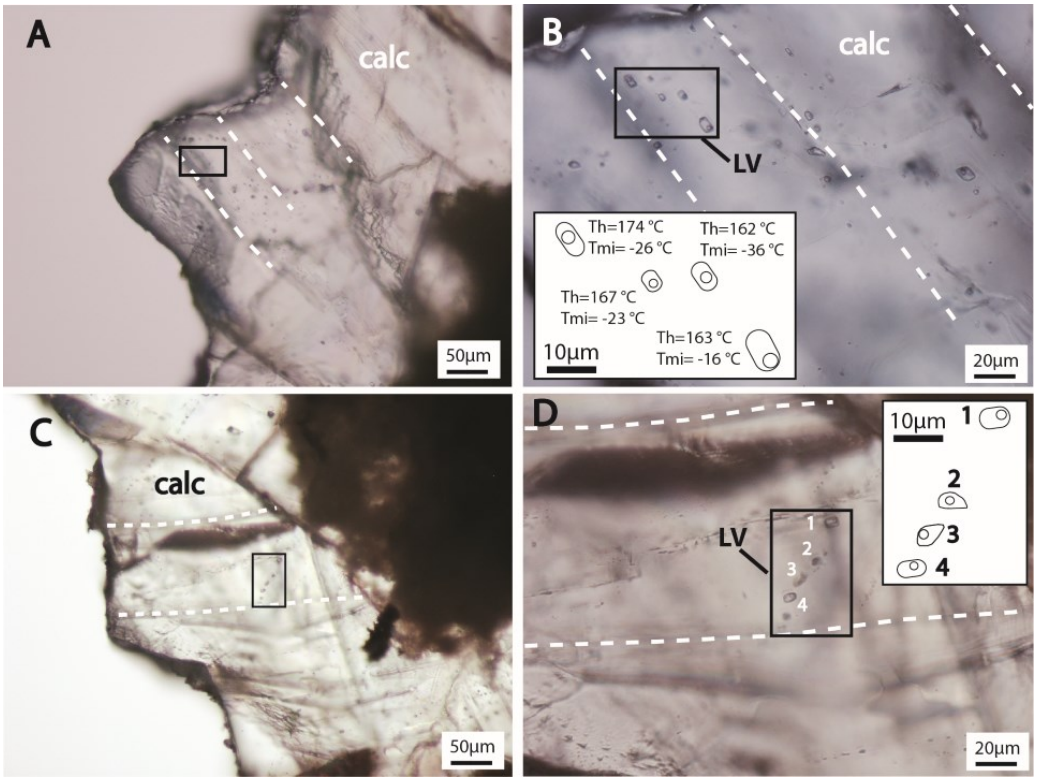

Figure 5.12. Fluid inclusion types in the DAMP prospect
(A) Calcite grains cleavage planes (dashed lines) and the location of 'possible' primary fluid inclusions. (B) Zoom in of inset in A. The picture shows primary fluid inclusions occurring in assemblages parallel to the twinning plane. The variation of *T*h and Tm_i in a single fluid inclusion assemblage suggest that fluid mixing has occurred. (C) A calcite twinning plane with secondary inclusions is outlined in the inset. (D) Zoom in of the inset showing a trail of secondary inclusions.

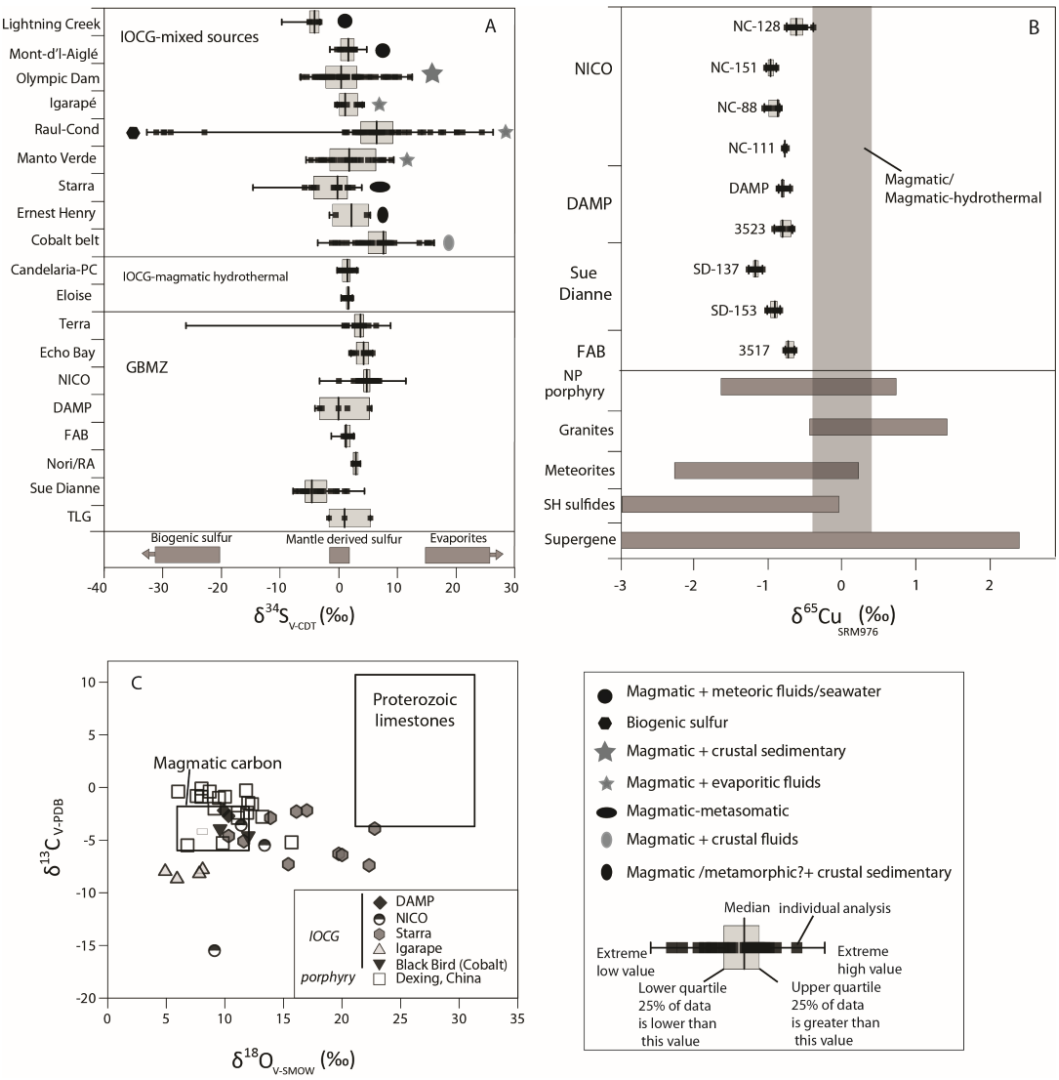

Figure 5.13. Oxygen, and C stable isotopes data distribution

(A) Comparison of the $\delta^{34}S$ values from the Nori/RA, DAMP and DAMP prospects and the Sue Dianne deposit with other IOCG deposits from the GBMZ, Peru, Australia, and Brazil. Symbols indicate inferred fluid sources in deposits where fluid mixing is proposed. Data from Robinson (1971), Badham (1973), Skirrow (1993), Rotherham et al. (1998), Perring et al. (2000), Baker et al. (2001), Marschik and Fontboté (2001), Mark et al. (2005), Simard et al. (2006), Bastrakov et al. (2007), Benavides et al. (2007), Dreher et al. (2008) and de Haller and Fontboté (2009), Johnson et al. (2012), Acosta-Góngora et al., in prep. (B) The $\delta^{65}Cu$ signature from the GBMZ chalcopyrite compared to that of porphyries and supergene sulfides, and bulk rock granites and meteorites. Data from Li et al. (2010), Larson et al. (2003), Mathur et al. (2005), Luck et al. (2003), Bishop et al. (2011). The magmatic/magmatic-hydrothermal field was defined using data from Li et al. (2010), Ikheata et al. (2011) and Ikheata and Hirata (2012). (C) Comparison of the $\delta^{18}O$ and $\delta^{13}C$ values of DAMP calcite with other IOCG and porphyry calcites. Data from Rotherham et al. (1998), Dreher et al. (2008), Li and Sasaki (2007), Calagari (2003) and Acosta-Góngora et al., in prep. Fields for the Proterozoic limestones and magmatic carbon from Santos et al. (2000) and Deines (1980).

Table 5.1.Number of samples and in-situ analysis of sulfur and copper

Location	Sample	Mineral	$\delta^{34}S$ (*n*)	$\delta^{65}Cu$ (*n*)
NORI	Vein A	Molybdenite	2	
	Vein G	Pyrite	5	
NICO	NC-128	Chalcopyrite		13
	NC-151	Chalcopyrite		8
	N-88	Chalcopyrite		9
	N-111	Chalcopyrite		4
DAMP	3523A	Pyrite	2	10
	3523B	Pyrite	2	
	3503B	Chalcopyrite	3	
	3523C	Chalcopyrite		10
Sue Dianne	SD-137	Chalcopyrite	6	14
	SD-123	Chalcopyrite	3	
	SD-21	Chalcopyrite	4	
	SD-109	Chalcopyrite	4	
	SD-140	Chalcopyrite	4	
	SD-144	Chalcopyrite	1	
	SD-76	Chalcopyrite	2	
	SD-153	Chalcopyrite		8
FAB	3518C1	Pyrite	5	
	3518C2	Pyrite	5	
	3517A	Chalcopyrite		7

n, number of analysis per sample

Table 5.2. Representative data (‰) of stable isotopes analysis

Location	Sample	Mineral	Host rock	$\delta^{18}O$	$\delta^{32}S$	$\delta^{13}C$	δD	$\delta^{65}Cu$	Comment
DAMP	3503B-9	Ccp	Rhyodacites		-3.3				Breccia infill material (hem>mag)
DAMP	3503B-10	Ccp	Rhyodacites		-2.9				Breccia infill material (hem>mag)
DAMP	3523A-8	Py	Rhyodacites		5.6				Breccia infill material (hem<mag-py)
DAMP	3523B-4	Py	Rhyodacites		-0.1				Breccia infill material (hem<mag-py)
DAMP	3505A	Calc	Rhyodacites	10.3		-2.7			Breccia infill material post-Cu mineralization (hem>mag)
DAMP	3505B	Calc	Rhyodacites	9.9		-2.2			Breccia infill material post-Cu mineralization
DAMP	DAMP-10	Ccp	Rhyodacites					-0.42	Breccia infill material post-Cu mineralization (hem<mag-py)
DAMP	DAMP-28	Ccp	Rhyodacites					-0.34	Breccia infill material post-Cu mineralization (hem<mag-py)
DAMP	3523A-4	Ccp	Rhyodacites					-0.48	Breccia infill material post-Cu mineralization (hem<mag-py)
DAMP	3523A-15	Ccp	Rhyodacites					-0.23	Breccia infill material post-Cu mineralization (hem<mag-py)
FAB	3518C1-1	Py	Rhyodacitic-porphyry		1.2				Py-mag(±ccp) microvein
FAB	3518C1-5	Py	Rhyodacitic-porphyry		-1.3				Py-mag(±ccp) microvein
FAB	3518C1-6	Py	Rhyodacitic-porphyry		1.0				Py-mag(±ccp) microvein
FAB	3518C2-9	Py	Rhyodacitic-porphyry		2.5				Py-mag(±ccp) microvein
FAB	3518C2-7	Py	Rhyodacitic-porphyry		1.9				Py-mag(±ccp) microvein
FAB	3517A-8	Ccp	Rhyodacitic-porphyry					-0.3	Py-mag(±ccp) microvein
FAB	3517A-3	Ccp	Rhyodacitic-porphyry					-0.2	Py-mag(±ccp) microvein
FAB	3517A-4	Ccp	Rhyodacitic-porphyry					-0.2	Py-mag(±ccp) microvein
NORI	Vein A-12	Mol	TLG siltstones		3.3				Tur-bt-vein (fine grained Mol)
NORI	Vein A-10	Mol	TLG siltstones		2.9				Tur-bt-vein (fine grained Mol)
NORI	Vein G-3	Py	TLG siltstones		2.5				Tur-bt-vein (py aggregates)
NORI	Vein G-11	Py	TLG siltstones		3.7				Tur-bt-vein (py aggregates)
NORI	T-2 (Qz)	Qz	TLG siltstones	12.2					Qz-K-fsp veins
NORI	Vein E (Qz)	Qz	TLG siltstones	10.4					Qz-K-fsp veins
NORI	S-H-Trench2	Bt	TLG siltstones	5.9			5.7		Coarse grain biotite adjacent to Turn-bt-(Mol-Urn) vein
NORI	Vein C	Bt	TLG siltstones	6.9			75.2		Coarse grain biotite adjacent to Turn-bt-(Mol-Urn) vein
NORI	Vein E (Qz)	Bt	TLG siltstones	7.8			27.2		Coarse grain biotite adjacent to Turn-bt-(Mol-Urn) vein
NORI	Sample H	Bt	TLG siltstones	5.8			-5.0		Coarse grain biotite adjacent to Turn-bt-(Mol-Urn) vein
SD	SD-137-4	Ccp	Rhyodacites		-5.6				Massive mag replacement, cpy in localized aggregates
SD	SD-137-5	Ccp	Rhyodacites		-5.6				Massive mag replacement, cpy in localized aggregates
SD	SD-137-3	Ccp	Rhyodacites		4.4				Massive mag replacement, cpy in localized aggregates
SD	SD-123-1	Ccp	Rhyodacites		-5.9				Volcanic breccia. Matrix replaced replaced by mag-fl-ccp
SD	SD-123-12	Ccp	Rhyodacites		-5.2				Volcanic breccia. Matrix replaced replaced by mag-fl-ccp
SD	SD-123-11	Ccp	Rhyodacites		-4.1				Volcanic breccia. Matrix replaced replaced by mag-fl-ccp
SD	SD-21-9	Ccp	Rhyodacites		-3.8				Structural breccia. Matrix infill material consists of ep-hem-ccp
SD	SD-21-8	Ccp	Rhyodacites		-7.8				Structural breccia. Matrix infill material consists of ep-hem-ccp

SD	SD-21-7	Ccp	Rhyodacites		-6.2		Structural breccia. Matrix infill material consists of ep-hem-ccp
SD	SD-109-3	Ccp	Rhyodacites		1.4		Volcanic Breccia? Massive mag-fl-ccp(±emp) replacement
SD	SD-109-2	Ccp	Rhyodacites		-0.6		Volcanic Breccia? Massive mag-fl-ccp(±emp) replacement
SD	SD-140-8	Ccp	Rhyodacites		-3.2		Volcanic breccia. Matrix replaced by massive mag>ep(±ccp)
SD	SD-140-7	Ccp	Rhyodacites		-1.3		Volcanic breccia. Matrix replaced by massive mag>ep(±ccp)
SD	SD-140-11	Ccp	Rhyodacites		1.0		Volcanic breccia. Matrix replaced by massive mag>ep(±ccp)
SD	SD-144-5	Ccp	Rhyodacites		-3.1		Volcanic breccia. Matrix replaced by massive mag>fl-ep(±ccp)
SD	SD-76-8	Ccp	Rhyodacites		-6.8		Felsic volcanics pervasively replace by mag-hem-ep(±ccp)
SD	SD-76-7	Ccp	Rhyodacites		-5.5		Felsic volcanics pervasively replace by mag-hem-ep(±ccp)
SD	SD-19	Qz	Rhyodacites	8.3			Barren quartz stockworks
SD	SD-21(Q)	Qz	Rhyodacites	10.2			Barren quartz vein (1.5 cm, thick)
SD	SD-ST-3	Qz	Rhyodacites	10.6			Silicified felsic volcanics. Qz-epdote altered zone. Quartz as stockworks
SD	SD-ST-2	Qz	Rhyodacites	9.2			Silicified felsic volcanics. Qz-epdote altered zone. Quartz as stockworks
SD	SD-1.74(Qz)	Qz	Rhyodacites	9.2			Barren quartz stockworks
SD	SD-137-03	Ccp	Rhyodacites			-0.83	Massive mag replacement, ccpin localized aggregates
SD	SD-137-01	Ccp	Rhyodacites			-0.81	Massive mag replacement, ccpin localized aggregates
SD	SD-137-06	Ccp	Rhyodacites			-0.79	Massive mag replacement, ccpin localized aggregates
SD	SD-137-7	Ccp	Rhyodacites			-0.76	Massive mag replacement, ccpin localized aggregates
SD	SD-137-11	Ccp	Rhyodacites			-0.64	Massive mag replacement, ccpin localized aggregates
SD	SD-153-62	Ccp	Rhyodacites			-0.57	Volcanic breccia. Matrix replaced by massive mag>ep(±ccp)
SD	SD-153-60	Ccp	Rhyodacites			-0.56	Volcanic breccia. Matrix replaced by massive mag>ep(±ccp)
SD	SD-153-61	Ccp	Rhyodacites			-0.50	Volcanic breccia. Matrix replaced by massive mag>ep(±ccp)
SD	SD-153-62.1	Ccp	Rhyodacites			-0.48	Volcanic breccia. Matrix replaced by massive mag>ep(±ccp)
SD	SD-153-59	Ccp	Rhyodacites			-0.40	Volcanic breccia. Matrix replaced by massive mag>ep(±ccp)
NICO	N-128-16	Ccp	Amp-ironstones			-0.31	Ccp interstitial to apy. Apy occurns in mineral aggregates randomly disseminated
NICO	N-128-09B	Ccp	Amp-ironstones			-0.17	Ccp interstitial to apy. Apy occurns in mineral aggregates randomly disseminated
NICO	N-128-05	Ccp	Amp-ironstones			0.06	Ccp interstitial to apy. Apy occurns in mineral aggregates randomly disseminated
NICO	N-151-27	Ccp	Amp-ironstones			-0.59	Ccp in apy-sch-py vein (1 cm thick)
NICO	N-151-10	Ccp	Amp-ironstones			-0.45	Ccp in apy-sch-py vein (1 cm thick)
NICO	N-111-03	Ccp	Amp-ironstones			-0.35	Apy(±ccp) disseminated along the bedding
NICO	N-111-03-1	Ccp	Amp-ironstones			-0.30	Apy(±ccp) disseminated along the bedding

Abbreviations. SD, Sue Dianne; Arsenopyrite = apy; amphibole = amp; biotite = bt, calcite = calc; chalcopyrite = ccp; epidote = ep; emplectite = emp; fluorite = fl; hematite = hem; k-fsp = potassic feldspar; magnetite = mag; quartz = qz; molybdenite =mol; tourmaline=tur; urnaninite= urn

Table 5.3. Fluid inclusions data from the DAMP and Nori/RA prospects

Location	Assemblage/n	Age	Type	*Te* (˚C)	*Tm*$_i$ (˚C)	$T_{l\text{-}v}$ (˚C)	*Th* (˚C)	Salinity[1] (wt.% NaCl equiv)	Salinity[2] (wt.% $CaCl_2$ equiv)	Comments
Nori/RA	VE3-7-C1A1 n=4	Unk	LV	n.m	-22 to -24	n.m	132-156	n.d.	n.d.	
Nori/RA	VE4-7-C1A2(3) n=2	Unk	LV	n.m	-24 to -21	n.m.	135-142	n.d.	n.d.	
Nori/RA	VE4-7-C2A1 n=2	Unk	LV	n.m	-22	n.m.	181-193	n.d.	n.d.	
Nori/RA	VE4-7-C1A2(2) n=4	Unk	LV	n.m	-23 to -21	n.m.	114-149	n.d.	n.d.	
Nori/RA	VE4-7-C1A1(2) n=2	Unk	LV	n.m	-24	n.m.	130-167	n.d.	n.d.	
Nori/RA	VE4-7-C2A2 n=3	Unk	LV	n.m	-33 to -35	n.m.	105-144	n.d.	n.d.	
Nori/RA	VE-10-2-C3A1 n=4	Unk	LV	-78	-21 to -18	n.m.	152-169	1	19-20	Some inclusions showed a change in L/V ratios after reaching Th
Nori/RA	VE-10-2-C3A1(2) n=2	Unk	LV	-78	-35	n.m.	175-182	2	25	
Nori/RA	VE-10-C2A2 n=3	Unk	LV	-76	-22	n.m.	162-202	2	20	
Nori/RA	VE10-3C2A1 n=3	Unk	LV	-51	-21 to -18	n.m.	164-207	1	19-20	Some inclusions showed a change in L/V ratios after reaching Th
Nori/RA	VE7-9C1A1-2p n=4	Unk	LVS	n.m.	Nm	128-141	151-206	30-32	n.d.	
DAMP	B-13-9-ssA1 n=3	S	LV	-64 to -62	-25 to -22	n.m.	184-218	n.d	n.d	
DAMP	B13-9-ssA2 n=4	S	LV	-63	-22 to -21	n.m.	189-193	n.d	n.d	
DAMP	B19-ss-A3 n=6	S	LV	-74 to 77	-24 to -23	n.m.	152-177	n.d	n.d	
DAMP	B19-07-ssA3 n=2	S	LV	-76 to -74	-27 to -28	n.m.	150-166	n.d	n.d	
DAMP	A18-6SSA1 n=5	S	LV	-65	-35	n.m.	120-126	0-2	25-27	Salinity calculated only in 3 inclusions
DAMP	B18-7-PA1 n=4	PP	LV	-70 to -67	-26 to -16	n.m.	162-174	n.d	n.d	
DAMP	B18-7PA1-2 n=2	S	LV	-70 to -67	-34 to-29	n.m.	173-182	n.d	n.d	

DAMP	B18-7PA13 n=2	S	LV	-70 to -67	-25 to -40	n.m.	147-153	n.d	n.d	
DAMP	B18-7PA2-2 n=2	S	LV	-74 to-76	-19 to -17	n.m.	162-170	n.d	n.d	
DAMP	B17-19PA4 n=5	PP	LV	-76	-27 to -33	n.m.	128-192	3	23	Salinity only calculated in one inclusions
DAMP	B-18-2013PA2 n=2	S	LV	-76, -74	-24	n.m.	182, .>230	10	14	
DAMP	A18-6SSA2 n=3	S	LV	-63	-43 to -19	n.m.	95-105	0.1	18-29	
DAMP	B17-7SSA1 n=2	S	LV	-80 to -77	-33 to -25	n.m.	139-144	n.d.	n.d.	

Abbreviations. Unk, 'unknown' inclusions; 'Possible' primary inclusions, PP; Secondary inclusions, S; n.d., not determined; n.m., not measured

6 Conclusions

The GBMZ in the Canadian Northwest Territories is an exploration target for IOCG deposits, such as those found in Australia and South America. However, its remote location and the historical absence of interest in this area (until the recent GEM project) has made the mining companies relauctant to carry out further mineral exploration in the area. In particular, the GBMZ lacks well constrained spatial and temporal links between the IOCG polymetallic systems with their country rocks and tectonic environment, systematic host-rock-alteration-mineralization associations, and adequate exploration tools (according to the terrain type, and the geochemical background of the rocks) that can lead to the discovery of economic systems. Therefore, the present work was an effort to fill some of these scientific gaps and to set up a geological framework up which, further research on these deposits can be done. Specifically, this study has defined the GBMZ IOCG metallogenic province time frame, temporal relationships between ore and gangue minerals, mechanisms of ore formation, and possible sources of metals and ore-mineral forming elements. Furthermore, this thesis also addresses the utility of magnetite as a indicator mineral in till exploration surveys in the GBMZ.

6.1 Magnetite geochemistry and its applications to IOCGs mineral exploration

In this study alteration/mineralization assemblages in several polymetallic iron oxide-rich systems in the GBMZ such as the NICO and Sue Dianne deposits, and DAMP, FAB prospects, and the vein hosted the Nori/RA prospect, were characterized. In all of these, magnetite is common, and in some locations it is the dominant iron oxide. Magnetite is not only associated with mineralization, but is found in the non-mineralized metasediments of the TLG (barren Ca-Fe alteration and metamorphic magnetites). In Nori/RA, FAB and NICO multiple magnetite stages were recognized to be pre- and syn-ore. Geochemical analysis of magnetite showed that fractionation of Co, Cr, V, Ni, and Cr into this iron oxide could be a

function of: host rock-fluid equilibration during regional metamorphism, post-metamorphic hydrothermal metasomatism of TLG metasedimentary rocks, preferential solubility of Co over Ni within the Fe-rich fluids, changes in oxygen fugacity (fO_2), and partitioning of elements into co-precipitating sulfides.

Trace element studies on magnetite can also be applied to mineral exploration programs in the GBMZ. At a regional scale, the Cr/Co is higher in barren and pre-ore magnetite than in magnetite co-precipitated with ore minerals and/or present in ore-rich veins and breccias. Locally, at the Nori/Ra prospect, the V/Ni ratio in magnetite differentiates between barren and ore-related magnetite, and at DAMP and Sue Dianne the Co/Ni ratio is extremely high and clearly different from those of other GBMZ magnetite samples. Thus, magnetite has the potential to be an important indicator mineral in till exploration surveys to track undiscovered IOCG deposits in the GBMZ.

6.2 Alternative mechanisms of ore concentration in IOCG deposits

IOCG systems containing economic concentrations of Au–Co–Bi±Cu (such as the NICO deposit) are rare. The developement of a pervasive Fe-Ca-rich amphibole, biotite and magnetite alteration assemblage (Ca-Fe-K alteration), and subsequent equilibration of the metal-carrying solutions could have triggered the ore precipitation; this process has been suggested for ore precipitation in the Tennant Creek district (Skirrow, 2002). The presence of re-crystallized sulfarsenides and arsenides spatially associated with Au and Bi(±Te) inclusions and crosscut by Bi±Au-rich micro-veins allows for alternative mechanisms of ore concentration to those conventionally suggested for IOCG and other magmatic-hydrothermal deposits (e.g., fluid mixing, boiling) to be proposed.

Two mechanisms are proposed to be responsible for the gold refining at NICO deposit. The first mechanism is consistent with an *in-situ* 'lock in' of Au by Bi as both were liberated from early Au-bearing Co-rich arsenopyrite I, loellingite, and cobaltite when conversion to arsenopyrite II took place. During this process, partial dissolution of Au and Bi by the hydrothermal fluids could

have occurred. The second mechanism deals with the presence of globular shaped Bi trails co-existing with hydrothermal fluids indicating that further refining of Au by Bi melts occurred; this is known as the liquid bismuth collector model (Douglas, 2000). Both processes may have been contemporaneous, or closely associated in time, and they satisfactorily explain the preserved ore textures at the NICO deposit. This study is the first one to recognize the significant role of the liquid Bi collector model in the formation of IOCG deposits.

6.3 Geochemistry of IOCG fluids in the GBMZ

The results of this part of the study are presented in Chapters 3and 4. The isotopic analyses carried on the GBMZ IOCG and-related systems (NICO, Nori/RA, Sue Dianne, DAMP, and FAB) suggest that most S, C and partially O and Cu have been derived from magmatic-hydrothermal fluids with some contribution from the TLG (the host rocks to the NICO deposit) and felsic volcanics from the Great Bear arc. In all the locations studied, most of the $\delta^{34}S$ values have a restricted range between -4‰ and 5‰. The bulk rock $\delta^{34}S$ values (-1 to 6‰) from the TLG metasediments indicate that is also possible that the metasedimentary rocks (containing scapolite and fine grained pyrite) could have contributed some S at the NICO deposit. The presence of evaporitic ($\delta^{34}S>10$‰) and/or organic-($\delta^{34}S<-20$‰) derived S as reported in other IOCG systems (Barton and Johnson, 1996; de Haller and Fontboté, 2009) is not indicated by our results. An anomalous $\delta^{13}C$ value of -15‰ from post-mineralization calcite (S3) at NICO deposit might indicate the presence of either biogenic carbon (Faure and Mensing, 2005) and/or Precambrian reduced carbon (Kerrich, 1986) in post-mineralization fluids. The presence of organic matter in the TLG has not been recognized in this study, but its occurrence at depth or equilibration of the hydrothermal fluids with deeper Precambrian basement cannot be discounted.

The nature of the samples greatly restricted the fluid inclusion study. The most obvious problem was that there was a lack of fluid inclusion-bearing gangue minerals that clearly co-precipitated with the ore minerals. Furthermore, the lack of clearly primary fluid inclusions in the minerals analyzed, and their complex

composition and high decrepitation and 'stretching' rate also proved to be challenging. In general, the pre- (NICO and DAMP) and syn-ore (NICO) inclusions from the GBMZ contain complex saline, NaCl-$CaCl_2$-H_2O brines and carbonic fluids.

In the Nori/RA and DAMP prospects, a meteoric water signature was identified in quartz (values of $\delta^{18}O_{fluid}$=-12 to 1‰) and calcite (values of $\delta^{18}O_{fluid}$=-2 to 2‰), respectively. However, this has to be interpreted carefully as only minimum trapping temperatures (no pressure correction) were used to obtain the isotopic calculation. Calcite from DAMP has a $\delta^{13}C$ and $\delta^{18}O$ value consistent with magmatic source for these components. Fluid inclusion studies in DAMP, suggest a possible fluid mixing between a less saline (meteoric) and more saline (magmatic?) hydrothermal fluid.

In NICO, the $\delta^{18}O$ values (6-8‰) of the fluid co-precipitating with magnetite and arsenopyrite are consistent with magmatic waters or metamorphic fluids (6-8‰). The LV and LVS fluid inclusion assemblages most closely associated with the Au mineralization are found in Bi-rich trails. The halite-saturated inclusions (LVS-Bi) indicate that the Bi and possibly Au was transported in saline to hyper saline brines (*T*h = 192-287 ºC up to >350 ºC; 32 to >37 wt. % NaCl equiv). The vapor saturated inclusions (LV-Bi) also have variable salinities (0.4-10 wt.% NaCl equiv, 8-22 wt.% $CaCl_2$ equiv;), with homogenization temperatures (*T*h) of 98 to 216ºC. The data from the LV inclusions suggest that Bi(±Au?) occurred as the result of multiple pulses of magmatic hydrothermal fluid. Individual assemblages do not suggest fluid mixing, but a positive correlation between Tm_i and *T*h indicates an evolution from a low temperature highly saline fluid to a higher temperature less saline fluid (or vice versa) with time. The pressure correction applied to fluid inclusions associated with the Bi-trails suggest a the deposit formed at a depth range between 4.9 and 8.1 km, which is common for IOCG deposits (<4-10 km; Skirrow, 1993; Perring et al. 2000; Rusk et al., 2010).

6.4 The metallogeny of the GBMZ and the source of metals

Trace element analyses carried out in this study and by Gandhi (1989), Camier (2002) and Azar (2007) demonstrate that neither the TLG or the GBMZ felsic rocks are enriched in Au, Co, Cu, and Ag, with respect to average continental crust values. Conversely, As and S are relatively enriched in the TLG. Therefore the hydrothermal system could have derived some of these elements from the host-rock. This is also consistent with the S isotopic data. To further test this hypothesis a simple mass balance calculation was carried out for the NICO and Sue Dianne deposits. This suggests that leaching relatively small volumes (0.1 to 2.9 km^3) of the TLG and felsic rocks could provide the Au, Co, Cu, Bi and Ag for the deposits. In the particular case of Cu, a "recycled origin" is also suggested by most the Cu isotopic data. The mass balance calculation assumes 100% efficiency of the leaching processes.

This mass balance estimation only shows that the metal budget is not a potential problem to form IOCG deposits the GBMZ. Nevertheless, it requires fluids capable of effectively leaching, concentrating and re-precipitating metals. The IOCGs are known for having extensive alteration halos (1 to >7 km; Richards and Mumin, 2013) relative to other hydrothermal systems like e.g., copper porphyries. Thus, this alteration evenly might result in the mobilization and re-precipitation of important masses of economic metals (e.g. Montreuil et al. 2013; Montreuil et al. accepted). Interesting enough, the isotopically lighter $\delta^{65}Cu$ data supports the fact that some Cu has been recycled from igneous and/or metamorphic rocks.

The overall stable isotope (S, Cu, C, O and O) and radiogenic isotopes (re-Os) studies suggest that the emplacement of the NICO deposit and other IOCG systems in the GBMZ have a magmatic-hydrothermal origin associated with upwelling calc-alkaline magmas from the Great Bear arc, emplaced between 1875 and 1865 Ma. Although, some components like As, S and Cu could have been derived from the hostrocks. The mass balance results open the debate about how much of the metals in magmatic-hydrothermal IOCG deposits could have possibly

been re-mobilized from the host rocks, and how much is actually introduced to the system by ore-bearing magmatic-hydrothermal fluids.

6.5 Summary of the study

This study has shown that the host TLG and felsic volcanic rocks have sufficient metal budget to form IOCG deposits of an analogous size to those of NICO and Sue Dianne. The last statement opens the debate about the possible sources of metals in IOCG deposits, e.g., are the metals been totally or partially recycled from the host rocks during early stages of alteration (e.g., Na-Ca alteration)? or by the contrary, are these originally derived from metal-rich fluids de-coupled from up-welling magmas? The isotopic evidence, though, has shown that the GBMZ IOCG metallogeny (1875-1865 Ma) is directly associated with the intermediate to felsic calc-alkaline magmatism of the Geat Bear arc (1875-1856 Ma). Therefore, these systems belong to the magmatic-hydrothermal family of the IOCG deposits, similar to those in the Peruvian and Chilean Andes (e.g., Candelaria-Punta del Cobre, Mantos Verdes), although, some components like S, As and Cu might have been partially acquired from the TLG and felsic volcanic host rocks of the Great Bear arc in the GBMZ IOCG systems. Nonetheless, the S isotope data are not consistent with an evaporitic-derived sulfur, as found in non-magmatic end-members of the IOCG classification.

Another important aspect of this work, is that, for the first time was recognized the important role of Bi (±Te) melts in the Au mineralization of in the NICO deposit. Furthermore, Au in NICO was remobilized from host Fe-Co-S-As mineral phases via retrograde alteration, which is a common Au-refining mechanism in orogenic and metamorphosed Au deposits, but has not been fully explored for IOCGs.

Finally, petrographic and geochemical studies carried out on magnetite, an abundant mineral in metamorphic rocks, and barren and IOCG associated alteration types in the GBMZ, showed that this iron oxide has the potential of becoming an important indicator mineral for till exploration surveys in the GBMZ based on different Cr/Co, Co/Ni and V/Ni ratios.

6.6 Suggestions for future studies

Although the present work addressed some of the most important geological gaps on the formation of NICO deposit and other IOCG systems in the GBMZ, many unresolved issues remain. Among the most important are: the sources of metals and iron, composition of solids from hyper-saline brines and fluid components from the carbonic-rich inclusions, and role of the pre-ore Fe-Ca-K metasomatic alteration on metal precipitation at the NICO deposit.

In this work, only a few samples from NICO deposit and the other systems from the GBMZ were analyzed for Cu isotopes. The results suggest that most copper might have been recycled from the host-rocks. However, a more detailed study in NICO and Sue Dianne systems, where three-dimensional sampling of the deposits is possible, might expand our knowledge about the source (s) of Cu (e.g., mantle derived vs recycled from host rocks) in IOCGs. More recently, the development of *in-situ* analyses of Fe stable isotopes have shown similar characteristics to those of Cu, where mantle-derived Fe can be traced from the analysis of magnetite. Further Cu and Fe isotopic studies should also be carried out at the more epithermal expressions of the GBMZ IOCG systems, such as the Echo Bay (e.g., Mag Hill) and possibly the Camsell River (e.g., Terra mine) districts. Comparision of both data sets (epithermal vs metasomatic), might indicate the occurrence of phase changes (e.g., boiling), changes in redox conditions, and or pH, which are main triggers of ore precipitation.

The possible dissolution of metals from the host rocks by magmatic-hydrothermal fluids was argued in this work by carrying out a mass balance calculation. Nevertheless, the parameters chosen for this estimation are rather simple, and need to be refined in order to obtain more accurate results. The future modelling should incorporate the following paremeters: detailed geochemistry (salinity, temperature and redox conditions), and volumes of the hydrothermal plumes and their parental magmas, permeability of the rocks and cooling rates of the magmas and aqueous fluids.

One of the most important discoveries of this study was the presence of LVS Bi-rich inclusions at NICO, which are not typically reported in other IOCGs. Nonetheless, due to limitations proper of the microthermometric analysis, it was not possible to determine the composition of some solids from the LVS-Bi inclusions. Therefore, Raman spectroscopy (RS) studies are recommended for those inclusions to determine the presence of Ca-, K- and Fe-rich solid phases. The RS will be also useful to determine the presence of volatiles like CH_4 and N_2 in the carbonic-rich inclusions. Moreover, future *in-situ* LA-ICP-MS analysis carried out on selected Bi-trails containing Au-like phases could also demonstrate conclusively that Bi melts scavenged gold from the hydrothermal fluids at NICO.

Finally, the possible role of the pre-ore ironstones formed at NICO deposit, as metal-sinks has been briefly discussed in chapter 4. However, most of the inferences made in this work result from comparing the NICO host rocks mineralogy and fluids temperature and composition, with that of the West Peko deposit and interpreting the thermodynamic modelling done by Skirrow and Walshe (2002) on that system. Given the temperature and salinity constraints acquired in this work, and what could be acquired from future research (e.g., RS), it will be of great interest to perform similar thermodynamic modeling for NICO, and hence, asses more accurately if the ironstones formation and subsequent equilibration with the ore-fluids capable of precipitating significant amounts of metals like Cu, Bi, Co and Au.

6.7 References

Azar, B., 2007, The lithogeochemistry of volcanic and subvolcanic rocks of the FAB Lake area, Great Bear magmatic zone, Northwest Territories, Canada: Unpublished B.Sc. thesis, Toronto, University of Toronto, 96 p.

Barton, M.D., and Johnson, D.A., 1996, Evaporitic-source model for igneous-related Fe oxide-(REE-Cu-Au-U) mineralization: Geology, v. 24, p.259-262.

Camier, W.J., 2002, Geology of the Sue-Dianne Proterozoic Cu-Ag-Fe oxide breccia complex, Mazenod Lakedistrict, Northwest Territories: Unpublished M.Sc. thesis, London, University of Western Ontario, 210 p.

De Haller, A., and Fontboté, L., 2009, The Raúl-Condestable iron oxide copper-gold deposit, central coast of Peru: ore related hydrothermal alteration, sulfur isotopes, and thermodynamic constrainst: Economic Geology, v. 104, v.365-384.

Douglas, N., Mavrogenes, J., Hack, A. and England, R., 2000, The liquid bismuth collector model: an alternative gold deposition mechanism, *in* C. G., Silbeck and T. C. T., Hubble eds., Understanding planet Earth; searching for a sustainable future; on the starting blocks of the third millennium, 15th Australian Geological Convention, eds: Geological Society of Australia, Sydney, 135 p.

Faure, G., Mensing, T.M., 2005, Chapter 26: Hydrogen and Oxygen. Isotopes – Principles and Applications: Third Edition. John Wiley & Sons, Inc. Hoboken, New Jersey, p.716-718.

Gandhi, S.S.,1989, Rhyodacite ignimbrites and breccias of the Sue-Dianne and Mar Cu-Fe-U deposits, southern Great Bear magmatic zone, Northwest Territories: Geological Survey of Canada Paper 89-1C, p. 263-273.

Kerrich, R., 1986, Fluid infiltration into fault zones: chemical, isotopic, and mechanical effects: Pure and Applied Geophysics, v. 124, p. 225-268

Montreuil, J.F., Corriveau, L., and Grunsky, E., 2013, A compositional data analysis of IOCG systems, Great Bear magmatic zone, Canada: To each alteration types its own geochemical signature: Geochemistry: Exploration, Environment, Analysis, doi: 10.1144/geochem2011-101.

Montreuil, J.F., Corriveau, L., and Potter, E. (accepted), Albitite-hosted uranium development within IOCG systems: The southern breccia, Great Beat magmatic zone, Northwest Territories, Canada: Mineralium Deposita.

Ootes, L., Goff, S., Jackson, V., Gleeson, S.A., Creaser, R.A., Samson, I.M., Evenson, N., Corriveau, L., and Mumin, H., 2010, Timing and thermochemical constraint on multi-element mineralization at the Nori/RA Cu-Mo-U prospect, Great Bear magmatic zone, Northwest Territories, Canada: Mineralium Deposita v. 45, p. 549-566.

Perring, C.S., Pollard, P.J., Dong, G., Nunn, A.J., and Blake, K.L, 2000: The Lightning Creek sill complex, Cloncurry district, northwest Queensland: A source of fluids for Fe oxide-Cu-Au mineralization and sodic-calcic alteration: Economic Geology, v. 95, p. 1067-1089.

Richards, J.P., and Mumin, H., 2013, Magmatic-hydrothermal processes within an evolving earth: Iron oxide-copper-gold and porphyry Cu±Mo±Au deposits:Geology, v. 41, p. 767-770.

Rusk, B.G., Oliver, N., Cleverley, J., Blenkinsop, T., Zhang, D., Williams, P., and Haberman, P., 2010, Physical and chemical characteristics of the Ernest Henry iron oxide copper gold deposit, Cloncurry, QLD, Australia; Implications for IOCG genesis, in Porter, T.M., ed., Hydrothermal iron oxide copper-gold & related deposits: A global perspective: Adelaide, PGC Publishing, v. 3, p. 187-204.

Skirrow, R.G., 1993, The genesis of gold-copper-bismuth deposits, Tennant Creek, Northern Territory: Unpublished Ph.D. thesis, Canberra, Australian National University, 158 p.

Skirrow, R., and Walshe, J., 2002, Reduced and oxidized Au-Cu-Bi iron oxide deposits of the Tennant Creek Inlier, Australia: An integrated geologic and chemical model: Economic geology, v. 97, p. 1167-1202.

Appendix A. Location of samples and drill holes

		NAD83/UTM coordinates (Zone 11N)		
Drill holes/	Location	Easting	Northing	Elevation
N-97-050	Nico	512492	7046781	301
N-00-205	Nico	Not provided by Fortune minerals		
N-00-222	Nico	512508	7046825	294
N-00-226	Nico	512429	7046890	306
N-00-227	Nico	512454	7046934	306
N-00-228	Nico	512476	7046988	299
N-00-235	Nico	512276	7046915	301
N-00-243	Nico	512369	7047012	290
N-00-249	Nico	512320	7046883	304
N-00-275	Nico	Not provided by Fortune minerals		
N-97-052	Nico	512649	7046632	292
N-98-157	Nico	512528	7046591	299
N-10-323	Nico	512432	7047046	292
N-10-322	Nico	511988	7046938	297
N-03-278	Nico	511931	7047098	272
N-03-276	Nico	512508	7046824	294
N-03-275	Nico	512499	7046801	299
N-98-184	Nico	512553	7046945	292
N-97-035	Nico	512534	7046895	302
SD-97-04	SD	504323	7070422	249
SD-97-05	SD	504277	7070434	252
SD-98-16	SD	504457	7070303	226
SD-98-30	SD	504321	7070399	252
SD98-42	SD	504419	7070371	232
SD-98-45	SD	504246	7070166	283
SD-98-31	SD	504316	7070346	254
SD-97-06	SD	504277	7070435	252

SD-98-30	SD	504321	7070399	252
3523A	DAMP	467202	7229191	
3523B	DAMP	467202	7229191	
3523C	DAMP	467202	7229191	
3503B	DAMP	467087	7229317	
Vein A	NORI	509007	7136522	
Vein G	NORI	509007	7136522	
3518C1	FAB	494483	7110513	
3518C2	FAB	494483	7110513	
3507A	Terra	448193	7276530	

SD, Sue Dianne

Appendix B. Sulfur isotope data

Location	Sample	LSI number	Extraction No./Lab No.	Mineral	Drill hole	d34SV-CDT (‰)	Mineralogy	HR	Mineralization style	Lens
DAMP	3503B	LSI-S-11-1-9	MIV-86-9/S-11-1-22 Ccp	Ccp		-3.3	py-ccp-bn	Felsic volcanics /Rhyodacites?	Breccia	
DAMP	3503B	"	MIV-86-11/S-11-1-22 Ccp	Ccp		-4.0	"	"	"	
DAMP	3503B	"	MIV-86-10/S-11-1-22 Ccp	Ccp		-2.9	"	"	"	
DAMP	3523B	"	MIV-86-5/S-11-1-9 PY	Py		1.5	"	"	"	
DAMP	3523B	"	MIV-86-4/S-11-1-9 PY	Py		-0.1	"	"	"	
DAMP	3523A	LSI-S-11-1-5	MIV-86-8/S-11-1-5 PY	Py		5.6	py-ccp-Cu-Bi sulf	Felsic volcanics /Rhyodacites?	Breccia	
DAMP	3523A	"	MIV-86-7/S-11-1-5 PY	Py		5.2	"	"	"	
FAB	3518C1	LSI-S-11-1-29	MIV-97-1/S-11-1-29 PY	Py		1.2	py-ccp	Felsic volcanics /Rhyodacites?	Breccia/Vein	
FAB	3518C1	"	MIV-97-	Py		0.8	"	"	"	

			2/S-11-1-29 PY					
			MIV-97-3/S-11-1-29 PY					
FAB	3518C1	"	MIV-97-5/S-11-1-29 PY	Py	1.1	"	"	"
FAB	3518C1	"	MIV-97-6/S-11-1-29 PY	Py	-1.3	"	"	"
			MIV-100-9/S-11-1-30 PY		1.0			
FAB	3518C1	"	(no GC)	Py		"	"	"
FAB	3518C2	LSI-S-11-1-30	MIV-100-8/S-11-1-30 PY (no GC)	Py	2.5	py-ccp	Felsic volcanics /Rhyodacites?	Breccia/Vein
FAB	3518C2	"	MIV-100-7/S-11-1-30 PY (no GC)	Py	1.3	"	"	"
FAB	3518C2	"	MIV-100-6/S-11-1-30 PY (no GC)	Py	1.8	"	"	"
FAB	3518C2	"		Py	2.3	"	"	"
FAB	3518C2	"	MIV-100-	Py	1.9	"	"	"

NICO	N-205-148.0-148.07	LSI-S-11-1-15	5/S-11-1-30 PY (no GC) MIV-89-9/S-11-1-15 APY	Apy	N-205	4.6	apy-ccp-(-Bi)-py	TLG (metasiltstones)	Vein	LL
NICO	N-205-148.0-148.07	"	MIV-89-12/S-11-1-15 APY	Apy	N-205	5.4	"	"	"	
NICO	N-205-148.0-148.07	"	MIV-89-11/S-11-1-15 APY	Apy	N-205	4.5	"	"	"	
NICO	N-205-148.0-148.07	"	MIV-89-10/S-11-1-15 Ccp	Ccp	N-205	5.3	"	"	"	
NICO	N-205-88.55-88.60	LSI-S-11-1-31	MIV-94-6/S-11-1-31 APY	Apy	N-205	4.3	apy1-apy2-py-ccp	TLG (metasiltstones)	Vein	ML
NICO	N-205-88.55-88.60	"	MIV-94-5/11-1-31 APY	Apy	N-205	5.0	"	"	"	
NICO	N-205-88.55-88.60	"	MIV-94-3/S-11-1-31 APY	Apy	N-205	5.1	"	"	"	
NICO	N-205-88.55-88.60	"	MIV-94-2/S-11-1-31 APY	Apy	N-205	5.0	"	"	"	
NICO	N-205-	LSI-S-	MIV-95-	Apy	N-205	4.5	apy-py-po	TLG	disseminated	ML

	99.24-99.35	11-1-23	5/11-1-23 APY					(metasiltstones)	along the bedding	
NICO	N-205-99.24-99.35	"	MIV-95-4/S-11-1-23 APY	Apy	N-205	4.2	"	"	"	
NICO	N-205-99.24-99.35	"	MIV-95-3/S-11-1-23 APY	Apy	N-205	4.6	"	"	"	
NICO	N-228-156.02-156.15	LSI-S-1-1-13	MIV-94-9/S-11-1-13 APY	Apy	N-228	4.8	apy-ccp-py	TLG (metasiltstones)	disseminated along the bedding	ML
NICO	N-228-156.02-156.15	"	MIV-94-8/S-11-1-13 APY	Apy	N-228	4.8	"	"	"	
NICO	N-228-156.02-156.15	"	MIV-94-7/S-11-1-13 APY	Apy	N-228	4.8	"	"	"	
NICO	N-228-156.02-156.15	"	MIV-94-10/11-1-13 APY	Apy	N-228	4.7	"	"	"	
NICO	N-228-163.80-163.90	LSI-S-11-1-11	MIV-98-9/S-11-1-11 PY	Py	N-228	4.3	apy-py ccp	TLG (metasiltstones)	Vein	ML
NICO	N-228-163.80-163.90	"	MIV-98-8/S-11-1-11 PY	Py	N-228	3.9	"	"	"	"
NICO	N-228-163.80-	"	MIV-98-11/LSI-11-	Py	N-228	3.6	"	"	"	"

	163.90		1-11 PY							
	N-228-163.80-		MIV-98-10/LSI-11-							
NICO	163.90	"	1-11 PY	Py	N-228	3.6	"	"	"	"
	N235-113.18-	LSI-S-11-1-16	MIV-94-1/S-11-1-16 APY	Apy	N-235	4.9	apy-Bi	TLG (metasiltstones)	disseminated in patches	LL
NICO	113.22									
	N235-113.18-		MIV-93-12/S-11-1-16 APY							
NICO	113.22	"		Apy	N-235	3.5	"	"	"	"
	N235-113.18-		MIV-93-11/S-11-1-16 APY							
NICO	113.22	"		Apy	N-235	4.2	"	"	"	"
	N235-113.18-		MIV-93-10/S-11-1-16 APY							
NICO	113.22	"		Apy	N-235	3.3	"	"	"	"
	N243-111.90-	LSI-S-11-1-14	MIV-95-7/S-11-1-14 APY	Apy	N-111	5.1	apy-ccp-py	TLG (metasiltstones)	disseminated along the bedding	ML
NICO	112.13									
	N243-111.90-		MIV-95-6/S-11-1-14 APY							
NICO	112.13	"		Apy	N-111	4.1	"	"	"	"
	N243-155.18-	LSI-S-11-1-18	MIV-93-1/S-11-1-18 Ccp	Ccp	N-243	4.4	apy-(py)-ccp	TLG (metasiltstones)	disseminated in patches	LL
NICO	155.90									
	N243-155.18-		MIV-92-12/S-11-1-18 APY							
NICO	155.90	"		Apy	N-243	5.1	"	"	"	"

NICO	N243-24.38-24.44	LSI-S-11-1-12	MIV-89-8/S-11-1-12 PY	Py	N-243	5.1	apy-Bi-py	TLG (metasiltstones)	Vein	UL
NICO	N243-24.38-24.44	"	MIV-89-7/S-11-1-12 PY	Py	N-243	4.5	"	"	"	"
NICO	N243-24.38-24.44	"	MIV-89-3/S-11-1-12 APY	Apy	N-243	4.3	"	"	"	"
NICO	N243-24.38-24.44	"	MIV-892/S-11-1-12 APY	Apy	N-243	4.8	"	"	"	"
NICO	N243-24.38-24.44	"	MIV-89-1/S-11-1-12 APY	Apy	N-243	5.2	"	"	"	"
NICO	N249-103.02-103.14	LSI-S-11-1-7	MIV-96-7/S-11-1-7 APY	Apy	N-249	5.0	apy-(-Bi)	metasiltstones	disseminated in patches	ML
NICO	N249-103.02-103.14	"	MIV-96-8/S-11-1-7 APY	Apy	N-249	3.9	"	"	"	"
NICO	N249-103.02-103.14	"	MIV-96-9/S-11-1-7 APY	Apy	N-249	5.3	"	"	"	"
NICO	N249-103.02-103.14	"	MIV-96-10/S-11-1-7 APY	Apy	N-249	4.6	"	"	"	"
NICO	NC13-7-	LSI-S-	MIV-88-	Apy		5.1	apy-(py)	Porphyry	disseminated	

	11-13	11-1-2	8/S-11-1-2 APY					in patches
NICO	NC13-7-11-13	"	MIV-88-3/S-11-1-2 APY	Apy	6.4	"	"	"
NICO	NC13-7-11-13	"	MIV-88-2/S-11-1-2 APY	Apy	5.7	"	"	"
NICO	NC13-7-11-13	"	MIV-88-1/S-11-1-2 APY	Apy	4.1	"	"	"
NICO	NC13-7-11-13	"	MIV-87-9/S-11-1-2 APY	Apy	6.2	"	"	"
NICO	NC13-7-11-13	"	MIV-87-8/S-11-1-2 APY	Apy	4.1	"	"	"
NICO	NC13-7-11-13	"	MIV-87-5/S-11-1-2 APY	Apy	3.4	"	"	"
NICO	NC13-7-11-13	"	MIV-87-11/S-11-1-2 APY	Apy	5.4	"	"	"
NICO	NC13-7-11-13	"	MIV-87-12/S-11-1-2 APY	Apy	-3.3	"	"	"
NICO	NC13-7-11-8	LSI-S-11-1-25	MIV-96-6/S-11-1-	Py	5.0	apy	Porphyry	disseminated in patches

NICO	NC13-7-11-8	"	25 PY MIV-96-5/11-1-25 PY	Py		3.8	"	"	"	
NICO	NC13-7-11-8	"	MIV-96-3/S-11-1-25 PY	Py		4.1	"	"	"	
NICO	NC13-7-11-8	"	MIV-96-2/S-11-1-25 PY	Py		4.5	"	"	"	
NICO	NC13-7-11-8	"	MIV-95-11/S-11-1-25 PY	Py		5.3	"	"	"	
NICO	NC13-7-11-8	"	MIV-95-10/11-1-25 PY	Py		5.4	"	"	"	
NICO	NC227-128.87-129.16A	LSI-S-11-1-1	MIV-90-4/S-11-1-1 Ccp	Ccp	N-227	5.0	apy-py-Bi-ccp-cob	metasiltstones	Vein	ML
NICO	NC227-128.87-129.16A	"	MIV-90-3/S-11-1-1 Ccp	Ccp	N-227	4.1	"	"	"	
NICO	NC227-128.87-129.16A	"	MIV-90-2/S-11-1-1 APY	Apy	N-227	2.5	"	"	"	
NICO	NC227-128.87-129.16A	"	MIV-90-1/S-11-1-1 APY	Apy	N-227	3.8	"	"	"	

NICO	NC227-128.87-129.16A	"	MIV-103-4/S-11-1-1 APY (no GC)	Apy	N-227	3.7	"	"	"	
NICO	NC227-128.87-129.16A	"	MIV-103-3/S-11-1-1 Ccp (no GC)	Ccp	N-227	5.7	"	"	"	
NICO	NC227-128.87-129.16A	"	MIV-103-2/S-11-1-1 Ccp	Ccp	N-227	5.5	"	"	"	
NICO	NC227-128.87-129.16A	"	MIV-103-1/S-11-1-1 APY	Apy	N-227	5.1	"	"	"	
NICO	NC275-157.77-157.83	LSI-S-11-1-28	MIV-101-9/S-11-1-28 APY (no GC)	Apy	N-275	4.7	apy-py-ccp	metasiltstones	disseminated along the bedding	LL
NICO	NC275-157.77-157.83	"	MIV-101-8/S-11-1-28 APY (no GC)	Apy	N-275	4.3	"	"	"	
NICO	NC275-157.77-157.83	"	MIV-101-7/S-11-1-28 ASP (no GC)	Apy	N-275	5.1	"	"	"	
NICO	NC275-157.77-	"	MIV-101-6/S-11-1-	Apy	N-275	6.3	"	"	"	

	157.83		28 APY (no GC)							
NICO	NC275-157.77-157.83	"	MIV-101-4/S-11-1-28 APY (no GC)	Apy	N-275	0.0	"	"	"	
NICO	NC275-157.77-157.83	"	MIV-101-3/S-11-1-28 APY (no GC)	Apy	N-275	6.9	"	"	"	
NICO	NC275-157.77-157.83	"	MIV-101-13/S-11-1-28 APY(no GC)	Apy	N-275	4.9	"	"	"	
NICO	NC275-157.77-157.83	"	MIV-101-12/S-11-1-28 PY(no GC)	Py	N-275	5.3	"	"	"	
NICO	NC275-157.77-157.83	"	MIV-101-11/S-11-1-28 PY(no GC)	Py	N-275	6.4	"	"	"	
NICO	NC275-157.77-157.83	"	MIV-101-10/S-11-1-28 APY(no GC)	Apy	N-275	4.8	"	"	"	
NICO	NC95-50-	LSI-S-11-1-26	MIV-88-9/S-11-1-	Apy	NC-95	6.7	apy-(py)	Porphyry	disseminated in patches	ML

	42.27-42.34		26 APY (no GC)						
NICO	NC95-50-42.27-42.34	"	MIV-88-6/S-11-1-26 P (no GC)	Py	NC-95	5.5	"	"	"
NICO	NC95-50-42.27-42.34	"	MIV-88-5/S-11-1-26 APY (no GC)	Apy	NC-95	5.6	"	"	"
NICO	NC95-50-42.27-42.34	"	MIV-102-9/S-11-1-26 APY (no GC)	Apy	NC-95	5.1	"	"	"
NICO	NC95-50-42.27-42.34	"	MIV-102-8/S-11-1-26 APY (no GC)	Apy	NC-95	5.5	"	"	"
NICO	NC95-50-42.27-42.34	"	MIV-102-6/S-11-1-26 APY	Apy	NC-95	5.6	"	"	"
NICO	NC95-50-42.27-42.34	"	MIV-102-5/S-11-1-26 APY	Apy	NC-95	5.5	"	"	"
NICO	NC95-50-	"	MIV-102-4/S-11-1-	Apy	NC-95	11.4	"	"	"

	42.27-42.34		26 APY						
NICO	NC95-50-42.27-42.34	"	MIV-102-3/S-11-1-26 APY	Apy	NC-95	4.7	"	"	"
NICO	NC95-50-42.27-42.34	"	MIV-102-12/S-11-1-26 Ccp	Ccp	NC-95	4.9	"	"	"
NICO	NC95-50-42.27-42.34	"	MIV-102-11/S-11-1-26 APY	Apy	NC-95	4.0	"	"	"
NICO	NC95-50-42.27-42.34	"	MIV-102-10/S-11-1-26 APY	Apy	NC-95	4.9	"	"	"
NORI	Vein A	LSI-S-11-1-35	MIV-100-12/S-11-1-35 MO (no GC)	Mo		3.3	mo	matasiltstones	Vein
NORI	Vein A	"	MIV-100-10/S-11-1-35 MO (no GC)	Mo		2.9	"	"	"
NORI	Vein G	LSI-S-11-1-36	MIV-98-4/S-S-11-	Py		2.6	mo-py	metasiltstones	Vein

NORI	Vein G	"	1-36 PY MIV-98-3/S-S-11-1-36 PY	Py		2.5	"	"	"
NORI	Vein G	"	MIV-98-2/S-S-11-1-36 PY	Py		2.4	"	"	"
NORI	Vein G	"	MIV-97-11/S-11-1-36 PY	Py		3.7	"	"	"
NORI	Vein G	"	MIV-97-12/S-11-1-36 PY	Py		3.3	"	"	"
SUE DIANNE	SD9705-137.13-137.28	LSI-S-11-1-03	MIV-91-4/S-11-1-21 Ccp	Ccp	SD-05	-5.6	Ccp	Ignimbrites	Breccia
SUE DIANNE	SD9705-137.13-137.28	"	MIV-91-2/S-11-1-21 Ccp	Ccp	SD-05	-5.8	"	"	"
SUE DIANNE	SD9705-137.13-137.28	"	MIV-90-12/S-11-1-21 Ccp	Ccp	SD-05	-5.5	"	"	"
SUE DIANNE	SD97-05-137.13-137.28	"	MIV-99-6/S-11-1-24 Ccp (no GC)	Ccp	SD-05	-5.5	"	"	"
SUE DIANNE	SD97-05-	"	MIV-99-5/S-11-1-	Ccp	SD-05	-5.6	"	"	"

	137.13-137.28		24 Ccp (no GC)						
SUE DIANNE	SD97-05-137.13-137.28	"	MIV-99-3/S-11-1-24 Ccp	Ccp	SD-05	4.4	"	"	"
SUE DIANNE	SD9842-123.43-123.59	LSI-S-11-1-10	MIV-92-1/S-11-1-10 Ccp	Ccp	SD-42	-5.9	Ccp	Ignimbrites	Breccia
SUE DIANNE	SD9842-123.43-123.59	"	MIV-91-12/S-11-1-10 Ccp	Ccp	SD-42	-5.2	"	"	"
SUE DIANNE	SD9842-123.43-123.59	"	MIV-91-11/S-11-1-10 Ccp (no GC)	Ccp	SD-42	-4.1	"	"	"
SUE DIANNE	SD9830-21.50-21.59	LSI-S-11-1-20	MIV-91-9/S-11-1-20 Ccp	Ccp	SD-30	-3.8	ccp-bn-(Cu-Bi-sulf)	Ignimbrites	Breccia
SUE DIANNE	SD9830-21.50-21.59	"	MIV-91-8/S-11-1-20 Ccp	Ccp	SD-30	-7.8	"	"	"
SUE DIANNE	SD9830-21.50-21.59	"	MIV-91-7/S-11-1-20 Ccp	Ccp	SD-30	-6.2	"	"	"
SUE DIANNE	SD9830-21.50-21.59	"	MIV-91-10/S-11-1-20 Ccp	Ccp	SD-30	-7.4	"	"	"

SUE DIANNE	SD9842-109.29-109.56	LSI-S-11-1-19	MIV-99-11/S-11-1-19 Ccp	Ccp	SD-42	-2.7	ccp-(Cu-Bi-sulf)-py	Ignimbrites	Breccia
SUE DIANNE	SD9842-109.29-109.56	"	MIV-100-3/S-11-1-19 Ccp (no GC)	Ccp	SD-42	1.4	"	"	"
SUE DIANNE	SD9842-109.29-109.56	"	MIV-100-2/S-11-1-19 Ccp (no GC)	Ccp	SD-42	-0.6	"	"	"
SUE DIANNE	SD9842-109.29-109.56	"	MIV-100-1/S-11-1-19 Ccp	Ccp	SD-42	-0.3	"	"	"
SUE DIANNE	SD9842-140.50-140.59	LSI-S-11-1-6	MIV-90-9/S-11-1-6 Ccp	Ccp	SD-42	-3.0	ccp	Ignimbrite	Breccia
SUE DIANNE	SD9842-140.50-140.59	"	MIV-90-8/S-11-1-6 Ccp	Ccp	SD-42	-3.2	"	"	"
SUE DIANNE	SD9842-140.50-140.59	"	MIV-90-7/S-11-1-6 Ccp	Ccp	SD-42	-1.3	"	"	"
SUE DIANNE	SD9842-140.50-140.59	"	MIV-90-11/S-11-1-6 Ccp	Ccp	SD-42	1.0	"	"	"
SUE DIANNE	SD9842-144.90-	LSI-S-11-1-6	MIV-93-5/S-11-1-	Ccp	SD-42	-3.1	ccp	Ignimbrite	Breccia

	145.02		04 Ccp						
SUE DIANNE	SD9842-76.52-76.62	LSI-S-11-1-03	MIV-92-8/S-11-1-03 Ccp	Ccp	SD-42	-6.8	ccp-bn	Ignimbrite	Breccia
SUE DIANNE	SD9842-76.52-76.62	"	MIV-92-7/S-11-1-03 Ccp	Ccp	SD-42	-5.5	"	"	"
TLG	TL-6			BR		-1.6	Lower siltstone unit		
TLG	TL-15			BR		5.5	Lower siltstone unit		
TLG	TL-4			BR		1.1	Lower siltstone unit		

Py, pyrite; apy, arsenopyrite; ccp, chalcopyrite; mo, molybdenite; BR, bulk rock analysis. UL, upper lense; ML, middle lense; LL, lower lense.

Appendix C. Copper isotopes data

Location	Sample	Laboratory analysis	δ^{65}Cu (‰)	Drill hole	Mineral	Comment	Mineralization
NICO	-88	N88-15	-1.02	N-205	Ccp	Ca-Fe altered metasiltstone	Vein
NICO	-88	N88-15.1	-0.96	N-205	"	Ca-Fe altered metasiltstone	Vein
NICO	-88	N88-13	-0.96	N-205	"	Ca-Fe altered metasiltstone	Vein
NICO	-88	N88-14	-0.89	N-205	"	Ca-Fe altered metasiltstone	Vein
NICO	-88	N88-03	-0.83	N-205	"	Ca-Fe altered metasiltstone	Vein
NICO	-88	N88-02	-0.82	N-205	"	Ca-Fe altered metasiltstone	Vein
NICO	-88	N88-8.2	-0.81	N-205	"	Ca-Fe altered metasiltstone	Vein
NICO	-88	N151-27	-0.99	N-228	"	Ca-Fe altered metasiltstone	Vein
NICO	-151	N151-29	-0.97	N-228	"	Ca-Fe altered metasiltstone	Vein
NICO	-151	N151-15	-0.95	N-228	"	Ca-Fe altered metasiltstone	Vein
NICO	-151	N151-33	-0.92	N-228	"	Ca-Fe altered metasiltstone	Vein
NICO	-151	N151-13	-0.86	N-228	"	Ca-Fe altered metasiltstone	Vein

NICO	-151	N151-10	-0.85	N-228	"	Ca-Fe altered metasiltstone	Vein
NICO	-111	N111-03	-0.75	N-243	"	Ca-Fe altered metasiltstone	disseminated along the bedding
NICO	-111	N111-01	-0.73	N-243	"	Ca-Fe altered metasiltstone	disseminated along the bedding
NICO	-111	N111-02	-0.73	N-243	"	Ca-Fe altered metasiltstone	disseminated along the bedding
NICO	-111	N111-03	-0.70	N-243	"	Ca-Fe altered metasiltstone	disseminated along the bedding
NICO	-128	NC-128-16	-0.71	N-227	"	Ca-Fe altered metasiltstone	Vein
NICO	-128	NC-128-04	-0.68	N-227	"	Ca-Fe altered metasiltstone	Vein
NICO	-128	NC-128-02	-0.65	N-227	"	Ca-Fe altered metasiltstone	Vein
NICO	-128	NC-128-03	-0.65	N-227	"	Ca-Fe altered metasiltstone	Vein
NICO	-128	NC-128-01	-0.62	N-227	"	Ca-Fe altered metasiltstone	Vein
NICO	-128	NC128-08	-0.60	N-227	"	Ca-Fe altered metasiltstone	Vein
NICO	-128	NC-128-09B	-0.57	N-227	"	Ca-Fe altered metasiltstone	Vein

NICO	-128	NC-128-13	-0.55	N-227	"	Ca-Fe altered metasiltstone	Vein
NICO	-128	NC-128-15	-0.54	N-227	"	Ca-Fe altered metasiltstone	Vein
NICO	-128	NC128-09	-0.48	N-227	"	Ca-Fe altered metasiltstone	Vein
NICO	-128	NC128-10	-0.46	N-227	"	Ca-Fe altered metasiltstone	Vein
NICO	-128	NC128-06	-0.45	N-227	"	Ca-Fe altered metasiltstone	Vein
NICO	-128	NC-128-05	-0.34	N-227	"	Ca-Fe altered metasiltstone	Vein
DAMP	523C	DAMP10	-0.82		"	Felsic volcanics/Rhyodacites	Mineralized Breccia
DAMP	523C	DAMP7	-0.81		"	Felsic volcanics/Rhyodacites	Mineralized Breccia
DAMP	523C	DAMP13	-0.78		"	Felsic volcanics/Rhyodacites	Mineralized Breccia
DAMP	523C	DAMP11	-0.78		"	Felsic volcanics/Rhyodacites	Mineralized Breccia
DAMP	523C	DAMP31	-0.77		"	Felsic volcanics/Rhyodacites	Mineralized Breccia
DAMP		DAMP30	-0.76		"	Felsic	Mineralized

	523C				volcanics/Rhyodacites	Breccia
DAMP	523C	DAMP29	-0.74	"	Felsic volcanics/Rhyodacites	Mineralized Breccia
DAMP	523C	DAMP8	-0.74	"	Felsic volcanics/Rhyodacites	Mineralized Breccia
DAMP	523C	DAMP9	-0.69	"	Felsic volcanics/Rhyodacites	Mineralized Breccia
DAMP	523C	DAMP28	-0.66	"	Felsic volcanics/Rhyodacites	Mineralized Breccia
DAMP	523A	3523A-01	-0.78	"	Felsic volcanics/Rhyodacites	Mineralized Breccia
DAMP	523A	3523A-04	-0.88	"	Felsic volcanics/Rhyodacites	Mineralized Breccia
DAMP	523A	3523A-07	-0.81	"	Felsic volcanics/Rhyodacites	Mineralized Breccia
DAMP	523A	3523A-09	-0.79	"	Felsic volcanics/Rhyodacites	Mineralized Breccia
DAMP	523A	3523A-02	-0.77	"	Felsic volcanics/Rhy	Mineralized Breccia

						odacites	
DAMP	523A	3523A-03	-0.75		"	Felsic volcanics/Rhyodacites	Mineralized Breccia
DAMP	523A	3523A-14	-0.67		"	Felsic volcanics/Rhyodacites	Mineralized Breccia
DAMP	523A	3523A-08	-0.65		"	Felsic volcanics/Rhyodacites	Mineralized Breccia
DAMP	523A	3523A-06	-0.63		"	Felsic volcanics/Rhyodacites	Mineralized Breccia
DAMP	523A	3523A-15	-0.63		"	Felsic volcanics/Rhyodacites	Mineralized Breccia
Sue Dianne	D-137	SD137-03	-1.23	SD9705	"	Felsic volcanis/Ignimbrites	Mineralized Breccia
Sue Dianne	D-137	SD137-01.1	-1.21	SD9705	"	Felsic volcanis/Ignimbrites	Mineralized Breccia
Sue Dianne	D-137	SD137-06	-1.19	SD9705	"	Felsic volcanis/Ignimbrites	Mineralized Breccia
Sue Dianne	D-137	SD137-07	-1.16	SD9705	"	Felsic volcanis/Ignimbrites	Mineralized Breccia

Sue Dianne	D-137	SD137-01	-1.16	SD9705	"	Felsic volcanis/Ignimbrites	Mineralized Breccia
Sue Dianne	D-137	SD137-14	-1.15	SD9705	"	Felsic volcanis/Ignimbrites	Mineralized Breccia
Sue Dianne	D-137	SD137-02	-1.15	SD9705	"	Felsic volcanis/Ignimbrites	Mineralized Breccia
Sue Dianne	D-137	SD137-15	-1.13	SD9705	"	Felsic volcanis/Ignimbrites	Mineralized Breccia
Sue Dianne	D-137	SD137-12	-1.11	SD9705	"	Felsic volcanis/Ignimbrites	Mineralized Breccia
Sue Dianne	D-137	SD137-11.2	-1.11	SD9705	"	Felsic volcanis/Ignimbrites	Mineralized Breccia
Sue Dianne	D-137	SD137-10	-1.10	SD9705	"	Felsic volcanis/Ignimbrites	Mineralized Breccia
Sue Dianne	D-137	SD137-13	-1.08	SD9705	"	Felsic volcanis/Ignimbrites	Mineralized Breccia
Sue Dianne	D-137	SD137-11	-1.08	SD9705	"	Felsic volcanis/Ignimbrites	Mineralized Breccia
Sue		SD137-11.1	-1.04	SD9705	"	Felsic	Mineralized

Dianne	D-137					volcanis/Ignimbrites	Breccia
Sue Dianne	D-153	SD153-62	-0.97	SD98-42	"	Felsic volcanis/Ignimbrites	Mineralized Breccia
Sue Dianne	D-153	SD153-60	-0.96	SD98-42	"	Felsic volcanis/Ignimbrites	Mineralized Breccia
Sue Dianne	D-153	SD153-61	-0.90	SD98-42	"	Felsic volcanis/Ignimbrites	Mineralized Breccia
Sue Dianne	D-153	SD153-62.1	-0.88	SD98-42	"	Felsic volcanis/Ignimbrites	Mineralized Breccia
Sue Dianne	D-153	SD153-58	-0.86	SD98-42	"	Felsic volcanis/Ignimbrites	Mineralized Breccia
Sue Dianne	D-153	SD153-57	-0.86	SD98-42	"	Felsic volcanis/Ignimbrites	Mineralized Breccia
Sue Dianne	D-153	SD153-57	-0.81	SD98-42	"	Felsic volcanis/Ignimbrites	Mineralized Breccia
Sue Dianne	D-153	SD153-59	-0.80	SD98-42	"	Felsic volcanis/Ignimbrites	Mineralized Breccia
FAB	517A	3517A-08	-0.73		"	Felsic volcanics/Rhy	Veins-breccia

					odacites	
FAB	517A	3517a-2	-0.72	"	Felsic volcanics/Rhyodacites	Veins-breccia
FAB	517A	3517A-06	-0.69	"	Felsic volcanics/Rhyodacites	Veins-breccia
FAB	517A	3517A-07	-0.69	"	Felsic volcanics/Rhyodacites	Veins-breccia
FAB	517A	3517A-05	-0.61	"	Felsic volcanics/Rhyodacites	Veins-breccia
FAB	517A	3517A-03	-0.60	"	Felsic volcanics/Rhyodacites	Veins-breccia
FAB	517A	3517A-04	-0.60	"	Felsic volcanics/Rhyodacites	Veins-breccia